



<https://theses.gla.ac.uk/>

Theses Digitisation:

<https://www.gla.ac.uk/myglasgow/research/enlighten/theses/digitisation/>

This is a digitised version of the original print thesis.

Copyright and moral rights for this work are retained by the author

A copy can be downloaded for personal non-commercial research or study,
without prior permission or charge

This work cannot be reproduced or quoted extensively from without first
obtaining permission in writing from the author

The content must not be changed in any way or sold commercially in any
format or medium without the formal permission of the author

When referring to this work, full bibliographic details including the author,
title, awarding institution and date of the thesis must be given

Enlighten: Theses

<https://theses.gla.ac.uk/>
research-enlighten@glasgow.ac.uk

TEM STUDIES OF III-V MOSFETs FOR ULTIMATE CMOS

Paolo Longo



**University
of Glasgow**

**Presented as a thesis for the degree of Ph.D. at the
Department of Physics and Astronomy, University of Glasgow.**

January, 2008

© Paolo Longo, 2008

ProQuest Number: 10753930

All rights reserved

INFORMATION TO ALL USERS

The quality of this reproduction is dependent upon the quality of the copy submitted.

In the unlikely event that the author did not send a complete manuscript and there are missing pages, these will be noted. Also, if material had to be removed, a note will indicate the deletion.



ProQuest 10753930

Published by ProQuest LLC (2018). Copyright of the Dissertation is held by the Author.

All rights reserved.

This work is protected against unauthorized copying under Title 17, United States Code
Microform Edition © ProQuest LLC.

ProQuest LLC.
789 East Eisenhower Parkway
P.O. Box 1346
Ann Arbor, MI 48106 – 1346

GLASGOW
UNIVERSITY
LIBRARY:

ABSTRACT

Over the past half-century electronic industry has enormously grown changing the way people live their lives. Such growth has been driven by the miniaturisation and development of the transistors which are the main components in an integrated circuit (IC) commonly referred as a chip. Until today electronic industry has been based on the use of Si and its native oxide SiO₂ in transistors. However, the performance limit of conventional Si based transistors is rapidly being approached and alternatives will soon be required. One of the proposed alternatives is GaAs. n-type GaAs has a mobility 5 times higher than Si. This makes it a suitable candidate for MOSFETs devices. So far, GaAs has not been used for practical MOSFETs because of the difficulties of making a good dielectric oxide layer in terms of leakage current and unpinned Fermi Level. Using processes pioneered by Passlack *et al*, dielectric gate stacks consisting of a template layer of amorphous Ga₂O₃ followed by amorphous GdGaO have been grown on GaAs substrates. Careful deposition of Ga₂O₃ can leave the Fermi Level unpinned. The introduction of Gd is important in order to decrease the leakage of current. The electrical properties of the Ga₂O₃/Gd_xGa_{0.4-x}O_{0.6} dielectric stack are related to the Gd concentration and the quality of the GaAs/Ga₂O₃ interface.

Over the past years in a unique partnership several research groups from the Physics and the Electronic and Electrical engineering Department have collaboratively worked for the realisation and development of such new generation of GaAs based transistors using the technology described above. The properties of such devices depend on structures at the nanoscale which is only few atoms across. Thus the characterization using the transmission electron microscope (TEM) becomes essential.

In this project TEM has been used to study several MBE grown III-V semiconductor nanostructures. In particular most of the thesis is focussed on the chemical characterisation of the GaAs/Ga₂O₃/GGO dielectric gate stack, mainly using electron energy loss spectroscopy (EELS) and high-resolution scanning Transmission electron microscopy (STEM) imaging. As said above the quality of such interfaces affects the properties of the whole device. Hence the results presented herein represent an important feedback for the realisation of world performance GaAs devices.

Background information on the type of III-V materials that were studied in this project is given in chapter 1. This information involves a description of the GaAs/Ga₂O₃/GGO interface. In addition the molecular beam epitaxy technique employed for the growth of these structures is explained.

Chapter 2 deals with the experimental apparatus and techniques employed to characterise the various materials. For instance, the chapter begins with a short introduction to the foundations of electron microscopy such as electron lenses and guns. The conventional transmission electron microscopy (CTEM) and STEM imaging techniques are explained along with electron energy loss spectroscopy (EELS). An introduction to the theory of energy loss near edge structure (ELNES) is also given. ELNES is dependent on the local chemical and structural environment of the absorbing atom. The three electron microscopes utilised in this project are also described. These instruments comprise a Tecnai F20 and T20 and SuperSTEM1. In the case of the SuperSTEM1 the method of the aberration correction is also outlined. However, most of the results presented in this thesis were obtained using the F20 and partly the T20. Finally a summary of the specimen preparation techniques are given at the end of this chapter.

Chapter 3 deals with modelling of the fine structure business. As said in chapter, the interactions which cause ELNES are complex and not well understood, making the interpretation of the fine structure from complex materials very difficult. By modelling the fine structure and investigating how changes in the model affect the spectral features, can improve the understanding of the data experimentally collected. A detailed description of the multiple scattering technique which was exclusively used is given.

However the Ga₂O₃/GGO dielectric gate stacks turned out to be electron beam sensitive. High electron dose changes the chemical structure. In chapter 4 some examples of e⁻ damage effects are shown. In particular phenomena such crystallisation and phase separation usually occur when the dose is high. These problems make almost impossible to acquire any ELNES data as a high dose is required in order to get a well-resolved spectrum. Thus the simulation work was halted as it did not seem to offer useful support for the main project.

Chapter 4 deals with the compositional analysis across the GGO layer of a wide range of samples using EELS spectrum imaging (SI). By recording EELS spectra over the energy range from the O K-edge to the As L_{2,3}-edges allows characteristic edges of Ga, As, Gd and O to be extracted. Their intensity can be converted to atomic fraction by using proper standards. The results shown in this

chapter show excellent agreement with the ones obtained using Rutherford backscattered spectroscopy as analytical technique.

Chapter 5 deals with investigation of the effects of three different etching processes on the GaAs/Ga₂O₃/GGO dielectric gate stack. This investigation was mainly carried out using energy filtering transmission electron microscopy (EFTEM) in the Tecnai T20. EFTEM provides a quick analysis of the structure. Thus it is really useful when large areas need to be analysed. One of the three etching processes has been characterised also using EELS SI. EELS SI offers much better spatial resolution and the possibility to apply the data processing developed in chapter 4 to quantitatively characterise the material and obtain information on the composition.

Background information on the EFTEM and the effects of the objective aperture on the acquisition of filtering images are also given.

The aim of the analysis described in chapter 5 is to develop a way to study the effects of etching processes on the GaAs/Ga₂O₃/GGO structure. This obviously represents a very important issue for fabrication purposes.

Finally in chapter 6, a detailed analysis of the interface GaAs/Ga₂O₃/GGO was carried out using HAADF STEM imaging. High angle annular dark field (HAADF) imaging carried out in the STEM has revealed to be an excellent method for characterizing the interfaces as the contrast is sensitive to the atomic number. Images were acquired using both F20 and SuperSTEM1 electron microscopes. The use of the second one has allowed to get a better insight on the interface as it is fitted with an aberration corrector. Hale's model [8] predicts that the interface appears to be different whether it is observed along the [110] or the [1-10] direction. Thus TEM specimens of two different samples have been prepared cutting the original wafer off along two perpendicular directions. This ensured the possibility to look at the interface along [110] and [1-10] directions. While some differences are seen, the period dribbling predicted by the Hale mode is absent. A more detailed investigation is required.

ACKNOWLEDGEMENTS

Firstly I would like to thank my principal supervisor Prof. Alan Craven for his continuous help over the last three years. I am also grateful to him as he offered me the EPSRC scholarship whose money has given the possibility to maintain myself here in Glasgow over the last three years.

I am also grateful for the training on the Tecnai T20 received from Mr Colin How. He was the very first person who taught me how to operate and drive a TEM. Dr. Jamie Scott taught me how to operate the Tecnai F20 either in CTEM and in STEM mode. From him I learned how to deal with the alignment operation in STEM mode which is more complicated than in CTEM mode.

I am very grateful for the general assistance provided by Dr Maureen MacKenzie and Dr Sam McFadzean throughout all my PhD time. In particular Dr Maureen MacKenzie helped me out in optimising the experimental conditions used for the acquisition of the data presented in chapter 4.

I would like to thank Mr Brian Miller for preparing all the TEM samples investigated throughout the PhD. He also gave the training on the specimen preparation.

The thesis would not been possible without materials to investigate. Therefore, I am grateful with Dr Martin Holland for providing the as grown material by MBE and Dr Richard Hill for the as etched processed material.

I would like to thank the other members of the SSP group former and not, for their entertaining environment. Unfortunately some of them have already left the group.

I would like also to thank my parents and brother Marco for their continual support and encouragement which has allowed me to undertake this work out of my country.

Finally I would like to thank few friends of mine who have made my life in Glasgow not only about PhD. In particular most the people who used to live in the same building when I first moved to Glasgow. Not to forget other Italian friends such as Bruno, Claudio, Matteo, Oberdan, Antonio, Ciccio, Alessandro, Ivan, Ignazio and the people from the Italian restaurant Villa Toscana. I do not want to forget my flatmate Gaurav I spend lots of time with playing football with the

playstation. He is still trying to beat me. Concluding I am also grateful with all the people from the Physics Department I play football with on Thursday at lunch.

DECLARATION

This thesis is the record of the work carried out by me in the Department of Physics and astronomy at the University of Glasgow. The work described herein is my own, except for Fig. 2.8 which is supplied by the SuperSTEM team, the results shown in Figs 6.5 and 6.6 which are provided by Paul Robb, Figs 6.7 and 6.8 provided by Michael Finnie and most of the SuperSTEM images shown in chapter 6 were recorded with the help of Dr B. Mendis. Some of the work given in this thesis can be found in the following papers:

"GdGaO: A gate dielectric for GaAs metal-oxide-semiconductor field-effect transistors" M Holland, CR Stanley, W Reid, I Thayne, GW Paterson, AR Long, P Longo, J Scott, AJ Craven, R Gregory, Vac Sci Technol B 25, 1024-1028, 2007

"Characteristics of GdGaO grown by MBE", M Holland, P Longo, GW Paterson, W Reid, AR Long, CR Stanley, AJ Craven, IG Thayne, and R Gregory, submitted to Microelectronics Engineering

"Elemental profiling of III-V MOSFET high-k dielectric gate stacks using EELS Spectrum imaging", P Longo, AJ Craven, J Scott, M Holland and IG Thayne, accepted for publication in the proceedings of MSM 2007

"EFTEM and EELS SI: tools for investigating the effects of etching processes for III-V MOSFET devices" P Longo, J Scott, AJ Craven, RWJ Hill and IG Thayne, accepted for publication in the proceedings of EMAG 2007

The thesis has not previously submitted for a higher degree.

CONTENTS

Abstract

Acknowledgements

Declaration

Chapter 1: Introduction	1
1.1 Moore's law	1
1.2 MOSFET system	2
1.3 MBE growth	6
1.4 Transmission Electron Microscopy	6
1.4.1 Conventional electron microscopy	8
1.4.2 Analytical Electron Microscopy	9
1.5 Theoretical calculations	12
1.6 Outline of the thesis	13
Chapter 2: Electron microscopy and analysis	14
2.1 Introduction	14
2.2 Electron microscope	14
2.2.1 <i>FEI Tecnai F20 and T20</i>	15
2.3 Electron sources/guns	15
2.3.1 Introduction	15
2.3.2 Field emission guns	16
2.3.3 Thermionic guns (LaB ₆)	17
2.4 Column	19
2.5 Imaging in CTEM	27
2.6 Imaging in STEM	27
2.6.1 Aberration corrected STEM	28
2.6.1.1 Electron lenses and aberrations	28
2.6.1.2 SuperSTEM1 instrument	29
2.6.1.3 Method of aberration correction in SuperSTEM1	32
2.7 Electron energy loss spectroscopy	33

2.7.1 ELNES	36
2.7.2 Specimen alignment for collection of EELS data	38
2.7.3 Gatan-ENFINA PEELS Spectrometer	40
2.7.4 Imaging Spectrometer GIF	41
2.7.5 Spectrometer alignment for collection of EELS data	43
2.7.6 Fast Beam switch (FBS)	45
2.8 TEM specimen preparation	48
2.8.1 Powders	48
2.8.2 Thin films	48
Chapter 3: Theoretical modelling and techniques	51
3.1 Introduction	51
3.2 Real space multiple scattering	51
3.2.1 Theory	51
3.2.2 Broadening	52
3.2.3 Core hole effects	53
3.2.4 Running a calculation	53
3.2.4.1 Atoms input	53
3.2.4.2 FEFF input	54
3.3 Oxygen K-edge: comparison between XANES simulations and experimental ELNES results	55
3.4 Conclusions	66
3.4.1 Radiation sensitivity of the GaAs/Ga ₂ O ₃ /GGO dielectric gate stack	66
Chapter 4: Compositional analysis of GGO layer as grown by EELS spectrum imaging (SI)	69
4.1 EELS SI	69
4.1.1 Zero-loss acquisition	71
4.1.2 Core-loss acquisition	72
4.1.3 Dose sensitivity and setting exposure time	76
4.1.4 Performing EELS SI	77

4.2 Compositional analysis	80
4.2.1 Introduction	80
4.2.2 Use of the RBS as standard	81
4.2.3 Use of the $Gd_3Ga_5O_{12}$ as standard	83
4.2.4 The Multiple linear-least squares fitting MLLS	84
4.2.5 Manual approach	86
4.2.6 Conversion of the edge intensity to atomic fraction using RBS and $Gd_3Ga_5O_{12}$ as standard	89
4.2.6.1 Use of RBS	89
4.2.6.2 Use of $Gd_3Ga_5O_{12}$	89
4.2.7 Thickness effects on the compositional analysis	90
4.2.8 Results for GGO films using $Gd_3Ga_5O_{12}$ and RBS as standard	96
4.2.8.1 Introduction	96
4.2.8.2 Sample 1	98
4.2.8.3 Sample 2	99
4.2.8.4 Sample 3	100
4.2.8.5 Sample 4	101
4.2.8.6 Sample 5	102
4.2.8.7 Sample 6	103
4.2.8.8 Sample 7	104
4.2.8.9 Discussion	105
4.2.8.10 Accuracy in the determination of the Gd concentration	109
4.2.9 Compositional analysis of GGO after capping with SiN	112
4.2.10 Compositional analysis of thin GGO layer after capping with Pt: simulation of gate metallisation process	114
4.3 Conclusions	118
Chapter 5: Investigation of etching processes by EFTEM and EELS SI	120
5.1 Introduction	120
5.2 EFTEM theory	121
5.3 Experimental conditions	125

5.4 Acquiring energy-filtering images	126
5.4.1 Effects of the objective aperture	127
5.4.1.1 Comparison of bright field images at different objective aperture	128
5.4.1.2 Comparison of Gd elemental maps at different objective apertures	129
5.4.1.3 Comparison of O elemental maps at different objective apertures	131
5.4.1.4 Comparison of Ga elemental maps at different objective apertures	132
5.4.1.5 Discussion	133
5.5 III-V MOSFET devices fabrication	138
5.6 Investigation of 3 etching process cases	140
5.6.1 Introduction	140
5.6.2 Case A	141
5.6.3 Case B	146
5.6.4 Case C	148
5.6.5 Conclusions of the analysis of etching processes	159
Chapter 6: Investigation of the GaAs/Ga₂O₃/GGO interface region	160
6.1 The GaAs/Ga ₂ O ₃ /GGO interface	160
6.2 HAADF STEM imaging	
6.2.1 Channelling of the HAADF STEM signal	164
6.2.1.1 SuperSTEM1 case	167
6.2.1.2 Tecnai F20 case	169
6.3 Experimental results of the GaAs/Ga ₂ O ₃ /GGO interface region	171
6.3.1 Investigation of the interface region GaAs/Ga ₂ O ₃	171
6.3.2 Investigation of the interface GaAs/Ga ₂ O ₃ /GGO	173
6.3.2.1 Sample A	174
6.3.2.2 Sample B	176
6.3.2.3 Sample C	181
6.4 Conclusions	184

Chapter 7: Conclusions and further work	185
7.1 Conclusions	185
7.2 Further work	187
References	192

CHAPTER 1: INTRODUCTION

The rapid and continuing growth of the electronic industry over the past half-century to become the globe's largest single industry has revolutionised the world, changing much of the way in which people live their lives. Semiconductor devices are the foundations of the electronic industry and the increase in their performance due to their development, miniaturisation, and integration is the principal driving force for growth in electronic industry. At the core of much of the growth of the semiconductor industry is the use of Si and its oxide, SiO₂, in transistors. However, the performance limit of conventional Si based transistors is rapidly being approached and alternatives will soon be required.

1.1 MOORE'S LAW

Over the years the development of the microelectronic industry has followed on the Moore's law, whose most important formulation is the doubling of the number of transistors on integrated circuits every two years. Almost every measure of the capabilities of digital electronic devices is linked to Moore's Law: processing speed, memory capacity and even the resolution of digital cameras. All of these improve roughly at exponential rates as well. Moore's Law describes this driving force of technological and social change in the late 20th and early 21st centuries. Moore's Law also refers to the rapidly continuing advance in computing power per unit cost because the increase in the number of transistor count is also a rough measure of computer processing power. Although Moore's Law was initially made in form of an observation, it became then accepted as goal for the entire microelectronic industry. This has driven entire engineering and marketing department of semiconductor industries to fulfil the trend of the increase in the processing power that it was presumed.

Regarding the future trends of the Moore's Law, computer industry technology "road maps" predicts that Moore's Law will continue for several chip generations. Obviously this does not mean that there will not be any engineering or scientific challenges. In particular, as said above, so far the microelectronic industry has been based on Si and its oxide. However at the moment the minimum thickness for the SiO₂ dielectric gate stack has been reached, further scaling will result in the formation of a dielectric layer with high leakage current and therefore useless for transistor purposes. New materials have to be investigated in order to fulfil Moore's Law for

the next decades. In particular, as shown in the International Technology Road Map for Semiconductor (ITRS), by the 2013 new technologies such as III-V based transistors along with carbon nanotube and nanowire will be employed. Therefore, it is likely such transistors will be seen in the electronic devices in 10 years time. At the moment the biggest effort of engineers and scientist is focused on the improvement of the performance.

1.2 MOSFET SYSTEM

One of the most important development in the electronic industry is the integrated circuit (IC) commonly referred to as a chip. An IC is a circuit composed of active and passive components such as transistors and resistors. ICs are important because they allow increased functionality at lower cost. By integrating several devices onto a smaller area, the IC allows reduced circuit size, reduced manufacturing cost, increased circuit complexity, lower power dissipation and higher overall switching speed. Performance improvements can be obtained through a systematic reduction in the size of its main active components: the transistors.

ICs can be divided into three categories: analogue, digital and mixed signal. At the core of each system is the transistor. Analogue ICs are used for the signal amplification and real time filtering signal. In digital ICs, the most important feature is the ability of the transistors to switch between conducting (on) and insulating (off) states. In mixed signal ICs analogue and digital devices are integrated onto a single chip. In this way they allow increased functionality. However, digital circuits are the basis of digital computers, microprocessors and memories. The digital ICs employ electron channel (n-channel) or hole channel (p-channel) oxide field of effect transistors (MOSFETs). Fig. 1.1 shows a schematic diagram of a n-channel GaAs based MOSFET.

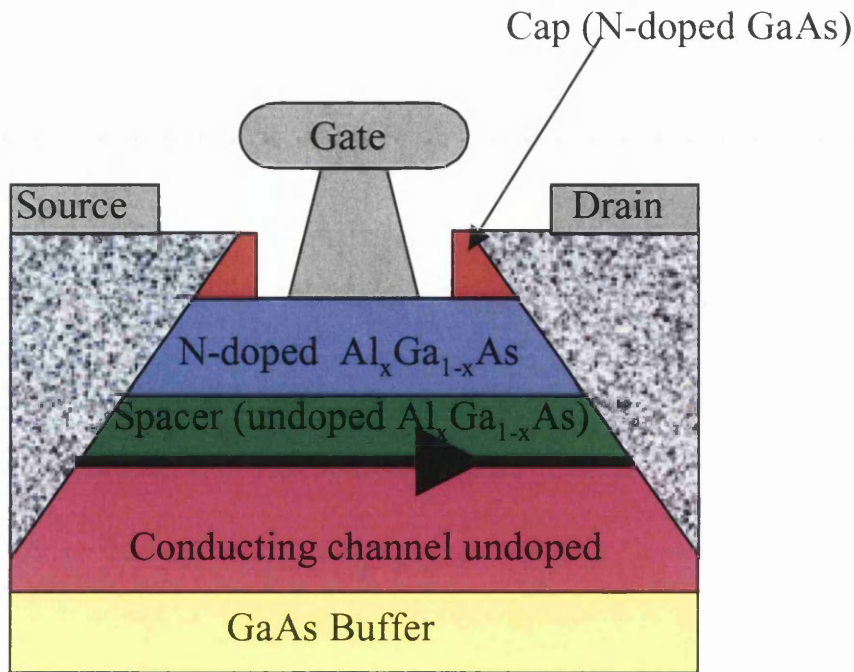


Fig. 1.1 Schematic diagram of a MOSFET system. The carriers are originated in the source, pass through the channel and are collected in the drain region. Source and drain in a MOSFET device are made by the same material and have the same architecture.

In this type of transistor, the current between the source and the drain is a function of both the source-drain voltage and the gate-source voltage. By the source, we mean the region where the majority of the carriers originate while the drain is the region where most of these carriers are collected. The channel is the region separating the source and the drain, its length is important to control the current of the whole system as well as the speed. The gate is the control electrode in a field effect transistor. The heterostructure in the channel region contains layers of N-doped $\text{Al}_x\text{Ga}_{1-x}\text{As}$ and undoped GaAs. Hence the electrons from the donors in the N-doped $\text{Al}_x\text{Ga}_{1-x}\text{As}$ layer travel into the GaAs conducting channel where they become trapped by the difference in the energy band gaps between the two materials. The presence of the undoped $\text{Al}_x\text{Ga}_{1-x}\text{As}$ spacer region further separates the carriers and the ionised donors thereby reducing the ionised impurity scattering. Moreover the shape of the designed to reduce its resistance whilst keeping

its contact with the heterostructure small. On the other hand, the capping layer of GaAs prevents the oxidation of the $\text{Al}_x\text{Ga}_{1-x}\text{As}$ underneath.

III-V technology in comparison with that for silicon has a big advantage: the electron mobility in GaAs is 5 times higher than in Si[1]. This high mobility can be translated into a new generation of high-speed circuits. Nevertheless this big advantage is accompanied by a disadvantage which is the difficulty of fabricating an insulating film with a very low value of bulk trapped charge and a low interfacial density of states at the GaAs interface[2]. During recent years, a great deal of effort has been put into trying to overcome this important crucial problem which has limited the development of III-V technology for MOSFET systems. At this stage it is important to give a general overview about the factors which limit the possibility of creating an appropriate insulating layer. The main factors are:

- 1) FERMI LEVEL PINNING
- 2) LEAKAGE CURRENT

Concerning the first point, it is well known that the Fermi level of GaAs is pinned at the oxide-substrate interface by a very high density of interface states [2]. Until that is overcome, it is impossible to produce any MOSFET systems. No carrier modulation is obtained when a bias voltage is applied to a gate electrode. The reason for the pinning of the Fermi Level appears to be associated with the fact that during the oxidation of GaAs the O_2 initially displaces surface arsenic atoms, and bonds to the gallium atoms in the second layer. Some experiments show that when two oxygen atoms are bonded to a central gallium atom, they withdraw charge from this atom, inducing state formation inside the gap. Therefore the gallium central atom is surely the cause of the Fermi level pinning by direct oxidation [3].

Concerning the second point, the large leakage current of Ga_2O_3 films severely limits their usefulness as a gate oxide for MOSFET applications [4,5]. The reason for this problem is due to the chemical nature of gallium atom. It is well known that Ga tends to have 3 different oxidation states 3+, 2+ and 1+. Therefore it is very difficult to obtain a pure Ga_2O_3 with all the Ga in the 3+, state. This suggests that the high electrical leakage current in the pure gallium oxide films might be caused by traps which are due to the presence of suboxides. This problem can be solved with the presence of heavy elements such as gadolinium which helps to stabilize higher oxidation states for metals with multiple oxidation states [6]. For instance introducing Gd into the Ga_2O_3 results in a low value of leakage of current.

Gd is strongly electropositive and always has an oxidation state of 3+. The presence of Gd helps to stabilize Ga in the highest oxidation state avoiding the presence of suboxides which can act as trap carriers.

It was found that gate dielectric structures such as $Gd_xGa_{0.4-x}O_{0.6-x}/Ga_2O_3/GaAs$ gave a low value of interface density of states (unpinned Fermi level) and a low value of leakage current [7]. Optimum gate oxide stack and oxide/GaAs interface properties have been obtained with a Ga_2O_3 template thickness of 9-11 Å followed by a thicker amorphous mixed oxide layer of Gd and Ga where the minimum required Gd mole percent is 15-17 at. %

The low interface density of states is due at the presence of a monolayer of Ga_2O molecules that forms a charge balanced (2 X 2) surface order that is electronically unpinned [3]. This results from the insertion of Ga_2O molecules as dimers restoring the surface As and Ga atoms to their near bulk charge. Further deposition results in the formation of a stoichiometric amorphous Ga_2O_3 phase [8].

The aim of this project is to assess the potential of III-V MOSFET's for digital devices. In a unique partnership several research groups in the University of Glasgow, are working collaboratively with Freescale Semiconductors. These groups work in the areas of semiconductor materials growth, nanoanalytical transmission electron microscopy, semiconductor materials transport characterization, semiconductor device modelling, nanofabrication technology and semiconductor device fabrication. As part of this collaboration, Freescale transferred appropriate intellectual property to enable the University of Glasgow to rapidly develop its sub-100 nm transistor technology to realise high speed III-V MOSFETs for digital applications. This technology development will permit the realisation of an integrated platform enabling the long-term convergence of digital, RF and optoelectronic components.

Many advances in materials and devices depend on structures at the nanoscale which is only few atoms across. The role of the TEM group is to understand the properties of these materials by examining their structure and chemistry on the nanoscale. This work is performed primarily with the Transmission Electron Microscope (TEM). This allows the characterisation of the structure and chemistry of materials down to atomic scale.

Moreover, using Electron Energy Loss Spectroscopy (EELS), which is a technique directly related to TEM, it is possible to reveal details of the bonds between atoms and this analysis can be performed at spatial resolutions better than 1 nm.

The work reported in this thesis describes the investigation of material and processes relevant to this project using the TEM. In particular, it has been focussed on the characterization of dielectric oxide layers. As noted above oxide layers play a crucial role in the development of a MOSFET system. In particular, the biggest problem for this type of transistor at the beginning was certainly related to the dielectric stacks. In MOSFET systems the dielectric stacks are prepared by MBE [9,10], these layers are amorphous oxides of Gd and Ga. In order to interpret the data from the amorphous materials and device some modelling was undertaken. This is the reason why x-ray absorption near edge structure (XANES) simulations were run and the results compared the experimental ones from energy loss near edge structure (ELNES). In both techniques the excitation of the core atomic electrons occurs by electromagnetic interaction. This will be explained in more detail in chapter 3.

1.3 MBE GROWTH

$Gd_xGa_{x-1}O/Ga_2O_3$ dielectric stacks, analysed in this thesis, have been grown onto (001)GaAs to form a III-V/oxide with a low interface state density and a high conduction band offset [8]. They have been grown in a Veeco dual chamber GEN III MBE system [9]. The semiconductor layers are grown in a III-V chamber before being transferred under vacuum into a second chamber for the oxide growth. The oxide chamber has effusion cells for Ga_2O_3 and Gd, and a Veeco RF oxygen plasma source. Ga_2O_3 is deposited on GaAs by heating polycrystalline Ga_2O_3 that sublimates to form a flux of Ga_2O and O_2 molecules. GdGaO is grown using fluxes from Ga_2O_3 and Gd effusion cells, and an additional flux of molecular oxygen.

After growth in the III-V chamber, the epitaxial layer is cooled in an As flux to form a protective As cap and transferred to oxide chamber. The As-stable (2x4)-(100) GaAs surface required for the Ga_2O_3 is established using RHEED in the oxide chamber. The As cap desorbs at about 350 °C. Temperatures are measured and verified using the c(4x4) to (2x4) RHEED transition without an As flux impinging on the (100)-GaAs surface, which occurs at ~430 °C. The wafer is heated to 470 °C and 490°C for Ga_2O_3 and GdGaO growth, respectively. There is a temperature window (460-510 °C) within which Ga_2O_3 can be deposited with a smooth surface (r.m.s. roughness < 5 Å).

The composition and growth rate of the GdGaO are adjusted by changing the Gd flux. The Ga_2O_3 -GaAs interface is assessed using 300 K photoluminescence (PL) [9].

1.4 TRANSMISSION ELECTRON MICROSCOPY

Historically the TEM was developed because of the limited image resolution in light microscopes, which is due to the wavelength of the visible light. Louis de Broglie (1925) first theorized that the electron had wave-like characteristics and its wavelength is much shorter than the visible light. Then Davisson and Germer demonstrated the wave nature of the electrons by carrying out their classical electron diffraction experiments. Later on (1932) Ruska and Knoll [53] proposed the idea of an electron microscope, developing the idea of electron lenses into a practical reality. The basic principles of electron microscopes follow those already established for optical microscopy, though magnetic lenses replace optical lenses, for manipulating charged electrons within a high-energy beam. In this way the spatial resolution barrier imposed by the visible light wavelength was overcome because of the much smaller wavelength of the electrons.

Nowadays, diverse ranges of electron microscopes exist. The three main types of electron microscopes are the scanning electron microscope (SEM), conventional transmission electron microscope (CTEM) and the scanning transmission electron microscope (STEM). SEM microscopes scan the electrons over the surface of a bulk specimen. Fast electrons scattered from the surface are collected and digital image is then built up. On the other hand, the electron beam in CTEM is actually transmitted through the specimen. In this case the electron beam requires much higher accelerating voltages and the specimen has to be very thin generally, less than 100nm. Here, the incident beam provides a parallel illumination of the desired areas of the specimen. STEM microscopy actually combines the most important features from the SEM and the CTEM. Here a high-energy electron beam is condensed to produce a small probe (<1nm) which is subsequently scanned over a thin specimen and the resulting image is given by the scattered beam.

In all the types of transmission electron microscopes, the fast electrons emerging from the specimen are gathered into three categories. The electron can pass through the specimen not interacting. In this case they will not deviate. Alternatively the electrons can scatter with atoms in the specimen leading to elastic or inelastic interaction (Fig. 1.2) For the conventional TEM microscopy, only elastic scattered electrons are important, while detailed chemical analysis requires the inelastic scattering of electrons.

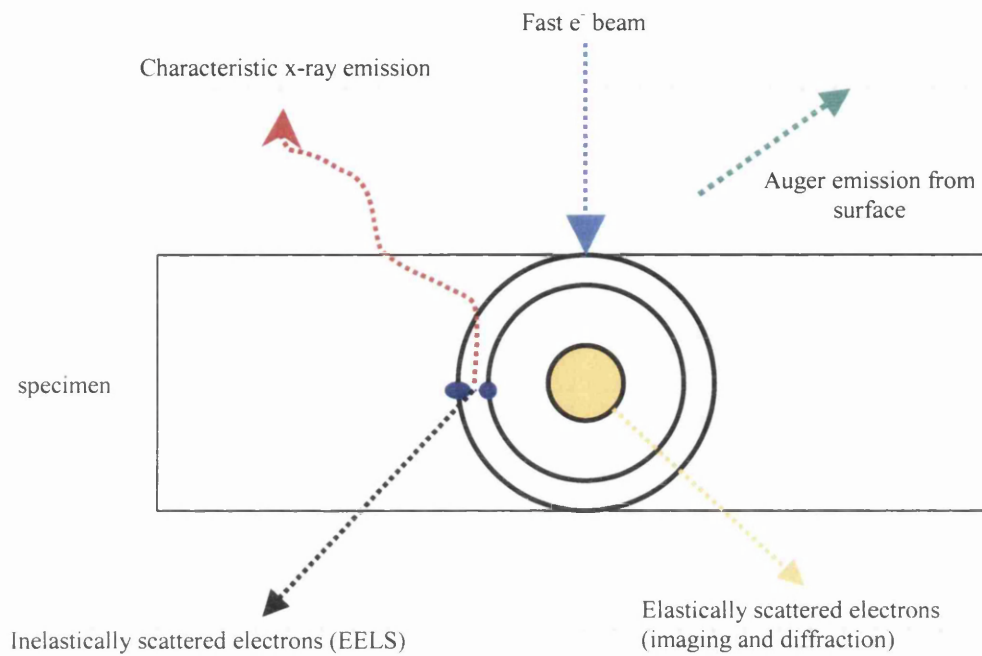


Fig. 1.2 A fast electron beam is incident on the target material. The resulting elastic and inelastic scattering events reveal qualitative and quantitative information on the microstructure and chemical composition of the sample.

1.4.1 Conventional Electron Microscopy

CTEM is successfully used to extract information on the morphology and crystal structure within samples. In diffraction mode, elastic scattering of the incident electron on the material results in the formation of a diffraction pattern. The diffraction pattern is composed of spots in the case of single crystals, rings for polycrystalline samples and diffuse rings for amorphous samples. In samples where there are single crystals, the diffraction pattern is formed by coherently scattering of electrons off sets of crystallographic planes. Therefore the diffraction pattern can be used as tool for the determination of the crystallographic orientation in the sample. The diffraction pattern can be also a useful tool when orienting the sample with respect to the electron incident beam.

Imaging in CTEM requires the use of a further system of lenses placed after the sample. These lenses have the function to alter the trajectories of the scattered electrons in order to recombine them in a magnified image of the specimen at the required plane in the column. It is possible to form either a bright field (BF) or dark field (DF) image, by exclusively selecting the direct beam in the diffraction pattern, or, one (or more) of the diffracted rays, to be reconstructed into an image through the use of apertures. Thus, the microstructure and morphology of sample may be observed. Removing the aperture and allowing many diffracted beams to interfere results in phase contrast image used in high-resolution microscopy (HRTEM) to image atomic columns. BF and DF images can also be formed in STEM mode, but instead of using apertures, the effective camera length is altered to adjust the scattering angles of electrons being collected by STEM BF and annular dark field (ADF) detectors. However there are other effects that contribute to the overall contrast effect. Diffraction contrast may be dominant when electrons scattered to low angles are collected. If electrons scattered to high angles are collected, the effect of coherent scattering is reduced. In this case incoherent scattered beams are most prominent. These high-angle beams are deflected by elastic scattering from the atomic nuclei due to Coulombic interactions. As a direct result of the dense concentration of positive charges within the nucleus, scattered electron are deflected to higher angles. Overall, the angle to which the fast electrons are scattered has a Z^2 dependency as it depends upon the interaction of the incident electron with the atomic nucleus [13]. Therefore, contrast observed in the final image is affected by the average atomic number of the target atoms. This is known as Rutherford scattering.

Although, the overall contrast, observed in BF and DF images, can reveal much about the sample, it is not possible to get definitive conclusions about the elemental composition without the use of analytical techniques.

1.4.2 Analytical Electron Microscopy

An analytical microscope has one or more detectors attached to the column. These detectors are specifically dedicated to the collection of signals generated by inelastic collisions between the fast electron beam and the atoms in the sample. In this way it is possible to obtain information about the composition and chemistry. When the fast electrons interact with the atoms in the specimen they can transfer some of their energy to the system by exciting the core loss

electrons of the atoms to states above the Fermi level (Fig. 1.3). If more than a critical amount of energy is transferred to an inner-shell electron, that electron is ejected leaving a hole in the inner-shell. When this happens the atom is left in an excited state because it has a higher energy than it would like. The atom is ionised.

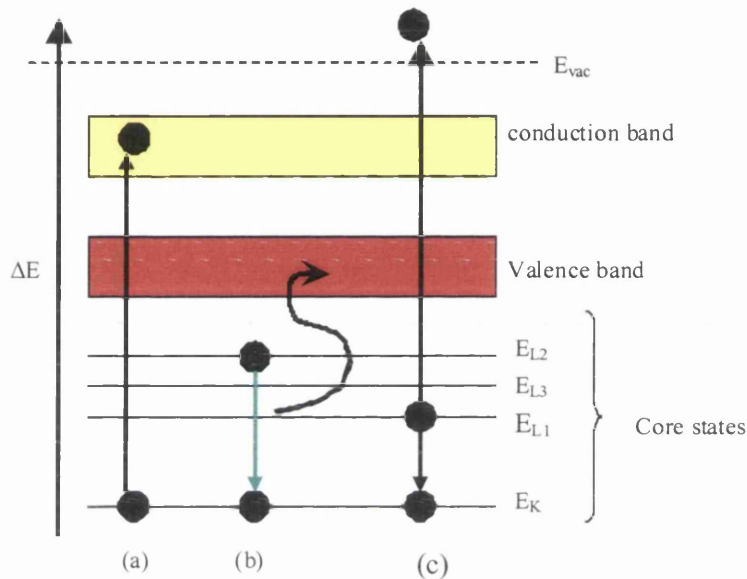


Fig. 1.3 Atomic electrons are excited (a) by absorption of energy from incident fast electrons. The atom then de-excites through emission of either x-rays (b) and Auger electrons (c)

The excited atom can return towards its lowest energy (ground state) by filling the empty state with an electron from an outer shell. This transition is accompanied by the emission of an X-ray or an Auger-electron. In both cases the energy of the emission is characteristic of the difference in energy of the electron shells involved.

The energy lost by the beam is then measured by an EELS spectrometer and exactly corresponds to the difference in energy of the initial and final state of the excited atom. This energy is strictly related to the chemical environment. Hence identification of the atom can be

easily carried out by measuring the energy lost of the direct beam. The EELS technique is not only important for establishing the chemical identity but also for determining the relative composition as well as measuring the thickness.

The emission of Auger electrons is an alternative process to X-ray emission as the ionised atom returns to ground state (Fig. 1.4). The ejected electron has an energy given by the difference between the original excitation energy and the binding energy of the outer shell from which the electron is ejected.

The Auger emission process is favoured in light atoms which present small binding energy. The Auger electrons collected come from the surface of the specimen, only such electrons have enough energy to escape from the surface. This is the reason why Auger electron spectroscopy belongs to the group of surface chemistry techniques.

One of the advantages of the x-ray analysis in the TEM over the Auger spectroscopy is that it is possible to extract information not only from the surface of the specimen but also from the deep regions.

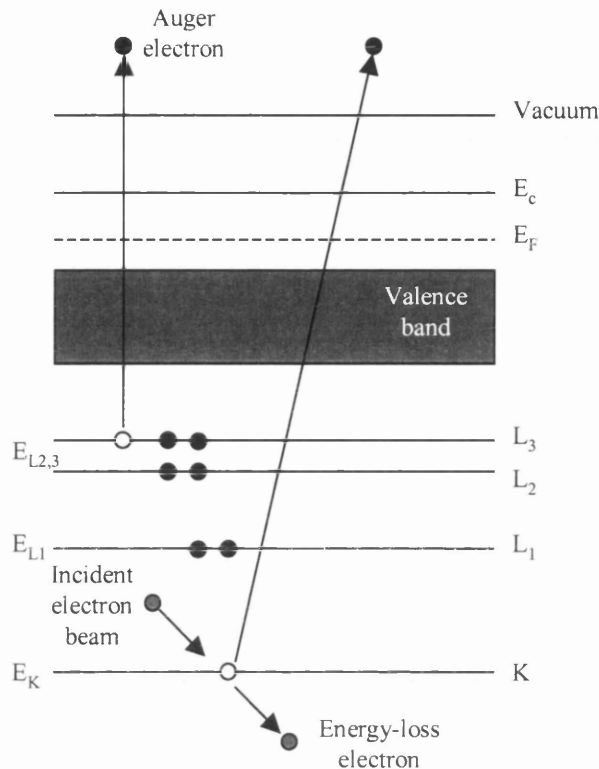


Fig 1.4. Schematic illustration of the emission of an Auger electron. The energy released when the L_1 electron fills the hole in the K shell is transferred to an electron in the $L_{2,3}$ shell which is ejected

1.5 THEORETICAL CALCULATIONS

The fine structure present close to the ionisation edge onset in experimentally collected EELS data is related to the unoccupied electronic states immediately above the Fermi level according to Fermi's Golden Rule. Since local chemistry and crystallography in a material affects the form of the electronic density of states (DOS), then changes in the local environment are observed as alterations to the overall shape of an ELNES spectrum [11]. Ab-initio calculations, which simulate the electronic structure in solids, have proven to be a key component in the successful interpretation of ELNES [12]. Calculations of the electronic structure of materials are necessarily based on quantum mechanical principles rather than classical theory. One

computational code, FEFF 8.2 has been used to calculate the electronic structure within our material. It is based on the multiple scattering approach.

The attractive feature of this type of calculation is that the chemical identity of neighbouring atoms as well as the unit cell dimensions and symmetry contained therein are easily altered. Hence associated alterations in the ELNES spectra can be easily identified. All the simulations and related theory will be discussed in more details in chapter 3.

1.6 OUTLINE OF THE THESIS

Chapter 2 describes the instrumentation as well as the collection and analysis methods employed. It also provides details on the theory behind electron microscopy and EELS analysis. Chapter 3 describes with more details the theory behind FEFF 8.2 calculations and the comparison between theoretical calculations and experimental ELNES spectra. Chapter 4 describes the compositional analysis of the Ga₂O₃/GGO dielectric gate stack as grown using EELS spectrum images (SI). Chapter 5 describes the analysis of the effects of 3 etching processes using energy filtering transmission electron microscopy (EFTEM). Furthermore one etching processes is investigated by EELS SI. This allows to make some comparisons between the two analytical techniques. Chapter 6 describes the analysis of the interface GaAs/Ga₂O₃/GGO at a sub-nanometer level by high-resolution STEM imaging. Some images acquired using the SuperSTEM1 will be shown. SuperSTEM1 is an aberration corrected microscope based at Daresbury Laboratories in the Cheeshire UK. A description of the aberration correction process will be also given.

CHAPTER 2: ELECTRON MICROSCOPY AND ANALYSIS

2.1 INTRODUCTION

The electron microscope has proven itself to be a key instrument for the investigation of materials at the nanoscale level. Associated with analytical techniques such as electron energy loss spectroscopy and energy (EELS), energy filtering transmission electron microscopy (EFTEM) and energy dispersive x-ray (EDX), information on the composition and chemistry of the material can be easily obtained.

This chapter will detail the relevant components of the (scanning) transmission electron microscope (S)TEM used in this thesis, with reference to the function of each component. Information regarding the composition and the elemental distribution of the material has been obtained using EELS and EFTEM in the Tecnai F20 and Tecnai T20 electron microscopes. Therefore a description of the spectrometers used for acquiring EELS and EFTEM data is included. A brief description of the theory behind EELS is given.

2.2 ELECTRON MICROSCOPE

Transmission electron microscopy works through the interaction and transmission of a fast electron beam through a sample material. The electron beam is generated by extracting electrons from the source and then accelerating them across a stable potential difference. The presence of a series of electromagnetic lenses placed after the source, controls the nature of the illumination arriving at the specimen. Other lenses are used to focus the electrons leaving the specimen in order to form the actual image of the specimen or its diffraction pattern. In this way it is possible to obtain structural information about the specimen. Inelastic collisions of the fast electrons can be analysed in an EELS spectrometer attached at the end of the column of the microscope. An EELS spectrometer has the capability to record the energy-loss of scattered electrons in the transmitted beam, which has been transferred to the sample atoms in order to excite the core electrons to higher energy states. The amount of energy-loss of the incident electrons is directly related to the chemical environment of the absorbing atom. Information about the composition can be easily extracted.

An EDX spectrometer has the capability to record the energy of any x-ray emitted by the sample atoms. This is the result of the de-excitation of the atoms. Therefore elements present in

the specimen can be easily identified and under suitable conditions their concentration can be determined.

2.2.1 FEI Tecnai F20 and T20

Both Tecnai F20 and T20 microscopes have used to collect all the experimental data presented in this thesis. In particular, the Tecnai F20 has the capability to switch from TEM to STEM. It is equipped with a field emission gun (FEG) and is fitted with a Gatan-Enfina electron spectrometer and an EDAX Sapphire x-ray detector.

The Tecnai T20 can only operate as TEM. It is equipped with thermionic source, a LaB₆ crystal, and fitted with a Gatan-GIF energy filter. Both microscopes operate at 200kV and their main components are detailed below, in the order they occur in the microscope. A brief description of each of their functions is given.

2.3 ELECTRON SOURCES/GUNS

2.3.1 Introduction

All electron microscopes require an electron source in order to illuminate the specimen material. Furthermore, the characteristics of a particular electron source are incredibly important in an electron microscope as these have a direct effect on the capability of the instrument as a whole. For instance, the brightness and the total current (for CTEM) from the source have a direct effect on the amount of details that can be obtained from a particular specimen [13]. In addition to having a source of electrons, the electrons must also be accelerated in a controlled manner. This is accomplished through the incorporation of the source in an assembly called an electron gun.

One of the most important characteristics of electron guns concerns the source brightness, which is defined as the current density per unit solid angle [14]. It can be shown that the brightness increases linearly with accelerating voltage and also that it determines the total current which can be focused into a given spot size onto the specimen. Hence, it determines whether the current is sufficient in order to be used in probe forming instruments that require a large current in a small probe. The stability of the emission current with time is another important factor in the operation of electron guns. For instance, in scanned images, the

presence of instabilities in the emission from the gun can produce image flicker that degrades the image quality [15]. In addition, the energy spread of the source is also important as the chromatic aberration of the electromagnetic lenses can increase the size of the incident probe. The energy spread is caused by instabilities in the accelerating voltage supply and also by the inherent energy spread of the various emission processes. In fact, this will be a limiting factor in probe forming systems that have been corrected for spherical aberration.

There are 2 main types of electron guns that are commonly used in electron microscopes. The first type is called a thermionic gun in which the source material is heated in order to provide the conduction electrons with sufficient energy to overcome the material's work function [14]. On the other hand, this barrier is overcome through the application of an intense electric field in the 2nd type of source which is called a field emission gun (FEG). The emission from a FEG may also be aided through the heating of the source material. This variation is termed a thermally assisted FEG (as opposed to a cold FEG in which no heating occurs). Furthermore, another FEG variation also exists in which the tip is both heated and coated with a material that lowers the work function (Schottky FEG). In general, FEGs generate an electron beam with a far higher brightness, a reduced size and a smaller energy spread compared to thermionic guns.

2.3.2 Field Emission Guns

The Tecnai F20 operates with a Schottky field emission gun (FEG). This type of gun operates only at low vacuum pressure in the range of 5×10^{-9} Torr and contains a W emitter with a ZrO₂ layer as tip, shaped to a point and orientated in the (100) direction. The normal operating temperature is around 1800K to aid emission of electrons, while a thin layer of ZrO₂ covers the tip and effectively lowers its work function. The emitter is mounted on and heated through a tungsten hairpin. In order to avoid electrons emitted from the hairpin entering the column, a negatively charged cap is placed around the emitter and only the tip juts out. Electrons emission is controlled by an extraction anode, positioned close to the emitter tip. The extraction voltage V can be changed to suit a particular experiment. For a given extraction voltage, the electric field (ϵ) around the tip is given approximately by: V/r , where r is the radius curvature of the emitter tip. It is actually made smaller than 1micron. In this way a high field is generated. The electron beam emitted by the source goes through an electrostatic gun lens whose strength controls the position of the first beam cross-over. When the microscope operates in CTEM mode, the beam cross over is normally formed beyond the end of the accelerator tube. Strong

excitation of the gun lens (STEM mode) produces a beam with a cross over point close to the gun lens.

The Tecnai F20 has an operating voltage of 200kV, producing electrons with a wave-length of 2.51pm which is much smaller than the atomic scale. The current density of a FEG gun is much higher than the one of the LaB₆. This certainly increases the energy resolution of the system making FEGs ideal emitters for EELS analysis.

Although a Schottky has many advantages which make it suitable as emitter for TEM applications, there is one feature that can cause some problems: “the side lobe emission” [54]. This is typical of all the Schottky emitters where the crystal faces of the tip are much larger than in a conventional cold FEG emitter.

Side-lobe emission occurs when crystal faces other than the (100) front face of the emitter also emit electrons. These faces are tilted relative to the (100) face and the electrons do not enter the beam normally but travel at an angle. These electrons then hit the extractor anode plate and are either backscattered or cause emission of secondary electrons. Some of these move back on trajectories that, depending on their energy, may cause them to pass through the central hole in the extraction anode and then get accelerated and come down the microscope. The problem is caused by the fact that the energy of these electrons is not the same as that of the primary electrons.

Due to the chromatic aberrations in the electron optics of the column, these electrons are focused differently from the primary-beam electrons and are spread around the central beam. Because emission occurs from only four crystal faces, the pattern that emerges is that of four lobes of electrons with increasing energy loss away from the central beam. The maximum value of the energy loss in the gun depends on the extraction voltage and gun lens setting and is given by $(V_{\text{extraction voltage}} - V_{\text{gun lens}})/2$. By using this equation it is possible to select the maximum loss energy of these electrons and choose its position in the EELS spectrum. Furthermore the insertion of the smallest C1 has the effect of intercepting a large fraction of these electrons in the main beam thus lowering their contribution to the EELS spectrum.

2.3.3 Thermionic guns (LaB₆)

The Tecnai T20 operates with a LaB₆ electron gun. Electrons in any material can be given the required energy to overcome that material’s particular work function and escape to the

The electrons that emanate from the filament are accelerated by the potential difference that exists between the cathode and anode ($\sim 100\text{kV}$). In addition, in order to control the trajectory of the emitted electrons, a small negative bias is applied to the Wehnelt cylinder. This acts as a simple electrostatic lens. For that reason, the electron paths converge to form a cross-over point between the Wehnelt and anode [14]. The value of the Wehnelt bias is chosen in order to provide the optimum condition of a reasonably high current and a small enough source size (at the cross-over point). As an example, the source size that is obtained from a 100kV tungsten filament is typically about $10\mu\text{m}$ in diameter compared to about $1\mu\text{m}$ for a 100kV LaB_6 filament. Furthermore, the brightness of 100kV tungsten and 100kV LaB_6 filaments is about 3×10^6 and $10^7 \text{ Acm}^{-2}\text{sr}^{-1}$, respectively [15]. These brightness values are not as high as the value that can be obtained from FEGs, which is about $10^7 - 10^9 \text{ Acm}^{-2}\text{sr}^{-1}$ for cold FEGs and about $5 \times 10^8 - 10^9 \text{ Acm}^{-2}\text{sr}^{-1}$ for Schottky FEGs. Figure 2.2 also reveals that the electron paths diverge (at an angle of α_0 to the optic axis) after the gun cross-over point. α_0 defines the angle of the electron beam that enters the condenser system after the gun assembly.

2.4 COLUMN

Once the electrons leave the gun, they are accelerated into a column where a series of electromagnetic lenses has the function to manipulate the electron beam and form the related image. This lens system can be divided into two different regions classified as pre-specimen and post-specimen (Fig. 2.2). The first one is before the specimen and the second one is after.

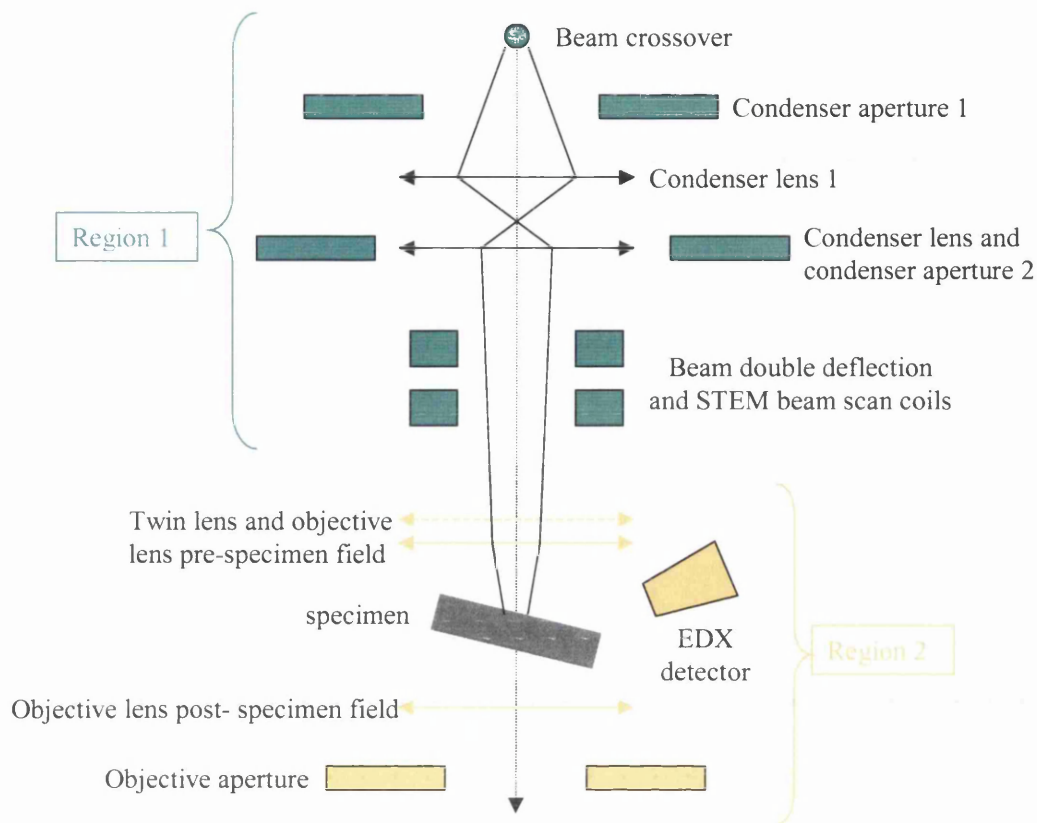


Fig. 2.2 The pre-specimen region, condenser and objective systems showing the beam path taken under the conditions used for EELS collection.

In the pre-specimen region the lens system is mainly composed by 2 condenser lenses and the respective apertures: C1 and C2. C1 lens controls the probe size, producing a de-magnified image of the gun cross over. The diameter of the incident probe will be decreased, reducing the number of interacting atoms in the sample. The condenser apertures can be used to remove stray scattered electrons or to allow the user to define the required angular-range of the incident electrons. However, this is achieved through the removal of electrons and therefore current from the beam. Choosing the right aperture is an important requirement when performing EELS and EDX. Enough current must be present in the beam in order to have a strong signal in the EELS and EDX detector without saturating them. In addition, for EDX collection it is

important that stray electrons, scattered when exiting the gun, are removed before being incident on the specimen, as they can generate signals from outside the area of interest.

Also contained in the pre-specimen Region 1, is the second condenser lens (C2). Altering the strength of C2 controls the convergence of the beam as it reaches the sample. In TEM mode, a strong C2 condenses the illumination to a spot, while weakening C2 allows a defocused beam to illuminate large areas of the specimen at once. The C2 aperture is placed inside the C2 lens field, as shown in Fig 2.2.

Consequently, it is important that the aperture is centred about the optic axis. Misalignment of the aperture results in a lateral movement of the beam position whenever C2 is adjusted, as well as tilting of the beam, and this changes the rotation centre. Therefore, reproducible illumination is achieved by positioning the aperture using the same magnification, and by defocusing the beam by the same amount, during each alignment.

Double deflection scan coils beneath the second condenser aperture position are used to deflect the electron beam. Current passed through one pair coils, placed either side of the optic axis, generates a magnetic field, B , which is oriented at right angles to the beam direction. Hence, the fast electrons trajectory is deflected in the positive-field direction. The second set of deflector coils is situated below the first pair and together they are used to induce a shift or tilt to the beam path before it hits the specimen. This set is called the DC or static beam shift coils and they aid alignment of the beam along the optic axis. A separate set of AC beam deflection coils working on a similar principle are used while in STEM mode, to get the probe rastering.

The fast electrons then enter the objective system, shown as Region 2 in Fig. 2.2.

Here, the objective lens has a pre-and post-specimen field. Since the specimen itself sits in the field of the objective lens, it is crucial to set the height of the sample rod such that the specimen sits in a specific plane, known as the eucentric plane. All other imaging planes are defined with respect to this eucentric plane. The objective lens current for imaging at the eucentric height is known for the Tecnai. Accordingly, when the objective lens is set to this value, the sample height is simply adjusted until a focused image is obtained. After the initial alignment with the sample at eucentric height, fine adjustments to the objective lens allow the user to tune the focus of the final image. Also, with this alignment, it is possible to tilt the sample rod about the alpha axis without inducing a lateral shift of the on-screen image (Fig. 2.3). Unfortunately, for samples requiring tilting about both alpha and beta axes, constant adjustments must be made to

return the sample to the eucentric plane as rotation in the beta axis requires movement of the sample in the z-direction, away from focus.

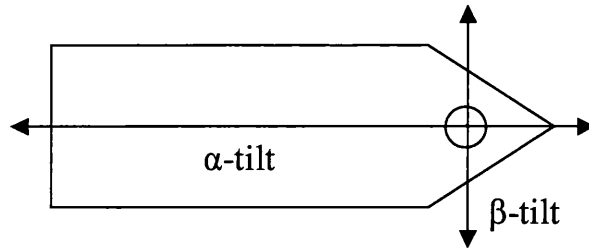
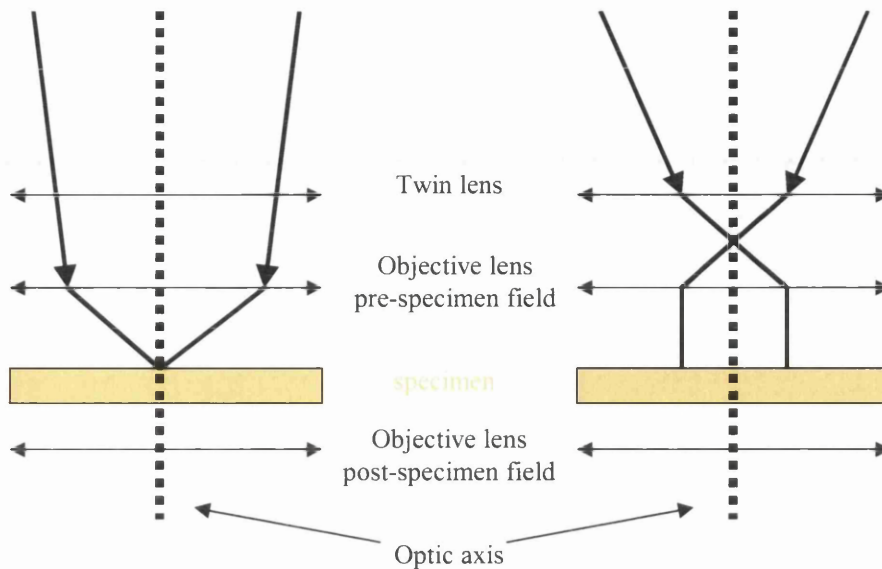


Fig. 2.3 Schematic of a typical double tilt rod, showing the α - and β -tilt axes.

It also important to note that the pre-specimen objective lens is constructed with a second mini-lens, called the twin lens, in the upper poly-piece. This allows the user to operate in either microprobe (CTEM) mode or nanoprobe (STEM) mode as shown in Figs 2.4a and 2.4b respectively. When active the twin lens produces a crossover in the electron beam that creates a microprobe in the plane of the specimen. Reversing its current effectively turns off the second mini-lens. With no field operating on the beam at this point a nanoprobe forms at the sample, this alignment is used for STEM analysis, as illustrated in Fig. 2.4a



Figs. 2.4a and 2.4b Ray diagram of the pre-specimen electron beam with the twin lens switched off nanoprobe and on CTEM mode

Diffraction of the beam by a crystalline specimen results in the formation of a diffraction pattern in the back focal plane (BFP) of the objective lens. The objective aperture is also situated in the BFP. Thus, when viewing the diffraction pattern in TEM, the aperture can be centred around either the central bright spot or one or more of the diffraction spots if the sample is crystalline. By switching back to imaging mode, a bright field, BF, image is constructed for the first scenario and a dark field, DF, image for the second.

Associated with each of the lenses discussed above, the Tecnai contains three sets of stigmators, which correct for the first order of astigmatism. Without correction, spatial resolution is diminished because a point in the specimen appears in the final image as an ellipse. Each set of stigmators are situated close to their respective lenses and must be properly aligned to make sure that beam shift is not artificially introduced into the overall beam alignment. To counteract lens astigmatism, stigmators are composed of two sets of quadrupole lenses. The first set is positioned at 90° intervals. The second set is located in the same plane as the first one, but is rotated by 45° , so that astigmatism in any direction may be corrected for.

Unlike scan coils, opposing pairs have opposite currents, and since the direction of the beam deflection alters with the direction of the current in the coils, the final result is that the electron beam is pressed from opposite ends by one pair, while being pulled in a orthogonal direction by the second pair, therefore an ellipse will become a circle.

The condenser stigmator ensures that the incident electron beam is circular when condensed to a spot on the specimen. While, the objective and diffraction stigmators are employed to remove astigmatism generated in the transmitted beam by imperfections in their associated lenses. Therefore, streaking observed in the final image, at high magnification, or arcs present in diffraction patterns of crystal samples, may be significantly reduced. Thus, providing more detail on the sample.

When a STEM probe is placed over amorphous material, a ronchigram or shadow image [16, 55, 56] appears on the fluorescent screen in diffraction mode. The lens transfer characteristic in the pre-specimen region of the column appear in the ronchigram, which is composed of the undiffracted discs of electrons at the centre of the diffraction pattern. A perfectly focused probe, where every electron is incident on a single point in the sample, would produce a flat ronchigram with no contrast. In reality, spherical aberration brings high angle rays to premature focus above the specimen producing two distinct regions: the central disc where the shadow image is reversed and the outer region where it is not. Astigmatism or misalignment in any of the probe forming optics, radically distorts the symmetry of the pattern. It is possible to align the gun optics, the condenser lens and apertures.

Once an in-focus ronchigram is obtained, the C2 aperture can be replaced by a smaller aperture.

Second sets of both DC double deflection coils are situated next in the column, in Region 3 in Fig. 2.5 they operate in a similar manner as described above, except now they are used to adjust the image or diffraction pattern. Also, it should be noted here that these DC coils are essential when positioning the beam at the centre of the EELS spectrometer aperture, when optimising conditions for EELS analysis.

The transmitted electron beam forms a diffraction pattern, which is then recombined by post-specimen lenses to form an image of the specimen in the imaging plane, at the base of the column. Alternatively, by altering the strength of the diffraction lens and hence its focal length,

the user is able to image the diffraction pattern instead. The Tecnai has the ability to magnify images several million times the original area of the specimen involved. This is achieved in CTEM mode through the use of the projector lenses present. In contrast, altering the magnification while in STEM mode simply alters the area of sample being scanned. The use of a many-projector lens system, ensures the electron beam crossover remains at the differential pumping aperture, regardless of magnification

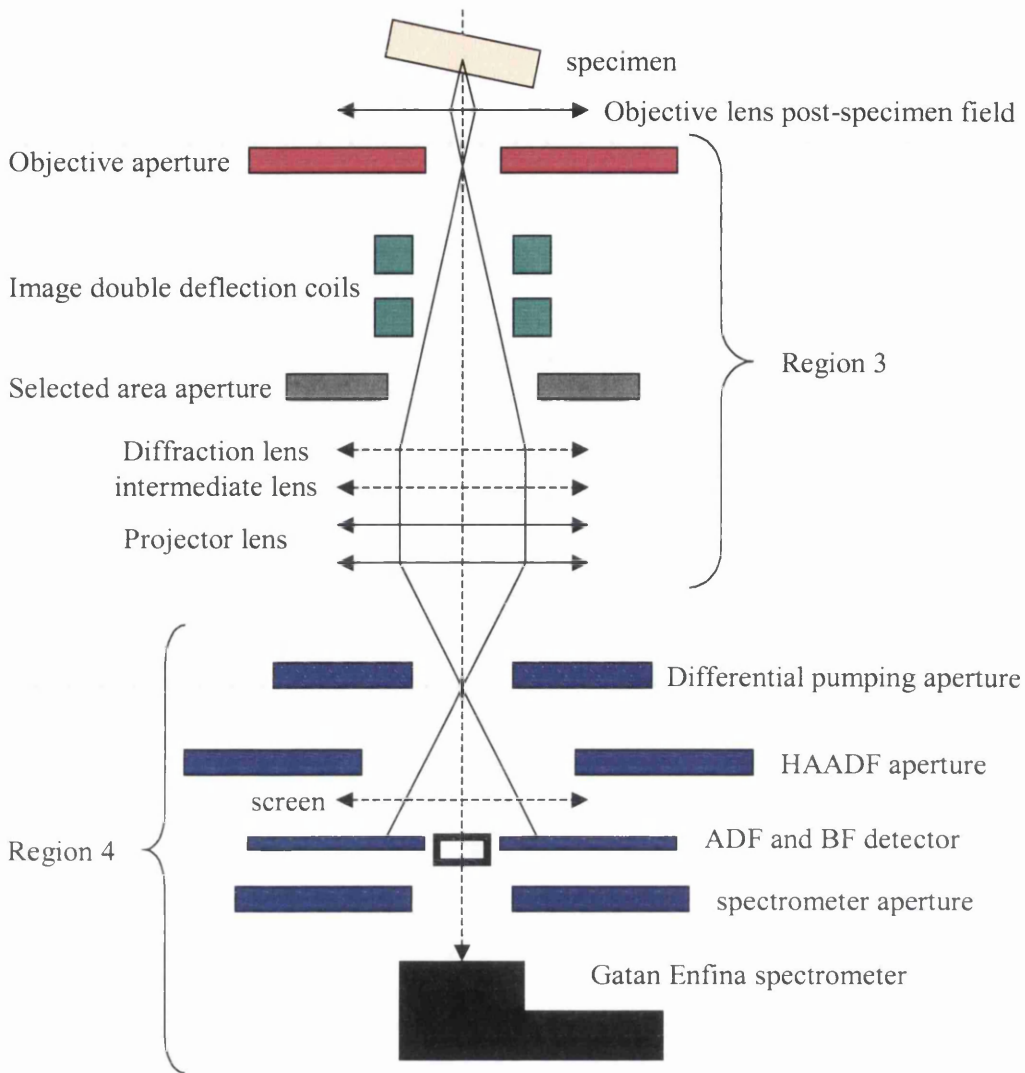


Fig. 2.5 Post-specimen, magnification optics and detector systems.

It is important that the entire microscope is held under vacuum so that the fast electron beam only interacts with atoms in the specimen. The column is held at a higher vacuum (10^{-6} Torr) than the project chamber (10^{-3} Torr). The pressure difference is sustained through the use of a differential pumping aperture (DPA) with an inner radius $\sim 200\mu\text{m}$, (Region 4 in Fig. 2.5). Clearly, the fast electron beam must pass through these two areas and so a small amount of

seepage between the two regions occurs. Another aperture maintains the pressure difference in the region separating the column from the gun ($\sim 10^{-9}$ Torr). Closing valves at these positions allows operations such as replenishing film for the camera, without opening up the entire microscope to atmospheric pressure.

2.5 IMAGING IN CTEM

When the microscope operates in CTEM mode a fluorescent screen positioned at the bottom of the column is used to view the samples. Positioned below the fluorescent screen there is a multi-scan camera (MSC). This is actually a charged-coupled device (CCD) containing an array of isolated cells. When the electron beam is incident on the detector, charge is then stored proportional to the incident intensity within each cell. This amount of charge is then read out cell by cell, amplified and digitised.

2.6 IMAGING IN STEM

The Tecnai F20 when operating in STEM mode has 3 different detectors (Fig 2.6). The uppermost is the high angle dark field detector (HAADF) followed further down in the column by the dark (DF) and the bright field (BF) detector. The DF and the BF are both situated at the same height in the microscope, therefore only one can be used at any given time. The BF is positioned on the optic axis while both the HAADF and the DF are placed concentrically with respect to the optic axis. The HAADF and the DF detectors allow recording electrons scattered at high angles. Thus they are more sensitive to the atomic number of the atoms. Heavier elements will scatter electrons much more than the light ones. This is the reason why in both detectors images appear to be more intense in areas where there is higher concentration of heavy elements. By choosing a suitable value for the camera length (L) it is possible to limit the contribution of either diffraction scattered and Z-scattered electrons to the final STEM image. The HAADF detector is designed to collect electrons scattered to even higher angles than those incident on the DF detector. This makes HAADF detector much more sensitive to atomic weight than the DF one.

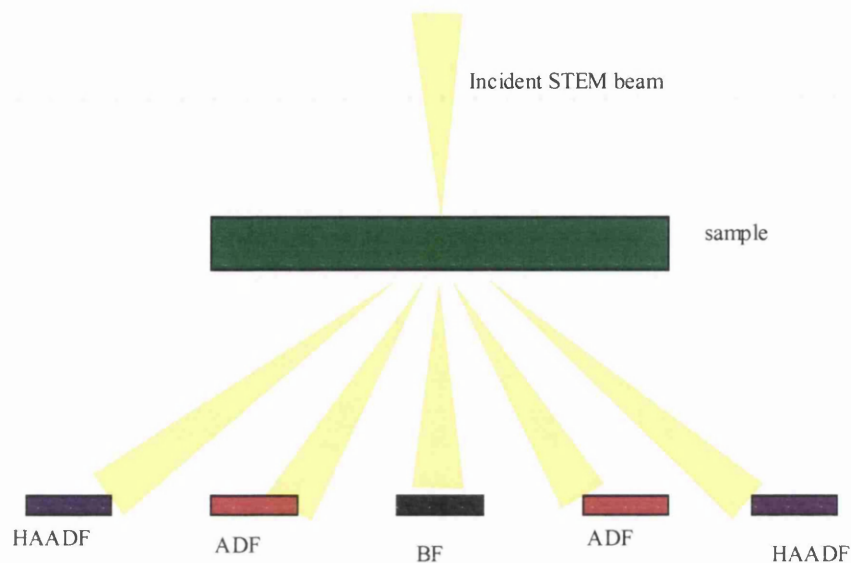


Fig 2.6 A convergent STEM beam of fast electrons is incident on the sample. A BF detector collects the direct beam and low angle scattered electrons while ADF and HAADF detectors collect electrons scattered at higher angles.

2.6.1 Aberration Corrected STEM

Since some of the high-resolution HAADF STEM images shown in chapter 6 have been acquired using SuperSTEM1 which is an aberration corrected dedicated STEM electron microscope, this section will briefly deal with the SuperSTEM1 and what is concerned with the method employed for the correction of the aberration.

2.6.1.1 Electron lenses and aberrations.

In an electron microscope the trajectories of the electrons, emitted from the gun, are controlled through the use of electromagnetic lenses. Usually, electromagnetic lenses are composed of a coil and a magnetic circuit that has a hole, called the bore, drilled through it. If the current flows through the coils a magnetic field is generated within the magnetic circuit. This magnetic field extends into a specifically designed gap in the magnetic circuit. Such magnetic field provides the focusing action on the electrons. Due to the presence of imperfections in the

magnetic lens system aberrations are always present. These aberrations cause the degradation of the focused beam spot and degrade the amount of details that can be obtained from an electron microscope. The quality of a lens is related to the aberration coefficient (C_3). A simple measure of the image resolution has to take into account the spherical aberration disk radius which is proportional to $C_3\beta^3$ and the Airy disk radius which is equal to $0.61\lambda/\beta$. β is the maximum ray angle that is imaged by the objective lens.

In 1937 Scherzer [57] described that spherical and chromatic aberration are always present in rotationally symmetric lenses. However in such analysis he assumed that the whole optical system was round and does not vary with time and has no charge on the axis. He also proposed that this aberration could be corrected using non-round lenses. These are essentially multipole lenses that are capable of generating negative value of C_3 . This is the reason why the positive aberration of a round lens can be cancelled using multipole lenses. This work has led to the creation of aberration correctors based on octupole/quadrupole and hexapole systems.

The probe size in a STEM plays an important role for the aberration correction procedure [58, 59] In particular, a first order approximation of the full width half maximum (FWHM) diameter of a STEM probe can be given as a combination of the three following quantities. These quantities are the diameter of the Gaussian de-magnified image of the finite source (d_g), the spherical aberration disk diameter of the objective lens (d_s) and the Airy disk diameter (d_d). d_g is equal to $(2\alpha\pi)(I/B)^{1/2}$ where α is the divergence semi-angle of the electrons from the de-magnified source, I is the demagnified source current and B is the brightness of the demagnified source. d_d is proportional to $C_3\beta_3$ and equal to $1.22\lambda/\beta$. Hence the spherical aberration can be minimised using large semi-convergence angle. d_g can be reduced by increasing the source demagnification, but this also reduces the current in the probe. Therefore, the choice of the probe convergence angle and the degree of the source demagnification are a compromise between the desired probe size and the desired probe current [60].

2.6.1.2 SuperSTEM 1 instrument

This instrument is a VG HB501 100kV dedicated STEM that has been retrofitted with a second generation of NION aberration corrector [61, 62]. The microscope is also equipped with a cold FEG usually operated with an extraction voltage below 4kV. The energy resolution of the gun

is 0.3eV. The specimen drifting rate is 5-10nm per hour which much less than in typical microscopes such as the F20 where it is 60nm per hour.

Fig. 2.7 shows a schematic description of the microscope. Its geometry is opposite to the F20 one where the gun is positioned on top of the microscope. In the SuperSTEM1 the gun is placed at the bottom of the column as in all the dedicated STEM microscopes. The microscope is equipped with a Gatan Enfina spectrometer with an energy resolution of 0.35eV. The HAADF detector fitted in the microscope has inner and outer angles of 70mrad and 210mrad, respectively. In addition another detector (a CCD camera) is positioned after the HAADF detector. This allows far field diffraction images to be taken and is important during the correction procedure for the measurements of the aberrations.

SuperSTEM1 is also fitted with a quadrupole coupling module (QCM) along the STEM column as shown in Fig. 2.7. This post-specimen lens system is composed of series of quadrupoles and octupoles. This extra lens system is important because the retrofit of the presence of NION corrector has shifted all the different microscope components below the specimen from their original positions. This lens system is also needed due to the larger probe convergence angle that is employed in the SuperSTEM1 (24mrad semi-angle). The QCM is used to compress the angular distribution of the transmitted electrons from the specimen in order to match the acceptance angle of the Gatan Enfina spectrometer.

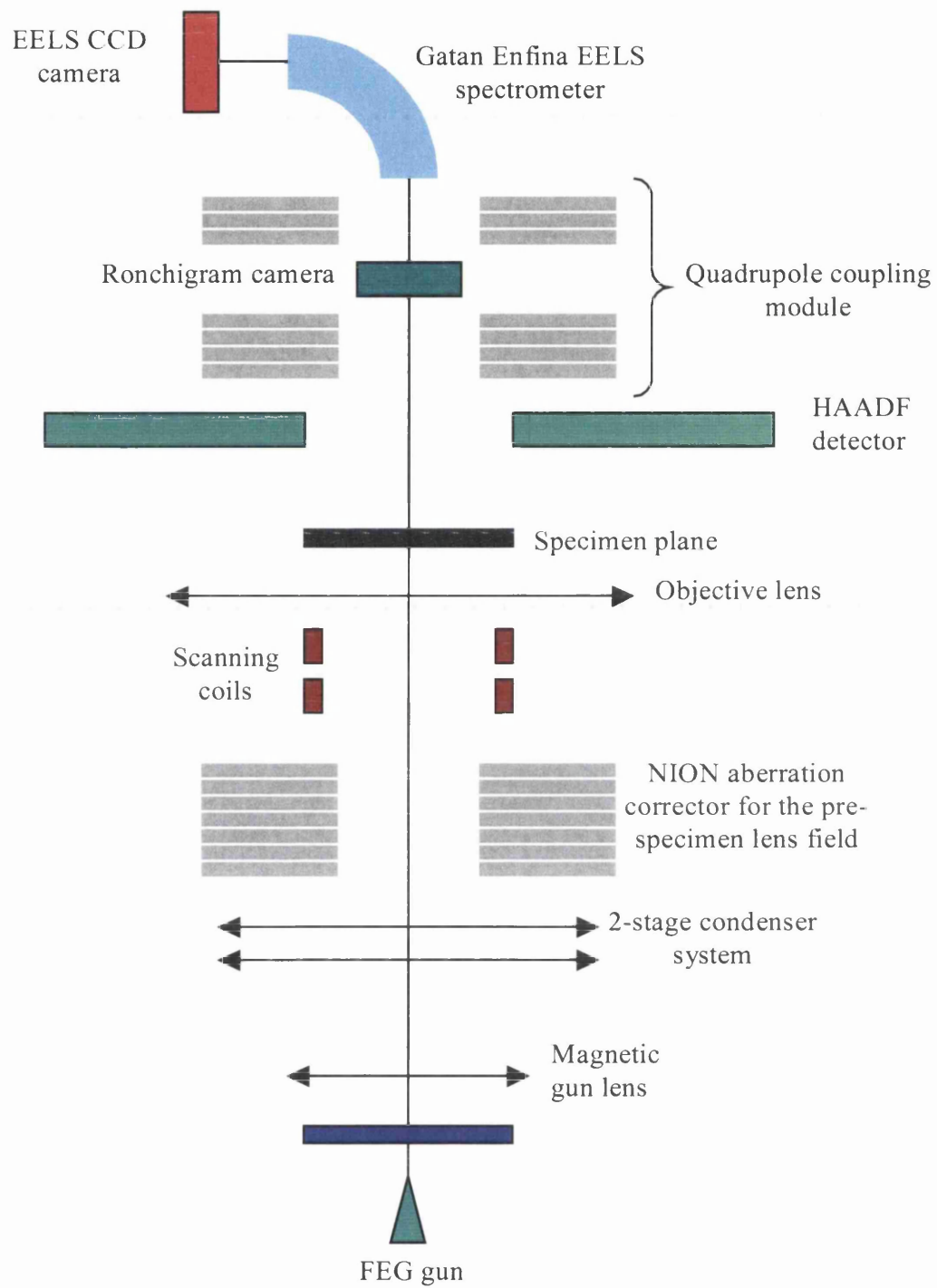


Fig. 2.7 Schematic view of the SuperSTEM1 electron microscope.

2.6.1.3 Method of aberration correction in SuperSTEM1

If the probe is stationary on the specimen, the transmitted electrons can be collect as a function of angle on the CCD camera. The image formed on the CCD camera is called Ronchigram. Fig. 2.8 shows the main features of a typical Ronchigram in a probe forming system where spherical aberration is present. In this case the probe has an associated defocus value and is incident on an amorphous material. Hence the low angle rays of the probe form a distorted bright field image of the specimen and this can be seen in the centre of Ronchigram. Due to the presence of spherical aberration, the high angle rays of the probe are perfectly focused on the specimen. As a result, these rays produce a ring of azimuthal infinite magnification in the Ronchigram. The Ronchigram shows the presence of spherical aberration in an optical system therefore, it can be used for tuning the microscope and correct the spherical aberration.

The NION aberration correction is an example of octupole/quadrupole corrector. It is composed of four quadrupoles, 3 octupoles and 24 additional multipoles which deal with parasitic aberration. Two quadrupoles have the function to squeeze the electron in a specific direction in order for the corresponding octupole to perform a correction of the aberration in a particular direction either x or y. The middle quadrupole forms a round beam in order for the corresponding octupole to correct the aberration along the 45-degree direction.

The entire correction process is only achievable through the use of computer control that enables accurate measurement of the aberrations and regulates the excitation of the corrector's components. Furthermore, auto-tuning software is also utilised in order to measure the value of the different aberration coefficients. The aberrations are measured from a Ronchigram image of amorphous material [51]. The software then changes the excitation of the various components in order to reduce all the aberration. This operation is repeated until the measured aberrations have been reduced to levels that are small for the desired probe size [52].

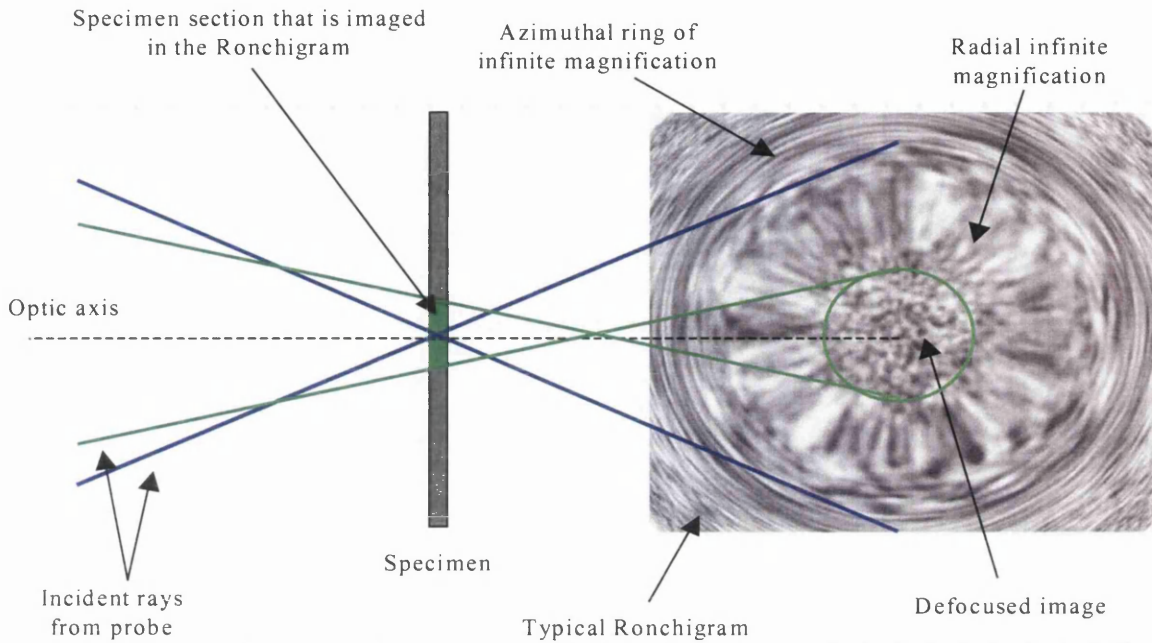


Fig. 2.8 A description of how a typical Ronchigram image is formed by different probe incident angles. Courtesy of SuperSTEM team.

2.7 ELECTRON ENERGY LOSS SPECTROSCOPY

The basic physical process behind energy loss spectroscopy (EELS) has been described in chapter 1. A typical energy-loss spectrum, Fig. 2.9, shows a zero-loss peak (ZLP) within the low loss region (below 40eV). The ZLP is far more intense than any other features in the spectrum as a result of the fact that it is composed from non-interacting and quasi-elastically scattered electrons. This peak has a finite width which is due to imperfect monochromaticity in the electron beam. In the Tecnai F20, the width of the ZLP is 0.70eV. This actually represents the finite resolution of the system and means that electrons which have lost only a very small amount of energy are also included in the ZLP. Low energy losses correspond to the excitation of electrons within the valence band. Valence electrons can be simultaneously excited and this determines the formation of a bulk plasmon, observed in the low loss region.

In the core loss region (above 40eV) energy transferred to the sample excites tightly bound, core electrons to unoccupied energy states above the Fermi level. The result of that is the appearance of ionisation edges on the background intensity. The background arises from the tail of the ZLP and any lower lying edges. The inset to Fig. 2.9 shows core loss Gd $M_{4,5}$ -edges at 1185eV overlapping Ga $L_{2,3}$ -edges at 1115eV. The energy of each edge onset is used to find the chemical identity of the constituent atoms.

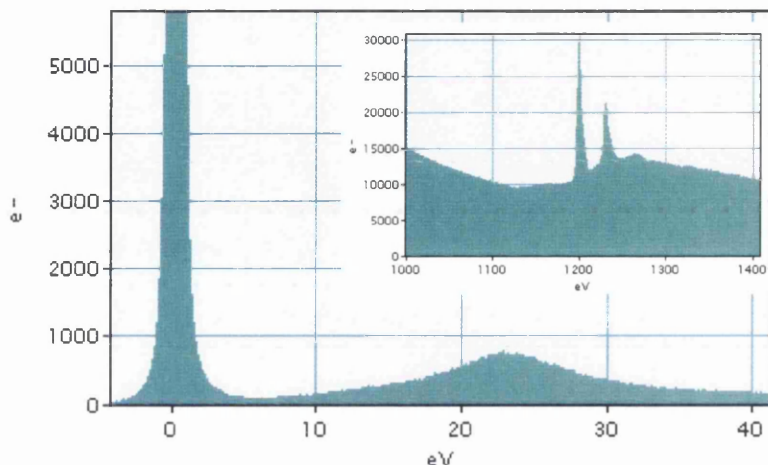


Fig. 2.9 Energy loss spectra from a GGO layer. Main spectrum is the ZLP and plasmon. Inset is the Gd $M_{4,5}$ -edges at 1185eV overlapping the Ga $L_{2,3}$ -edges at 1115eV.

Core loss intensity increases with thickness in a homogeneous samples because there are more atoms present. However, in thicker specimens, it is possible that an incident electron undergoes many scattered events. This is known as plural scattering and results in a redistribution of the intensity from close to the ionisation edge onset, up to higher energies. The likelihood of n scattering events occurring is very much dependent on the overall thickness, t , and the mean free path, λ , characteristic to the material under investigation. The probability (P_n) of an electron being scattered follows Poisson Statistics (*Equation 2.1*), since the probability of each scattering event is assumed to be independent of all other scattering events.

$$P_n = \left(\frac{1}{n!}\right) \left(\frac{t}{\lambda}\right)^n e^{-\frac{t}{\lambda}}$$

Equation 2.1

In Fig. 2.10, P_n is observed to fall off significantly as n increases, for set values of t and λ . Hence, if an EELS spectrum is collected from a thin region of the specimen, plural scattering does not occur, though care must be taken.

Another effect that can influence the shape of EELS ionisation edges is electron channelling, which can occur in crystalline samples under certain diffraction conditions [11]

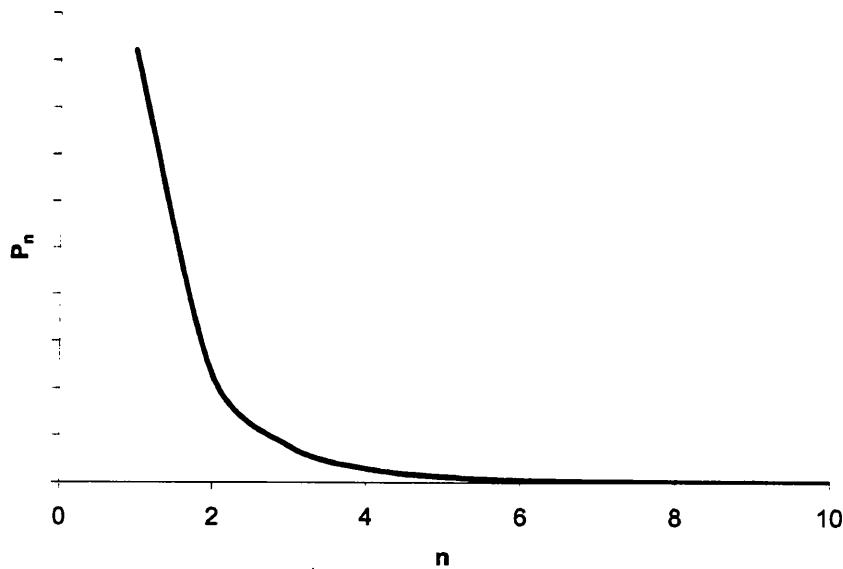


Fig. 2.10 By Poisson statistics, the likelihood of an electron scattering events drops significantly for increasing values of n .

2.7.1 ELNES

Energy loss near edge structure (ELNES) is defined as the oscillations observed on a core loss ionisation edge up to 30eV above the edge onset. These oscillations are dependent on how the atoms interact with each other during the bond formation. An atomic bond is formed by the overlapping of the orbitals which brings to the formation continuous bands of electronic states. The energy of these bands is strictly related to the level of interaction between the two atoms. During the excitation process, it is very likely that the electron beam imparts more energy to the sample than is strictly necessary to excite it to the first empty state above the Fermi level. Therefore an electron is not necessarily constrained to reside in the first unoccupied state, which would result in EELS spectra with delta functions for ionisation edges. Instead this extra energy opens up a range of final states in which the electrons may reside in. This is the reason why ELNES can be used to investigate the electronic states above the Fermi level of the excited atom. The density of states (DOS) above the Fermi level is not uniform, some energy levels contain a much higher density of available states than others. An excited atom will preferentially reside in an energy region where a high density of available states is present. *Equation 2.2* shows that the intensity of a peak in the ELNES (the probability of an electron residing in a given energy state, $P(E)$) will increase as the number of available states within the unoccupied DOS, $\rho(E)$, increases.

$$P(E) \propto |M(E)|^2 \rho(E) \quad \text{Equation 2.2}$$

The atomic transition matrix, $M(E)$ (defined in *Equation 2.3*), and can vary slowly over the region contained within ~30eV above the ionisation edge threshold. Therefore, the fine structure observed on ionisation edges is generally attributed to the structure of $\rho(E)$.

$$M(E) = \frac{2\gamma}{a_0 q^2} \left| \langle f | e^{iq \cdot r} | i \rangle \right| \quad \text{Equation 2.3}$$

Where $|i\rangle$ and $|f\rangle$ describe the initial and final state electron wavefunctions, respectively, q defines the momentum transfer, a_0 , is the Bohr radius and γ is a relativistic quantity defined as:

$$\gamma = \frac{1}{\sqrt{1 - \frac{v^2}{c^2}}} \quad \text{Equation 2.4}$$

Therefore, the peaks in the fine structure are altered when the local bonding environment changes. By expanding the operator term, we get:

$$\exp(iq.r) = 1 + i(q.r) + \text{higher order terms} \quad \text{Equation 2.5}$$

Therefore, the result of *Equation 2.3* will be divided into the sum of 3 components. Since the initial and final electron states are orthogonal the first term in *Equation 2.5* is unity and accordingly the first component of *Equation 2.3* is zero. This second integral gives rise to $(q \cdot \langle f | r | i \rangle)$ where the matrix element is the optical dipole matrix element. This is an odd function and will be zero only if the $|i\rangle$ and $|f\rangle$ wavefunctions have same symmetry about the centre of the excited atom, since their product will be given. However, the integral can take a nonzero value if $|i\rangle$ is, for example, an s-state with even symmetry and $|f\rangle$ is a p-state with odd symmetry, then the two halves of the integral do not cancel. In this situation electronic transitions are observed. The third component represents higher order transitions, though these terms are insignificantly small and so have no major effect on the ELNES. This simple system is the basis for the dipole selection rule, below.

To a good approximation, the electron transitions obey the “Dipole Selection Rule”, *Equation 2.6*, governing allowable transitions between angular momentum states, ℓ , which results in asymmetry-projected DOS.

$$\Delta\ell = \pm 1 \quad \text{Equation 2.6}$$

Dipole forbidden transitions have been documented, [17] using large collection semi-angles, as this allows increased momentum transfer to the sample. In order to rule out the possibility of these forbidden transitions, e.g. 2p→3p from occurring, the collection semi-angle (β) is kept relatively small. In this case, it is solely the density of p-like states that determines the shape

associated with a K-edge ELNES, while L-edge ELNES reflects mainly the density of d-like states, although, the s-like states are reflected to a lesser extent. Therefore symmetry plays an important role. Additionally, the core wavefunction is taken as highly localised at the atomic site of an atom under excitation. Consequently, $\rho(E)$ is construed as a site and symmetry projected DOS. If the local chemical or coordination environment is altered, there is a resulting perturbation to the unoccupied DOS, $\rho(E)$, due to the interaction of the atomic orbitals in a solid. This perturbation is mirrored in the ELNES, which permits identification of different phases of a material, e.g. graphite, diamond and amorphous phases of C are clearly identifiable from their C K-edge ELNES [18] altering the chemical identity in iso-structural materials, such as TiC, TiN and TiO, results in alterations to the non-metal K-edge ELNES, [19]

2.7.2 Specimen alignment for collection of EELS data

For the collection of EELS data, it is important that the cross-sectioned specimens are correctly oriented. For this purpose, the diffraction pattern from the GaAs substrate, which has been grown in the [001] direction, has been used. Tilting of the sample has been performed at the beginning of the alignment process in CTEM mode. This operation is facilitated by placing the cross section specimen in a double tilt rod, such that their glue line was perpendicular to the α -tilt axis.

Once the specimen is inside the microscope, the diffraction pattern from the GaAs substrate has been tilted so that the [110] zone axis is parallel to the electron beam. In this case the growth direction remains normal to the electron beam (Fig. 2.11)

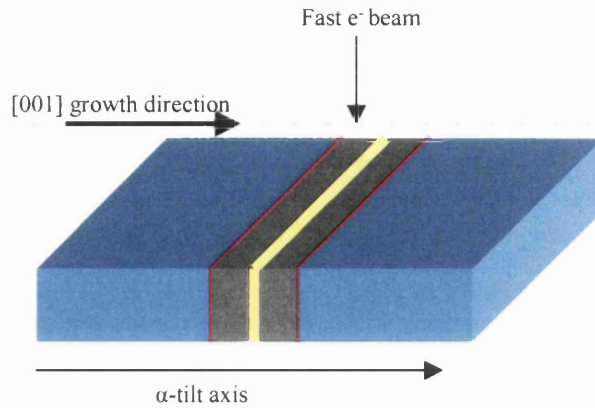


Fig. 2.11 Diagram of Ga₂O₃/GdGaO dielectric gate stack on a GaAs substrate. The sample is tilted such that the growth direction remains perpendicular to the incident beam.

STEM is essentially a nanoprobe diffraction mode. Condenser and objective optics are here aligned, in order to generate very small probe sizes. Diameters of 0.3-5nm can be easily obtained on the TF20. For most of the experiments performed on the Tecnai F20 an extraction voltage of 3.5kV and a dispersion of 1eV/ch have been chosen. By using such dispersion, it is possible to have in the same spectra the O K-edge (532eV), the Ga L₃ and L₂ edges (1115eV and 1142eV), the As L₃ and L₂ edges (1323eV and 1359eV) and the Gd M₅ and M₄ edges (1185eV and 1217eV).

By inserting the smallest C2 condenser apertures, it is possible to reduce the beam current and also the probe size.

In STEM mode the C2 condenser aperture was centred about the central region of the ronchigram, and adjustments were then made to the condenser stigmator and the objective focus to obtain as little contrast in the central region as possible. Thus, when the beam is scanned over the specimen, a focused and stigmated image can be obtained.

2.7.3 *Gatan-ENFINA PEELS Spectrometer*

EELS data for this project has been acquired using a Gatan-ENFINA 1000 parallel electron energy loss (PEELS) spectrometer and has been collected in STEM mode. The ENFINA spectrometer combining with STEM has the capability of investigating small areas of the sample with a high spatial and energy resolution. This is one of the main advantages of the Enfina spectrometer over the GIF one. An aperture is directly positioned at the entrance of the spectrometer and controls the amount of signal entering by restricting the allowable angular range of electrons. The main component of the Gatan Enfina 1000 parallel recording spectrometer used are shown in Fig. 2.12. Two spectrometer quadrupole and sextupole lenses can be adjusted to ensure the source is focussed on the detector. The electrons pass through an electrically isolated drift tube, and are deflected as they pass through a magnetic field. The electrons with the greatest energy loss are deflected most, in a process that is analogous to the splitting of white light in a prism. In the perpendicular direction the electrons off axis experience a restoring force at the entrance and exit of the prism, bringing them to a focal point in the dispersion plane. The electrons reach an yttrium aluminium garnet (YAG) scintillator, which is optically coupled to a semiconductor photodiode array. This collection method known as parallel energy loss spectroscopy (PEELS), allows the spectrum to be collected over a wide energy range simultaneously, rather channel by channel. The spacing between diode elements is $25\mu\text{m}$, but the spectrometer dispersion is typically $2\mu\text{m}/\text{eV}$. The necessary magnification between the spectrometer and scintillator is achieved using four quadrupole lenses and can range from 0.05 to $1\text{eV}/\text{channel}$, defining the energy range studied. A voltage may also be applied to the electrically isolated drift tube to vary the energy offset. The Gatan Enfina 1000 has a 1340×100 CCD.

To record a core-loss edge, a voltage is applied to the drift tube so that the energy loss range of interest is recorded on the diode array. For example, to record the O K-edge at 532eV , a voltage would be applied to the drift tube so that the channel on the diode array that had been set to 0eV for the ZLP would now correspond to an energy loss of $\sim 480\text{eV}$.

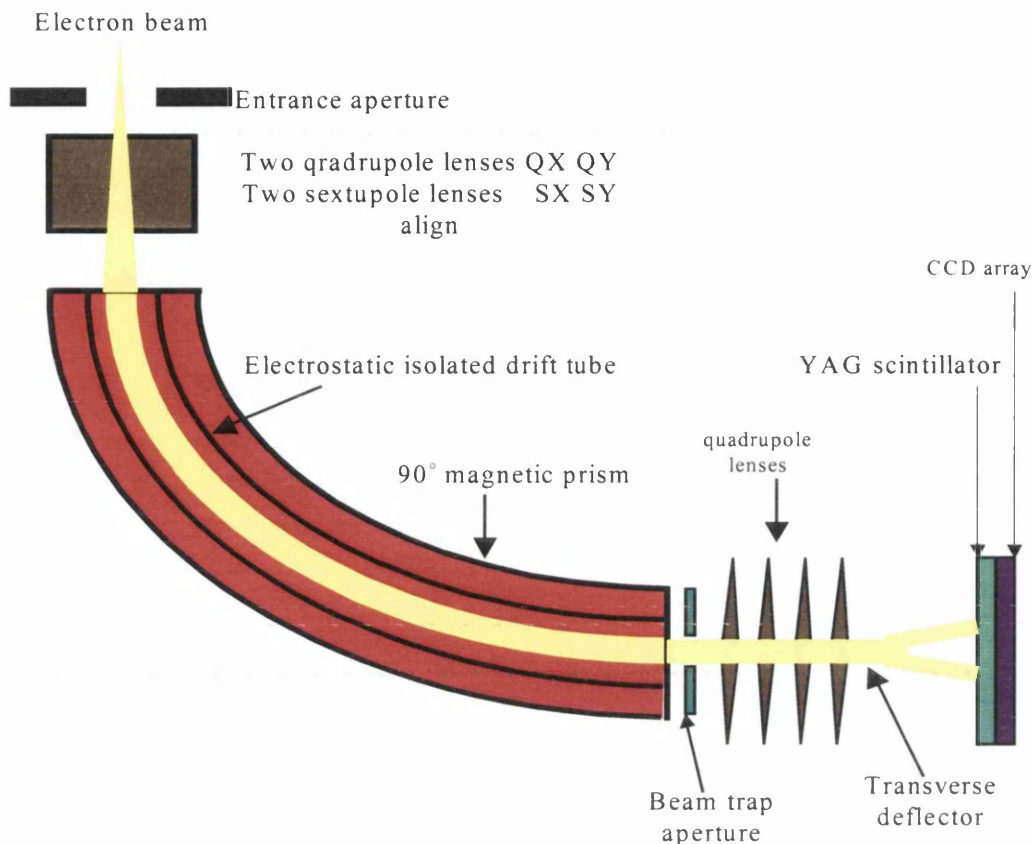


Fig. 2.12 Path of an electron beam as it travels through the Gatan Enfina 1000 PEELS spectrometer.

2.7.4 Imaging spectrometer GIF

EFTEM data for this project has been acquired using a Gatan Imaging Filter (GIF) 2001 and has been collected in CTEM mode in a Tecnai TEM T20.

The GIF spectrometer is described in Fig. 2.13. There are some differences between the Enfina and the GIF 2001. The most important is the presence of an energy selecting slit after the magnet. There are also more quadrupoles and sextupoles in the post-magnet optics of the GIF. The first two quadrupoles before the slit are used for increasing the dispersion of the spectrometer onto the slit and the other quadrupoles after, have two different functions:

- 1) They can project an image of the spectrum at the slit onto the CCD. In this mode the system is actually operating like a standard PEELS spectrometer.
- 2) They can compensate for the energy dispersion of the magnet and project a magnified image of the specimen onto the CCD. This actually represents an advantage of the GIF over the PEELS spectrometer. In this way, images, containing some electrons selected by the slit, will be generated

The GIF allows the user to generate electron spectroscopic images with a chromatic aberration comparable to that in the normal TEM. Such images can be acquired in a few seconds allowing the user to investigate large area of the specimen in a relatively short time.

Both the GIF and the ENFINA under STEM mode have the capability of performing a EELS Spectrum imaging (SI). In the case of the ENFINA, the beam will be scanned across a defined area on the specimen and EEL spectra will be acquired from each point in the specimen. In the case of the GIF the same area on the specimen will be imaged constantly changing the energy of the slit. If the GIF is attached under a TEM microscope with STEM capability it will be possible to perform EELS SI. Hence, the EELS SI package can be used in the ENFINA as well as in the GIF, but the EFTEM SI cannot be used with an ENFINA. However ENFINA is optimised for EELS SI.

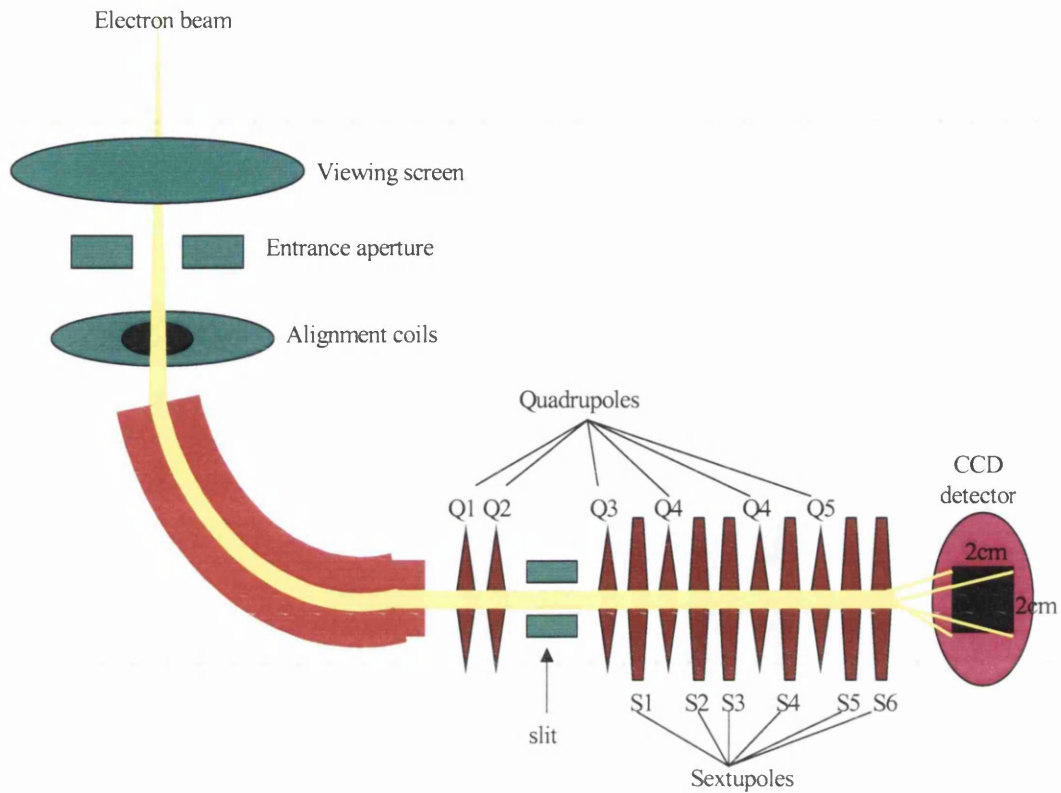


Fig. 2.13 Schematic view of a Gatan GIF spectrometer. The complex lens is composed of quadrupoles and sextupoles which make the optics of the GIF really complicated. Obviously the use of an appropriate computer control is required for operating.

2.7.5 Spectrometer alignment for collection of EELS data

The Gatan-ENFINA spectrometer optics is optimised using the ZLP. A ZLP is recorded through a hole in the sample using a dispersion of 0.05eV/channel and the 2mm spectrometer aperture. Typically 0.05 seconds is used as integration time to avoid the saturation of the detector. The voltage applied to the drift tube is altered to set the maximum of the ZLP to 0eV. The ZLP is tuned until the FWHM reaches the minimum value, typically 0.7eV for the F20 (Fig 2.14).

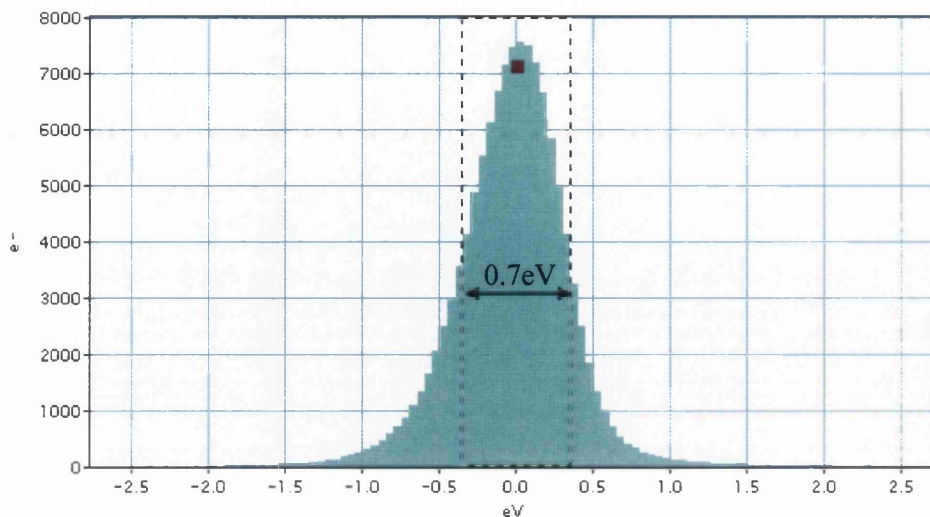


Fig. 2.14 A ZLP with FWHM of 0.70eV, collected in STEM with $V=3500V$ and probe diameter of 0.7nm.

For the acquisition of high-energy part of the EELS spectrum is necessary to drop the camera length down to 30mm. In this way the beam which goes through the spectrometer is more intense leading to a bigger signal to noise ratio. The signal will increase therefore, it is necessary to set the offset to a value where saturation of the detector is avoided.

Once the camera length is changed, the electron beam needs to be centred on the spectrometer and this can be achieved by using the multifunction button to shift the diffraction pattern until the highest intensity of the EELS spectrum is obtained. In this way the intensity of the beam going through the spectrometer will be the highest possible. For almost all the core-loss analysis described in this thesis, a dispersion of 1eV/channel and a 5mm spectrometer aperture have been chosen. Using these conditions the presence of the most intense signal in the EELS spectrum has been ensured. However the use of such large spectrometer aperture increases the amount of electron going into the spectrometer. Hence the signal to noise ratio of the EELS SI will be bigger. Chapter 4 will describe in details all the EELS SI work carried out for this thesis.

2.7.6 Fast Beam Switch (FBS)

As noted above, the ZLP represents an important feature for EELS spectroscopy. It gives information on specimen thickness, atomic density and more importantly by correlating the ZLP with the core loss edge for a given element, it is possible to determine the position of the core loss edge threshold and correct for the effect of the multiple scattering.

However, this part of the spectrum, due to the high intensity, may cause some problems such as damage the scintillator. In all the ordinary TEM systems, the simultaneous acquisition of the zero loss and core loss EELS spectrum would not be possible as the zero loss is very intense and its acquisition at the same condition of the core loss would damage the scintillator. The difference in intensity between them can be as high as 10^5 . Thus the acquisition time for the ZLP and the core loss is by this factor different. In all the ordinary TEM systems, time and intensity strongly limit the possibility of acquiring core loss and ZLP in the same spectrum.

Recently a fast electrostatic system has been developed for the Glasgow F20. This provides a fast shutter for the spectrometer. This system is called Fast Beam Switch (FBS). Fig 2.15 shows a diagram of the Tecnai F20 with various components of the FBS system and the effect of the FBS insertion on the beam respectively.

The electron beam is actually deflected from its original path [63]. This mechanism allows the acquisition of either the zero loss and the core loss in the same area exactly at the same experimental conditions. During the core loss acquisition which may requires several seconds, the electron beam is not deflected, while during the ZLP acquisition, the electron beam is deflected out of the spectrometer a part from the short time needed for the exposure.

The main advantage of using the FBS is the possibility of the simultaneous acquisition of both the zero loss and core loss spectrum. On the other hand the disadvantage is that the overall acquisition time of the whole spectrum is doubled. Therefore the beam will sit on the same area of the sample for a longer time, this certainly will increase the possibility of damage effects.

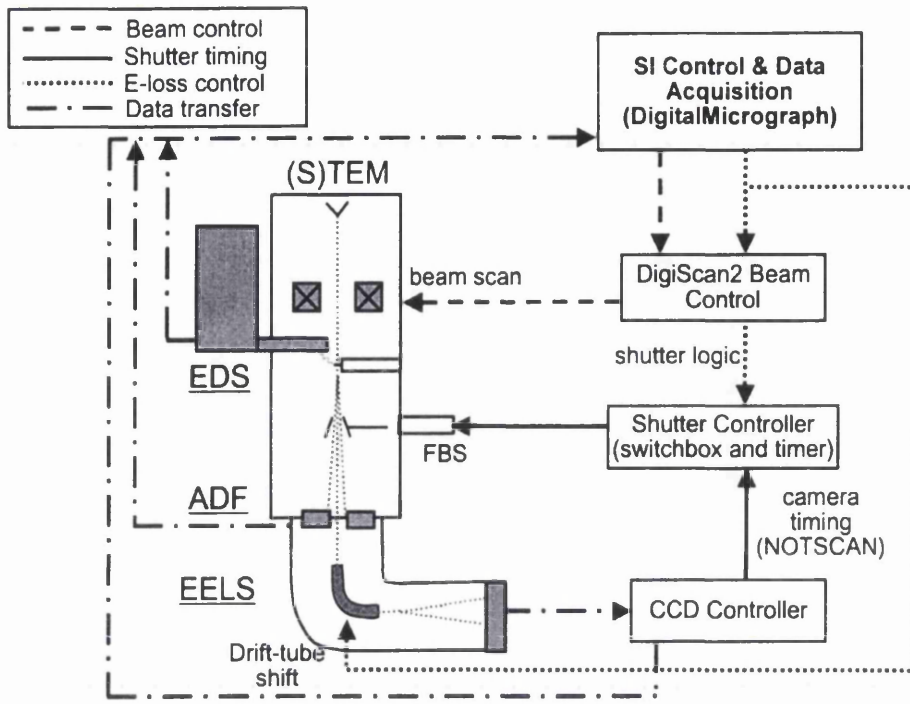


Fig. 2.15 Diagram illustrating the signal paths between the various components of the fast beam switch system.

The FBS system is mounted in the 35mm port opposite to that used to the Fischione HAADF detector. The plates for the beam deflection are inserted and retracted by a pneumatic mechanism. The movement of this mechanism is interlocked with the HAADF detector in the opposite 35mm port to avoid collisions. It is not possible to use the HAADF detector and FBS at the same time. This is not a very big issue as when the FBS system is used, generally the camera length is quite short 30-50mm and the HAADF signal is too weak under these conditions. In this case the DF essentially acts as the HAADF detector.

An important point is when the FBS is on, the electron beam is deflected away from the spectrometer entrance aperture, it is also deflected from the DF detector.

As said above FBS system allows to acquire simultaneously low and core loss spectrum under the same experimental conditions. The effects of the plural scattering can be removed and it is also possible to determine exactly the threshold of an ionisation edge. Fig. 2.16 gives an example of that for $\text{Gd}_3\text{Ga}_5\text{O}_{12}$. Zero loss, low and core loss spectrum are shown in the same dataset.

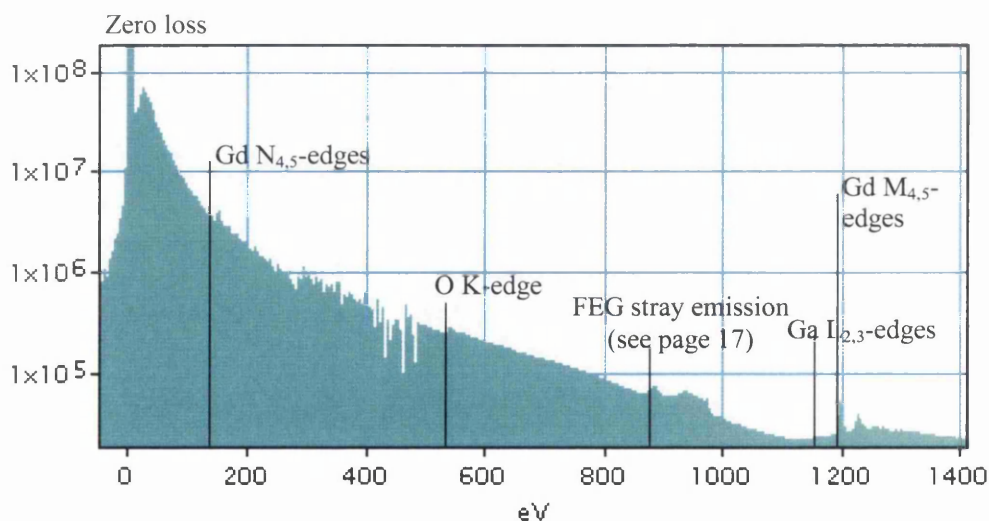


Fig. 2.16 EELS spectrum of $\text{Gd}_3\text{Ga}_5\text{O}_{12}$. Zero loss and all the other ionisation edges in the spectrum are present in the same dataset. This allows us to determine the position of the threshold with extreme accuracy.

2.8 TEM SPECIMEN PREPARATION

2.8.1 *Powders*

In order to examine polycrystalline powders in an electron microscope, they were first crushed in an agate mortar and pestle, to break them up into smaller particles and expose new, clean surfaces. Propanol was used to disperse them. A few drops were removed from the top of the suspension with a Pasteur pipette, so that only the smallest particles were picked up, and transferred to holey carbon film. In order to let the solvent evaporate, the disc of holey carbon film was transferred in the oven at a relative low temperature.

This synthesis route has been used to prepare TEM sample of Ga_2O_3 and $\text{Gd}_3\text{Ga}_5\text{O}_{12}$. All the other TEM samples analysed in this thesis, have been prepared by a cross section encapsulation method.

2.8.2 *Thin films*

A standard cross-section encapsulation method has been used to prepare 3mm electron transparent specimens from GaAs/ Ga_2O_3 /GGO samples. In the first step, two thin strips were cut from the original wafer prepared by MBE method in the Department of Electrical & Electronics Engineering here at the University of Glasgow.

These two strips were then ground, using fine emery paper, until both sections were of equal length and width. These sections were then mounted on glass slides using hot wax, with the oxide layer facing toward the glass slide. The GaAs substrate was thinned to $180\mu\text{m}$ by grinding and polishing.

The next step was the encapsulation. An epoxy-resin was used to glue the two pieces of Ga_2O_3 /GGO face to face and then to glue them into a pre-cut region in a molybdenum rod that was subsequently encased in a brass tube, as shown in Fig. 2.17. The finished product was left in the oven for two hours at a temperature of 130° , to allow the epoxy-resin to harden. Once set, the hydrocarbon in the epoxy is unlikely to interfere with the sample during an EELS analysis.

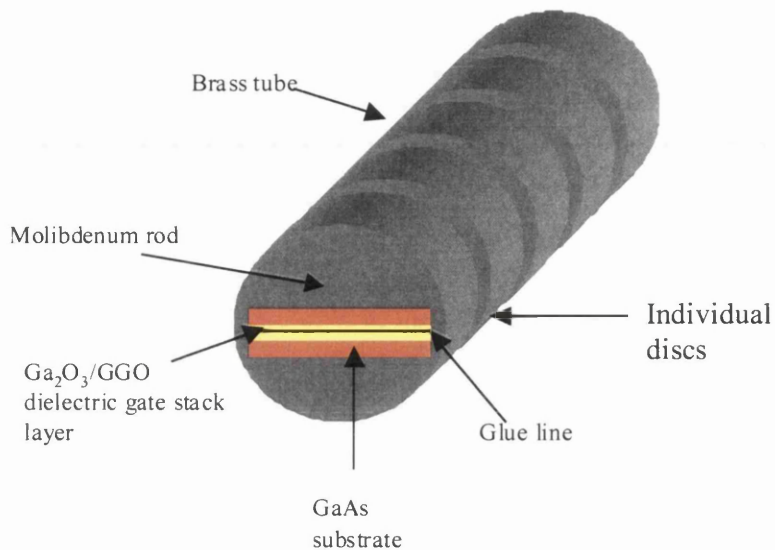


Fig. 2.17 The final encapsulated rod, cut into 800 μm discs

The brass rod was cut into discs by using a diamond saw. The discs were then ground using coarse silicon carbide paper, followed by finer grades of paper to obtain a final disc with 120 μm thick. Finally, both surfaces were polished on a rotating wheel using 3 μm diamond paste for removing residual scratches.

A disc was then mounted on a centre of a small glass stub by using wax, and loaded into a dimple grinder. The stub was centred on a rotating table. Both sides were dimpled in turn to leave a centre thickness of less than 10 μm .

Once this thickness has been reached, the disc was placed under reflux in soxhlet apparatus for 1.5 hours, using inhibisol solvent. When the inhibisol condenses, it is held in the upper part of the apparatus and dissolves any hydrocarbon present in the disc. Thereafter the solvent is returned to its original flask. The temperature for the evaporation of the inhibisol is lower than that for the hydrocarbon, allowing this process to be repeated over the time necessary to cleanse all the components. This operation is also important because allows to completely remove the debris from dimple grinding along with any residual wax present.

The final thinning process is the ion milling by using a Gatan precision ion polishing system (PIPS). The disc was carefully centred in a suitable sample holder and placed into the PIPS where two Ar ion beams milled away material from both sides at the centre of each dimpled surface. The sample during this process is kept rotating and the two Ar ion guns are placed above and below with respect to the sample. Each beam is incident on the surface with an angle of 4° .

For these films, an ion beam energy of 4kV was used until a hole was observed in the glue line. Once the hole appeared the ion energy was dropped down to 2kV in order to obtain a smooth surface and less damage. To check out that the sample was likely to be electron transparent, the milled disc was placed into a high-resolution optical microscope. The sample is electron transparent when thickness fringes appear all around the glue line.

CHAPTER 3: THEORETICAL MODELLING AND TECHNIQUES

3.1 INTRODUCTION

In the previous chapter, the ELNES on ionisation edges has been described as an experimental fingerprint of the crystal structure. However, although the ELNES details are associated with the electronic structure in the material, a direct interpretation of the features observed in the ELNES spectra is not easy. This is because the nature of the bonding interaction between the atoms is very complex and affected by many variables. All these variables influence the form of the unoccupied electronic states and consequently, the fine structure in the near edge region. Currently three main approaches for modelling the electronic structure of materials, have been formulated: molecular orbital theory (MOT) [20]; solid state band structure (BS) theory [21]; real space multiple scattering (RSMS) theory [22, 23]. For the work of this thesis the program FEFF 8.2 based on RSMS theory has been chosen to model the electronic structure for Ga_2O_3 , $\text{Gd}_3\text{Ga}_5\text{O}_{12}$ and GdGaO_3 . Moreover, in this thesis, it is shown that the combination of experimental ELNES and FEFF 8.2 simulated electronic structure, gives the possibility of investigating the magnetic properties within the material of interest.

3.2 REAL SPACE MULTIPLE SCATTERING

3.2.1 Theory

FEFF electronic structure calculations are based on an approach devised by Lee and Pendry [24] to simulate x-ray absorption spectra (XAS). The Density of States (DOS) is found through use of the real space Green's function formalism. This method also simulates the excitation of a core electron by high-energy photons, using a wave description for the atomic electrons. In this way, the excited core electron is considered as outgoing photoelectron wave, which is scattered by neighbouring atoms in the target material. An interference pattern is induced when the scattered photoelectron wave returns to the absorbing atom and interacts with the outgoing electron wave, resulting in the near edge structure observed in the corresponding absorption spectrum. The scattering potentials of neighbouring atoms determine the relative change in phase of the electron wave. Single scattering events by an excited photoelectron, with a short mean free path ($\text{MFP} < 20 \text{ \AA}$), dominate the X-ray Absorption Far Edge Structure (EXAFS)

region. By comparison, structures in the X-ray Absorption Near Edge Structure (XANES) energy region results mainly from multiple scattering events. The photoelectron has a longer inelastic MFP at low energies, allowing scattering events from comparatively larger volumes of specimen to contribute to interference effects at the absorbing site. Though originally devised to simulate the extended x-ray energy loss fine structure (XAFES) energy range, subsequent improvements to the FEFF code have resulted in significantly increased accuracy of the near-edge structure energy region by incorporating scattering paths to infinite order, known as full multiple scattering (FMS). Further discussion of the related theory can be found in many informative texts such as: [22, 23, 25, 26, 27].

Both XAS and EELS involve the excitation of an atomic electron by electromagnetic interaction; an electron to form ELNES spectra and a photon for XANES spectra. Therefore both theories, despite having very different origins, result in similar equations to describe the resulting near-edge structure. Consequently, it is appropriate to use the XANES spectra simulated by FEFF8.2 for comparison to the ELNES spectra collected by EELS.

Although in principal scattering occurs throughout the bulk of the material, in practice to the decay of the outgoing wave with distance, scattering is dominant by the nature, and positioning of, the nearest neighbour atoms. Hence, the FEFF cluster-based computational approach is appropriate. Also by systematically extending the cluster radii it is possible to ascertain the importance of certain chemical scatters and their scattering path. This type of simulation is therefore useful in the study of crystalline solids but can equally be applied to amorphous systems and non-periodic structures such as defects in materials.

3.2.2 Broadening

FEFF O-K XANES spectra are calculated for the excited state and thus, will intrinsically incorporate lifetime broadening to account for the uncertainty in both core hole and excited final state lifetimes. Therefore, final FEFF ELNES data is simply convolved with a Gaussian function of the required width for a comparison to experimental data.

3.2.3 Core hole effects

FEFF is an excited state code. It automatically takes into account both the finite lifetime of the excited electron, and the electron hole that is consequently left behind. This is achieved through the Z^* approximation, where an electron is removed from a core energy state and added to the valence band. Thus, an excited oxygen atom will possess an excited state $1s^1 2s^2 2p^5$ electronic configuration rather than the ground state configuration, $1s^2 2s^2 2p^4$.

3.2.4 Running a calculation

3.2.4.1 Atoms input

For crystalline materials, a program called ATOMS2.46b is a quick and simple tool to generate FEFF input files, complete with the requisite atomic list. In order to achieve this, it is important to get basic crystallographic information on each system under investigation such as the space group of the unit cell, its cell parameters and the atomic coordinates of each non equivalent atom contained therein. An example ATOMS input file is given:

```
title name: Ga2 O3
space C 2/m
a 12.214 b 3.0371 c 5.7981
alpha 90.0 beta 103.81 gamma 90.0
core O1
edge K
rmax 10
atoms
Ga 0.09050 0.0 0.79460 Ga1
Ga 0.15866 0.5 0.31402 Ga2
O 0.1645 0.0 0.1098 O1
O 0.1733 0.0 0.5632 O2
O -0.0041 0.5 0.2566 O3
```

The atom under the excitation is placed at centre of the FEFF cluster by 'core'. The maximum cluster radius (R_{\max}) has to be defined as 10\AA from the core atom. This is generally more than adequate to simulate a bulk crystalline environment. The interaction of the excited atom with

atoms further than this are fairly insignificant and in any case, would be lost when instrumental broadening is incorporated. The element symbols to the left hand side of their respective atomic coordinates, identify the constituent atoms while those to the right hand side serve as crystallographic labels.

3.2.4.2 *FEFF input*

The FEFF input file contains a list of each atom in the spherical cluster, starting with the central atom under excitation and followed by the other atoms in order of distance from the centre. Therefore, it is possible to discern distinct ‘shells’ surrounding the excited atom.

A total of six modules must be run in sequence for a full calculation. They are detailed below:

- ‘POT’ constructs the appearance of the scattering potentials observed by the excited photoelectron and estimates the absolute energies. A distance R_{SCF} is set by the user to define the number of atoms to be included in the SCF cycle. Generally, for obtaining accurate potentials, ~70 atoms were included.
- ‘XSPH’ formulates relativistic dipole matrix elements from core atomic wavefunctions and normalised continuum wavefunctions. Scattering phase shifts are calculated by matching at the muffin-tin radii. Also, the x-ray cross-section, and the angular momentum projected DOS are obtained by this second module. It is important to note that a degree of broadening is intrinsic to DOS spectra as a direct consequence of the finite cluster size used to simulate the bulk environment.
- ‘FMS’ or ‘full multiple scattering’ module, to calculate the XANES spectrum resulting from a cluster of atoms out to a user defined radius, R_{FMS} . Normally, the number of shells included in the full-MS calculation has been systematically increased, until the general shape of the O K-XANES converged. Simulations have been performed for clusters containing up to ~250atoms.
- ‘PATHS’ details the major multiple scattering paths. To obtain convergence of the fine structure in the XANES region, a ‘full multiple scattering’ calculation is performed which sums all scattering paths to infinite order.
- ‘GENFMT’, or the general path F-matrix module, computes the effescattering amplitudes, f_{eff} , and x-ray absorption fine structure (XAFS) parameters for all scattering paths.

- 'FF2CHI', or scattering amplitude to χ , combines XAFS parameters to find a total EXAFS or XANES spectrum that includes instrumental broadening effects through convolution of the data with a Gaussian function of width specified by the user using the 'CORRECTIONS' card.

Various cards are also used throughout the calculation. For example, although the core atom is always taken as the atom under excitation, the absorption edge must be specified by the user, using the card 'EDGE'. The presence of the card 'NOHOLE' allows calculation of the ground state, without inclusion of core hole effects.

3.3 OXYGEN K-EDGE: COMPARISON BETWEEN XANES SIMULATIONS AND EXPERIMENTAL ELNES RESULTS

This section details the results from a systematic EELS investigation of the K-edge fine structure found for oxygen atoms in some compounds containing Ga, Gd and O. All EELS spectra presented have been collected on the Tecnai F20 electron microscope and Enfina spectrometer described in chapter 2. In addition, results from theoretical calculations such as FEFF 8.2 are presented as an essential aid to our understanding of how structure, observed in the near edge region of each oxygen K-edge, is formed. Electrons in the oxygen atoms are being excited from core 1s to p-like electronic states. The shape of the ionisation edge reflects the structure of the unoccupied partial p-DOS and this in itself is a reflection of the local environment of the excited atoms.

FEFF8.2 simulations for crystalline materials such as beta Ga_2O_3 , $\text{Gd}_3\text{Ga}_5\text{O}_{12}$ and GdGaO_3 , were carried out. All the elements present in these compounds are contained in the amorphous oxide layer. The results obtained from the simulations are compared to the experimental ELNES from the same crystalline materials. In this way, it has been possible to cross check the differences between the results from the FEFF simulations and the experimental ELNES ones. The FEFF calculation is based on an atomic cluster with the excited atom at the centre. The crystallographic data on the compound necessary for ATOMS INP is available at the ICDS (Inorganic Chemical Database Service).

The first material simulated was $\beta\text{Ga}_2\text{O}_3$. The parameters used for this calculation are given in Fig. 3.1 and were downloaded from the ICDS:

ICSD Details [Print](#)

1 entry selected.

CC=Collection Code: [AB2X4]=ANX Form: [cF56]=Pearson: [e d a]=Wyckoff Symbol: [Al2MgO4]=Structure Type:

Click the ANX, Pearson or Wyckoff Symbol to find structures with that symbol.

CC=83645

Help

Title A reinvestigation of beta-gallium oxide.

Authors Ahman, J.;Svensson, G.;Albertsson, J.

Acta Crystallographica C (1996) **52**, 1336-1338

Reference [Link Xref SCOPUS SCIRUS Google](#)

Also: Phase Transition (1992) **38**, 127-220

[Link Xref SCOPUS SCIRUS Google](#)

Compound **Ga2 O3** - Gallium oxide - beta [**A2X3**] [**mS20**] [**i5**] [**Dy3Ni2**]

Cell 12.214(3), 3.0371(9), 5.7981(9), 90., 103.83(2), 90.

C12/M1 (12) V=208.85

Remarks R=0.022000 : TEM =273.2 : TYP =Dy3Ni2 : PDF =43-1012 : Stable above 923 K (2nd ref., Tomaszewski)

Atom (site)	Oxid.		x, y, z, B, Occupancy					
Ga1	(4i)	3	0.09050(2)	0	0.79460(5)	0.0038(1)	1	
Ga2	(4i)	3	0.15866(2)	0.5	0.31402(5)	0.0040(1)	1	
O1	(4i)	-2	0.1645(2)	0	0.1098(3)	0.0060(4)	1	
O2	(4i)	-2	0.1733(2)	0	0.5632(4)	0.0056(4)	1	
O3	(4i)	-2	-.0041(2)	0.5	0.2566(3)	0.0042(4)	1	

Fig. 3.1 Details of the structure of β -Ga₂O₃ including the coordinates of the chemically different atoms present in this unit cell and the lattice parameters. There are 5 different atoms, 2 gallium and 3 oxygen.

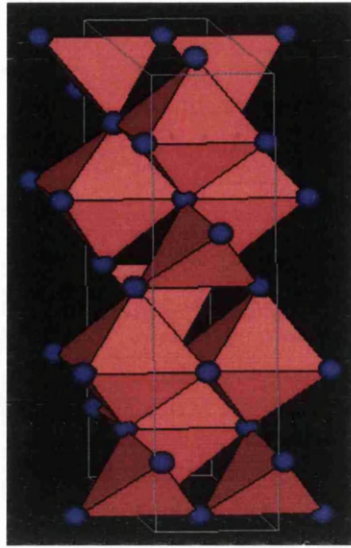


Fig. 3.2 Unit cell of β -Ga₂O₃. There are polyhedra around the atoms of gallium. The blue balls are the atoms of oxygen. It is possible to see that there are 2 different type of gallium one with a tetrahedral coordination and the other one in octahedral.

Fig. 3.1 shows that this type of structure is quite complicated because there are 2 different gallium environments, the first one with a tetrahedral coordination (4 oxygen surrounding the gallium atom), and the second one with a octahedral coordination (6 oxygen surrounding the gallium atom). It's possible to see this situation in the Fig. 3.2 in which is shown the structure with oxygen polyhedra around the gallium atoms. The blue balls are the oxygen atoms. Looking at figure 3.1, it's possible to see that there are 3 different oxygen sites. This means that there are three different chemical environments for the oxygen. Therefore three different calculations need to be for the oxygen absorption edge changing only the excited atom. In this way three different XANES spectra have been obtained, one for each type of oxygen present in the structure (Fig. 3.3)

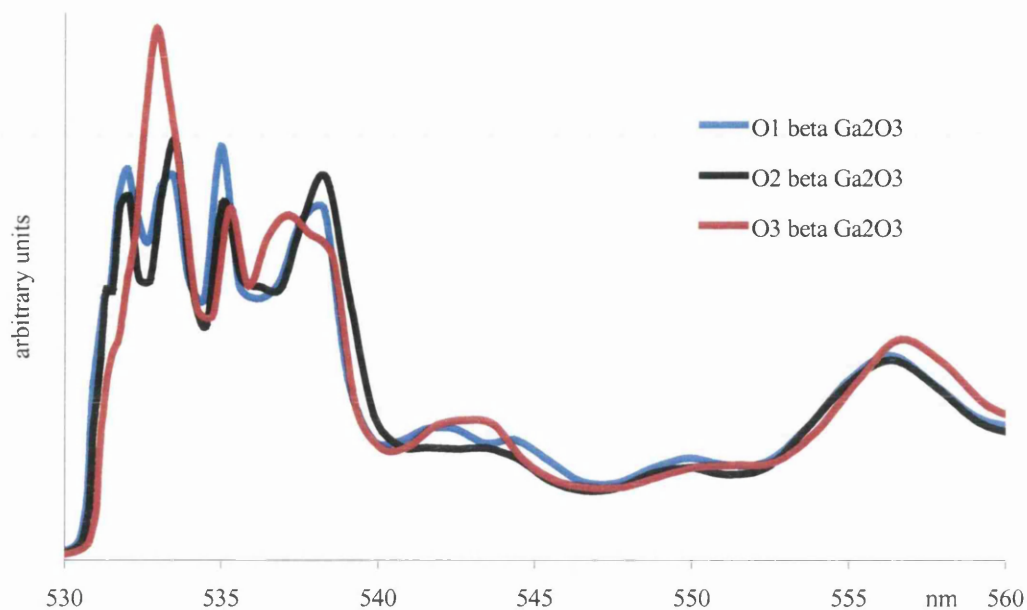


Fig. 3.3 Comparison among the FEFF8.2 simulated XANES spectra for the 3 different O sites in the crystalline beta Ga_2O_3 .

Visualizing the oxygen environments is more difficult. The FEFF input file gives the coordinates of the surrounding metallic element and these positions can be shown as in Fig. 3.3 for O2. By a vector calculation I was able to determine the distance between the oxygen and plane of the gallium atoms. Looking at Fig. 3.4, around the O2 there are 4 atoms located in a tetrahedral structure. (green colour for the octahedral gallium and blue colour for the tetrahedral one). For O1 and O3 the metals are in the form of a triangle around the O.

In O1, the O is 0.40 Angstrom off the plane. For O3, the oxygen is essentially on the plane formed by the 3 atoms of gallium (only 0.08 Angstrom above it).

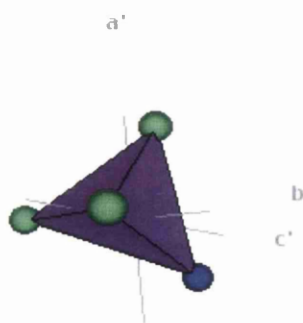


Fig. 3.4 View of the neighbour atoms around the O2.

With Dr Scott, the ELNES shape for $\beta\text{Ga}_2\text{O}_3$ was measured, Fig. 3.5 shows a comparison of the experimental data with the as simulated data and after some broadening of about 0.8eV.

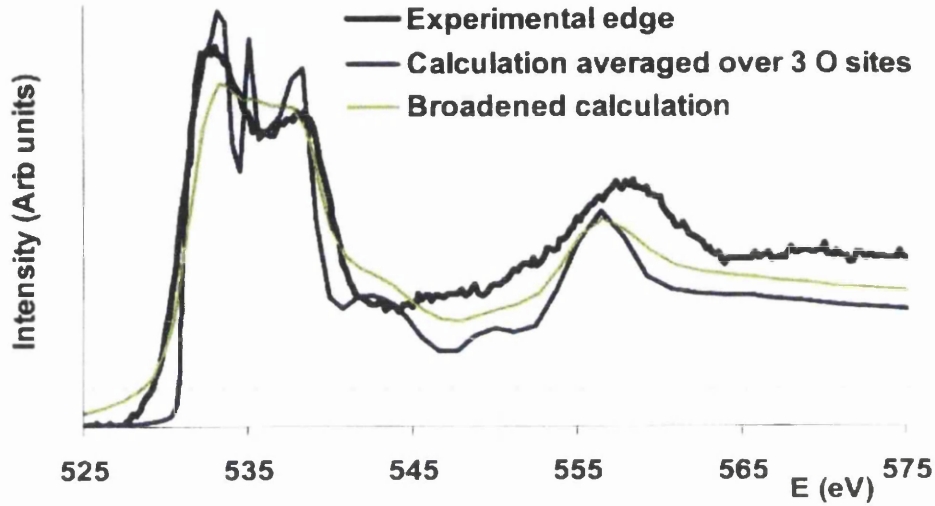


Fig. 3.5 Comparison of the experimental edge, the calculation averaged over 3 O sites edge and the broadened calculation one.

First of all it is important to mention that the resolution offered by the simulations offer much better resolution than the experimental results which are affected by many variables such as instrumentation. Those factors strongly limit the resolution of the ELNES spectra.

1 entry selected.
 CC=Collection Code: [AB2X4]=ANX Form: [cF56]=Pearson: [e d a]=Wyckoff Symbol: [Al2MgO4]=Structure Type:

Click the ANX, Pearson or Wyckoff Symbol to find structures with that symbol.

CC=84874 [Help](#) [CIF](#) [Export](#) [Bonds](#) [Pattern](#) [Structure](#) [Jmol](#) [Cweb](#)

Title Electron density study of garnets: Z3 Ga5 O12; Z = Nd, Sm, Gd, Tb.

Authors Sawada, H.

Reference Journal of Solid State Chemistry (1997) **132**, 300-307
[Link XRef SCOPUS SCIRUS Google](#)

Compound **Gd3 Ga5 O12** - [Unnamed_Garnet] Trigadolinium pentagallium oxide [**A3B5X12**] [**cI160**] [**h d c a**] [**Al2Ca3Si3O12**]

Cell 12.3829(5), 12.3829(5), 12.3829(5), 90., 90., 90.
IA3-D (230) V=1898.75

Remarks R=0.018000 : TYP =Al2Ca3Si3O12 : MIN =Unnamed_Garnet :
 At least one temperature factor missing in the paper.

Atom (site)	Oxid.		x, y, z, B, Occupancy			
Gd1	(24c)	3	0.125	0	0.25	0 1
Ga1	(16a)	3	0	0	0	0 1
Ga2	(24d)	3	0.375	0	0.25	0 1
O1	(96h)	-2	0.0289(2)	0.0542(2)	0.6494(2)	0 1

Fig. 3.6 Details of the structure of Gd₃Ga₅O₁₂ including the coordinates of the chemically different atoms present in this unit cell and the lattice parameters. There are 4 different atoms: 2 gallium, 1 oxygen and 1 gadolinium.

The second case is Gd₃Ga₅O₁₂. The parameters to run this calculation are found in the ICDS (Fig. 3.6).

In this case, there is only one type of oxygen, but there are two different type of gallium (Ga1 in octahedral coordination with 6 oxygen around the gallium atom and Ga2 in tetrahedral coordination with 4 oxygen around). There is only one type of gadolinium, which is in distorted eight-fold coordination. Fig. 3.7 shows the unit cell of this compound as Ga and Gd polyhedral around the oxygen and the oxygen is in tetrahedral coordination, as shown in Fig 3.8.

Fig. 3.9 shows the comparison between the experimental data (ELNES spectra) with the simulated one (XANES), again showing good agreement.

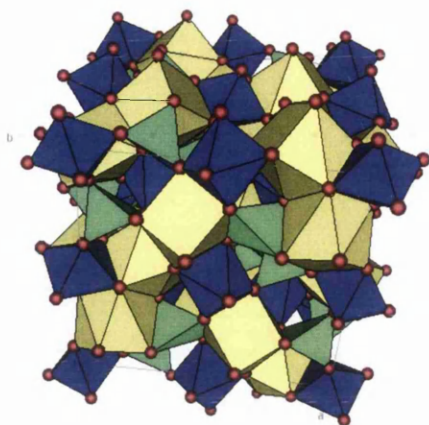


Fig. 3.7 Unit cell of $Gd_3Ga_5O_{12}$ putting oxygen polyhedra around Ga1, Ga2 and Gd
 Green: Ga2
 Blue: Ga1
 Yellow: Gd
 Red balls: oxygen

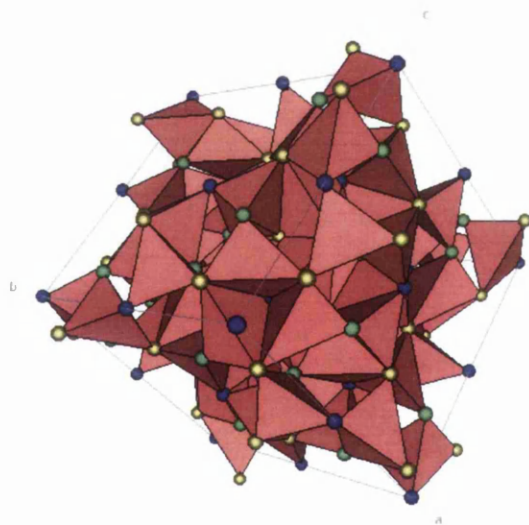


Fig. 3.8 Metal polyhedra around the oxygen showing that there are 2Gd 1Ga1 and 1Ga. The tetrahedron is distorted. The distance of the 4 faces from the oxygen atom is not the same for each face.
 Face1 (Ga1, Gd, Gd) distance is 0.97
 Face2 (Ga2, Gd, Gd) distance is 0.47
 Face3 (Ga2, Ga1, Gd) distance is 0.67
 Face4 (Ga1, Ga2, Gd) distance is 0.35

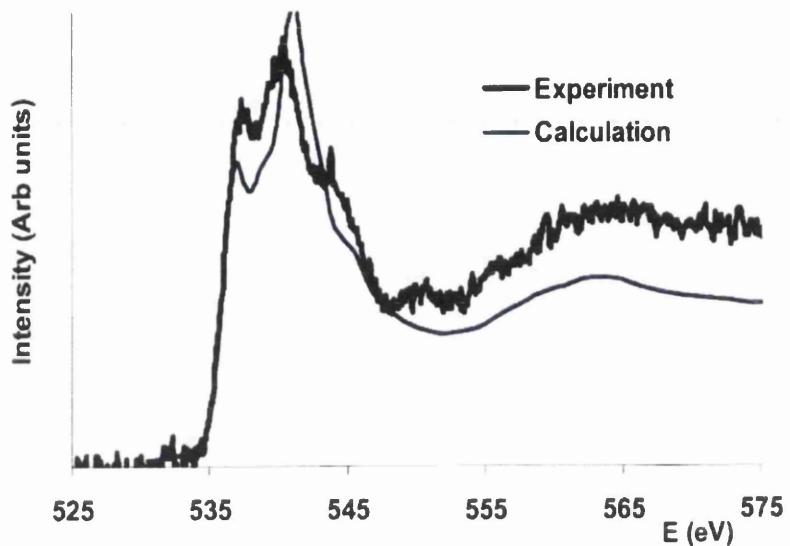


Fig. 3.9 Comparison between the experimental ELNES edge and simulated one. The agreement between these two shapes is very good.

The third simulation is of GdGaO_3 that has a composition similar to one of those amorphous oxide layer grown by MBE here in Glasgow. In the GGO sample, the Gd concentration is roughly 19.1%. Therefore, a FEFF simulation of a crystalline sample with similar composition is needed. Looking at the inorganic database, there is only one type mixed Gd and Ga oxide with Gd concentration of 20%. Its chemical formulae is: GdGaO_3 . The parameters for running the simulation have been downloaded from the ICSD shown in Fig. 3.10.

1 entry selected.

CC=Collection Code: [AB2X4]=ANX Form: [cF56]=Pearson: [e d a]=Wyckoff Symbol: [Al2MgO4]=Structure Type:

Click the ANX, Pearson or Wyckoff Symbol to find structures with that symbol.

CC=492 [Help](#) [Export](#) [Bonds](#) [Pattern](#) [Structure](#) [Jmol](#) [Cweb](#)

Title Single-crystal synthesis and structural refinement of Gd Ga O₃.
Authors Guitel, J.C.;Marezio, M.;Mareschal, J.
Reference Materials Research Bulletin (1976) **11**, 739-744
[Link XRef](#) [SCOPUS](#) [SCIRUS](#) [Google](#)
Compound **Gd Ga O₃** - Gadolinium gallium oxide **[ABX₃] [oP20] [d c2 b] [GdFeO₃]**
Cell 5.334, 5.548, 7.621, 90., 90., 90.
PBNM (62) V=225.53
Remarks R=0.015000 : TYP =GdFeO₃ :

Atom (site)	Oxid.	x, y, z, B, Occupancy
Gd1	(4c)	3 0.98530(5) 0.05933(5) 0.25 0 1
Ga1	(4b)	3 0 0.5 0 0 1
O1	(4c)	-2 0.09502(85) 0.47235(86) 0.25 0 1
O2	(8d)	-2 0.69999(57) 0.29887(60) 0.04913(47) 0 1

Fig. 3.10 Details of the structure of GdGaO₃ including the coordinates of the chemically different atoms present in this unit cell and the lattice parameters. There are 4 different atoms: 2 oxygen, 1 gallium and 1 gadolinium

Gadolinium and gallium are respectively in distorted eight fold and octahedral coordination (Fig. 3.11) and two types of oxygen with different environments. O1 surrounded by 4 atoms and O2 surrounded by 5 atoms. Figs. 3.12 and 3.13 show the view of the neighbour atoms around the O2 and the view of the neighbour atoms around the O1 and the unit cell respectively.

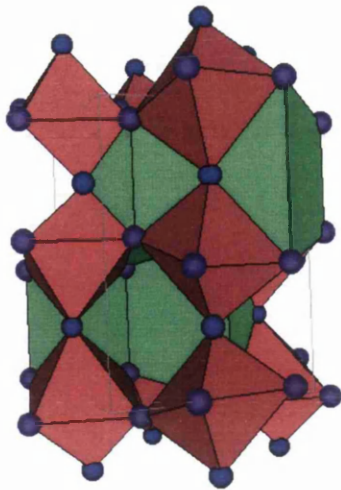


Fig. 3.11 Unit cell with oxygen polyhedra around Gd (green) and Ga (brown)

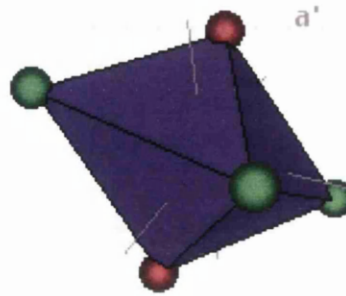


Fig.3.12 View of the neighbour atoms around the O2. As you can see the oxygen lies on the plane composed by the 3 Gd atoms (green), and 2 Ga (brown) are far away

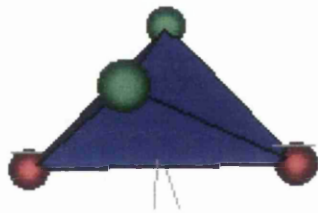


Fig. 3.13 View of the neighbour atoms around the O1 There are 2 Gd (brown colour) and 2 Ga (green colour)

In this structure there are 2 different oxygen sites. Therefore it is necessary to run 2 different simulations changing only the core atom. Fig. 3.14 shows the average of the O XANES spectra for this compound compared to the experimental ELNES spectra of the amorphous Gd:

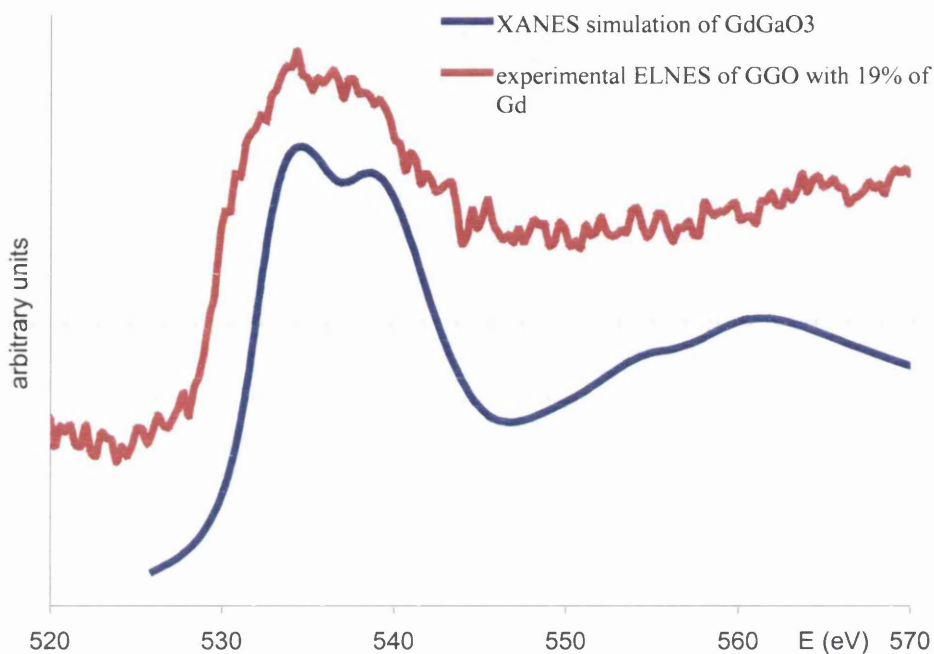


Fig. 3.14. Comparison of the experimental ELNES for the amorphous GGO with 19% of Gd and XANES simulation for GdGaO₃. The simulation has been broadened in order to get a better match with the experimental results.

The match between the experimental ELNES and the simulated XANES spectrum, is good. As described in section 3.5, amorphous layers of GGO are particularly beam sensitive. The acquisition of the EELS spectrum has to be performed with extreme care, trying to keep the dose as low as possible in order to preserve the material from any damage due to the long exposure to the electron beam. This explains why the ELNES spectrum is relatively noisy.

However by broadening the XANES simulated spectrum is possible to improve the match with the experimental ELNES spectrum.

3.5 CONCLUSIONS

FEFF8.2 has provided an insight into the origins of the ELNES observed on experimentally collected O K-edges. A good match between simulations and experimental results has been observed in $\beta\text{Ga}_2\text{O}_3$, $\text{Gd}_3\text{Ga}_5\text{O}_{12}$ and GdGaO_3 .

FEFF8.2 is a very useful program. It gives the possibility of performing magnetic simulations by changing the *feff.inp* file. This facility has been successfully used for the investigation of the magnetic properties in $\text{Gd}_3\text{Ga}_5\text{O}_{12}$.

Unfortunately the $\text{Ga}_2\text{O}_3/\text{GGO}$ dielectric gate stacks turned out to be electron beam sensitive. High electron dose changes the chemical structure. In chapter 4 some examples of e^- damage effects are shown. In particular phenomena such crystallisation and phase separation usually occur when the dose is high. These problems make almost impossible to acquire any ELNES data as a high dose is required in order to get a well-resolved spectrum. Thus the simulation work was halted as it did not seem to offer useful support for the main project.

3.5.1 Radiation sensitivity of the *GaAs/Ga₂O₃/GGO dielectric gate stack*

The $\text{Ga}_2\text{O}_3/\text{GGO}$ layer is quite electron beam sensitive. Under the action of the electron beam, crystallisation and phase separation usually occur, care needs to be taken in choosing the experimental conditions. As said earlier in the thesis $\text{Ga}_2\text{O}_3/\text{GGO}$ layer has to be amorphous in order to show the best electrical characteristics. Crystallisation of the GGO layer causes deterioration of the performance of the device as the gate leakage current increases. The fact that the dielectric oxide layer has to be totally amorphous represents a key point for the realisation of a III-V MOSFET device with good performance. Figs. 3.30a and 3.30b shows two high-resolution TEM bright field images of the dielectric gate stack $\text{Ga}_2\text{O}_3/\text{GGO}$ on crystalline GaAs acquired, after two different exposure time. A Fourier Transform has been taken in an area on the GGO region in order to establish how amorphous the oxide layer is. After short exposure time to the electron beam, just by looking at the FFT in Fig. 3.30 the oxide layer appears to be fairly amorphous without the presence of any spots on the FFT. The situation is slightly different after longer exposure time. In the FFT, show in Fig. 3.15b, two

spots are clearly visible. This indicates that the GGO layer is starting to crystallise after longer exposure.

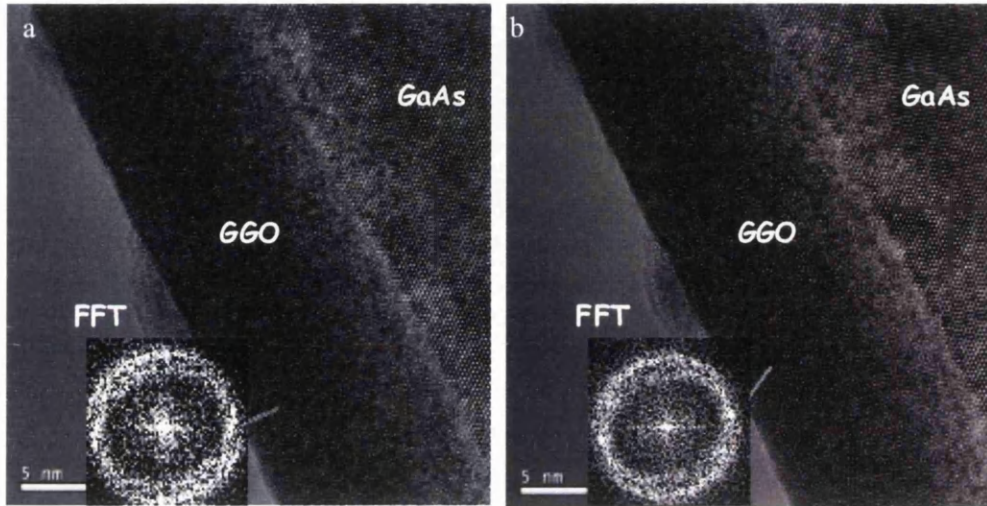


Fig. 3.15a HRTEM bright field image acquired after short exposure time to the electron beam. The FFT inset indicates that the GGO layer is almost all amorphous. Fig. 3.15b HRTEM bright field image acquired after longer exposure time to the electron beam. In this case the FFT reveals the presence of some spots which indicate the start of the ordering process.

However the crystallisation is not the only phenomenon observed during the damage process. The interaction of the high-energy electron beam with the specimen might damage the structure. Once the structure is changed the specimen is not representative of the original material leading to the difficulty to interpret TEM images, diffraction pattern and the EELS spectra. Phase separation is a process that usually requires relatively a less dose than the crystallisation, therefore it is more likely to happen. Fig. 3.16 shows an example of phase separation and crystallisation into a chemically different structure. After prolonged exposure time to the electron beam during the acquisition of an EELS SI across a GGO layer with 19% of Gd concentration, it turned out that in some areas the GGO might have crystallized into $Gd_3Ga_5O_{12}$ where the Gd concentration is 15%. The prolonged exposure time to the electron

beam has actually created regions on the GGO respectively rich in Gd and Ga with respect to the initial composition.

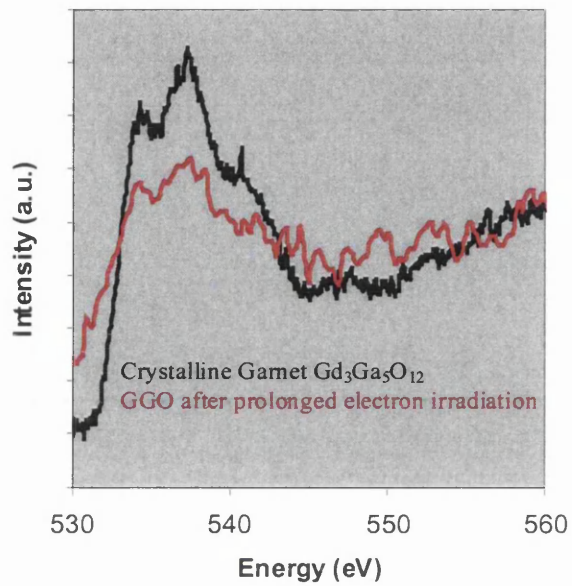


Fig. 3.16 Comparison of ELNES of the O K-edge of partly crystallised GGO (19.1% Gd) and the Garnet standard.

CHAPTER 4: COMPOSITIONAL ANALYSIS OF AS GROWN GGO LAYER BY EELS SPECTRUM IMAGING (SI)

4.1 EELS SI

A detailed description of the spectrum imaging technique is given by Hunt et al. but briefly a spectrum image is obtained by scanning a finely focussed electron probe along a line or an area. This region of interest is identified within a survey image, and a raster is defined over that region. An entire EELS spectrum is taken in each pixel of the raster (Fig. 4.1).

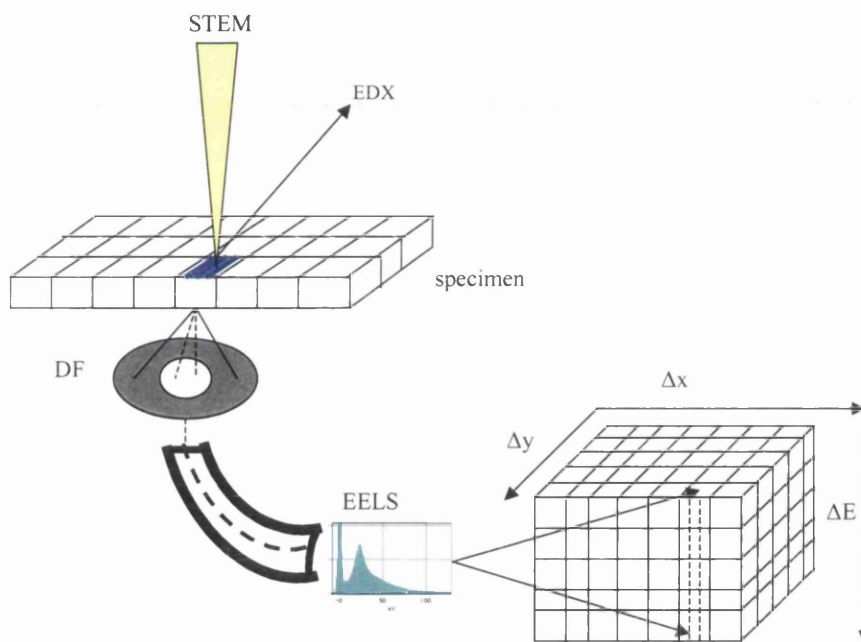


Fig. 4.1 Form of data produced by system when beam is scanned in a raster pattern over a specimen. Two dimensions are the x and y direction of the sample and the third one is the energy.

The pixel size in the raster is chosen according to the spatial resolution required of the EELS map and the actual probe size. An acquisition area is defined in the survey image (Fig. 4.2) and divided into a specified number of pixels. In the case of a box, these pixels will be a square of a certain side length depending directly on the actual spatial resolution of the SI. The advantage of a spectrum mapping over point spectrum measurements is the possibility of recognising trends in the EELS transition in relation to the position of microstructural features in the sample. Rastering also increases the possibility that beam sits in the right spot somewhere in the sample.

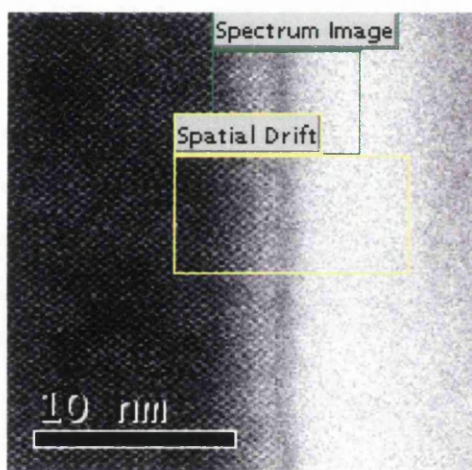


Fig. 4.2 STEM ADF survey image of the interface GaAs/Ga₂O₃/GGO. The green box defines the area where the 3-D EELS SI has been collected. A region suitable for the spatial drift correction procedures is defined by the yellow box.

The survey image can be either a DF or HAADF depending on the setting of the camera lens. In the case of Tecnai F20 two detectors the Fischione HAADF and the Gatan ADF can be used for recording the reference image used for the acquisition of the EELS SI. The choice of the detectors depends on the camera length. At long camera length the Fischione HAADF detector is more efficient, but at short camera length such as 30mm the ADF actually records a HAADF

image and the Fischione detector records virtually nothing. For the acquisition of the core-loss region of the EELS spectrum a short 30mm camera length is selected, this gives a better signal to noise ratio as high-energy edges are not very intense, thus difficult to record with a decent signal to noise ratio. While in the case of the acquisition of the zero-loss 150mm camera length is selected. A shorter camera length will result in a very intense signal which can damage the detector as the zero-loss is several orders of magnitude more intense than the core-loss region part of the EELS spectrum.

The EELS SI approach can be used for investigating either the core-loss and the low-loss region of the EELS spectrum including the zero-loss. This gives the possibility to investigate the chemistry and the composition in any regions of the specimen and also it is possible to extract information on the dielectric properties of the sample.

As far as this thesis is concerned EELS SI has been mainly used for the compositional analysis across the GGO layer using the core-loss region part of the EELS spectrum. Details will be given in the next sections. However the acquisition of the zero-loss has been performed for gaining information of the thickness across the oxide layer which can give an idea of plural scattering contribution to the spectrum. The thickness t has been measured in terms of the total inelastic mean free path λ . This parameter t/λ is related to the zero-loss peak intensity I_0 and the total intensity under the spectrum I_{tot} by the equation:

$$\frac{t}{\lambda} = \ln\left(\frac{I_{tot}}{I_0}\right) \quad \text{Equation 4.1}$$

4.1.1 Zero-loss acquisition

Low-loss EELS SI datasets have all been collected at 150mm camera length (L) with an energy dispersion of 0.1ev/channel. Usually an acquisition time of 0.25msec has been employed. These conditions ensure the collection of EELS spectra with the highest signal to noise ratio without saturating the detector.

4.1.2 Core-loss acquisition

The aim of this work here has been to perform a compositional analysis of Gd, Ga, O and As across the dielectric gate stack layer. Table 4.1 shows the known edge onsets for these elements.

Element	Edge	Edge onset	Edge intensity
Ga	L ₃	1115eV	Major feature
	L ₂	1142eV	Major feature
	M _{2,3}	103eV	Weak feature
	M ₁	158eV	Very weak feature
	L ₁	1298eV	Weak feature
As	L ₃	1323eV	Major feature
	L ₂	1359eV	Major feature
	M _{4,5}	41eV	Major feature
	M _{2,3}	140eV	Very weak feature
	M ₁	203eV	Very weak feature
	L ₁	1526eV	Weak feature
Gd	O _{2,3}	20eV	Major feature
	N _{4,5}	140eV	Major feature
	M ₅	1185eV	Major feature
	M ₄	1217eV	Major feature
	N _{2,3}	271eV	Weak feature
	N ₁	376eV	Very weak feature
	M _{3,2}	1544eV	Weak feature
	M ₁	1881eV	Very weak feature
O	K	532eV	Major feature

Table 4.1 Each of the elements under investigation are listed with the onset energies of EELS ionisation edges.

As far as the compositional analysis of such systems is concerned, two different energy-sets can be used, respectively called the high and the low energy-set. In both cases, the use of a

dispersion of 1eV/channel allows collection of all the edges of interest in one single spectrum ensuring also the highest signal on the detector.

Fig. 4.3 shows the background subtracted low energy set which includes Ga M_{2,3}-edges at 103eV, Gd N_{4,5}-edges at 140eV and O K-edge at 532eV. The advantages of this energy set are only the high signal to noise ratio. The disadvantages are:

- Ga M₁-edges, As M_{2,3}-edges and Gd N_{4,5}-edges all overlap.
- The background level is far too high

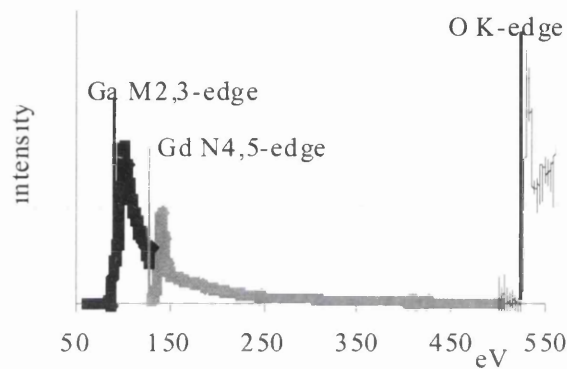


Fig. 4.3 Background subtracted EELS low energy set.

Fig. 4.4 shows the background subtracted EELS high-energy set. The disadvantages are:

- Ga L_{2,3} overlaps with Gd M_{4,5}
- The overall signal is low and more noisy
- The presence of the FEG stray emission

The advantages are:

- All the edges Ga L_{2,3} Gd M_{4,5}, As L_{2,3} and O K are easy to extract
- Good signal to background ratio

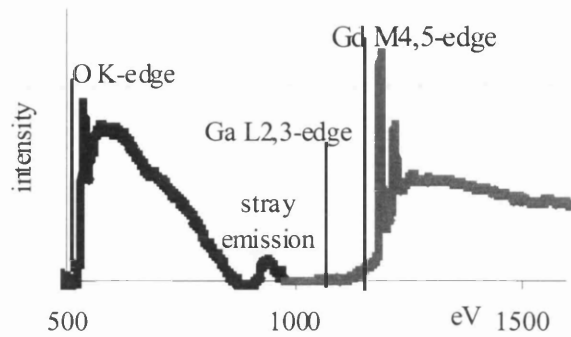


Fig. 4.4 Background EELS subtracted high energy set

The high energy set has been chosen because it presents a good signal to background ratio and all the edges are easy to extract. Gd $M_{4,5}$ -edges lie on Ga $L_{2,3}$ -edges as shown in Fig. 4.5 and this could be a problem. The way the separation is performed consists in the extraction of the full shape of the Ga $L_{2,3}$ -edges (Fig. 4.6) from the spectra in the GaAs region. By scaling this shape to fit the region prior to the Gd $M_{4,5}$ -edges in the spectra from the GGO it is possible to extract Gd $M_{4,5}$ -edges as shown in Fig. 4.7. In this way Gd $M_{4,5}$ -edges and Ga $L_{2,3}$ -edges have been extracted from the GGO region.

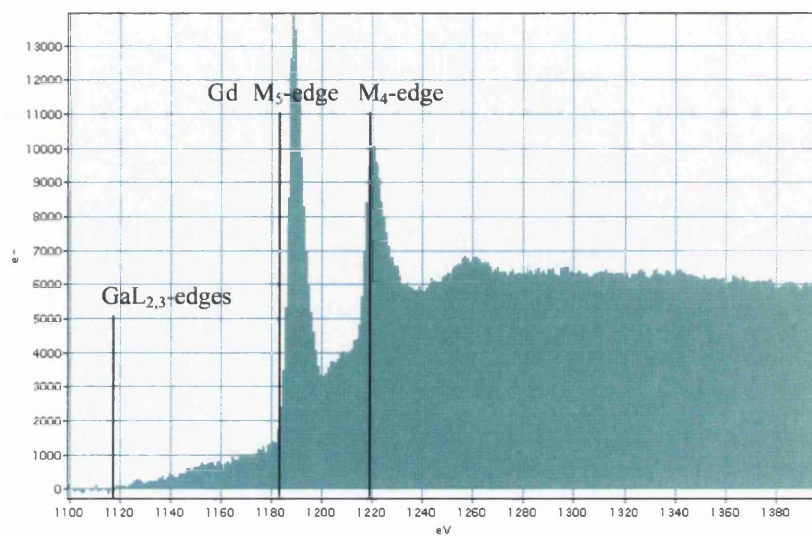


Fig. 4.5 Ga L_{2,3}-edges and Gd M_{4,5}-edges respectively at 1115eV and 1184eV. Both edges have been extracted from the EEL part of the spectrum over 1100eV in the GGO region of the EELS SI

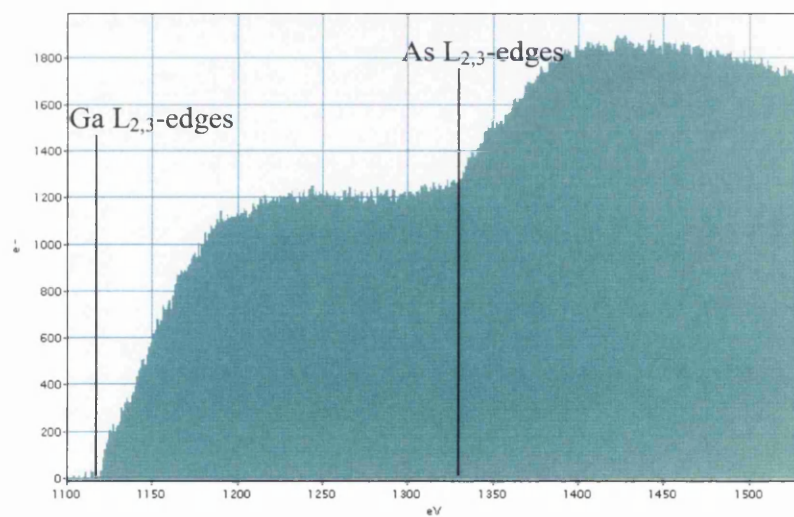


Fig. 4.6 Ga L_{2,3}-edges and As L_{2,3}-edges respectively at 1115eV and 1323eV both extracted from the EEL spectrum part over 1100eV in the GaAs region of the EELS SI

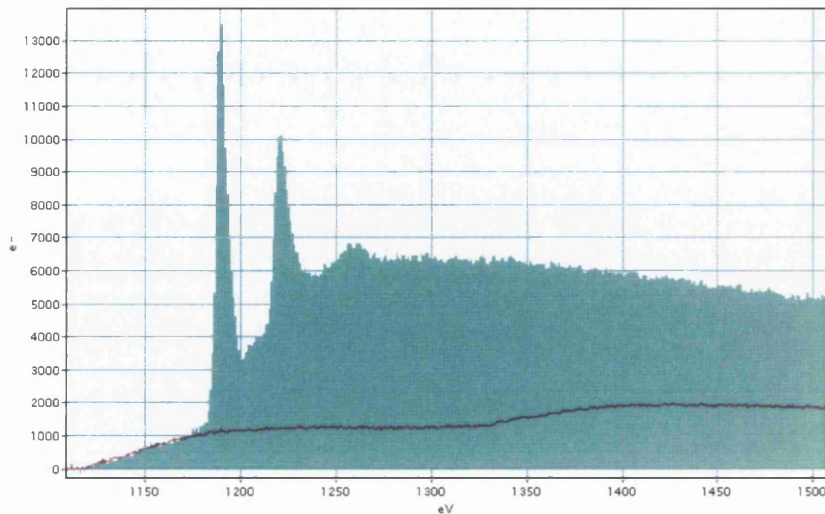


Fig. 4.7 GaL_{2,3}-edges from GaAs (red line) scaled to those from GGO in the region before the Gd M_{4,5}-edges.

4.1.3 Dose sensitivity and setting exposure time

As shown in section 3.5.1, the Ga₂O₃/GGO dielectric stack layer is quite sensitive to the electron beam. Care needs to be taken when setting the experimental conditions. In particular an important parameter to take into account is the electron dose which represents the number of electrons per unit area. The more electrons will hit the same area the more likely it is the sample to be damaged. Fig. 4.8 shows a comparison of the O K-edges extracted from the Ga₂O₃ template layer region after prolonged exposure time and from an amorphous Ga₂O₃ layer at a relatively low dose

The shape of the two O K-edges is different as a result of the prolonged exposure time to the electron beam which have caused a change in the chemistry leading to a phase separation.

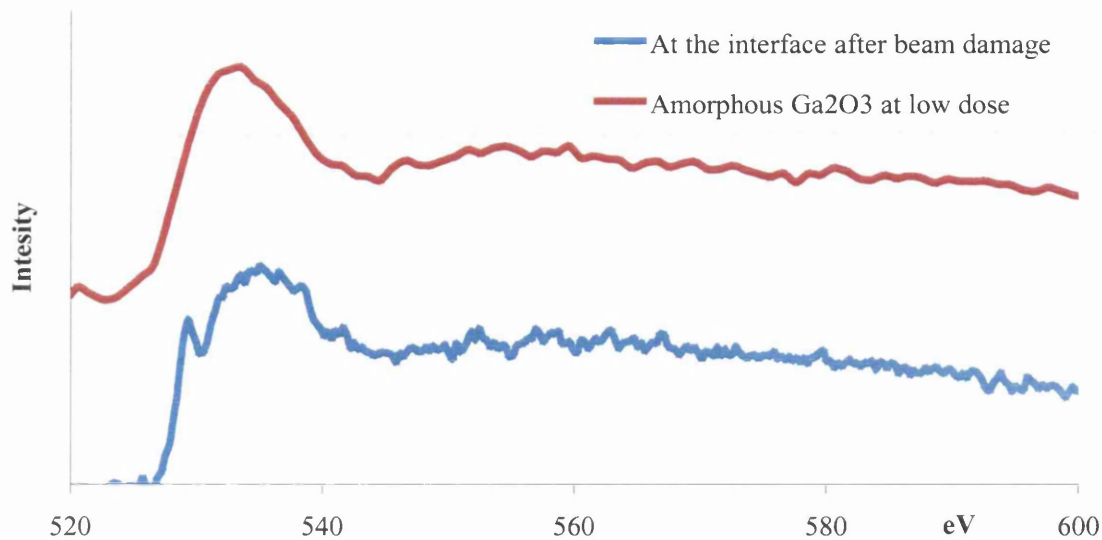


Fig. 4.8 Comparison of ELNES of O K-edge of the interface GaAs/Ga₂O₃/GGO acquired after prolonged exposure time and crystalline Ga₂O₃.

As described above, radiation sensitivity of these materials is an important issue to take into account when acquiring an EELS spectrum. The acquisition time has to be long enough to acquire a decent signal but short enough to avoid any damage. To determine the best value for the acquisition time and so the dose, the electron beam is constantly kept on the same area of the specimen until a variation of the shape of the O K-edge is observed. This represents a good way to work out the optimum acquisition time. However it has been observed that the tendency of the GGO to crystallize is related to the actual composition, samples at high Gd concentration tends to be more affected by the electron beam showing a high tendency to crystallise.

4.1.4 Performing EELS SI

Fig. 4.9 shows a STEM dark field image (DF) of the GGO layer on the GaAs substrate. The region selected for the SI is shown in the rectangular box. In the case of the study of thick GGO layers (over 30nm wide), the requirements have been to work out the elemental composition in the region of the GGO layer next to the interface with the Ga₂O₃ and not a detailed profile of

the elemental distribution across the dielectric gate stack. Thus 0.7nm probe size ensures the acquisition of EELS spectra with a decent signal to noise ratio. Related to that probe size, 2.2nm pixel size was used as it ensures the presence of enough pixels on the SI. All the data was acquired using a dispersion of 1eV/channel, a convergence angle α of 18mrad and a collection angle β of 44mrad. The spectrum offset was set at 480eV.

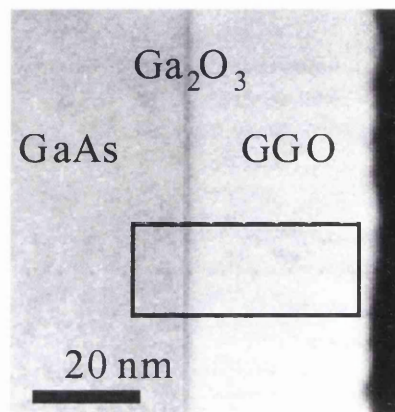


Fig. 4.9 A typical STEM DF survey image used for the acquisition of EELS spectrum images. The black box indicates the area of the SI.

The EELS SI has been performed under two different ways, the conventional mode and the sub-pixel scanning.

Regarding the conventional SI acquisition mode (Fig. 4.10a), the beam during all the acquisition time sits on the same spot on the specimen and then it moves to the other pixel. In this way the electron dose depends on the acquisition time and the probe size. Remaining just below the required dose for damaging the GGO layer, the background subtracted GaL_{2,3}-edges shown in Fig 4.10b looks quite noisy making the interpretation not easy.

Regarding the sub-pixel scanning, since the probe size is much smaller than the pixel size, the probe is rastered over the pixel during the acquisition (Fig. 4.11a). This spreads the electron dose more or less uniformly across the pixel size rather than concentrating it at the position of the stationary probe as in the conventional mode. Fig. 4.11b shows the background subtracted

Ga_{L_{2,3}}-edges extracted from the EELS SI using a dose which does not cause any damage on the specimen. In this case the Ga_{L_{2,3}}-edges appears to be less noisy and easier to interpret.

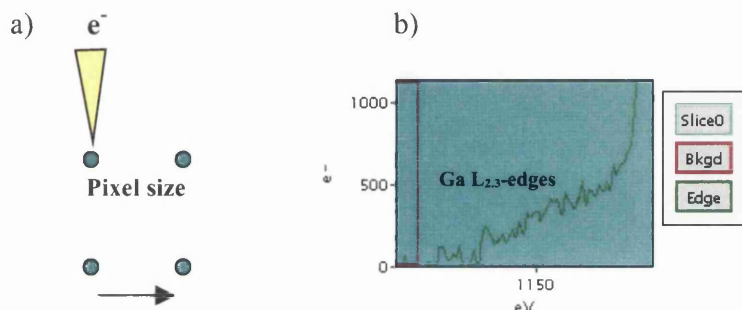


Fig 4.10a. Conventional mode point by point. The beam is sitting in the same position for all the acquisition before moving to the next pixel. At a given probe size the electron dose will be higher, hence the acquisition time has to kept short giving a more noisy spectrum. Fig. 4.10b shows the background subtracted Ga L_{2,3}-edges, extracted under a dose condition which does not cause any damage. In this case, Ga L_{2,3}-edges look quite noisy.

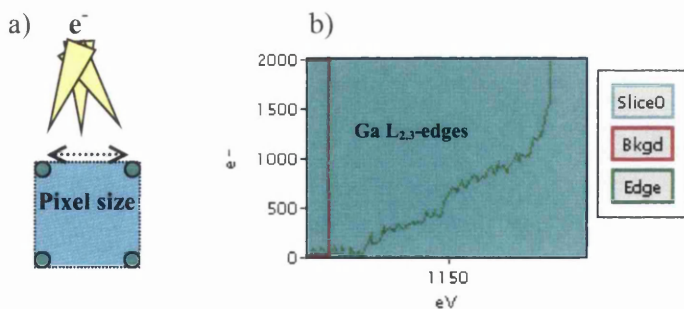


Fig. 4.11a Sub-pixel scanning mode. The beam is scanned in the area of interest, hence the dose is decreased. In this way it is possible to increase the acquisition time and acquire a better resolved signal e.g. Ga L_{2,3}-edges as shown in Fig. 4.11b.

Fig. 4.12 shows one energy slice of the SI. The signal to noise ratio in each pixel is rather low for the desired analysis and so the spectra in lines of pixels parallel to the interface can be summed to improve the signal to noise ratio, showing one of the advantages of the SI technique. Summing parallel to the interface maintains the spatial resolution normal to the interface only if the raster is properly aligned and there is no drift. For the first point it is important to make sure that the electron beam in STEM mode generates a survey image with interface perfectly vertical as shown in Fig. 4.9. For the second point it is crucial to minimize any drifting even if using a pixel size of 2.2nm the spatial resolution is not greatly affected by minimal drifting of the specimen.

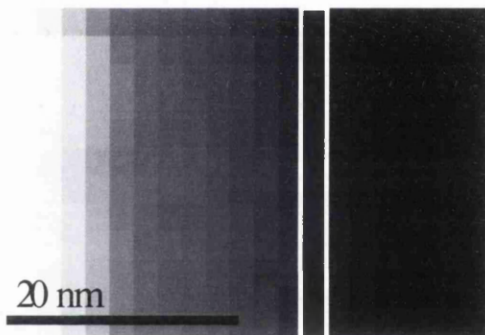


Fig. 4.12. One energy slice of a 25 x 12 pixel SI. By summing the spectra in the pixels in the box parallel to the interface, the signal to noise ratio can be improved.

4.2 COMPOSITIONAL ANALYSIS

4.2.1 Introduction

As far as the quantification analysis is concerned two different approaches for the extraction of the edges from the EELS SI have been investigated in this thesis. One is using the multiple linear least square fitting (MLLS) routine and a manual approach which consists in the manual extraction of all the edges involved in quantification process. The MLLS routine is quite fast

and gives the possibility to separate easily Ga L_{2,3}-edges and Gd M_{4,5}-edges. In the manual approach the extraction of all the edges is repeated for all the columns of pixels. The main advantage of the manual approach over the MLLS is the more precision in the separation process performed pixel by pixel which will result in a more reliable quantification of the elemental distribution across the GGO layer. On the other hand it is very time consuming. Therefore the MLLS routine has been employed only for the acquisition of elemental maps whose intensity gives a quick idea of how the elements are distributed across the GGO layer. For a more accurate compositional analysis the manual approach has been used.

Once the Ga L_{2,3}-edges, the Gd M_{4,5}-edges and the O K-edge are extracted, their intensity is converted to atomic fractions using an appropriate standard, as suitable cross-sections are not available for the Gd M_{4,5}-edges. Two different standards have been used. The first quantitative analysis has been performed by calibrating to the composition of one wafer which has been determined by Rutherford Backscattered Spectroscopy (RBS). The O concentration has been assumed to be always 60% as RBS is not particularly sensitive for light elements. Thus gadolinium gallium garnet (Gd₃Ga₅O₁₂) has been investigated as it allows an independent determination of the O concentration along with the Ga and Gd.

4.2.2 Use of the RBS as standard

Rutherford backscattering (or RBS, for Rutherford Backscattering Spectrometry) is an analytical technique in materials science. It is named for Ernest Rutherford. A high energy beam (2 to 4 MeV) of low mass ions (e.g. He⁺⁺) is directed at a sample. A detector is placed such that particles which scatter from the sample at close to a 180 degree angle will be collected. The energy of these ions will depend on their incident energy and on the mass of the sample atom which they hit, because the amount of energy transferred to the sample atom in the collision depends on the ratio of masses between the ion and the sample atom. Thus, measuring the energy of scattered ions indicates the chemical composition of the sample.

Additionally, in the case that the incident ion doesn't hit any of the atoms near the surface of the sample, but instead hits an atom deeper in, the incident ion loses energy gradually as it passes through the solid, and again as it leaves the solid. This means that RBS can be used as a means to perform a depth profile of the composition of a sample. This is especially useful in analysis of thin-film materials. For example, films about half a micrometre in thickness can be profiled

using a 2 MeV He^{++} beam, or films up to about 10 micrometres thick can be profiled with a 2 MeV H beam.

RBS is now a very widely used analytical technique, which has the great advantage that it is absolute, requiring no standards for quantification (since the probability of interaction – the cross section- is given by the Coulomb potential).

Due to the irradiation of a high-energy beam, the part of the layer next to the surface is damaged. The first 20-30nm on the surface is usually damaged and not reliable for quantitative analysis. Light elements present a small cross section and hence are not easy to detect.

All the RBS experiments have been performed by Rich Gregory of Freescale Semiconductor Inc. Fig. 4.13 shows an example of RBS analysis for a GaAs/Ga₂O₃/GGO dielectric gate stack layer with 40nm of GGO layer.

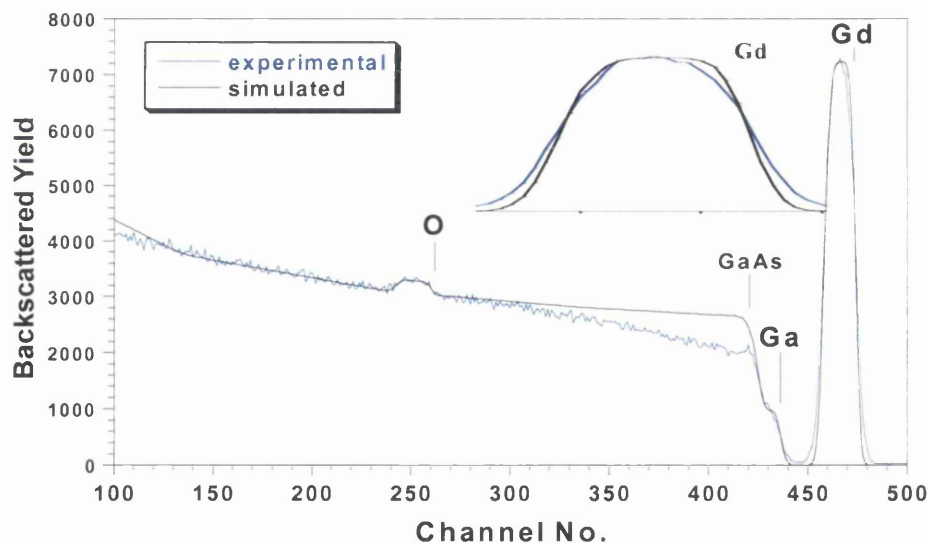


Fig. 4.13 RBS results for a 40nm GGO layer on top of GaAs as substrate compared to the same from a theoretical simulation. The agreement is good. Inset is the Gd results with the x-axis broadened to make all the features visible. The experimental parameters used for obtaining this dataset are: 1) beam 2MeV He^{2+} ; 2) the angle of incidence is normal; 3) the detector angle and the detector solid angle are respectively 105° and 115msr; 4) the integrated charge Q (dose) is 50 μC .

As shown in Fig. 4.13, the O signal is relatively noisy and has low intensity. Hence a direct extraction of the concentration is not accurate. The O concentration has been assumed to be 60% throughout the GGO layer in all the RBS analysis. As far as the EELS analysis is concerned the composition can be easily worked out by comparing the Gd/O ratio in the unknown sample to that in the standard whose composition has been determined by RBS. The Gd M_{4,5}-edges and the O K-edge have been extracted in the region of the standard sample next to the interface. Such region is not affected by the damage that occurs during a RBS analysis. Hence the composition extracted is accurate. The O concentration for the EELS analysis has been assumed to be 60% throughout all the GGO layer assumed by RBS. This represents a limit of RBS for the study of such materials which present thin interfacial layers.

4.2.3 Use of the $Gd_3Ga_5O_{12}$ as standard

The $Gd_3Ga_5O_{12}$ has been used as standard as it can provide an independent determination of the O concentration and this represents a clear advantage over the RBS. In the $Gd_3Ga_5O_{12}$ the O, the Ga and Gd have a concentration of 60%, 25% and 15% respectively. All the samples have been provided by Freescale and then reduced to powder using the method described in section 2.8.1. Fig. 4.14 shows a STEM DF image of the edge of a $Gd_3Ga_5O_{12}$ grain. The EELS spectra have been acquired in the SI mode using the sub-pixel scanning method in order to spread the dose and preserve the sample from the damage caused by the electron beam. As can be seen from the image in Fig. 4.14, the area chosen for the SI has uniform thickness.

The concentration of the GGO layer in the unknown sample has been worked out by comparing the Gd/O, Gd/Ga and Ga/O ratios to those in the $Gd_3Ga_5O_{12}$ whose composition is known. In this way it has been possible to work out the O concentration across the GGO giving a more reliable result.

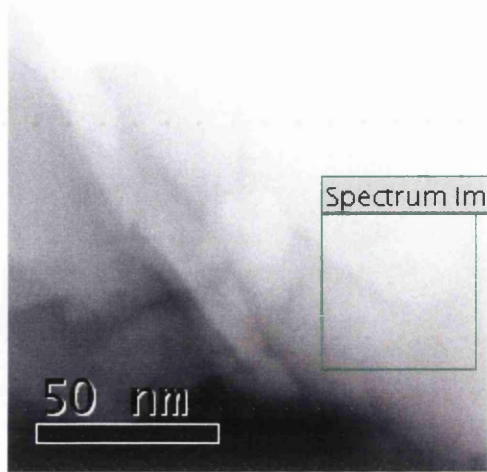


Fig. 4.14 STEM DF image of $\text{Gd}_3\text{Ga}_5\text{O}_{12}$ powder dispersed onto a holey carbon film. The green box represents the area where the beam has been scanned for the acquisition of the EELS SI.

4.2.4 The multiple linear-least squares fitting MLLS

The multiple linear least squares (MLLS) [64] fitting routine provides a very useful means for mapping difference spectral phases or features by reference to their spectral signature. Specifically, the MLLS algorithm fits reference spectra as specified by the user to the dataset of interest. Once the MLLS is complete, the algorithm returns the fit coefficients corresponding to the optimal linear combination of the specified reference spectra to the input data. In other words, the routine will fit reference spectra to a dataset and tell exactly how much of each is present. When applied to spectrum imaging, this technique becomes even more useful since not only how much of each reference preset is given but also its distribution. Hence if MLLS is correctly applied to a spectrum-image dataset, it provides the ability to map the spatial distributions of the input reference spectra.

A simple use for MLLS fitting is in chemical phase mapping. By specifying reference spectra that represent the main phases present, the analysis returns fit-coefficient maps showing the spatial distribution of the reference spectra. These maps may be interpreted as distribution maps. For spectrum imaging analysis this can be especially convenient since often the reference spectra can be extracted from the SI dataset itself.

MLLS fitting is also a very useful technique in EELS for separating overlapping edges. As the conventional approach to EELS edge quantification involves using the pre-edge region to model and subtract the underlying background signal, difficulties can arise where features from a preceding edge makes accurate background extrapolation impossible. MLLS offers a way for overcoming this problem. By specifying reference spectra that represent the overlapping signals present in the spectrum, the MLLS routine can then separate the signals and obtain the amount of each component.

In the case of this work MLLS has been used for mapping Ga $L_{2,3}$ -edges and Gd $M_{4,5}$ -edge. Performing MLLS in this case is very useful. First of all it is necessary to extract from the EELS SI the part of the spectrum over 1100eV (Fig. 4.15). Just by fitting the extracted EELS SI with the Ga $L_{2,3}$ -edges and Gd $M_{4,5}$ -edges spectrum previously extracted using the procedure described in section 4.1.3, it is possible to obtain quickly the elemental maps for Ga and Gd point, respectively shown in Figs 4.16 and 4.17, point by point across the GGO layer.

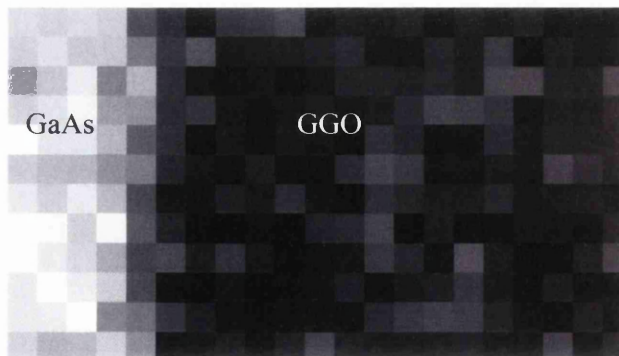


Fig. 4.15 Extracted EELS SI from the region of the spectrum over 1100 eV.

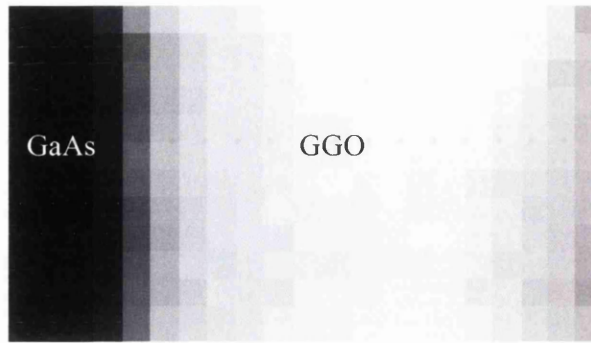


Fig. 4.16 Elemental distribution of Gd across the GGO layer point by point obtained by using the MLLS routine.

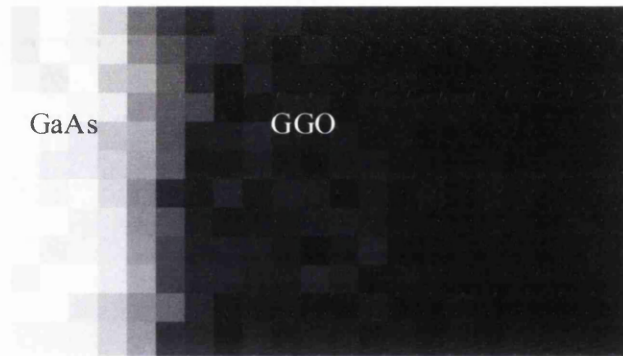


Fig. 4.17 Elemental distribution of Ga across the GGO layer point by point, obtained by using the MLLS routine.

4.2.5 *Manual approach*

The manual approach consists in the extraction of all the edges from all the columns of pixels. The separation process has to be repeated for each column. It is evident that this process is quite time consuming especially when the GGO layer is thick and there are many column of pixels to analyse but at least it allows the separation process to be performed as accurate as

possible for all the columns of pixels as it is not affected by all the errors introduced during the MLLS routine.

First of all it is important to extract the intensity of Gd $M_{4,5}$, Ga $L_{2,3}$ and O K edges, and this could be easily done following the procedure described in section 4.1.3 . A 60eV integration window has been used for each edge. Figs 4.18a, b and c show the 60eV integration window applied respectively on O K-edge, Gd $M_{4,5}$ -edges and Ga $L_{2,3}$ -edges.

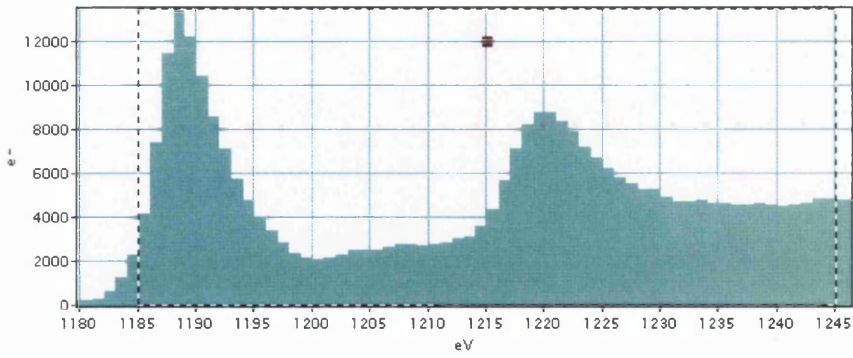


Fig. 4.18a The 60eV integration window applied on the extracted Gd M_{4,5}-edges.

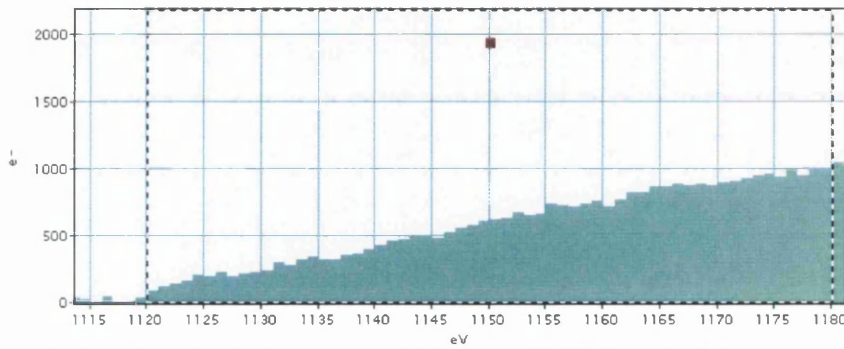


Fig. 4.18b The 60eV integration window applied on the GaL_{2,3}-edges extracted from the GGO region.

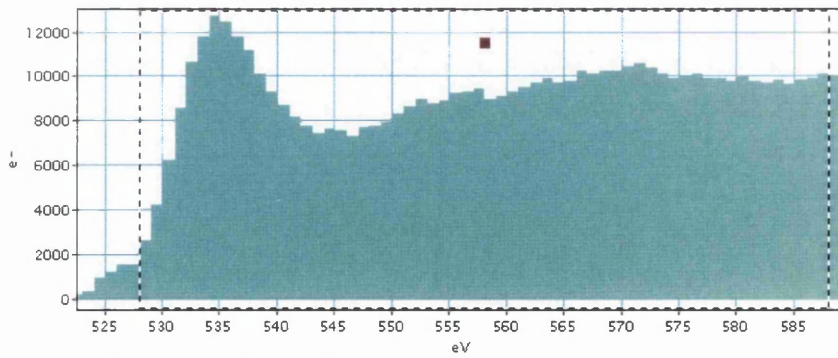


Fig. 4.18c The 60eV integration window applied on the extracted O K-edge.

4.2.6 Conversion of the edge intensity to atomic fraction using RBS and $Gd_3Ga_5O_{12}$ as standard.

Once the Gd $M_{4,5}$ -edges, Ga $L_{2,3}$ -edges and O K-edge have been extracted using the manual approach as described in section 4.2.5, the atomic fractions have been determined using both the RBS and the $Gd_3Ga_5O_{12}$ as standard.

4.2.6.1 Use of RBS

As said in section 4.2.2 in thick layers the first 20nm is quite damaged as a result of the sputtering process that occurs during the RBS analysis. Hence the calibration has been performed extracting the edges from the region near the interface with the Ga_2O_3 in the unknown sample and in the one previously characterized by RBS. The atomic fractions can be easily extracted relying on the Gd/O edge intensity ratio. Both Gd and O present the highest signal to noise ratio. O concentration is always 60% as the same assumption is made by RBS. The Gd concentration can be easily worked using *Equation 4.2*:

$$\frac{(I_{Gd})_{RBS}}{(I_O)_{RBS}} \cdot \frac{[Gd]_{RBS}}{[O]_{RBS}} = \frac{(I_{Gd})_{Unknown}}{(I_O)_{Unknown}} \cdot \frac{[Gd]_{Unknown}}{[O]_{Unknown}} \quad \text{Equation 4.2}$$

I_{Gd} and I_O are the edge intensity of Gd and O extracted from the standard and the unknown GGO layer while $[Gd]$ and $[O]$ the atomic fractions. $[O]$ is assumed to be always 60%, therefore the only unknown quantity is the Gd concentration in the unknown sample. Once the $[Gd]$ is determined the $[Ga]$ can be easily found as the total sum of the Gd, Ga and O atomic fractions is 100.

4.2.6.2 Use of $Gd_3Ga_5O_{12}$

The determination of the Gd, O and Ga atomic fractions using $Gd_3Ga_5O_{12}$ as standard relies on the use of conversions factors which convert the edge intensity ratios in atomic fractions:

$$\frac{(I_{Gd})_{Gd_3Ga_5O_{12}}}{(I_O)_{Gd_3Ga_5O_{12}}} K = \frac{(I_{Gd})_{Unknown}}{(I_O)_{Unknown}} \quad \text{Equation 4.3}$$

$$\frac{[Gd]_{Gd_3Ga_5O_{12}}}{[O]_{Gd_3Ga_5O_{12}}} K = \frac{[Gd]_{Unknown}}{[O]_{Unknown}} \quad \text{Equation 4.4}$$

$$\frac{(I_{Gd})_{Gd_3Ga_5O_{12}}}{(I_{Ga})_{Gd_3Ga_5O_{12}}} L = \frac{(I_{Gd})_{Unknown}}{(I_{Ga})_{Unknown}} \quad \text{Equation 4.5}$$

$$\frac{[Gd]_{Gd_3Ga_5O_{12}}}{[Ga]_{Gd_3Ga_5O_{12}}} L = \frac{[Gd]_{Unknown}}{[Ga]_{Unknown}} \quad \text{Equation 4.6}$$

$$\frac{(I_{Ga})_{Gd_3Ga_5O_{12}}}{(I_O)_{Gd_3Ga_5O_{12}}} M = \frac{(I_{Ga})_{Unknown}}{(I_O)_{Unknown}} \quad \text{Equation 4.7}$$

$$\frac{[Ga]_{Gd_3Ga_5O_{12}}}{[O]_{Gd_3Ga_5O_{12}}} M = \frac{[Ga]_{Unknown}}{[O]_{Unknown}} \quad \text{Equation 4.8}$$

K, L and M are the conversions factors. In $Gd_3Ga_5O_{12}$ the atomic fractions [Gd], [Ga] and [O] are 15%, 25% and 60% respectively. By combining all the equations together, it is possible to work out the atomic fractions of Gd, Ga and O in the unknown sample.

By using $Gd_3Ga_5O_{12}$ as standard it has been possible to determine the composition of the GGO layers in a number of sample without making any assumption such 60% of O concentration.

4.2.7 Thickness effects on the compositional analysis

When performing an EELS analysis is very important to be aware of the thickness on the background and the shape of the ionisation edges. In particular when the specimen is reasonably thick ($t/\lambda > 1$) the background level will raise as a result of the increase of the multiple scattering changing the shape of the energy-loss spectrum and washing out ionisation edges [28].

All the samples investigated over this thesis have thicknesses in the range 0.2-0.6 in units of t/λ . However the effects of the thickness on the compositional analysis in thick samples ($t/\lambda > 0.8$) and thin samples ($t/\lambda < 0.2$) have been investigated. Two different areas on the specimen have been chosen for the EELS SI analysis. Figs 4.19 and 4.20 show the thickness profile for the thin and the thick region respectively.

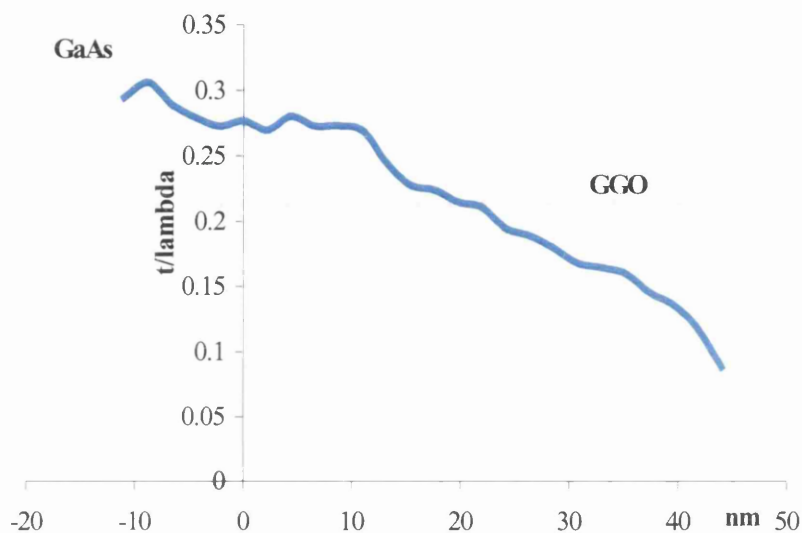


Fig. 4.19 Thickness profile of the thin area of the specimen. The profile extends all the way from the GaAs left hand to the GGO surface right hand. The zero on the x-axis represents the interface between the GaAs substrate and the oxide layer.

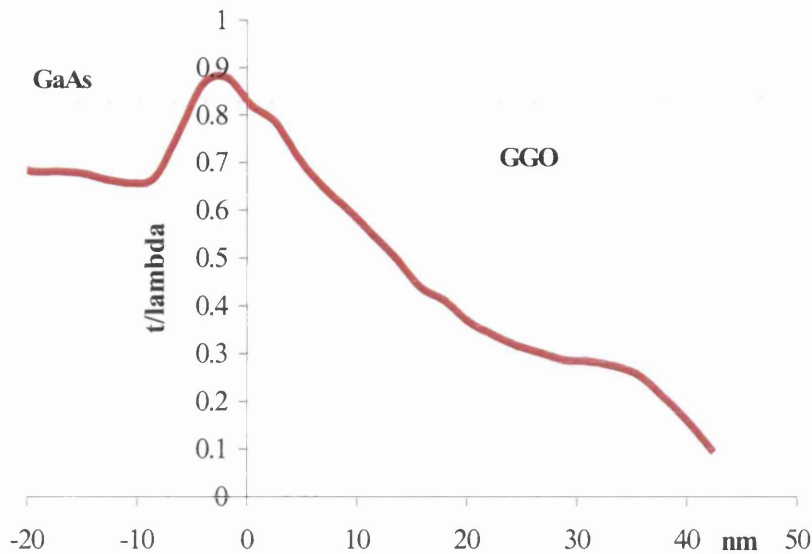


Fig. 4.20 Thickness profile of the thick area of the specimen. The profile extends all the way from the GaAs left hand to the GGO surface right hand. The zero on the x-axis represents the interface between the GaAs substrate and the oxide layer.

The thickness profiles for the two areas of the sample seem relatively different. In particular in the thin area, there is no peak at the interface between the GaAs/Ga₂O₃/GGO as seen in the thick area.

Now the interesting thing is to compare the composition from these two areas. As discussed in section 4.2.5 the compositional analysis is performed looking at the edge intensity ratio.

Fig. 4.21 shows a comparison of the edge intensity profiles ratio, extracted from the GGO layer, between Gd and O from the thin and the thick area of the specimen. The 0 on the x-axis has been set at the interface with the Ga₂O₃ template layer.

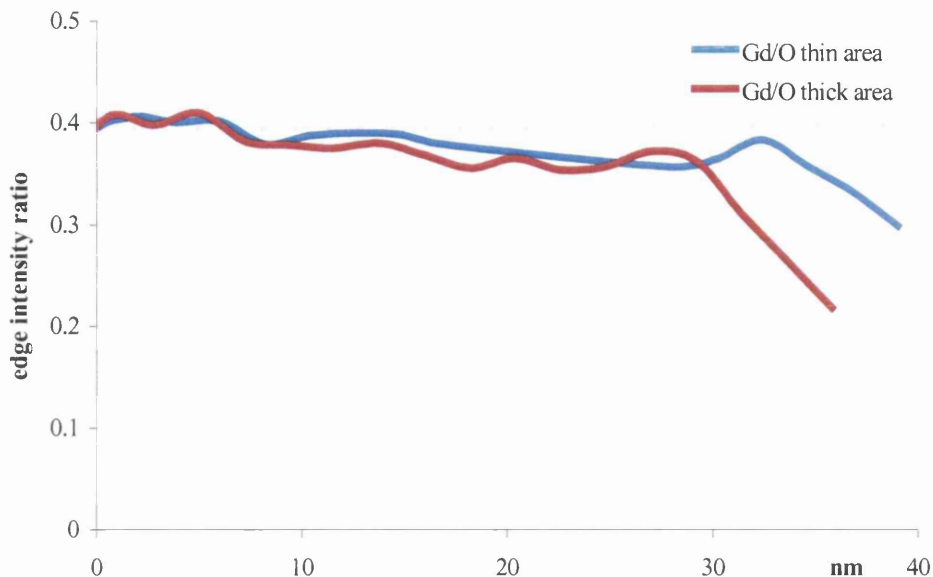


Fig. 4.21 Comparison of the atomic ratio Gd/O profiles extracted from the thin and the thick area of the specimen.

As shown in Fig. 4.21 there is a good agreement between the two ratio profiles. However a major difference between the two areas is at the surface region of the GGO layer on the right hand part of Fig. 4.21. In this case the difference could be related to some damage effects due to TEM specimen preparation. In both areas the surface of the GGO layer is relatively thin.

The same sort of experiment has been applied to a different sample. Two different areas of the TEM specimen have been analysed. Both areas have relatively similar composition even if one of them is thinner. Also in this case the agreement is almost perfect in the region near the $\text{Ga}_2\text{O}_3/\text{GGO}$ interface, However in this case, there is not a massive difference in terms of thickness between the two areas. One of them is definitely thinner than the other one.

Figs 4.22 and 4.23 show the edge intensity profiles ratio of Gd, O and Ga across the GGO layer in the thin and the thick area respectively. The thickness profile is displayed on the second y-axis in both Figs. The 0 on the x-axis has been set at the interface $\text{Ga}_2\text{O}_3/\text{GGO}$. Fig. 4.24 shows the actual comparison between all the edge intensity ratio profiles from the thick and the area of the specimen.

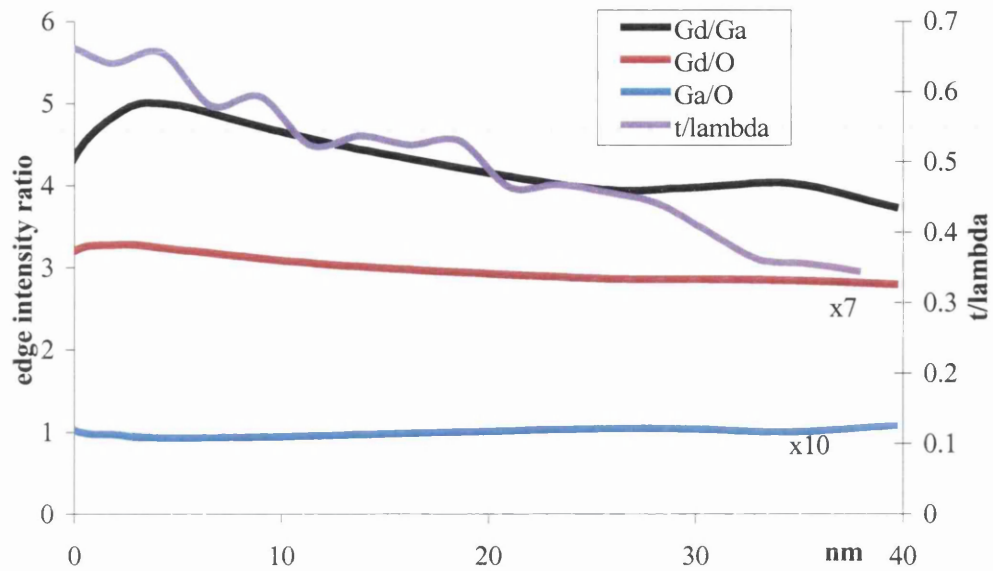


Fig. 4.22 Edge intensity ratio of Gd, Ga and O across the GGO layer in the thick region. The thickness profile (t/λ) is displayed on the second y-axis.

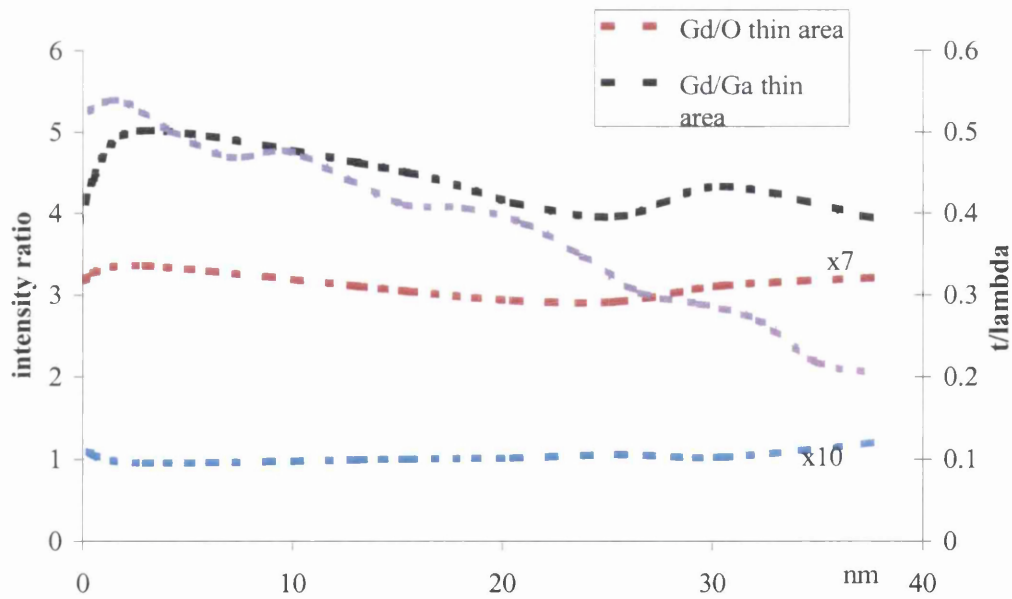


Fig. 4.23 Edge intensity ratio of Gd, Ga and O across the GGO layer in the thin region. The thickness profile is displayed on the second y-axis.

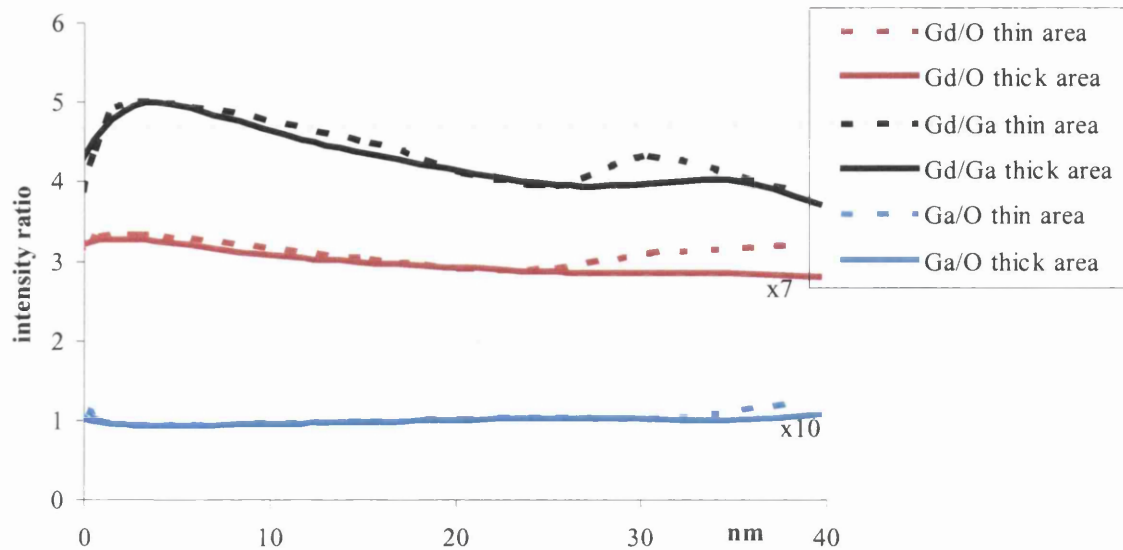


Fig. 4.24 Comparison between the edge intensity ratio profiles of Gd, Ga and O from the thin and the thick area of the specimen.

As shown in Fig. 4.24 both areas present the same edge intensity ratios, hence the same composition, up to 40nm on the x-axis where in the thin region, the Gd concentration appears to raise as Gd/O and Gd/Ga increase. Ga/O seems to increase from the same point. It seems that the thickness has affected the Gd $M_{4,5}$ -edges shape and obviously this has interfered with the compositional analysis. Another explanation could be the damage effects due to the TEM specimen preparation. The presence of a cap layer on top of the GGO layer would certainly avoid the presence of any damage effects from the TEM specimen preparation.

Concluding this section the thickness within a range $0.8-0.3 t/\lambda$ does not affect the compositional analysis. The presence of eventual spikes of the thickness profile may determine an increase on the beam spreading which can affect the analysis in that area. Basically the variations encountered on the compositional analysis for the Gd concentration are in the range of 0.4-1% with the respect of the overall composition. Such accuracy is more or less the same obtained using RBS and it is well accepted by engineers. When the thickness becomes to be less than $0.3t/\lambda$ bigger variations on the compositional results might show up.

4.2.8 Results for GGO films using $Gd_3Ga_5O_{12}$ and RBS as standards

4.2.8.1 Introduction

In this thesis the results of the compositional analysis from 7 different thick GGO layers sample 1-7 respectively, are reported. Table 4.2 summarises the growth conditions and Gd concentration adjacent to the substrate. Figs. 4.25-4.31 give the results of the analysis. The MBE conditions used for growing these samples are different leading to variations in the composition across the GGO layer. The Gd content in the GGO layer is important. If it is less than 19% then the band offset is too low and the leakage current is correspondingly high [4]. If the Gd concentration is too high, it will lead to microcrystalline growth which also gives a high leakage current as in sample 4. The GGO layer is grown using a flux of Gd atoms, Ga_2O and O_2 molecules. Its growth rate is largely affected by the flux of Gd atoms. By increasing the temperature of the Gd cell the growth rate of the GGO increases and so does the Gd concentration. In all the samples investigated herein the flux of Ga_2O_3 molecules has been changed by varying the cell temperature in the 1470°C -1740°C range. It has been found that the GGO growth is not affected by the Ga_2O molecules flux. However, when the temperature of the Ga_2O_3 cell is lower than 1500°C, the Gd concentration rapidly rises. The implication is that there is a change in the growth regime at the Ga_2O flux equivalent to a temperature of the Ga_2O_3 of 1500°C. Above this flux, the GGO is growing with an excess of Ga_2O molecules and the Gd concentration is largely determined by the availability of Gd atoms. Below this flux, the scarcity of Ga atoms leads to a rapid increase in the Gd concentration. At temperatures of Ga_2O_3 cell above 1500°C, the Gd concentration is limited up to 25-26% as in samples 3 and 6. The Gd concentration in the oxide layer is also limited by the O_2 flow rate. In particular, at low rates the Gd concentration tends to increase. Samples 4 and 6 have been grown using the same Gd flux and a different Ga_2O flux. In sample 4, the Ga_2O_3 cell has been kept at temperature of 1470°C while in sample 6 at 1520°C. In sample 4, the Gd concentration is 35% while in sample 6 it is around 25%. Sample 1 has been grown with the highest Ga_2O_3 cell temperature (1720°C) and as a result of that it presents the lowest Gd concentration (19%). Looking at the composition in sample 1, 2, 3 (Figs. 4.25-4.27) the Gd content tends to decrease on moving away from the interface. On the other hand sample 5, 6 and 7 (Figs. 4.29-4.31) present a more uniform Gd concentration across the GGO layer. The common factor samples 5, 6 and 7 which show this improved depth uniformity is that they were grown around 15°C cooler than all the

other layers. The implication is that the cause of the depth non-uniformity in the GGO layers is thermally activated and is very sensitive to the substrate temperature.

Table 4.2 shows the MBE growth condition employed to grow samples 1-7.

Therefore, it is now clear that variations on the growth conditions drastically affect the composition across the GGO layer and so the electrical properties. To investigate the composition across the GGO layers certainly helps to optimise the MBE growth conditions.

	TGa ₂ O ₃ (deg C)	TGd (deg C)	Growth time mins	Growth rate (A/min)	Gd%	T sub (deg C)
Sample 1	1735	1440	90	7.40	19%	510
Sample 2	1510	1395	95	5.17	21%	505
Sample 3	1470	1380	150	2.85	25.2%	510
Sample 4	1470	1435	75	6.61	35%	510
Sample 5	1545	1425	95	5.42	20.5%	490
Sample 6	1520	1450	85	7.21	25%	490
Sample 7	1545	1470	70	10.97	22.8%	490

Table 4.2 MBE growth conditions of Sample 1, 2, 3, 4, 5, 6 and 7 and Gd adjacent to the template layer.

4.2.8.2 Sample 1

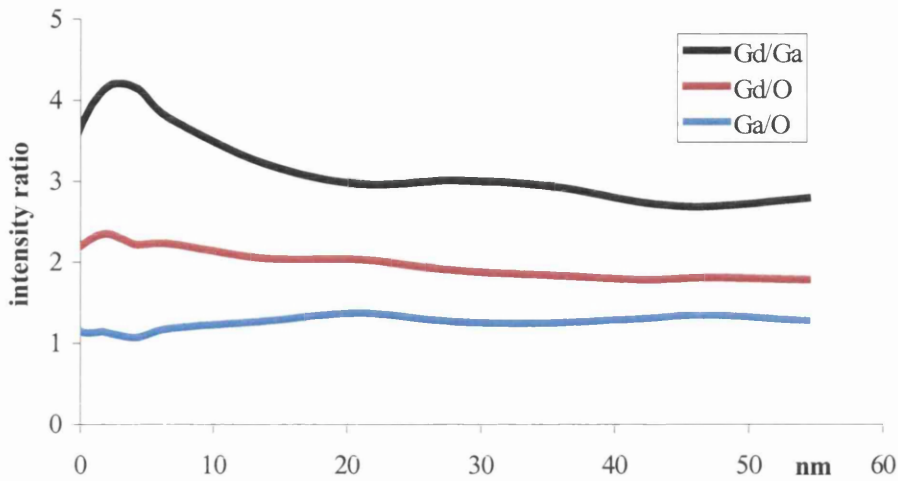


Fig. 4.25a Edge intensity ratio of Gd, Ga and O extracted across the GGO layer in sample 1. The 0 on the x-axis has been set on the main boundary between the GGO and the Ga₂O₃ template layer.

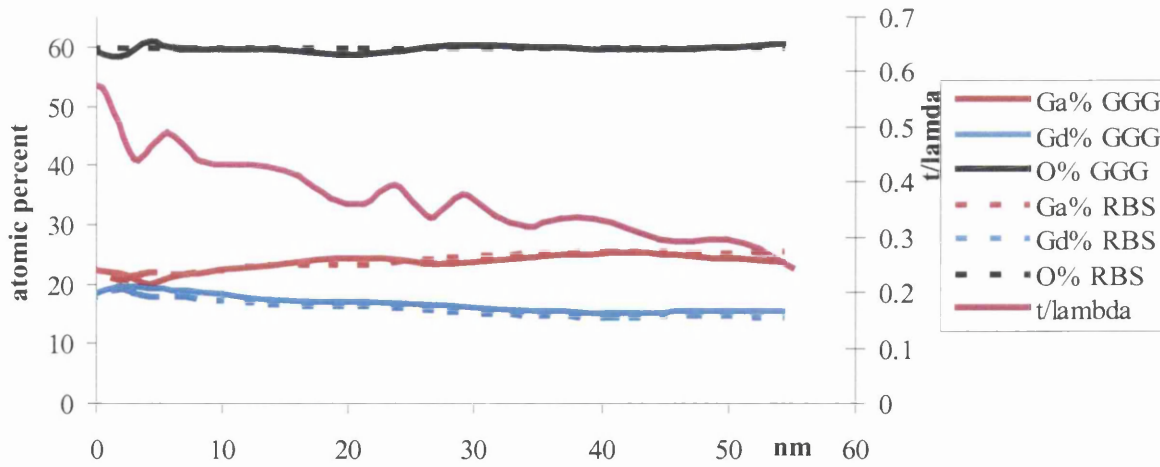


Fig. 4.25b Gd, Ga and O atomic fractions across the GGO layer in sample 1. RBS and Gd₃Ga₅O₁₂ as standard have been used and the results shown. On the second y-axis the t/λ profile is displayed. The 0 on the x-axis has been set on the main boundary between GGO and Ga₂O₃ layer.

4.2.8.3 Sample 2

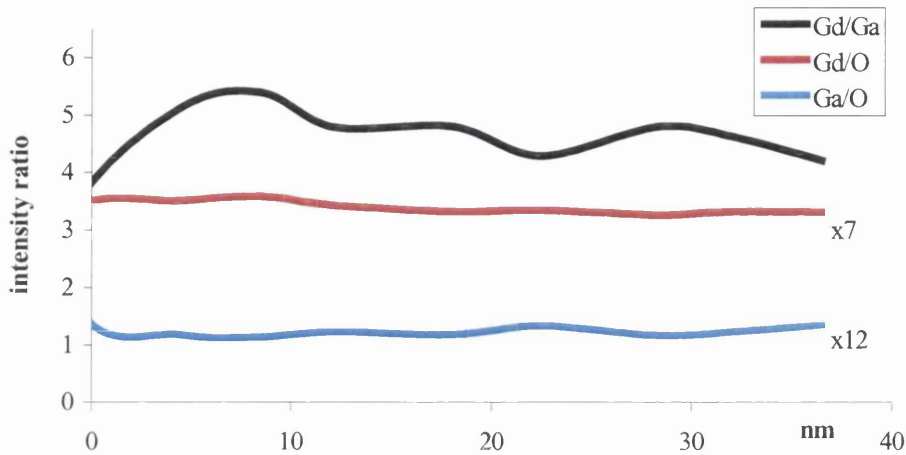


Fig. 4.26a Edge intensity ratio of Gd, Ga and O extracted across the GGO layer in sample 2. The 0 on the x-axis has been set on the main boundary between the GGO and the Ga_2O_3 template layer.

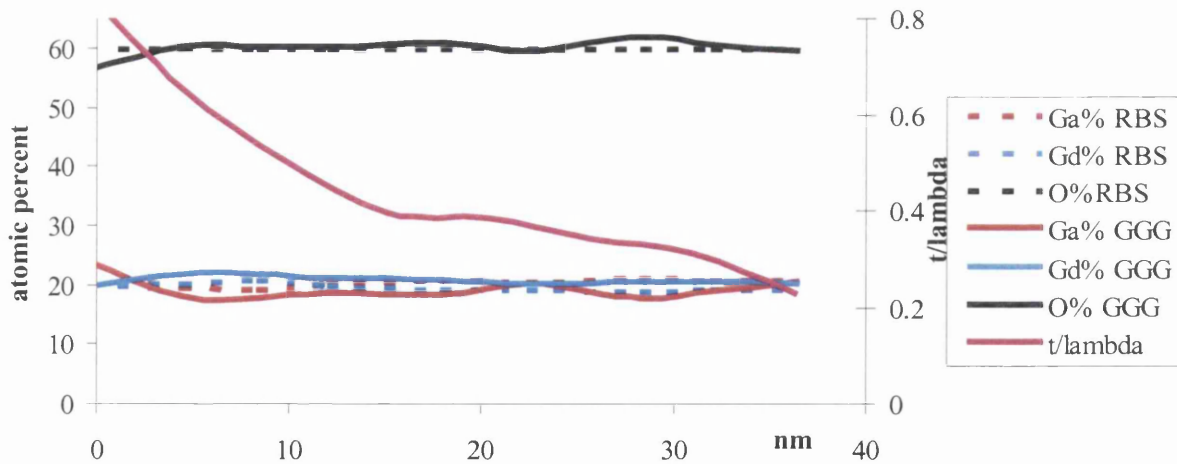


Fig. 4.26b Gd, Ga and O atomic fractions across the GGO layer in sample 2. RBS and $\text{Gd}_3\text{Ga}_5\text{O}_{12}$ as standard have been used and the results shown. On the second y-axis the t/λ profile is displayed. The 0 on the x-axis has been set on the main boundary between GGO and Ga_2O_3 layer.

4.2.8.4 Sample 3

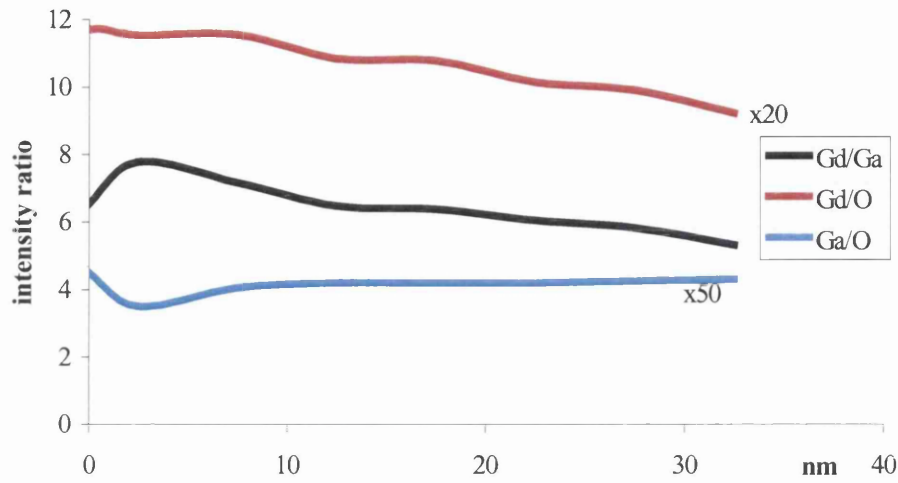


Fig. 4.27a Edge intensity ratio of Gd, Ga and O extracted across the GGO layer in sample 3. The 0 on the x-axis has been set on the main boundary between the GGO and the Ga₂O₃ template layer.

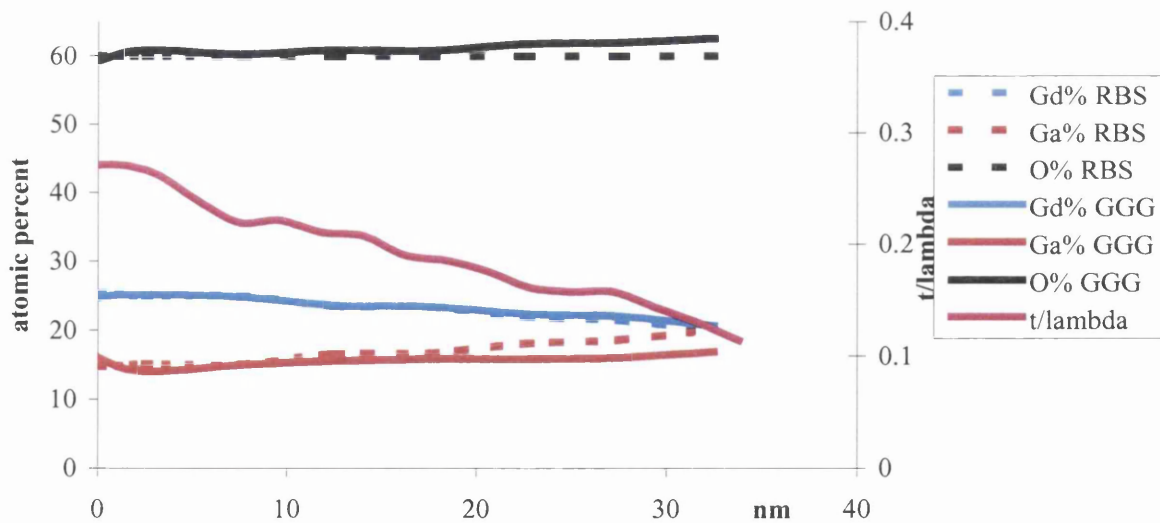


Fig. 4.27b Gd, Ga and O atomic fractions across the GGO layer in sample 3. RBS and Gd₃Ga₅O₁₂ as standard have been used and the results shown. On the second y-axis the t/λ profile is displayed. The 0 on the x-axis has been set on the main boundary between GGO and Ga₂O₃ layer.

4.2.8.5 Sample 4

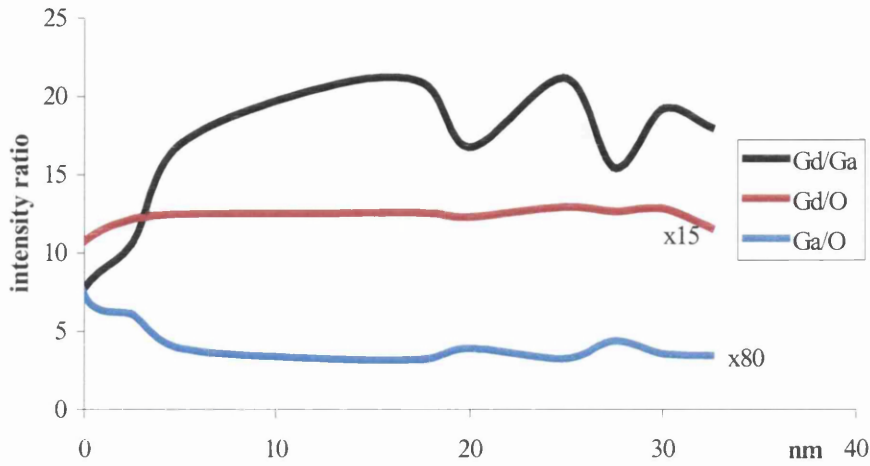


Fig. 4.28a Edge intensity ratio of Gd, Ga and O extracted across the GGO layer in sample 4. The 0 on the x-axis has been set on the main boundary between the GGO and the Ga_2O_3 template layer.

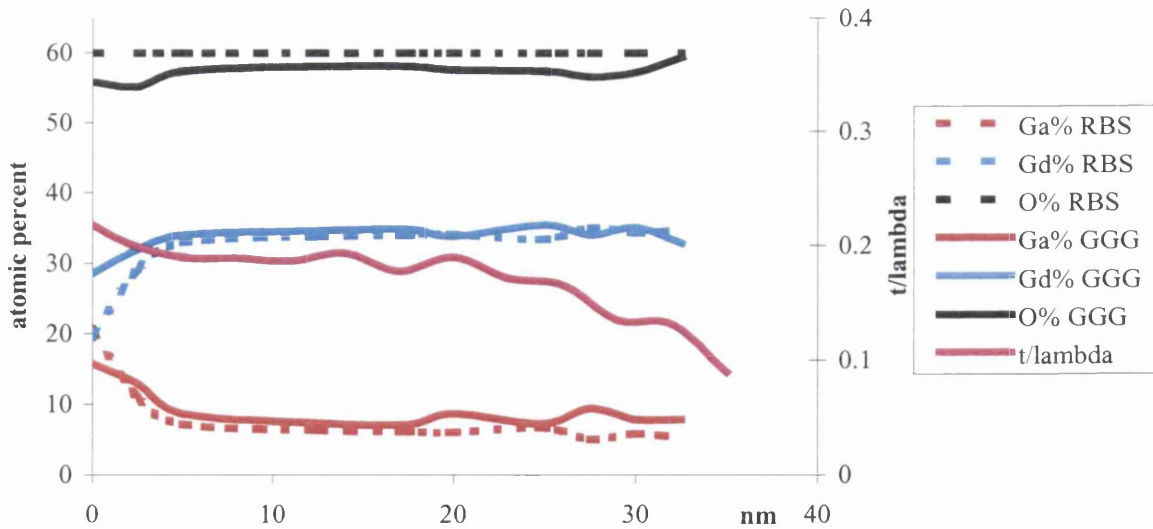


Fig. 4.28b Gd, Ga and O atomic fractions across the GGO layer in sample 4. RBS and $\text{Gd}_3\text{Ga}_5\text{O}_{12}$ as standard have been used and the results shown. On the second y-axis the t/λ profile is displayed. The 0 on the x-axis has been set on the main boundary between GGO and Ga_2O_3 layer.

4.2.8.6 Sample 5

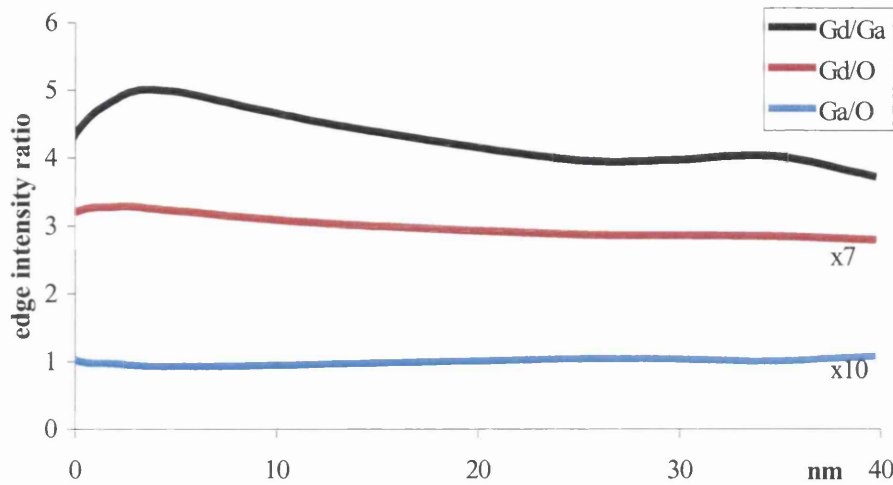


Fig. 4.29a Edge intensity ratio of Gd, Ga and O extracted across the GGO layer in sample 5. The 0 on the x-axis has been set on the main boundary between the GGO and the Ga_2O_3 template layer.

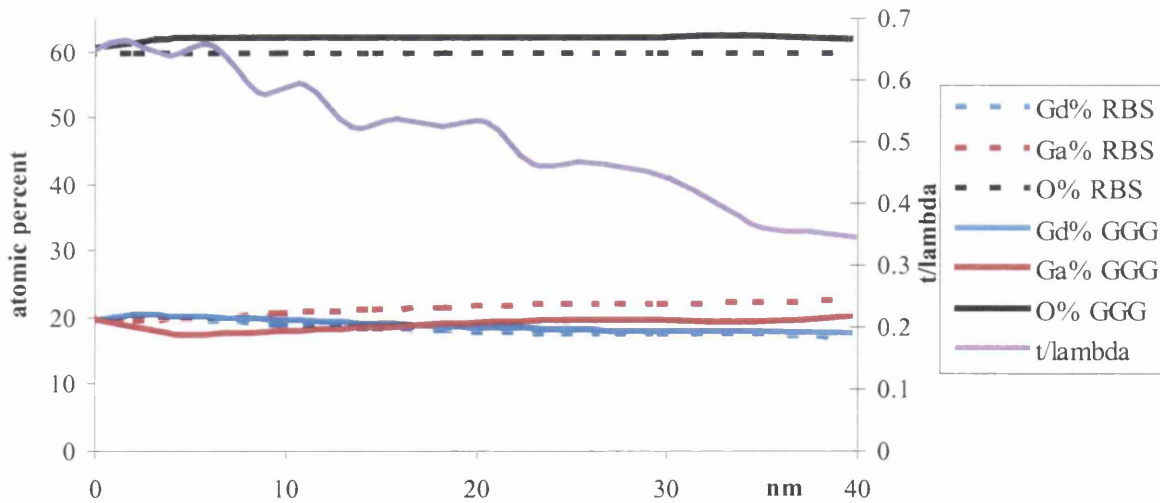


Fig. 4.29b Gd, Ga and O atomic fractions across the GGO layer in sample 5. RBS and $\text{Gd}_3\text{Ga}_5\text{O}_{12}$ as standard have been used and the results shown. On the second y-axis the t/λ profile is displayed. The 0 on the x-axis has been set on the main boundary between GGO and Ga_2O_3 layer.

4.2.8.7 Sample 6

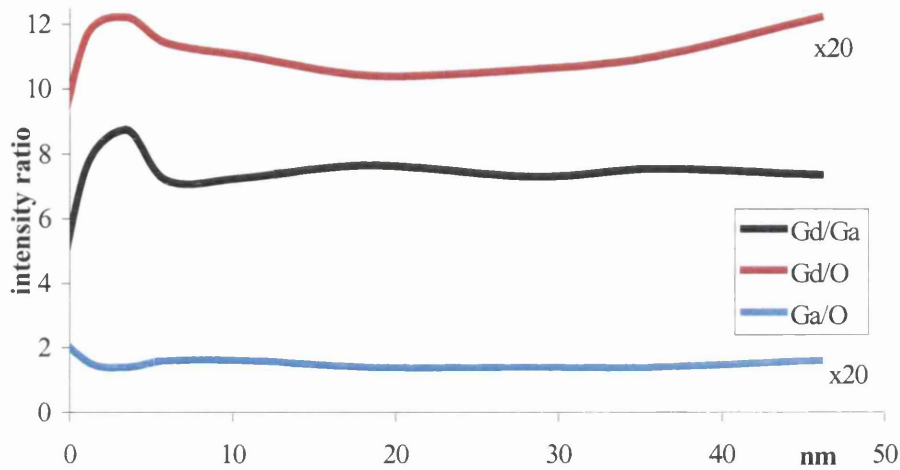


Fig. 4.30a Edge intensity ratio of Gd, Ga and O extracted across the GGO layer in sample 6. The 0 on the x-axis has been set on the main boundary between the GGO and the Ga₂O₃ template layer.

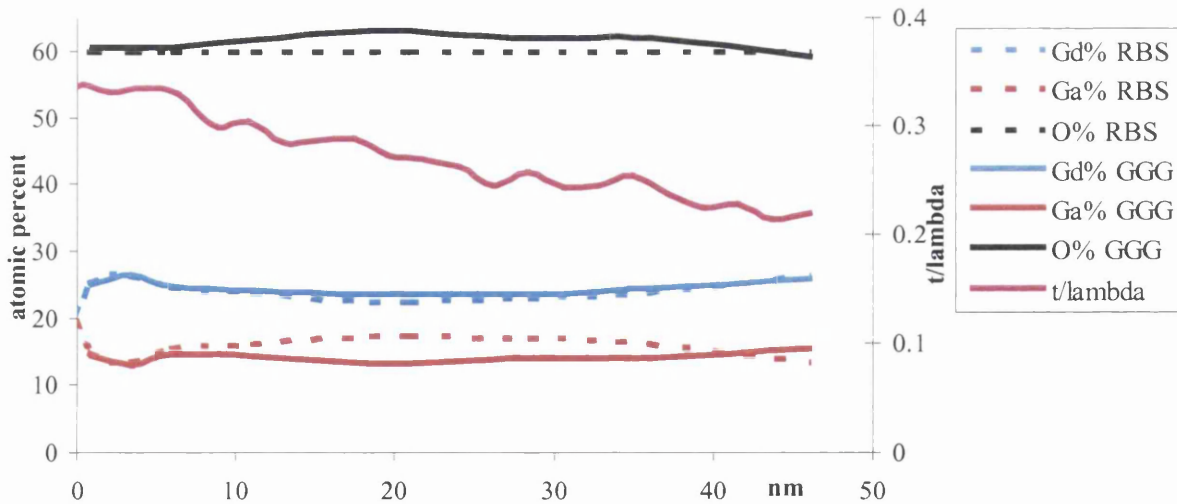


Fig. 4.30b Gd, Ga and O atomic fractions across the GGO layer in sample 6. RBS and Gd₃Ga₅O₁₂ as standard have been used and the results shown. On the second y-axis the t/λ profile is displayed. The 0 on the x-axis has been set on the main boundary between GGO and Ga₂O₃ layer.

4.2.8.8 Sample 7

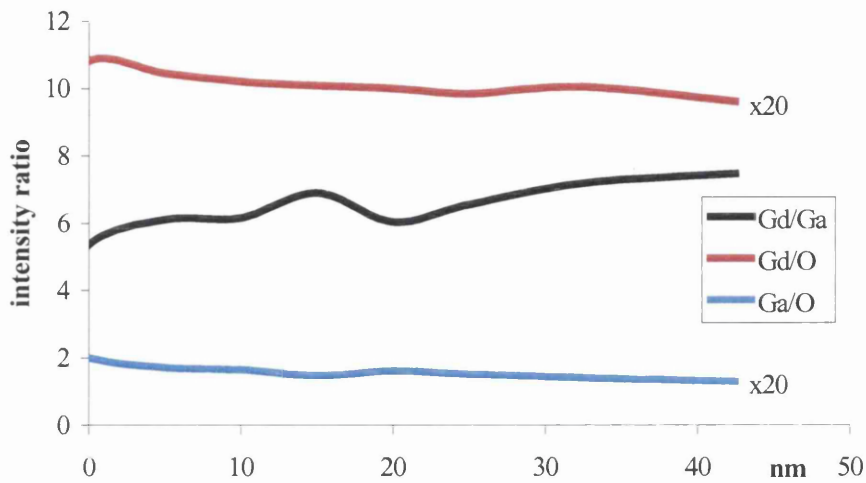


Fig. 4.31a Edge intensity ratio of Gd, Ga and O extracted across the GGO layer in sample 7. The 0 on the x-axis has been set on the main boundary between the GGO and the Ga_2O_3 template layer.

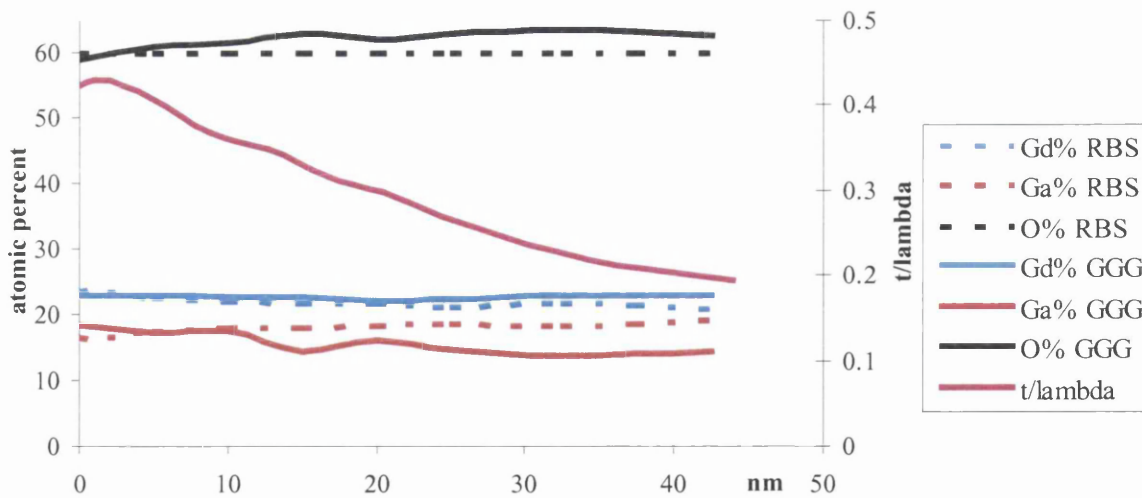


Fig. 4.31b Gd, Ga and O atomic fractions across the GGO layer in sample 7. RBS and $\text{Gd}_3\text{Ga}_5\text{O}_{12}$ as standard have been used and the results shown. On the second y-axis the t/λ profile is displayed. The 0 on the x-axis has been set on the main boundary between GGO and Ga_2O_3 layer.

4.2.8.9 Discussion

The Gd concentration in Sample 1 decreases on moving away from the interface. The highest value is 19.5% right at the interface with the template layer. The lowest value is 15.5% at the very end of the GGO layer. Therefore, the Gd concentration changes by 20%. The O concentration is relatively constant at 60% across the GGO layer despite very little fluctuations can be observed when the $\text{Gd}_3\text{Ga}_5\text{O}_{12}$. The Ga concentration appears to steadily increase towards the surface. The atomic fractions have been worked out using both RBS and $\text{Gd}_3\text{Ga}_5\text{O}_{12}$ as standard. The agreement between these two datasets is excellent. The small fluctuations observed on the O atomic fraction could be due to some small errors introduced during the manual extraction of the edges or variations on the thickness profile. As shown in Fig. 4.25b the t/λ profile, that is proportional to the thickness, is quite irregular in that region of the specimen.

The Ga, Gd and O atomic fractions have been worked out using the Gd/Ga, Ga/O and Gd/O extracted edge intensity shown in Fig. 4.25a in the case of using $\text{Gd}_3\text{Ga}_5\text{O}_{12}$ as standard and only the Gd/O in the case of using RBS as standard.

In Sample 2 the Gd concentration decreases towards the surface from 21% at the interface with the template layer down to 19.5%. In this case the variation in the Gd concentration is less strong than in Sample 1. However the agreement between the RBS and $\text{Gd}_3\text{Ga}_5\text{O}_{12}$ datasets, shown in Fig. 4.26b, is not good as in the previous case. There is a discrepancy of 1% in both Ga and Gd atomic fractions profiles. In the case of $\text{Gd}_3\text{Ga}_5\text{O}_{12}$, the O concentration is 61% all across the GGO layer with some fluctuations also. The thickness profiles changes drastically from $0.8t/\lambda$ down $0.2t/\lambda$ at the very end of the GGO layer. As shown in Fig 4.21 a thickness of $0.8t/\lambda$ does not affect much the composition. In this case the effects from the presence of a surface layer on the specimen are not particularly strong as the specimen is not very thin and there is not a massive increase in the O concentration towards the edge of the GGO layer. Hence it is likely that the composition obtained using $\text{Gd}_3\text{Ga}_5\text{O}_{12}$ as standard offers the most accurate result and the O content is slightly higher than 60% as assumed using RBS as standard.

The Gd, Ga and O atomic fractions have obtained using the Gd/O, Ga/O and Gd/Ga extracted edge intensity ratios shown in Fig. 4.26a.

In Sample 3, the Gd concentration, shown in Fig 4.27b, decreases on moving away from the interface with template layer. The highest value is 25.1% near the interface and the lowest one is 20.6% at the very end of the GGO layer. As shown in Sample 1, also in this case the Gd concentration changes by 20%. Therefore, it is quite likely that for growing both oxide layers in Sample 1 and Sample 3, the same substrate temperature has been used. However in the case of Sample 3 a higher Gd cell temperature has been used as it presents higher Gd content.

The Gd concentration obtained from the two standards is in excellent agreement right across the film. Near the substrate there is good agreement between RBS and $Gd_3Ga_5O_{12}$ result for the Ga and O concentrations as well. The fluctuations of the points about a smooth curve suggest a random error on the points of $\sim 0.5\text{at}\%$.

However, there appear to be systematic changes in the O and Ga concentrations as the top surface of the GGO is approached. The O concentration appears to vary from a minimum of 59.8% near the substrate up to a maximum of 62.6% at the edge. However there is also the possibility that there may be a small systematic error present in the analysis. The TEM sample could have surface layers with a modified composition resulting from the TEM specimen preparation. Such layers would have a bigger effect in the thin regions close to the edge of the specimen. t/λ profile, shown in Fig. 4.27b, varies from 0.26 at the interface down to 0.11 at very end of the GGO layer. It seems that such fluctuations in the atomic fractions show up at a t/λ value of 0.15. At that thickness the sample is very thin and all the effects of surface layer on the TEM specimen will be very strong. This is likely to be the reason why there is a discrepancy between the $Gd_3Ga_5O_{12}$ and the RBS datasets and the O concentration is rising towards the surface.

The Ga, Gd and O atomic fractions have obtained using the Gd/O, Gd/Ga and Ga/O extracted edge intensity ratios shown in Fig. 4.27a.

Sample 4 presents the highest Gd content (35.2%). This is the only case where the Gd content increases on moving away from the interface. Fig. 4.28b shows a comparison of the Gd, Ga and O atomic fractions obtained using RBS and $Gd_3Ga_5O_{12}$ as standard. In the case of the Gd concentration the agreement is good across the GGO layer except for the region next to the interface. In the case of the O and the Ga content the discrepancy between the two datasets is bigger. The O concentration obtained using $Gd_3Ga_5O_{12}$ presents a minimum of 56% at the interface, it increases up to 57-58% and stays constant at that range across the GGO layer up to the last 5nm at the very end where it rises. This rise is most likely due to the presence of a

surface layer whose effect shows up when the thickness of the TEM specimen sample gets really thin, below $0.13t/\lambda$ as shown in the t/λ profile (Fig. 4.28b).

In Sample 5 the Gd concentration, shown in Fig. 4.29b, decreases on moving away from the interface. The highest Gd concentration is 20.5% and the lowest one is 18% at the very end of the GGO layer. The Gd concentration changes by 10%. The Gd concentration obtained using the two standard is in excellent agreement all over the GGO layer. However in the case of Ga and O atomic ratios there is discrepancy between the RBS and the $Gd_3Ga_5O_{12}$ results. The O concentration is constant at 62% all over the GGO layer. The Ga concentration increases towards the surface of the GGO from 18% up 20.5% in the $Gd_3Ga_5O_{12}$ case while in the RBS case it changes with the same rate but 2% higher. Looking at the thickness profile shown in Fig. 4.29b, it decreases from $0.65t/\lambda$ at the interface down to $0.35t/\lambda$. At this range of thicknesses, the effects from the presence of a surface layer should not show up and as a result of that the O concentration does not increase towards the edge of the GGO layer as seen in Sample 3.

In Sample 6 the Gd concentration, shown in Fig. 4.30b, slightly decreases on moving away from the interface. The highest value is 25% right next to the interface and the very end of the GGO layer. In particular, it seems to decrease reaching a minimum of 23.5% at the centre of the oxide layer and increase towards the surface. The agreement between the Gd concentration, obtained using the RBS and the $Gd_3Ga_5O_{12}$ respectively as standard, is excellent throughout the entire GGO layer. The agreement is good for O and Ga concentrations only in the region near the interface and the edge of the GGO layer. However, there appear to be some systematic changes in the O and Ga concentrations as the centre of the GGO layer is approached. The O concentration seems to vary from 60% at the interface and the edge up to 63% at the centre of the GGO layer. In the case of the Ga concentration there is massive difference between the RBS and the $Gd_3Ga_5O_{12}$ approaching the centre of the oxide layer where in the first case it is 17% and in the second one 13.5%. Looking at the thickness profile, shown in Fig. 4.30b, there appear to vary from $0.35t/\lambda$ down to $0.22t/\lambda$ at the very end of the oxide layer.

In sample 7, the Gd concentration, as shown in Fig. 4.31b, appears to be constant throughout the GGO layer at 22.8%. The Gd concentration obtained from the two standards is in excellent agreement right across the film. Near the substrate there is good agreement between RBS and $Gd_3Ga_5O_{12}$ result for the Ga and O concentrations as well. However, there appear to be

systematic changes in the O and Ga concentrations as the top surface of the GGO is approached. The O concentration appears to vary from a minimum of 59.8% near the substrate up to a maximum of 63% at the edge. However there is also the possibility that there may be a small systematic error present in the analysis. The TEM sample could have surface layers with a modified composition resulting from the TEM specimen preparation. Such layers would have a bigger effect in the thin regions close to the edge of the specimen. t/λ profile, shown in Fig. 4.31b, varies from 0.43 at the interface down to 0.20.

In all the samples analysed so far there is a good agreement between the results of the Gd concentration from the RBS and the $\text{Gd}_3\text{Ga}_5\text{O}_{12}$. This suggests that the Gd is always fully oxidised reacting with the highest oxidation state which is +3. In this way the total composition with respect only to Gd and O will be M_2O_3 where M is the metal. The O concentration is 60% as assumed by RBS. However between the results of the Ga and O concentration from the RBS and the $\text{Gd}_3\text{Ga}_5\text{O}_{12}$ there is not a good agreement except for in the case of Sample 1. In all the other cases variations on the O concentration lead to differences on the Ga concentration.

As said above, the effects from the presence of a surface layer containing O on the TEM specimen become stronger as the thickness decreases. As a result, O intensity in the EELS spectrum will increase leading to an increase of the total O concentration. In order to understand how the presence of the surface layer affects the composition when obtained using $\text{Gd}_3\text{Ga}_5\text{O}_{12}$, the O concentration has been plotted in function of t/λ for each sample. Only in samples 3, 4 and slightly less 7, when t/λ is less than 0.3, the O concentration steadily increases as the thickness decreases. In these cases, the presence of the surface layer affects the compositional analysis. However, in most of the other cases the O concentration does not seem to increase steadily as the sample gets thinner.

Another source of errors to take into account is the poor signal to noise ratio of the Ga $L_{2,3}$ -edges signal which is compared to the Gd $M_{4,5}$ -edges and the O K-edges.

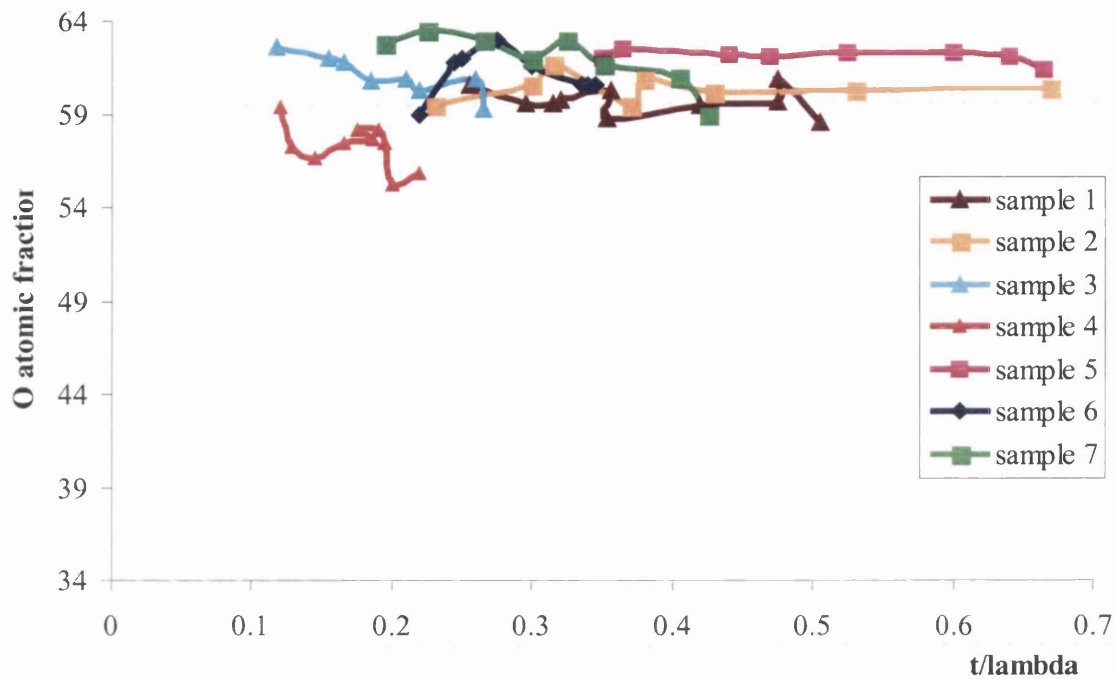


Fig. 4.32 Comparison of the O concentration across the GGO layer from samples 1-7 in function of t/λ .

4.2.8.10 Accuracy in the determination of the Gd concentration

In section, the effects of the thickness have been extensively described. It has been found that the effects of the thickness do not largely affect the compositional analysis. However there are other effects that need to take into account when performing such analysis across the GGO layer. For instance, it is important to mention that all the specimens were prepared using standard cross-sectioning. As a result to the milling process that occurs during the last stage of the preparation, the specimen is likely to be much thinner towards the edge and in most of the cases, damaged. Hence the results unlikely would reflect the real composition. The effects from the presence of surface layers containing O become stronger when the sample gets really thin and this usually occurs towards the edge leading to an increase of the O concentration. Such behaviour has been encountered in all the samples where the surface region is very thin. A

possible solution to the problem could be the use of cap layer on top of the GGO layer. The presence of a cap layer would be preserve the edge of the GGO layer from any damage effects and at the same time would ensure the thickness of the specimen to stay as flat as possible limiting the effects of the surface layer on the composition. However as explained in section, the choice of the cap layer might affect the results at the interface region.

Another source of errors is the noise especially from the Ga $L_{2,3}$ -edges as it is the least intense. This would affect more the composition when worked out using the $Gd_3Ga_5O_{12}$ rather than RBS samples as standard. Unfortunately the signal to noise ratio cannot be improved any further as it is limited by the high sensitivity of the GGO layer to the electron beam. The only way to improve it could be summing for higher number of pixels along the y-axis on the EELS SI parallel to the GaAs/oxide stack interface. This obviously would drastically increase the time for the acquisition of the entire EELS SI.

Given all the sources of uncertainties detailed earlier in the chapter, the error related to the EELS SI analysis as described in this thesis is in the order of 0.5-1%. Fig. shows the Gd and Ga atomic fractions from two different areas within the same sample. Both areas have a t/λ varying from 0.8-0.1 and 0.3-0.1. The agreement between the datasets of the two different regions is really good and shows variations on the composition not bigger than 1%. This also highlights the high reproducibility of such analysis across the GGO layer.

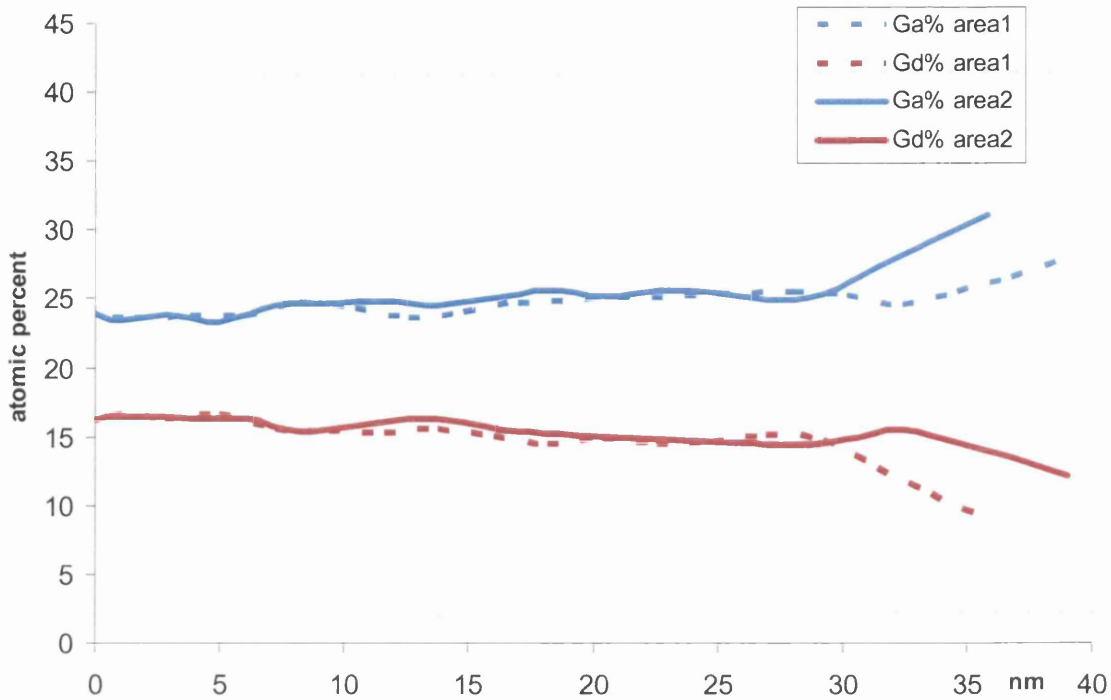


Fig. 4.33. Comparison between the Gd and Ga atomic fraction across the GGO layer of two different areas in the same TEM specimen.

As said in section 4.2.2 RBS along with EELS SI has been used for characterizing almost all the sample analysed over the last 3 years. The comparison between the results of the atomic fractions obtained using both RBS and EELS SI has been made for the region near the interface which is unlikely to be damaged by the sputtering process. Fig 4.34 shows a comparison the Gd concentrations obtained by EELS with those obtained by RBS for a range of wafers, using one of them as the calibration. The agreement is excellent. RBS is not sensitive to light elements such as O, this is the reason why only the Gd concentration has been compared.

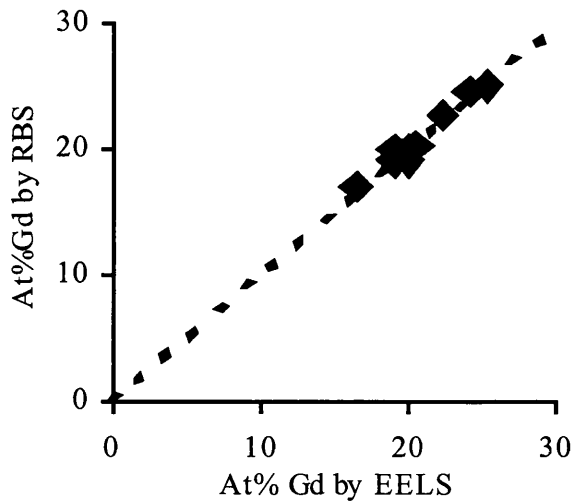


Fig. 4.34 Comparison between EELS SI and RBS results for the Gd concentration. The dashed line indicates perfect agreement.

4.2.9 Compositional analysis of GGO after capping with SiN

In section 4.2.7 the results of a number of thick GGO layers have been described. It has also been mentioned that in some cases there could be the possibility of small systematic errors present in the analysis. The TEM sample could have surface layers with a modified composition resulting from the TEM specimen preparation. Such layers would have a bigger effect in the thin regions close to the edge of the specimen. Multiple scattering could change the shape of the $L_{2,3}$ -edges as the specimen thickness changes. Since the shape from the GaAs is taken adjacent to the GGO, the multiple scattering effects would be the same for the regions of GGO close to the substrate but change as the thinner edge is approached. Finally, the contribution from the stray scattering in the gun becomes more significant as the specimen becomes thinner and this could cause a systematic change of the background under the Ga $L_{2,3}$ -edges. The TEM specimen preparation may cause some damages on the edge of the GGO where the specimen becomes much thinner or the formation of surface layer containing O.

The GGO layer can be preserved by all the errors mentioned above by depositing a cap layer on top of the oxide surface. 50nm of SiN have been deposited on top of the GGO layer in Sample

8. Fig. 4.35 shows a TEM bright field image of Sample 8 after depositing with 50nm of SiN on top of the GGO layer. The GGO is now preserved from damage which the TEM specimen preparation may cause at the edge. In this way it is possible to see how the surface looks. It appears relatively rough. At the interface between the GGO layer and the SiN it is possible to see the presence of a layer that appears relatively bright. Examination of the spectra from this layer shows the presence of a SiO_x layer (Fig. 4.36). Fig. 4.36 shows the Gd/O and Ga/O extracted edge intensity ratios of Sample 8. As the edge of the GGO layer is approached both of them drastically decrease. This is due to an increase in the O concentration at the interface leading to the formation of a SiO_x layer.

These results show that deposition of SiN on top of the GGO layer leads to a formation of a SiO_x at the interface with the cap layer. This represents an important information since SiN is widely used in the microelectronic industry for passivation purposes.

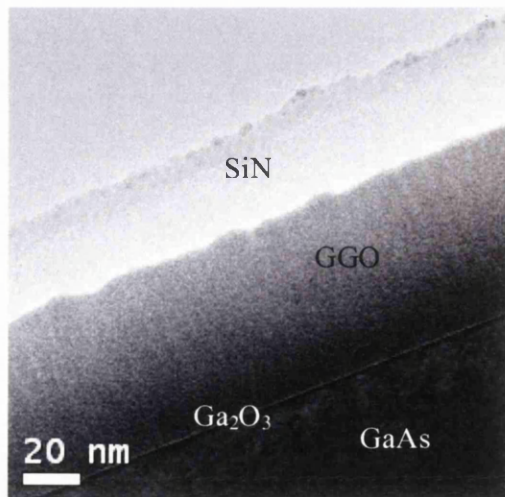


Fig. 4.35. TEM bright field image of Sample 8 with a SiN cap layer deposited on top of the GGO layer.

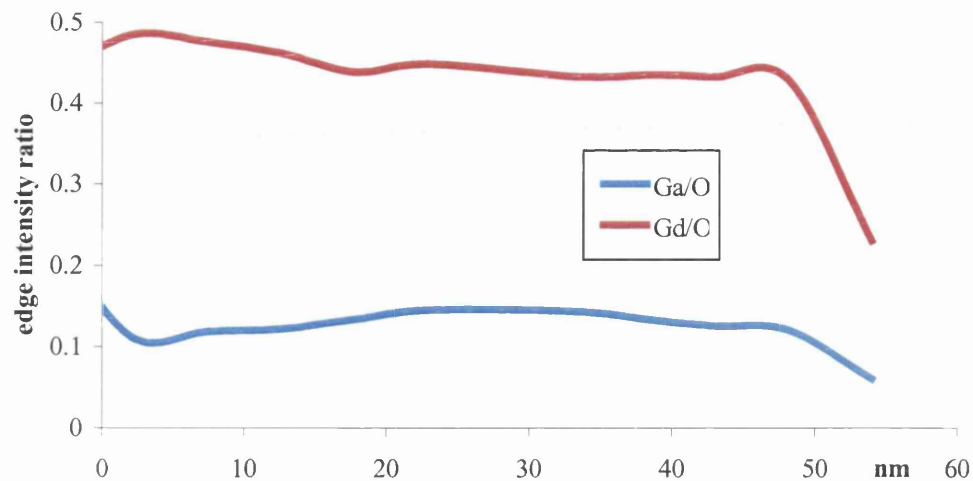


Fig. 4.36 Elemental intensity ratio across the GGO layer in Sample 8 with SiN deposited on top of the GGO layer. Both ratios decrease as the edge of the oxide layer is approached.

4.2.10 Compositional analysis of thin GGO layers after capping with Pt: simulation of gate metallisation process

In the previous sections a way to determine the composition in thick GGO layers (>40nm) has been shown. Once the technique has been developed for thick GGO layers, more challenging situations where the $\text{Ga}_2\text{O}_3/\text{Gd}_x\text{Ga}_{0.4-x}\text{O}_{0.6}$ dielectric gate stacks layer is ~10nm thick have been investigated. A cap layer of 30nm of Pt and 30nm of Au has been deposited on top of the GGO layer in order to simulate the effects of the gate metallisation process [29]. This structure is shown in Fig. 4.37.

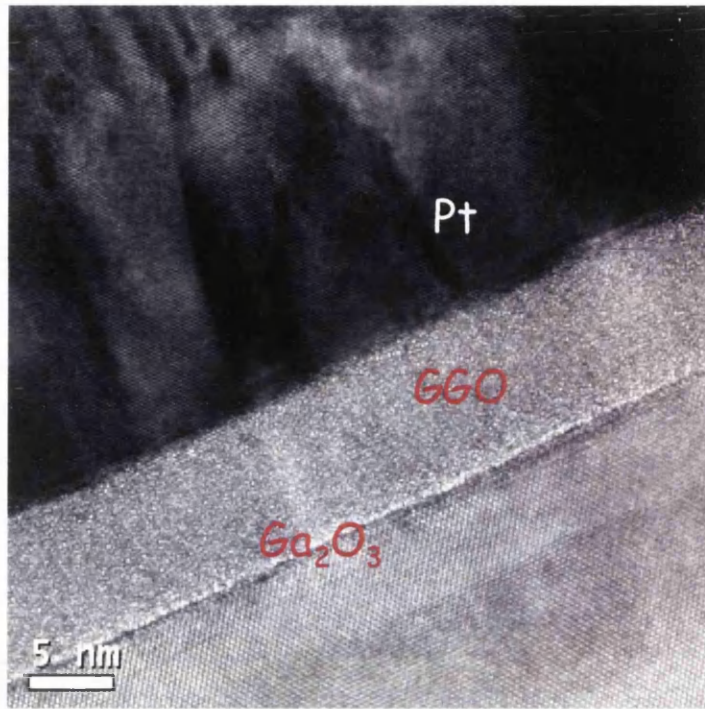


Fig. 4.37 High-resolution bright field TEM image of the dielectric gate stack region after the deposition of Pt on top of the GGO layer.

As seen in Fig. 4.37 both GaAs/Ga₂O₃/GGO and GGO/Pt interfaces show some roughness. In particular, irregularities at the interfaces level cause variations of the thickness of the total oxide layer stack of the order of 0.5nm.

Fig. 4.38 shows the region selected for the spectrum image on the unannealed specimen. 1.2nm has been chosen as pixel size. In this case the GGO layer is 10nm, therefore it is necessary to use a smaller a pixel size in order to obtain more pixels on the EELS SI.

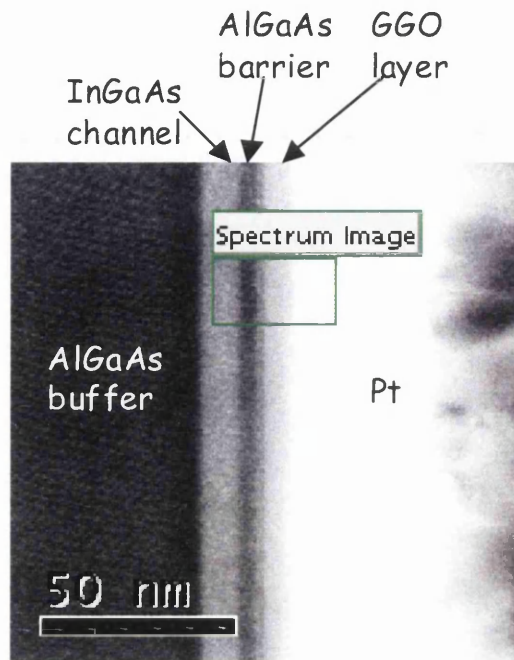


Fig. 4.38 ADF STEM survey image used for the acquisition of the EELS SI the green box represents the where the electron beam was scanned.

The intensities of the O K-edge, the Gd $M_{4,5}$ -edges and the Ga $L_{2,3}$ -edges were extracted using the MLLS procedure described in section 4.2.4 and are shown in Fig. 4.39. The MLLS routine has been used because it gives a quick idea of how the elements are distributed across the GGO layer. The origin has been set to match the point where the O intensity is at half maximum value and this is assumed to be the mean boundary between the substrate and the Ga_2O_3 template layer. The O intensity extends to the left of the Gd intensity at the substrate side of the GGO. This shows the presence of the Ga_2O_3 template layer, which is ~ 1 nm wide. Looking at all the edge intensity profiles there is no evidence of the formation of any PtOx layer at the interface between the GGO and the Pt layer. Pt does not react easily with O so the formation of PtOx requires the presence of certain reaction conditions. It is well know and widely discussed above in section 4.2.8 that the presence of a SiN layer deposited on top of the GGO layer determined the formation of a few nanometers layer of SiOx.

The edge intensities were converted to atomic fractions using manual approach described in section 4.2.5 and are shown in Fig. 4.40. In this case the origin has been set to be the main

boundary between the GGO and the Ga_2O_3 template layer. As shown in Fig. 4.38, the O concentration is relatively constant at 58% across the GGO layer. The Gd concentration appears to increase on moving towards the edge of the oxide layer from 21.8% up to 24.7%. Only in Sample 4 (section 4.2.7.5) an increase of the Gd concentration on moving away from the substrate has been seen. In that case the Gd concentration is over 35% and the GGO layer is 50nm wide. A possible explanation for this big increase of the Gd concentration towards the edge of the GGO layer could be the fact that the GGO layer in this case is much thinner and perhaps this could affect the MBE growth experimental conditions determining a modification of the distribution of all the elements across the GGO layer.

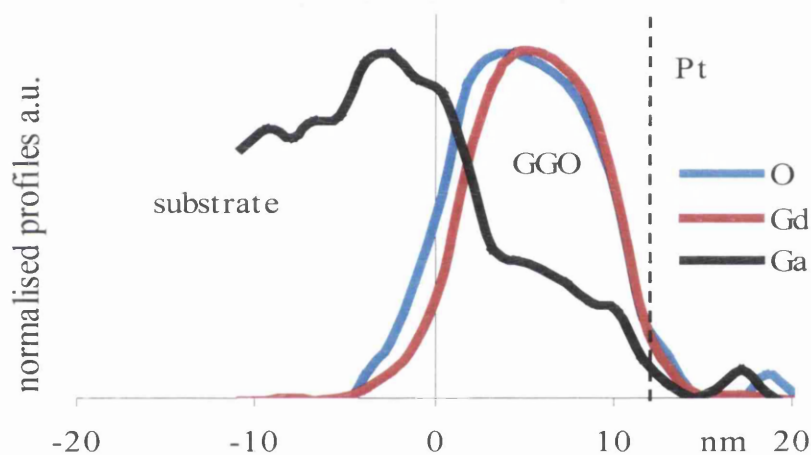


Fig. 4.39 Edge intensities normalised to the maximum values, obtained from the area drawn in Fig. 3 in the unannealed sample. The zero on the x-axis represents the interface between the Ga_2O_3 and the GaAs.

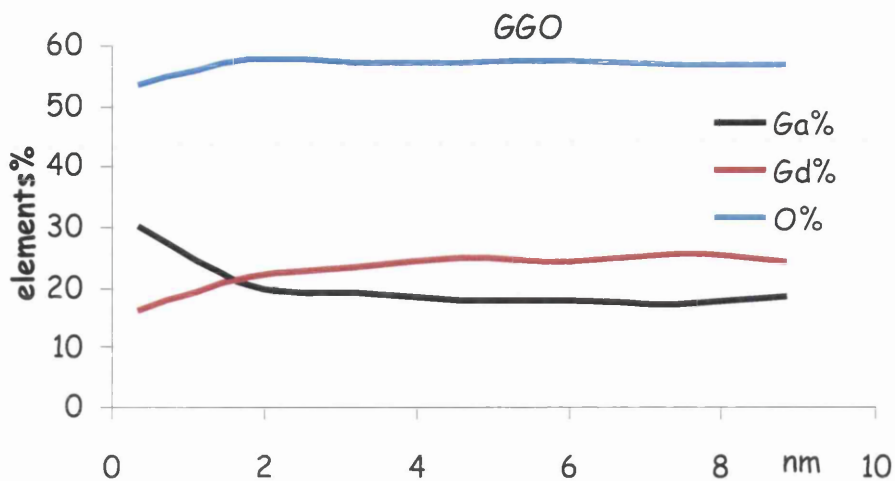


Fig. 4.40 Elemental concentration across the GGO layer of the selected area in Fig. 4.38.

4.3 CONCLUSIONS

Recording spectra over the energy range from the O K-edge to the As L_{2,3}-edges allows intensities of characteristic edges from O, Ga, As and Gd to be obtained with good precision provided the operating conditions are chosen to minimise the interference from the stray scattering arising in the gun. The Ga and Gd intensities can be separated successfully using the shape of Ga edges in the GaAs. The intensity can be converted to atomic fractions using either calibration to a composition obtained by RBS or directly to a standard of known composition, here gadolinium gallium garnet. The agreement between the Gd:O ratios obtained by RBS and those obtained by EELS calibrated to one RBS data point is excellent. The random error in the O concentration is ~0.5%. The agreement between the RBS calibration and the garnet calibration is good but some samples show deviations as the thinner edge of the sample is approached. In other samples such deviations can be explained by errors in the Ga L_{2,3}-edges determination or actual variations on the composition.

Having established a reliable and accurate technique, the next step is to determine what spatial resolution normal to the substrate can be achieved in this radiation sensitive system and to

explore whether it is possible to gain chemical information about the interface from either chemical shifts or edges shapes.

CHAPTER 5: INVESTIGATION OF ETCHING PROCESSES BY EFTEM AND EELS SI

5.1 INTRODUCTION

Electron energy loss spectroscopy (EELS) is the analysis of the energy distribution of electrons that have passed through the specimen and interact inelastically with it [11]. It is a powerful technique that provides information on elemental composition and electronic structure in a particular area of the material. There are currently two techniques which allow EELS to gain spatial resolution. The first method is to combine the EELS with scanning transmission electron microscopy (STEM) to give a spectrum image (SI) where an EELS spectrum is collected at each point in the scan. This technique has been extensively described in chapter 4. The second method is to use energy filtered transmission electron microscopy (EFTEM) which requires the use of an imaging filter as spectrometer. EFTEM provides rapid elemental maps to identify unknown elemental distributions and give some information on the composition whereas SI imaging gives very detailed information on the local chemistry and composition with much higher sensitivity than EFTEM. However, the acquisition time can be much longer so that it must be possible to identify the area of interest. Thus the use of EFTEM in combination with SI is a very powerful approach with EFTEM identifying areas that require detailed analysis by SI.

Here EFTEM approach is applied to an investigation of three ion-etching processes on GaAs/Ga₂O₃/GGO.

The aim of this study is to develop a way to study the effects of etching processes on Ga₂O₃/GGO dielectric gate stacks. This obviously represents a very important issue for fabrication purposes. Electrical properties in MOSFET devices are sensitive to the elemental distribution in the dielectric gate stack, the nature of the interfaces across the channel and the oxide region, and the actual architecture. Hence a good understanding of the local composition and chemistry is required in order to make successful devices. The type of analysis presented here is important in optimising the performance of III-V MOSFET devices.

A key step in the fabrication process is the etching process. This is important in order to define the regions where the gate and the ohmic contacts will be deposited. It is extremely important that the dielectric gate stack layer under the gate is preserved from the etching process and completely removed from all the other parts. Hence, ~80nm silicon nitride (SiN) has been used

as mask for the etching process. After the etching, a further ~80nm of SiN is deposited to provide a protective cap layer for the surface during TEM specimen preparation.

A detailed description of EFTEM theory is given in this chapter in order to understand the limits and the advantages of this technique over the EELS SI. Furthermore one of the 3 etching process cases has been investigated using EELS SI and this in combination with EFTEM has proved to be a useful way to give key information from problem covering an area large compared to the spatial resolution required.

In this chapter a detailed description of the EFTEM theory is given. The EELS SI technique has already been covered in chapter 4. This chapter also describes the effects of the objective aperture on the Ga, O and Gd elemental maps obtained by EFTEM.

5.2 EFTEM THEORY

EELS is the basis for the EFTEM. An EELS spectrum contains a wealth of information about electronic structure of the atoms and composition in the specimen. Any TEM image is composed by electrons, many of them have passed through the specimen without losing any energy, but some of them have lost an amount of energy which is directly related to the chemical environment of the atoms within the specimen. EFTEM utilizes a special spectrometer which has the capability to filter the energy of electrons that have interacted with the specimen. In this way, concentrating on a particular ionisation edge, it is possible to build up images which show a two-dimensional distribution of specific element. It is also possible to remove the contribution from inelastic scattering. For EFTEM there are currently two different alternatives. A dedicated EFTEM with an in-column filter [28] or a post column energy-filter such as the GIF manufactured by Gatan [30, 31] which can be installed as an attachment at the end of the electron-optical column of almost any TEM. Both types of energy filters are devices which can form images with electrons in a selected energy range.

The inelastic scattering process in EELS is energy-dependent and, hence, it may be used to obtain analytical information from a small specimen area. By using any spectral feature in the EEL spectrum, it is possible to monitor simultaneously the variation of this feature over a wide area in the specimen. Just by selecting the electrons over a narrow energy window that includes only the zero-loss peak, it is possible to remove the contribution of the electrons that have inelastically scattered. If the energy window is placed at higher energy-loss, the plasmon peak

can be selected. The plasmon resonance peak is proportional to the density of valence electrons. However the most extensive analytical use of energy-filters is for core-loss imaging and elemental mapping. The ability of an energy filter to show a two-dimensional distribution of specific element makes it a powerful for analytical studies.

By selecting an energy window around an ionisation edge, it is possible to obtain images where the intensity is correlated to the concentration of a specific element. The signal of this element in the image is superimposed to other signals such as diffraction contrast, thickness variations, elastic contrast and most importantly the background. Essentially there are two different methods for removing the background: the two image and the three image method, which generate a jump ratio image and an elemental map respectively. For the first method, two images need to be acquired with energy windows before and after the ionisation edge of interest. The one above the edge is then divided by the one before the edge to produce a jump ratio image [32, 33]. This jump ratio image is not particularly sensitive to the elemental concentration, hence useless for quantitative purposes, but it is very efficient for minimizing the background effects. The advantages are that it requires minimal mathematical processing of the data, therefore the noise resulting is not increased. However specimen thickness variations may create non-elemental contrast [33, 34].

For the second method 3 images need to be acquired (Fig. 5.1). In this way the background contribution can be removed from the integration window after the edge [11]. Two images need to be recorded in front of the ionisation edge, and one after. Background shape is determined by the power law: $I_{bg}=AE^{-r}$ where I is the intensity, E is the energy loss averaged to the centre of the energy window ΔE and A and r are fitting parameters. If all the windows have the same width the intensity of the background will be given by the equation:

$$I_b = \sqrt{I_1 I_2} \left(\frac{I_2}{I_1} \right)^q \quad \text{Equation 5.1}$$

$$q = \frac{\ln E_s - \frac{1}{2}(\ln E_1 + \ln E_2)}{\ln E_2 - \ln E_1} \quad \text{Equation 5.2}$$

The numbers 1 and 2 refer to the pre-edge images 1 and 2 respectively.

If the data is noisy or small concentrations of the element have to be detected or the background shape does not have the form of AE^{-r} , the method fails.

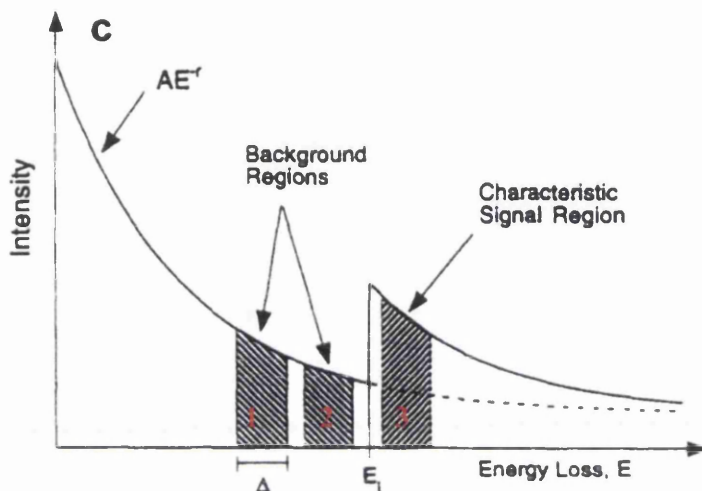


Fig 5.1 EELS spectrum showing the 2 pre-edge background regions and the post-edge region. The two pre-edge images are used for the acquisition of the background contribution

For an absolute quantification, the measured net signal under the ionisation edge collected inside a collection angle β and within an energy range ΔE [$I_{edge}(\beta, \Delta E)$] is directly related to the number of scattering atoms per unit area N :

$$N = \frac{I_{edge}(\beta, \Delta E)}{I_{ZL}\sigma(\beta, \Delta E)} \quad \text{Equation 5.3}$$

Where I_{ZL} represents the intensity of the window positioned on the low-loss portion of the spectrum including the zero-loss (zero-loss) and σ is the partial scattering cross-section. For performing a quantitative analysis it is necessary to acquire an elemental map at the ionisation edge and divide it by a zero-loss filtered image and the appropriate ionisation cross-section.

This procedure is widely used with good results for biological and amorphous samples [35]. However, diffraction contrast in crystalline sample can cause serious problems. [36] On the other hand, atomic ratio images can be obtained using the same procedure for two elements like A and B. This is called relative quantification. The relative quantification offers the advantage of minimizing non-element specific effects, like diffraction contrast and thickness variations as the division partly cancels them. The equation gives the atomic concentration ratio of the elements A and B

$$\frac{N_A}{N_B} = \frac{I_{edge,A}(\beta, \Delta E)\sigma_B(\beta, \Delta E)}{I_{edge,B}(\beta, \Delta E)\sigma_A(\beta, \Delta E)} = \frac{C_A}{C_B} \quad \text{Equation 5.4}$$

The quantification in this case, consists of the acquisition of 2 elemental maps and the determination of the appropriate cross-section [11].

In this case the quantification of elemental maps relies on the accuracy of the ionization cross-section σ . A more experimental method, which produces more accurate results especially for heavy elements, consists in the use of standard with known composition. This method relies on the use of the k factor [37]. This method of quantification is widely used in EFTEM. The k is related to the ionization cross-section by:

$$k_{AB} = \frac{\sigma_B(\beta, \Delta E)}{\sigma_A(\beta, \Delta E)} \quad \text{Equation 5.5}$$

However the tabulated values for the k factor and the ionization cross-section σ for EELS cannot be directly used for EFTEM as they are usually measured for wide energy windows ΔE . For EFTEM narrow ΔE is used leading to an increased sensitivity to small features in the near-edge structure.

For quantification purposes some variables such as exposure time, energy slit width, collection angles have to be identical as well as the illumination conditions. The background extrapolation is also related to the thickness of the TEM specimen. In thicker region the contribution from the plural scattering becomes predominant changing the shape of ionisation edges. In elemental mapping it degrades the sensitivity and surely introduces errors on the background-fitting routine [38]. Ideally the best attempt would be to analyse a thin area containing a feature of interest. This area has to be thin in order to lower the effects of the plural scattering.

A useful quantitative parameter for measuring the plural scattering contribution to the spectrum is to relate the specimen thickness to the total inelastic mean free path λ . The parameter t/λ is related to the zero-loss peak intensity by:

$$t / \lambda = \ln \left(\frac{I_{tot}}{I_0} \right) \quad \text{Equation 5.6}$$

Where I_{tot} is the total intensity under the spectrum and I_0 the zero-loss peak intensity. At incident energies of 100keV the effects of the plural scattering can be ignored for $t/\lambda < 0.5$. For values of t/λ in the range between 0.5 and 1.5 the quality of the elemental maps are strongly degraded.

The spatial resolution obtained in an EFTEM image is limited by several factors such as delocalisation of inelastic scattering which is due to the ionisation of an atom by a distant fast electron, chromatic aberration of objective lens (C_c (chromatic aberration constant) and width of slit Δ), diffraction limit due to objective aperture, spherical aberration due to objective lens (C_s), statistical noise due to low inelastic cross-sections, radiation damage of the specimen and some instrumental instabilities (high voltage drift, sample drift etc.). In the best cases taking in account all these factors, the spatial resolution of EFTEM elemental maps would be limited to 1nm. When doing EFTEM at high magnification elastic contrast that is always present in EFTEM images may become visible. As mentioned before the goal of EFTEM using core-loss ionisation edges is the visualization of pure elemental/chemical contrast.

Navidi-Kasmai and Kohl [39] found that for crystalline specimens, elastic contrast is unavoidable and increases with the specimen thickness. A reliable image contrast interpretation is only possible by making a comparison between experimental images with simulated ones. However simulations are only available for thin specimen.

5.3 EXPERIMENTAL CONDITIONS

All the EFTEM work, described herein, has been performed in a TEM FEI Tecnai T20 equipped with a LaB₆ emission gun and a Gatan GIF 2001 attached to the microscope. The LaB₆ source has much lower brightness than the FEG and significantly hinders the elemental sensitivity for high-resolution mapping at the sub-nanometer level. However the total beam

current is 10-100 times higher than that available for the FEG. For those applications where it is necessary to map large areas of the sample at intermediate magnification, the higher beam current of LaB₆ offers a large number of pixels to map in a reasonable time.

For the investigation of the 3 etching processes reported here, the aim was to perform a qualitative analysis of all the features across the sample. A spectrometer aperture of 3mm was used and no objective aperture has been inserted. In this way the highest energy loss signal possible was obtained. Perhaps for improving the spatial resolution, an objective aperture needs to be inserted in order to enhance the signal to background ratio for ionisation edges. Without an objective aperture, the spatial resolution would deteriorate as a result of the increased effects of the aberrations but on the other hand the total current going to the spectrometer will be higher. However the EFTEM work presented in this thesis has been performed only for qualitative characterisation purposes. As described in section 5.7.4 the combination of EFTEM with EELS SI is shown to be an advanced tool for the characterisation of large areas.

5.4 ACQUIRING ENERGY-FILTERING IMAGES

The width Δ of the energy-selecting slit is a compromise between two factors. The slit should be narrow enough to avoid edge overlap and significant background extrapolation errors [40, 41, 42] but it should be large enough to provide adequate counting statistics and average out the near edge structure effects that are negative for elemental analysis. As said above the chromatic aberration is related to the width of the energy-selecting Δ . The bigger Δ is the bigger the loss of resolution from chromatic aberration is.

For the elements of interest here the best compromise choice for Δ is 15-40eV depending on the element of interest. Big energy-selecting slits have been used for mapping edges at high energy such as As L_{2,3}-edges and Ga L_{2,3}-edges respectively at 1323eV and 1115eV. The use of large energy-selecting slit for such weak edges minimises the acquisition time and decreases the effects of any instrumental or specimen instability. For the conditions employed here, acquisition times of 2.5-35 seconds have been applied. Long acquisition times have been used for high-energy edges.

Any drift that occurs between images in a series can be corrected by calculating the cross correlation function during post-processing.

5.4.1 *Effects of the objective aperture*

The size of the objective aperture is one of the most important factors limiting the spatial resolution of EFTEM elemental maps. Without any objective aperture inserted, the chromatic aberration (C_c) and the spherical aberration (C_s) have their biggest effects and obviously this limits the spatial resolution. The spatial resolution is also limited by the contribution of the diffraction pattern to the image. Usually the size of this angular diffraction contribution is much larger than the typical slit width used in EFTEM which is about 20eV. Placement of the slit anywhere in the spectrum will result in the restriction of this angular range of scattering. The shape of the diffraction pattern is a function of the energy-loss. It is well known that the diffraction of high-energy loss electrons leads to distributions more like Kikuchi maps than spots patterns [43]. Hence normalizing for the zero-loss cannot completely remove these diffraction effects from the EFTEM maps. By inserting an objective aperture it is possible to reduce the size of the diffraction pattern in the spectrometer. As a result of that, in theory, the signal to background ratio for the ionisation edges will be improved leading to the acquisition of much cleaner images. However this does not work very well for high energy-loss edges as the signal to noise ratio will be greatly reduced. The insertion of a small objective aperture clearly has some advantages in terms of spatial resolution but on the other hand the total signal going to the spectrometer will decrease leading to a deterioration of the signal to noise ratio. An analysis of this type of effects is reported here. For the same sample, Gd, O and Ga elemental maps have been acquired for different objective apertures. In the first case, there is no objective aperture and in the other 2 cases the objective apertures 2 (60 μ m) and 4 (20 μ m), that determine roughly a collection angle β of 20mrad and 7mrad respectively, have been inserted respectively. All the Gd, O and Ga elemental maps have been recorded using a Δ of 15eV, 25eV and 10eV respectively. The Gd, Ga and O elemental maps have been acquired using the ionisation edges of Gd $N_{4,5}$ -edges at 140eV, Ga $M_{2,3}$ -edges at 103eV and O K-edge at 532eV respectively. The Gd $N_{4,5}$ -edges are a very strong feature with a high signal while the Ga $M_{2,3}$ -edges are not particularly strong. Therefore, the signal to noise ratio is not high in the case of the Ga $M_{2,3}$ -edges. The O K-edge is the main feature of the O in the core-loss region. It is particularly strong but due to the fact that it is placed at much higher energy than Gd $N_{4,5}$ -edges, the overall signal is much lower. Hence it is necessary to employ longer acquisition times and to use wider energy selecting slit Δ .

5.4.1.1 Comparison of bright field images at different objective aperture

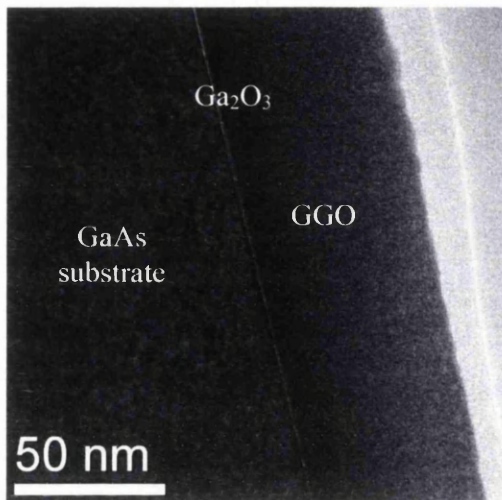


Fig. 5.2a TEM bright field image without objective aperture.

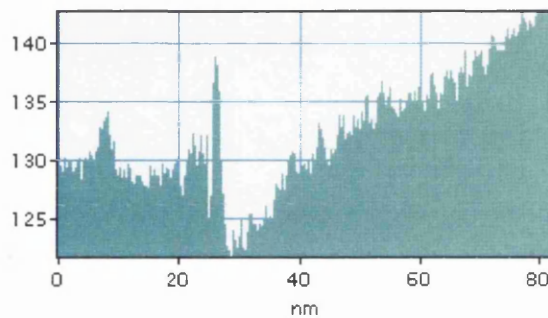


Fig. 5.2b Intensity profile of TEM bright field image shown in Fig. 5.2a.

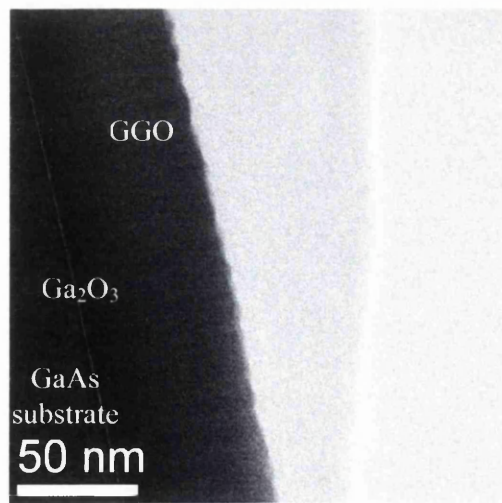


Fig. 5.3a TEM bright field acquired with objective aperture number 2.

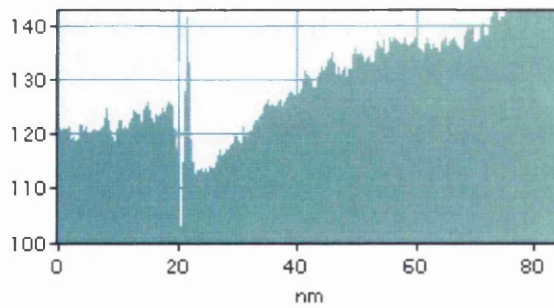


Fig. 5.3b Intensity profile of TEM bright field image shown in Fig. 5.3a.

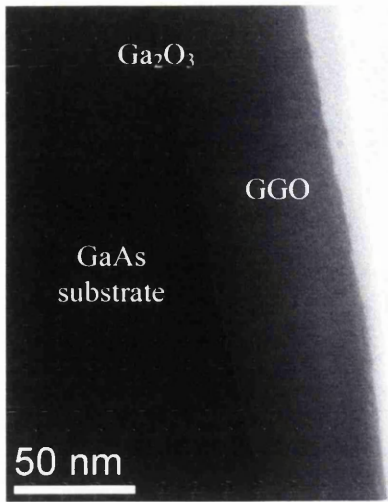


Fig. 5.4a TEM bright field acquired with objective aperture number 4.

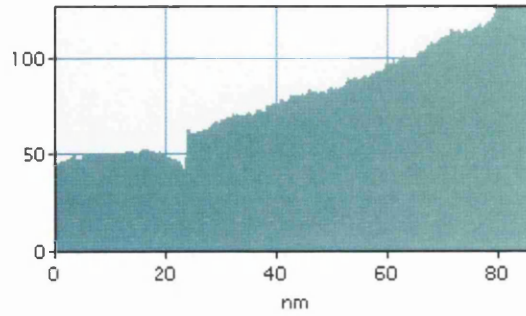


Fig. 5.4b Intensity profile of TEM bright field image shown in Fig. 5.4a.

5.4.1.2 Comparison of Gd elemental maps at different objective apertures

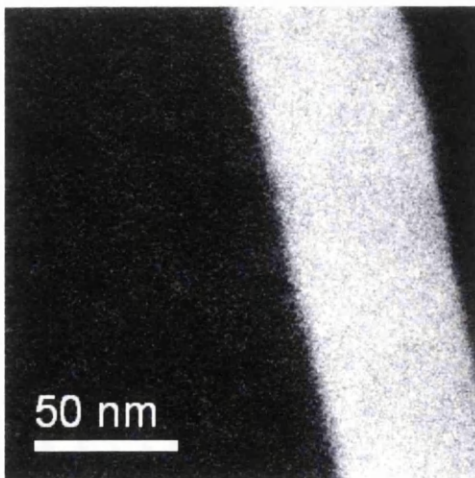


Fig. 5.5 EFTEM Gd elemental map without objective aperture.

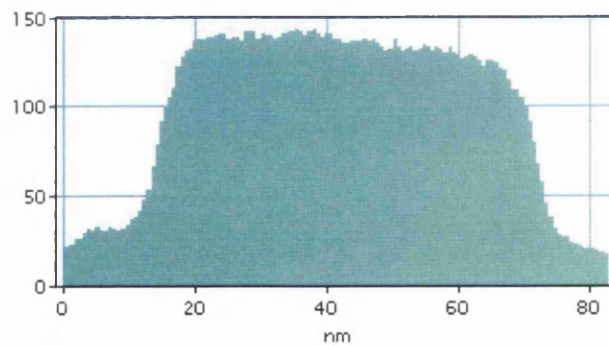


Fig. 5.6 Intensity profile of EFTEM Gd elemental

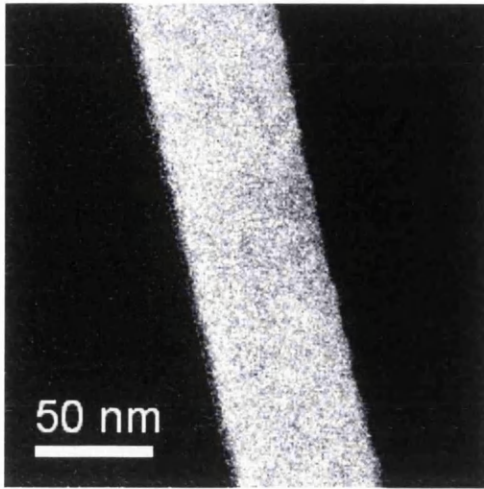


Fig. 5.7 EFTEM Gd elemental map with objective aperture number 2.

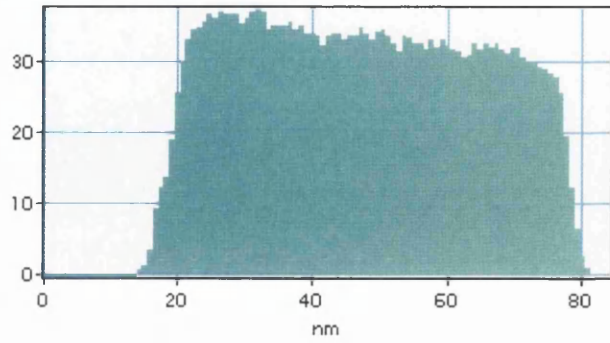


Fig. 5.8 Intensity profile of EFTEM Gd elemental shown in Fig. 5.7

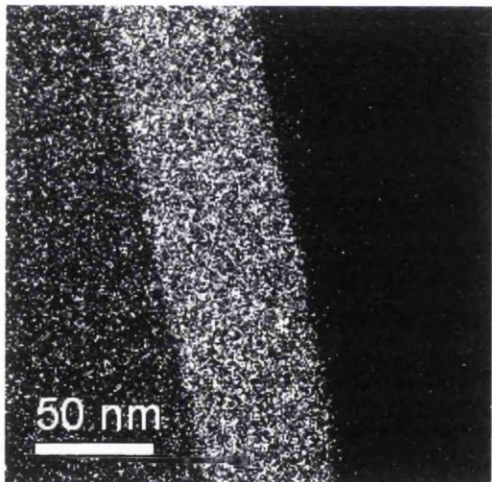


Fig. 5.9 EFTEM Gd elemental map with objective aperture number 4.

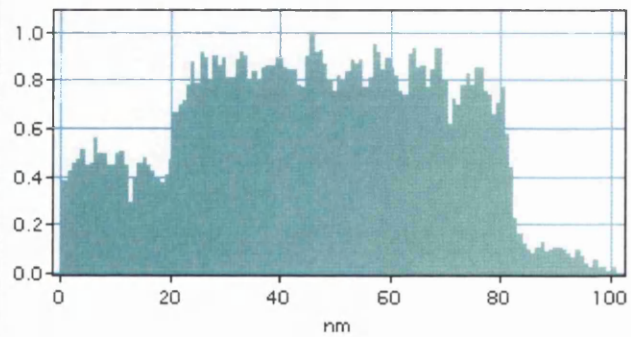


Fig. 5.10 Intensity profile of EFTEM Gd elemental shown in Fig. 5.9.

5.4.1.3 Comparison of O elemental maps at different objective apertures

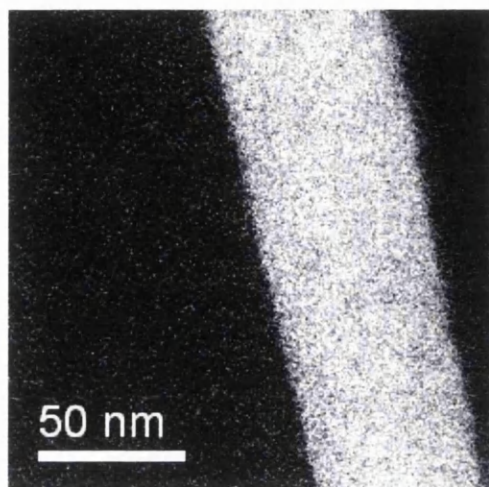


Fig. 5.11 EFTEM O elemental map without objective aperture.

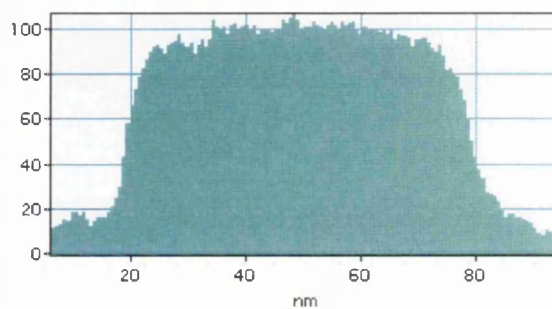


Fig. 5.12 Intensity profile of EFTEM O shown in Fig. 5.11

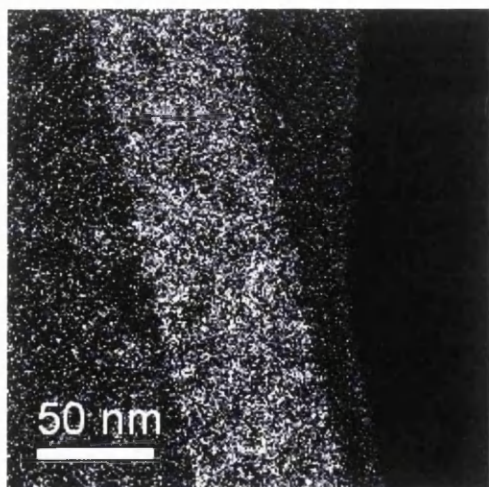


Fig. 5.13 EFTEM O elemental map with objective aperture 2.

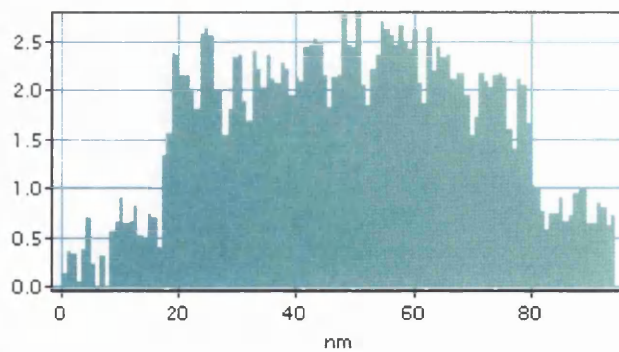


Fig. 5.14 Intensity profile of EFTEM O shown in Fig. 5.13

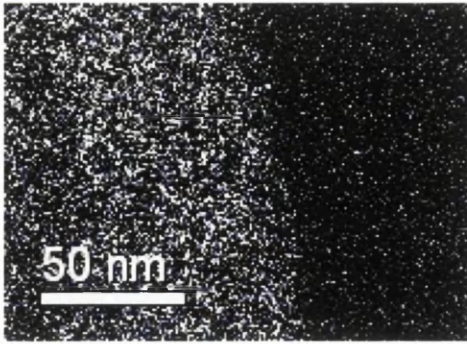


Fig. 5.15 EFTEM O elemental map with objective aperture 4.

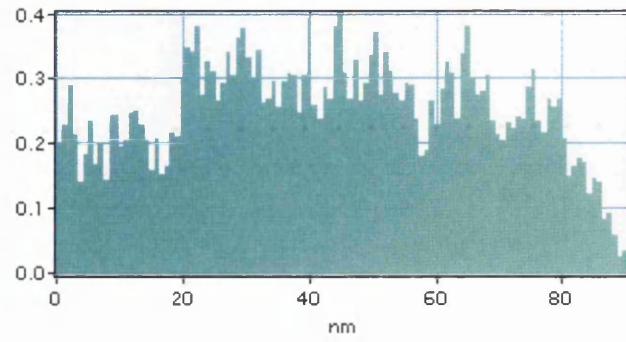


Fig. 5.16 Intensity profile of EFTEM O shown in Fig. 5.15

5.4.1.4 Comparison of Ga elemental maps at different objective apertures

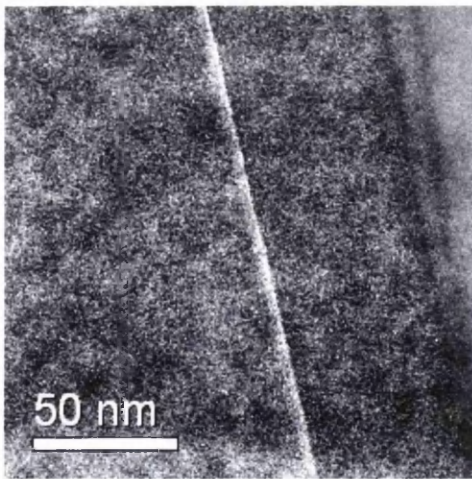


Fig. 5.17 EFTEM Ga elemental map without objective aperture.

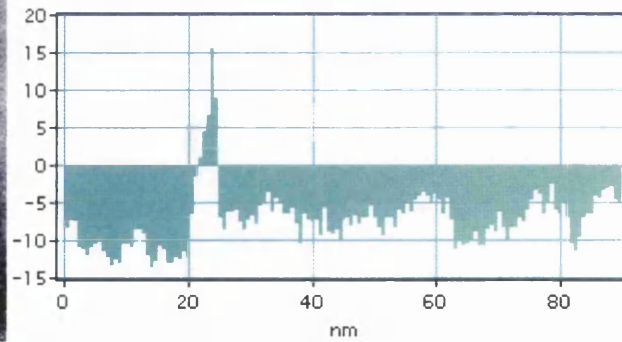


Fig. 5.18 Intensity profile of EFTEM Ga shown in Fig. 5.17

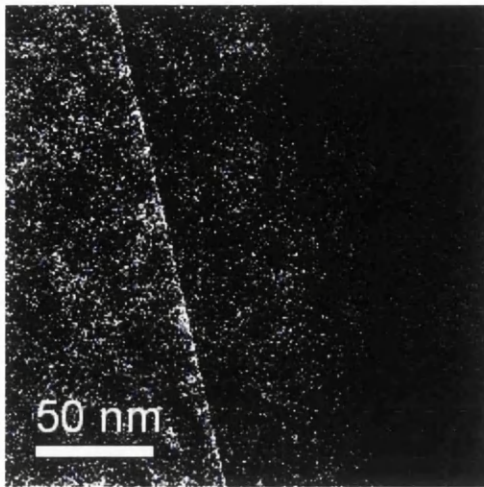


Fig. 5.19 EFTEM Ga elemental map with objective aperture 2.

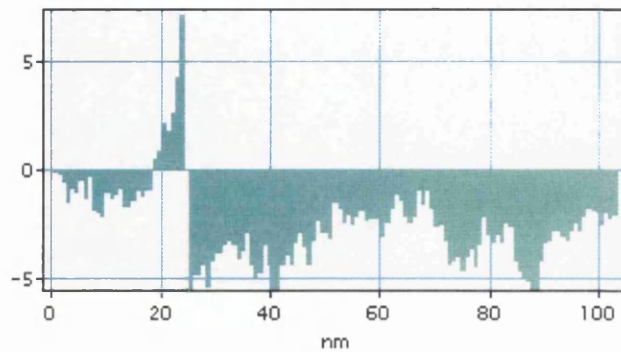


Fig. 5.20 Intensity profile of EFTEM Ga shown in Fig. 5.18

5.4.1.5 Discussion

Looking at all the Gd elemental maps shown in Figs 5.5, 5.7 and 5.9, there is not a huge difference between the one acquired without objective aperture and the one acquired after inserting the objective aperture number 2. However the number of counts drastically decreased as shown in the intensity profiles in Figs. 5.6 and 5.8 the number of counts decreases from 140 to 35. After inserting the objective aperture 2, the decrease in the number of counts is accompanied by the presence of sharper edges on the Gd elemental map which lead to an improvement in the spatial resolution. This will be better discussed later on the paragraph. There is less background contribution, the intensity profile tends to decrease sharply at the interface with the GaAs on the left hand side and at the very end of the GGO surface on the right hand side. The intensity profile decreases much more on moving away from the interface with the GaAs as a result of the variation in the Gd concentration and specimen thickness. However after inserting the objective aperture number 4 the signal clearly deteriorates and the background subtraction is not as effective as in the previous case. The number of counts is less than 1. Therefore, the signal to noise ratio will drastically decrease making the interpretation of

the data really complex. Fig. 5.21 shows a comparison of the intensity profile of all the Gd elemental maps normalized to the same maximum, acquired without and after inserting the objective aperture 2 and 4. The improvement by inserting the objective aperture 2 is clearly evident.

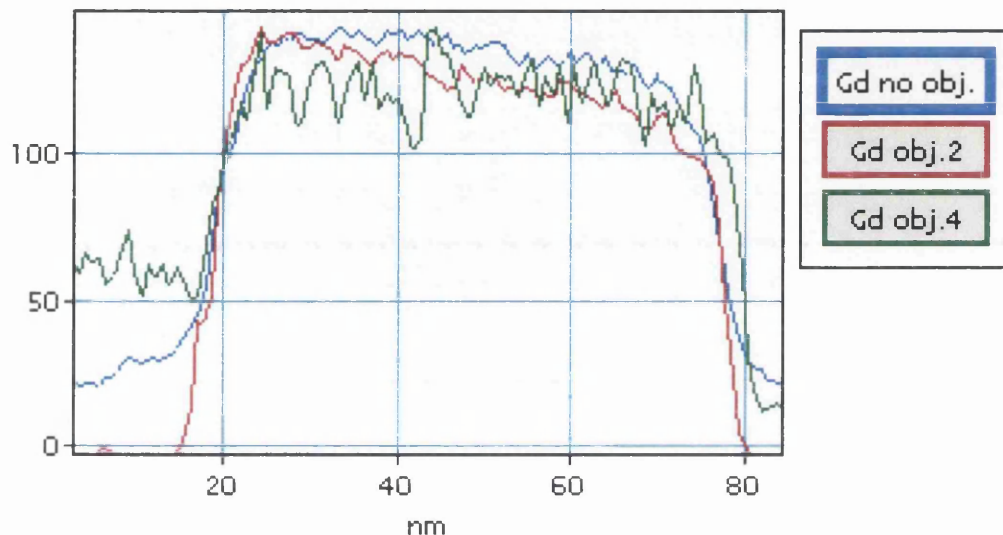


Fig. 5.21 Comparison of the intensity profile of the Gd elemental map acquired before and after inserting the objective aperture number 2 and 4.

Looking at O elemental maps shown in Figs 5.11, 5.13, 5.15, the insertion of an objective aperture clearly deteriorates the quality of data. The insertion of an objective aperture has the effect of generating noisy maps which are hard to interpret and as a result of that the background contribution is still present. The number of counts decreases from 100 without aperture to 2.5 and 0.4 when inserting aperture 2 and 4 as shown in Figs 5.12, 5.14 and 5.16 respectively. As shown in Fig 5.22 after inserting the objective aperture 4 the signal to noise ratio becomes even worse making the interpretation really complicated. As said above the O K-edge at 532eV is much less intense than Gd N_{4,5}-edges at 140eV as a result of that the signal to

noise ratio will be poorer. Hence the benefit in terms of spatial resolution of having an objective aperture is not visible here.

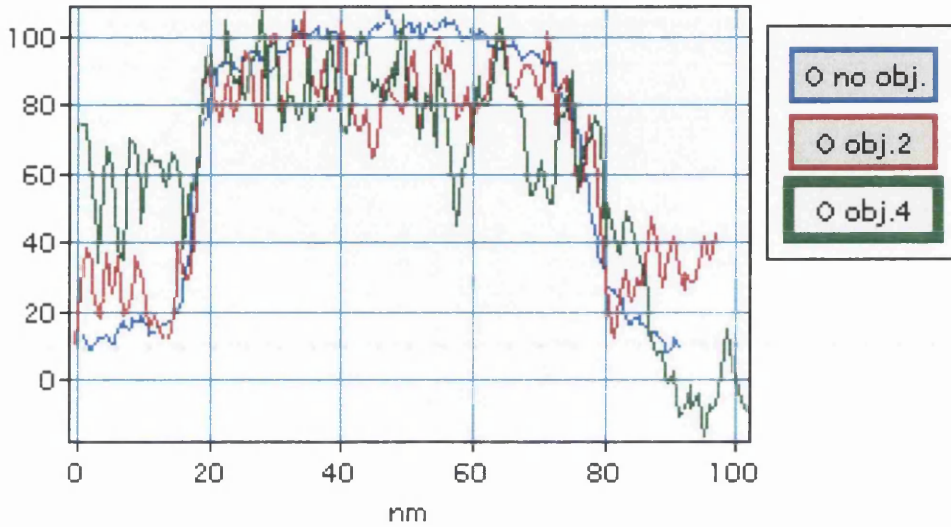


Fig. 5.22 Comparison of the intensity profile of the Gd elemental map acquired before and after inserting the objective aperture number 2 and 4.

The Ga elemental maps, in Figs. 5.17 and 5.19, both show the presence of the Ga_2O_3 template layer. The Ga is basically everywhere in the sample since both the GaAs in the substrate and the GGO layer contain Ga. The reason why the Ga_2O_3 shows up in the two elemental maps could be due to two different effects. First of all the Ga_2O_3 template layer is much lighter than the GGO and the GaAs, therefore the elastic scattering will be weaker leading to higher intensity as shown in Figs 5.2b and 5.3b. If this is the main reason, we might expect the same effect on the O elemental maps but no major intensity peaks have been detected at the Ga_2O_3 region in all the O elemental maps. Moreover, as shown in Figs 5.2b and 5.3b the difference in the intensity in the bright field images across all the areas is not sufficient big to explain the

Ga₂O₃ layer showing up in the Ga elemental map. Hence this does not represent the dominant reason. Ga M_{2,3}-edges at 103eV are relatively weak in a region of the EELS spectrum where the background is very high. Therefore it is likely that the background shape is not AE^{-r} and the subtraction procedure has failed in the GaAs and GGO region leading to the Ga to show up strongly only in the Ga₂O₃ region.

Fig. 5.23 shows a comparison of the intensity profile of all the Ga elemental maps normalized to the same maximum, acquired without and after inserting the objective aperture 2.

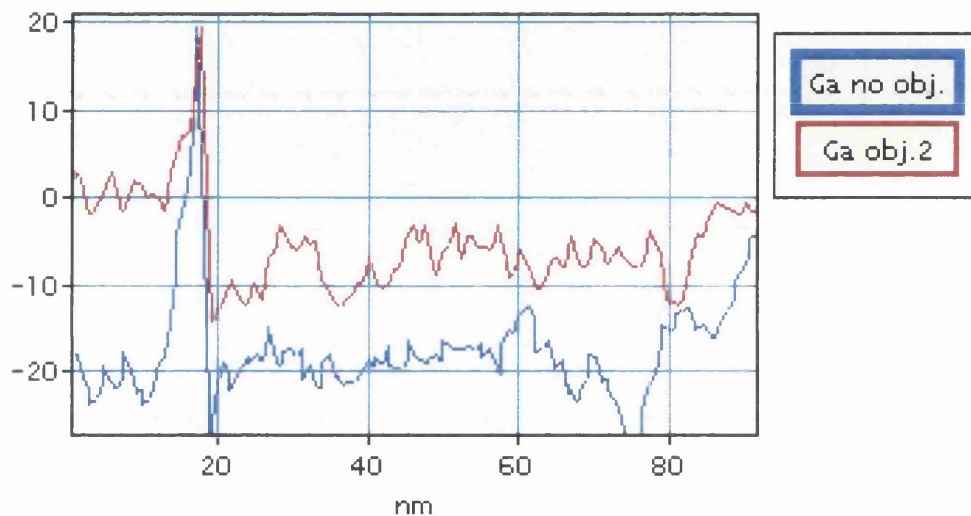


Fig. 5.23 Comparison of the intensity profile of the Ga elemental map acquired before and after inserting the objective aperture number 2.

In both cases the intensity profile across the elemental map is negative in the GaAs and GGO region as a result in the failure of the background subtraction procedure for these regions. Ga₂O₃ shows up in both cases.

As said above the spatial resolution of the elemental maps improve when inserting an objective aperture. When inserting the objective aperture 2 the profile of the Gd elemental map becomes sharper at the interface with the GaAs on the left hand side. From high-resolution EELS SI analysis of the interface GaAs/Ga₂O₃/GGO see section 6.3.1.1, the Gd edge intensity profile has a sharpness of 2-3nm. This value is related to many factors such as actual spatial resolution, probe size and most interface roughness of the interface. Looking at the intensity profiles of the Gd map acquired without objective aperture the sharpness at the interface on the left hand side seems to be roughly 8nm as shown in Fig. 5.24. When inserting the objective aperture 2 the sharpness in the same region appears to improve showing a value of 5-6nm as shown in Fig. 5.25.

It is evident that the EFTEM data acquired presented here shows a spatial resolution much poorer than the EELS SI.

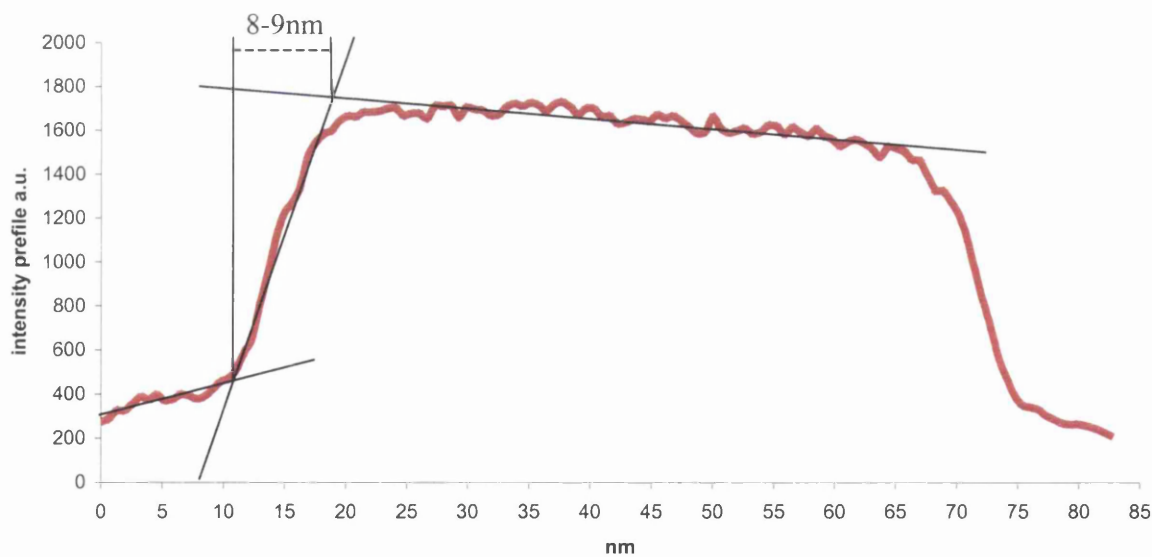


Fig. 5.24 Intensity profile of the Gd elemental map without objective aperture shown in Fig. 5.5. The distance between the line perpendicular to the x-axis, drawn from the conjunction point between the line of the profile at the left of the GGO layer and the line of the profile at the interface, is 8-9nm. This number gives a clear indication of the spatial resolution.

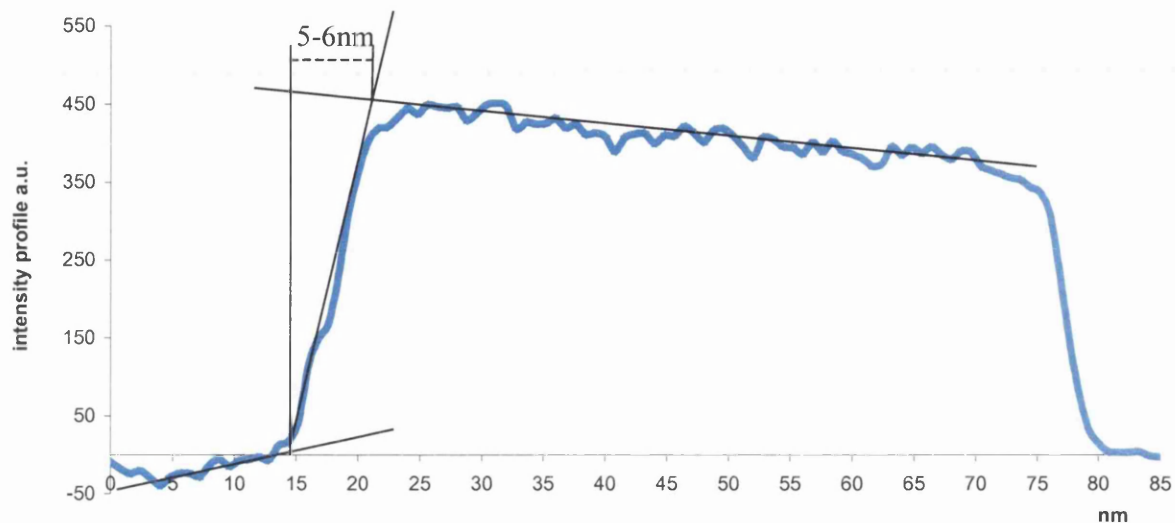


Fig. 5.25 Intensity profile of the Gd elemental map after inserting objective aperture 2 shown in Fig. 5.7. The distance between the line perpendicular to the x-axis, drawn from the conjunction point between the line of the profile at the left of the GGO layer and the line of the profile at the interface, is 6nm. This number gives a clear indication of the spatial resolution.

Concluding this section, the use of an objective aperture has a benefit only when using high intense ionisation edges such as Gd $N_{4,5}$ -edges but in the case of less intense edges such as O K-edges the presence of an objective aperture causes the acquisition of noisy elemental maps as a results of the big portion of signal cut off by the objective aperture.

5.5 III-V MOSFET DEVICES FABRICATION

All the III-V MOSFET devices investigated over the last 3 years have been fabricated using the self-alignment process (SA). Such devices are called self-aligned devices. SA techniques have been widely used in the Si industry for many years. In the case of III-V materials, some modifications of the process need to be applied as the GGO is not of good quality as the native silicon oxides. Here in Glasgow, in order to produce viable III-V MOSFET devices, a process which combines techniques from Si and III-V processing has been developed. A schematic flow of the process is described in Figs. 5.26, 5.27, 5.29, 5.30 and 5.31. The first stage consists

of the gate metallisation process where the metallic gate is deposited on top of the GGO layer, followed by conformal deposition of SiN. The horizontal planes are then anisotropically etched, leaving vertical SiN spacers on the sidewalls of the gate. The SiN spacers are then used as mask for the GGO contact etch. The ohmic metallisation is then carried out over the entire device region. At this point a thick layer of ohmic metal covers all the horizontal regions but due to the non-conformal nature of the evaporation the ohmic metal will be much thinner on the vertical surface of the SiN on the sidewalls. To remove all the ohmic metal from all these vertical surfaces an isotropic metal etch is then carried out. In this way the SA process is completed.

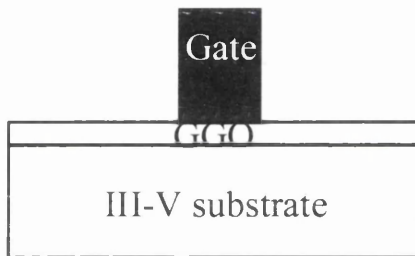


Fig. 5.26 Gate metallisation. Gate is deposited on top of the dielectric oxide layer.

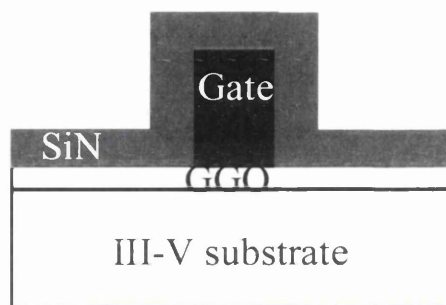


Fig. 5.27 Conformal SiN deposition

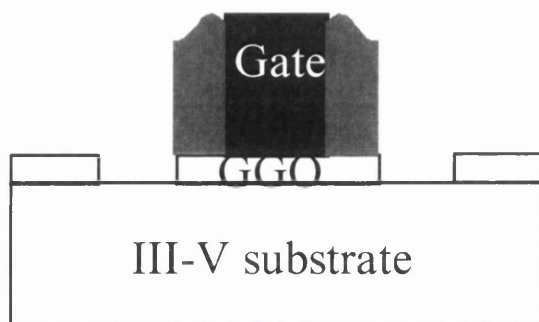


Fig. 5.29 Self aligned GGO etch

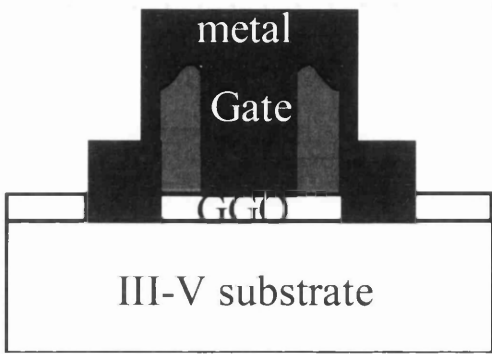


Fig. 5.30 Ohmic metal deposition.

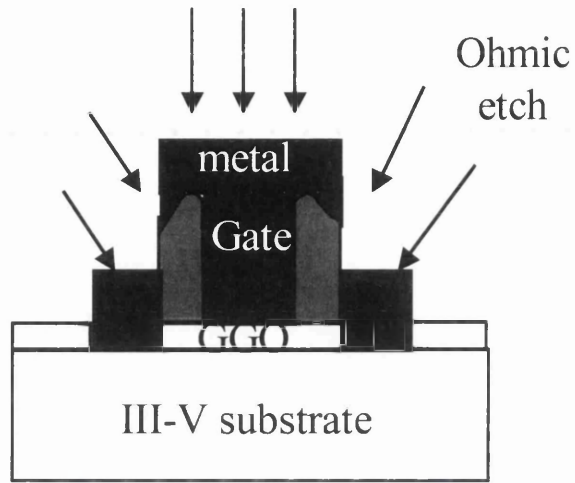


Fig. 5.31 Isotropic ohmic metal etch.

5.6 INVESTIGATION OF 3 ETCHING PROCESS CASES

5.6.1 Introduction

As shown in section 5.5, the etching process represents a key step in the fabrication of MOSFET devices. This is important to define the regions where the gate and the ohmic contacts will be placed. It is extremely important that the dielectric gate stack layer under the gate is preserved from the etching process and completely removed from all the other parts. ~80nm silicon nitride (SiN) is used as a mask for the etching process. After the etching, a further ~80nm of SiN is deposited to provide a protective cap layer for the surface during TEM specimen preparation. Fig. 5.32 shows the ideal schematic structure after the etching process.

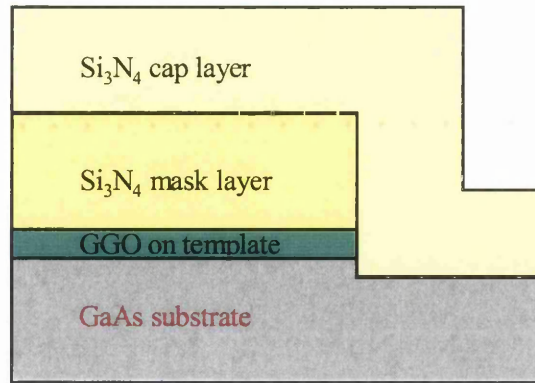


Fig. 5.32 Schematic of the ideal etched structure after capping.

Three different ion etching processes A, B and C have been investigated. For intellectual property reasons, the etching processes themselves are not detailed and the three processes labeled A, B and C.

5.6.2 Case A

Fig. 5.33 shows the bright field image of a sample which has undergone ion etching process A. The structures resulting from the etching are shown. By comparison with the ideal etched structure shown in Fig. 5.32, it seems that the GGO has not been totally etched as part of the GGO layer still extends over the sidewall and there is a redeposited layer on the sidewall resulting from the sputtering process which occurs as a result of the etching process.

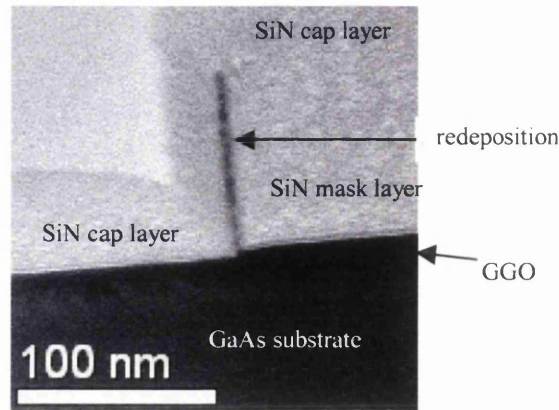


Fig. 5.33 TEM bright field image of the etched region of the sample.

In this specimen, Ga, As, Gd, O, N and Si are present. Therefore elemental maps were recorded in order to qualitatively characterize the specimen. The three windows method was used for the Si L_{2,3}-edges at 99eV, the Gd N_{4,5}-edges at 140eV, the Ga L_{2,3}-edges at 1115eV and O K-edge at 532eV respectively. The jump ratio method was used for the As L_{2,3}-edges at 1323 eV. Si L_{2,3}-edges overlap with Ga M_{2,3}-edges at 103eV. As said in section 4.1.2, the Ga M_{2,3}-edges are very weak therefore their overlapping effect with the higher intense Si L_{2,3}-edges is negligible. The Si elemental map has been recorded using an energy-selecting slit Δ of 20eV, the two background images centred at 79eV and 89eV respectively and the post-edge image centred at 109eV. In the case of the Si, only the Si L_{2,3}-edges at 99eV and the Si K-edge at 1839eV are available for mapping purposes. The Si L_{2,3}-edges have been chosen as they are at much lower energy in the EELS spectrum compared to the Si K-edge. This obviously makes the analysis much easier as the edge-signal in the first case is much higher than in the second one. An exposure time of 1.5 seconds has been employed for the acquisition of such elemental map. The Gd elemental map has been recorded using an energy-selecting slit Δ of 15eV, an acquisition time of 3 seconds, the two background images at 120eV and 130eV respectively, a post-edge image at 150eV. The Gd N_{4,5}-edge at 140eV has been chosen as it is the most intense feature for the Gd in all the EELS spectrum. The Gd M_{4,5}-edges at 1185eV are also intense features. They have not been used in EFTEM for two main reasons. The first one is that they are at high energy in the EELS spectrum leading to a generation of a weaker signal. The second

reason is the overlapping with the Ga L_{2,3}-edges at 1115eV. A separation technique developed for EELS SI and described in chapter 4 is not available here.

The Ga elemental map has been obtained using a Δ of 40eV, an acquisition time of 15 seconds, the two background images at 1043eV and 1083eV respectively and a post-edge image at 1135eV. A post-edge image at 1135eV allows us to stay far enough from the Gd M_{4,5}-edges. Fig. 5.34 shows the background contribution for the Ga elemental map obtained using these conditions and the energy-window used for the acquisition of the post-edge image.

As shown Fig. 5.34, the part of the EELS spectrum where the 40eV energy window is positioned, is not influenced by the Gd M_{4,5}-edges.

Another edge available for the Ga is the M_{2,3}-edges at 103eV. It has not been used in order to avoid any interference with the Si L_{2,3}-edges at 99eV as all the system is surrounded by SiN. The Ga M_{2,3}-edges are very weak and hard to detect compared to Si L_{2,3}-edges that are stronger and easy to detect. The acquisition of the Ga M_{2,3}-edges would determine the simultaneous generation of Si L_{2,3}-edges elemental maps.

The O elemental map has been recorded using a Δ of 30eV, an acquisition time of 6.5 seconds, the two pre-edge images at 477eV and 512eV respectively and a post-image at 547eV. Apart for the K-edge, no other edges are available for the O.

The As jump ratio image has been recorded using a Δ of 30eV, an integration time of 35 seconds a pre-edge image at 1344eV and a post-edge image at 1359eV.

Figs. 5.35, 5.36, 5.37 and 5.38 show the Gd, Si, Ga and O elemental maps respectively. Fig 5.39 shows the As jump ratio image.

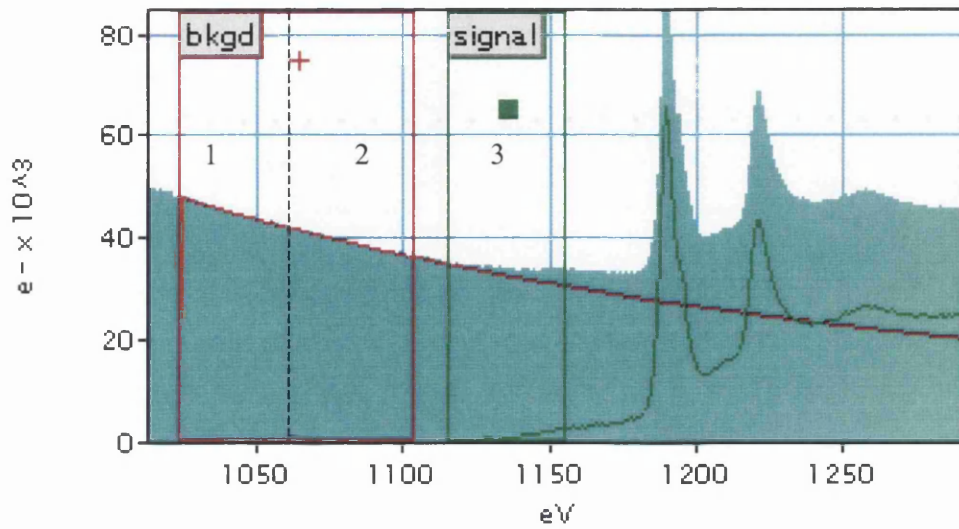


Fig. 5.34. Ga L_{2,3}-edges with the background contribution obtained using the 2 pre-edge images. The 40eV energetic window is placed with the centre at 1135eV. In this window there are the electrons filtered for the acquisition of the post-edge image.

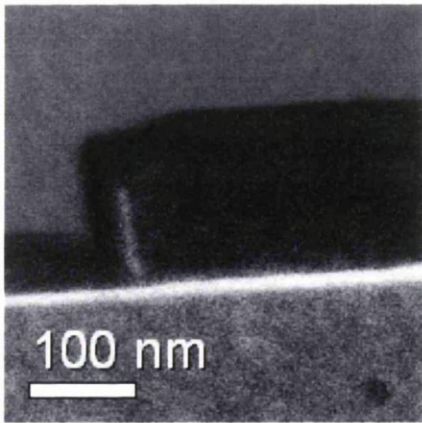


Fig. 5.35 Gd M_{4,5}-edges elemental map.

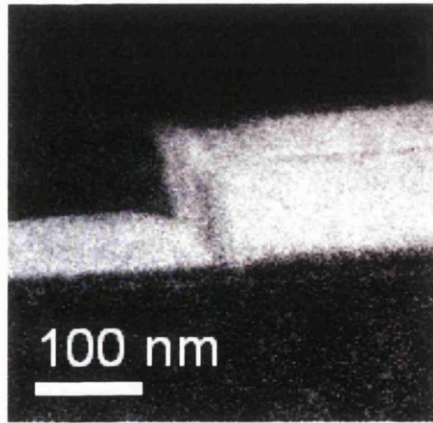


Fig. 5.36 Si L_{2,3}-edges elemental map.

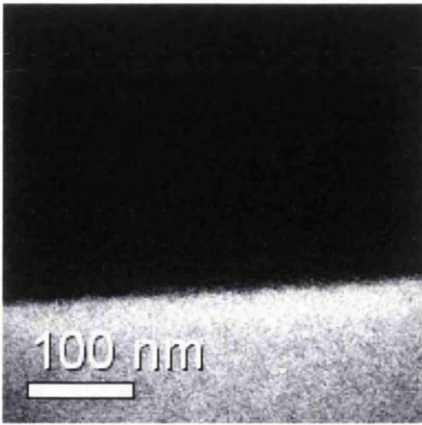


Fig. 5.37 Ga L_{2,3}-edges map.

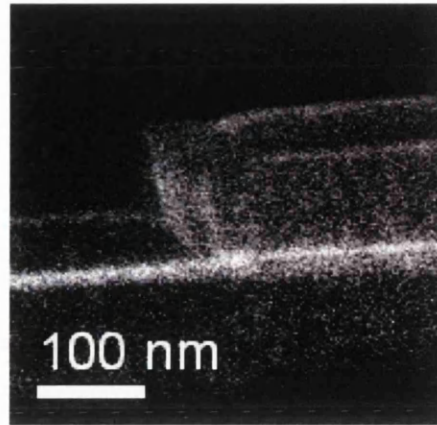


Fig. 5.38 O K-edge map.

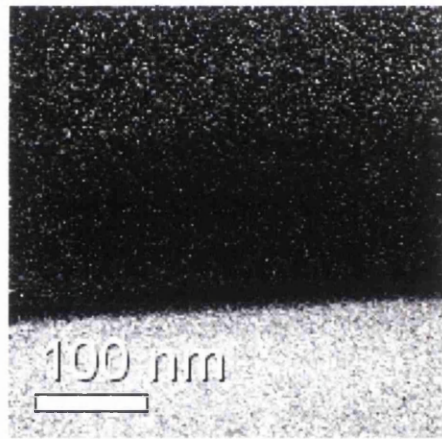


Fig. 5.39 As L₂-edge jump ratio image.

The mask and the cap layers are essentially made of SiN and the redeposited layer on the sidewall appears to be made from Gd as shown in Fig. 5.35. It could be also made of O as shown in Fig. 5.38, but in this case the interpretation of the elemental map is complicated as the Si tends to oxidize at all the interfaces. Hence what shown in Fig. 5.38 might just be SiO_x as discussed below. According to the Gd and Ga elemental maps, the GGO layer is etched only in

part as it extends all over the sidewall to the left-hand side on the GaAs substrate. The O elemental map (Fig. 5.38) shows that O decorates all the SiN interfaces. This is due to the presence of "SiO_x" which appears to form at the surfaces of the SiN. The As and the Ga are uniformly distributed in the GaAs substrate, as expected.

The etching process A seems to be very slow. There is evidence that little etching of the GGO layer occurs with the formation on the sidewall of a thin redeposited layer essentially composed of Gd and O as shown in Figs 5.35 and 5.38. The formation of such redeposited layer is due to the sputtering process used in the dry etching process.

5.6.3 Case B

Fig. 5.40a shows, a bright field image of the sample which has undergone ion etching process B. The area in the box is shown at higher magnification in Fig. 5.40b

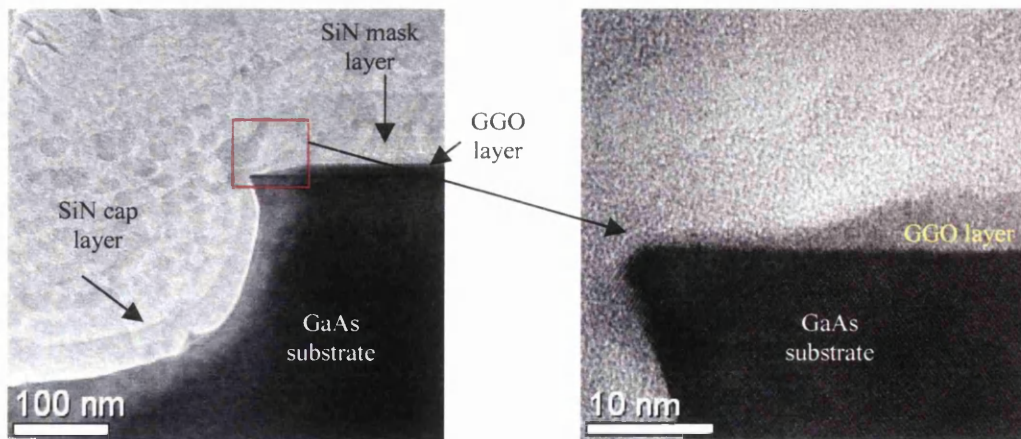


Fig. 5.40a TEM bright field of the region where there was the etching.

Fig. 5.40b High resolution TEM bright field image of the area selected in the box in Fig. 5.38a

The etching process in this case appears to be more successful than the case A. There is no evidence of the redeposited layer seen in the previous case. However the end of the GGO layer on the sidewall seems particularly damaged as shown in Fig. 5.40b. In this case the sidewall is much deeper and this clearly represents a sign of over-etching. The GaAs substrate surface to the left-hand part of the sidewall appears to be relatively rough.

In this case Gd, Si, O, Ga, As and N are present but because no particular features have been observed, only Gd, Si and O elemental map have been recorded. The three window method has been used for the acquisition of the Gd $N_{4,5}$ -edges, Si $L_{2,3}$ -edges and O K-edge respectively at 140eV, 99eV and 532eV. The Gd elemental map has been recorded using a Δ of 15eV, the two background images at 120eV and 130eV, a post image 150eV and an acquisition time of 3 seconds. The Si elemental map has been acquired using a Δ of 20eV, the two background-images at 79eV and 89eV respectively, a post-image at 109eV and acquisition time of 3 seconds. The O map has been recorded using a Δ of 30eV, the two background-images at 477eV and 512eV, a post-image at 547eV and an acquisition time of 5 seconds.

Figs 5.41, 5.42 and 5.43 show the Gd, Si and O elemental maps respectively.

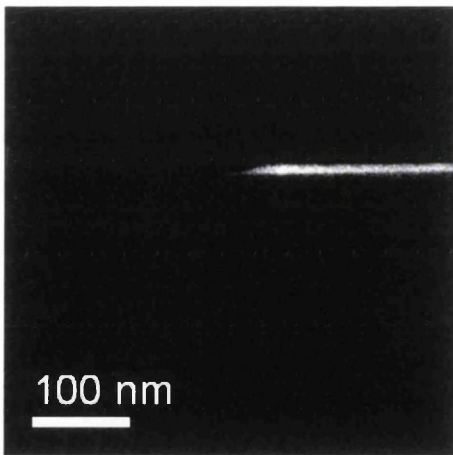


Fig. 5.41 Gd $N_{4,5}$ -edges elemental map.

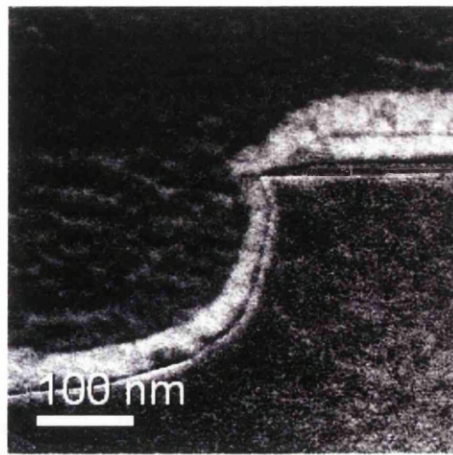


Fig. 5.42 Si $L_{2,3}$ -edges elemental map.

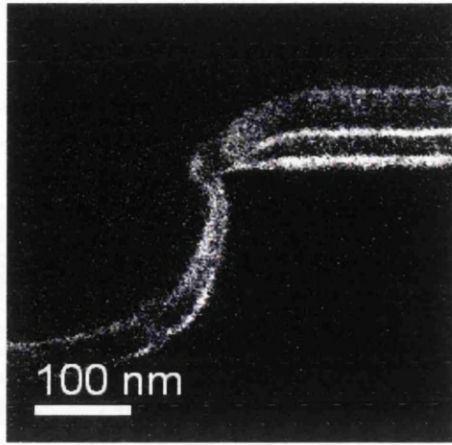


Fig. 5.43 O K-edge map.

The Gd elemental map in Fig. 5.41 shows the effects of the etching process on the GGO layer. The O elemental map (Fig. 5.43) shows that O decorates all the SiN interfaces. As in the previous case, this is due to the presence of "SiO_x" which appears to form at the surfaces of the SiN.

As far as this etching case process is concerned, it is important to say the structure has been over etched. This may be why no signs of redeposition is observed on the sidewall. The reason could be related to high rate used during the process. Hence it would be interesting to know the effects of this etching process when it is performed at a slow rate.

5.6.4 Case C

The bright field image (Fig. 5.44) shows structures resulting from the etching process C. In particular, there is an amorphous layer on the GaAs substrate and a redeposited layer on the sidewall resulting from the sputtering process which occurs during an etching process. In this specimen, Ga, As, Gd, O, N and Si are present. Therefore elemental maps were recorded in order to qualitatively characterize the specimen. The three windows method was used for the acquisition of the Si L_{2,3}-edges at 99eV, the Gd N_{4,5}-edges at 140eV, the Ga L_{2,3}-edges at 1115eV and O K-edge at 532eV elemental maps. The jump ratio method was used for the As

$L_{2,3}$ -edges at 1323 eV and to show up the difference between thresholds of the Si $L_{2,3}$ -edges in SiN (103.7eV) and in "SiO₂" (106.7eV).

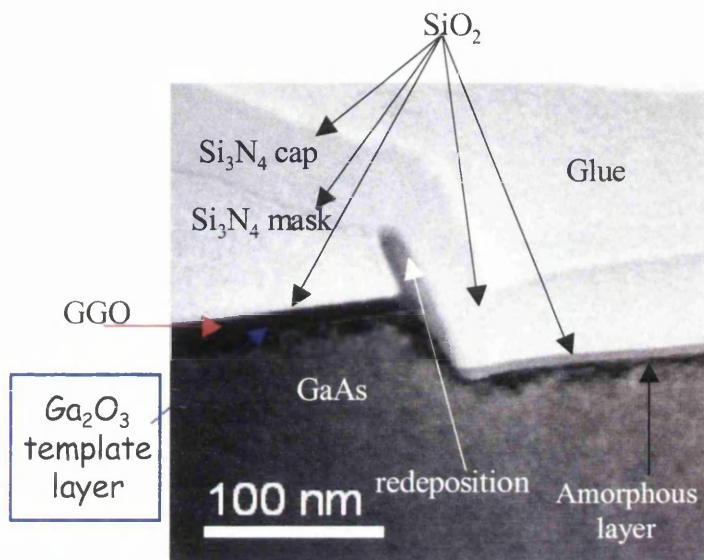


Fig. 5.44 TEM bright field image of the region where there was the etching. It shows the effects of the etching process on the structure.

The Si $L_{2,3}$ -edges map has been recorded using the Δ of 20eV, the two background images at 79eV and 89eV, the post-edge image at 109eV and an acquisition time of 2.5 seconds. The Gd $N_{4,5}$ -edges has been acquired using a Δ of 15eV, the two background images at 120eV and 130eV respectively, a post-edge image at 150eV and an acquisition time of 3.5 seconds. The Ga $L_{2,3}$ -edges map in this case has been recorded using a Δ of 40eV, the two pre-edge images at 1050eV and 1090eV respectively, a post-edge image at 1135eV and an acquisition time of 31 seconds. The O K-edge elemental map has been acquired using a Δ of 30eV, the two background images at 477eV and 512eV respectively, a post-edge image at 547eV and an acquisition time of 5 seconds. The As L_2 -edge jump ratio image has been recorded using a pre-edge image at 1340eV, a post-edge image at 1359eV, a Δ of 30eV and an acquisition time of 35 seconds. Mapping the layer of Si oxide is extremely difficult especially, when the layer is surrounded by SiN. The Si $L_{2,3}$ edge threshold is at 103.7 eV and 106.7 eV in Si₃N₄ and SiO₂

respectively. The simplest approach is to use the 2 window method, simply dividing the post-edge image for the pre-edge image. The 2 window method in this case was performed taking a pre edge image at 104 eV and post image at 108 eV. In this case the pre-edge and post-edge image include respectively the $\text{SiL}_{2,3}$ edge presents in the Si_3N_4 and in the Si oxide. An energy-selecting window Δ of 3eV has been used. The use of such small Δ has determined the acquisition of noisy images as a result of the low intense signal. However the signal to noise ratio can be improved by increasing the acquisition time, but on the other hand this could lead to an increase of the drifting which deteriorates the spatial resolution. Moreover the use of a long acquisition time at such small Δ would highlight instabilities in the spectrometer. Thus, an acquisition time of 2.5 seconds has been employed taking in account all these problems.

Figs 5.45, 5.46, 5.47 and 5.48 show the Si, Gd, Ga and O elemental maps respectively. The mask and the cap layers are essentially composed of SiN and the redeposited layer on the sidewall appears to be made from Gd, Ga and O. By comparison to the Gd elemental maps from the etching process A and C shown in Figs 5.35 and 5.46 respectively, it is interesting to note that the thickness of the redeposited layer on the sidewall is roughly the same. This suggests that the material deposited on the sidewall is re-sputtered leaving a layer of constant thickness. The Gd concentration in this layer would then be controlled by the rate at which it arrives.

It is very hard to understand from these elemental maps how the elements are distributed across the redeposited layer. The O elemental map (Fig. 5.48) shows that O decorates all the SiN interfaces. This is due to the presence of " SiO_x " which appears to form at the surfaces of the SiN. Figs. 5.49 and 5.50 show the As and " SiO_x " jump ratio maps respectively. The As is uniformly distributed in the GaAs substrate, as expected, and is also present in the modified layer on the substrate. According to these EFTEM results, this modified layer is composed of O, As and Ga. The Si jump ratio map in Fig. 5.50 tends to highlight the areas containing " SiO_x " rather than SiN but clearly creates other contrast. Nonetheless, this map indicates the oxidation of the SiN surfaces.

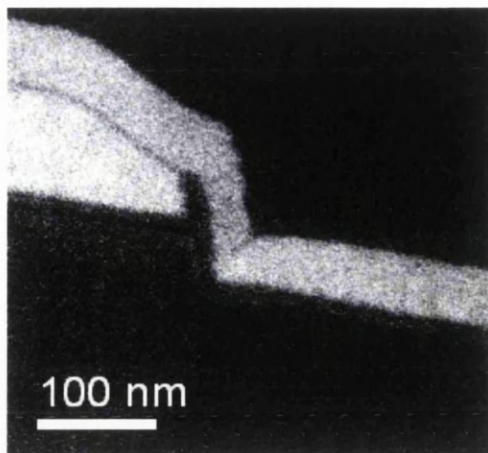


Fig. 5.45 Si L_{2,3}-edges elemental map.

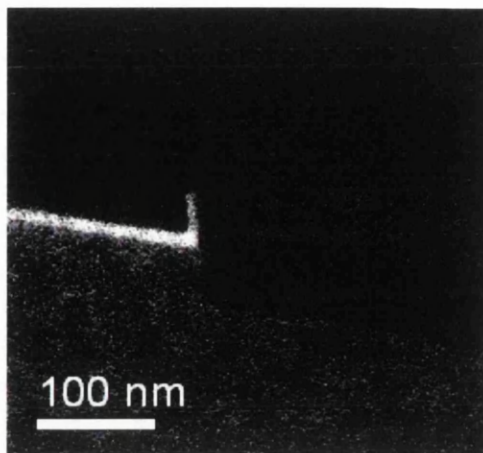


Fig. 5.46 Gd N_{4,5}-edges elemental map.

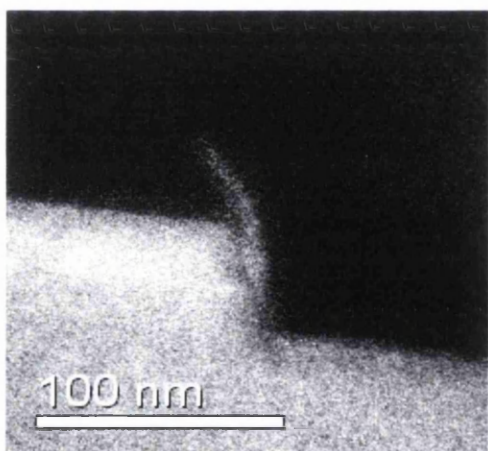


Fig. 5.47 Ga L_{2,3}-edges elemental map.

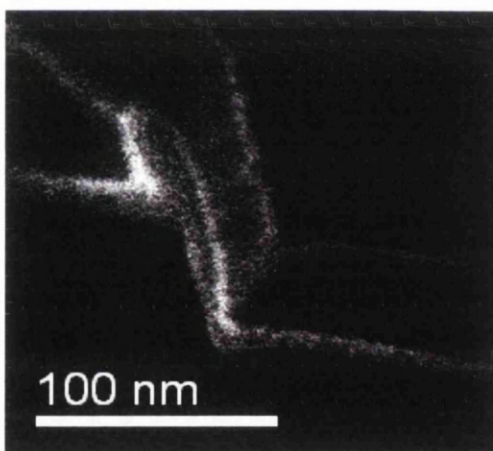


Fig. 5.48 O K-edge elemental map.

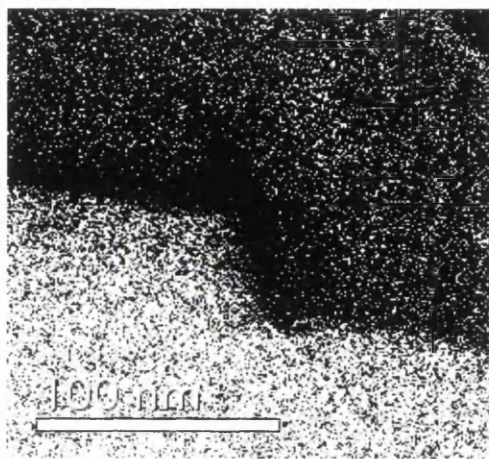


Fig. 5.49 AsL₂-edge jump ratio image.

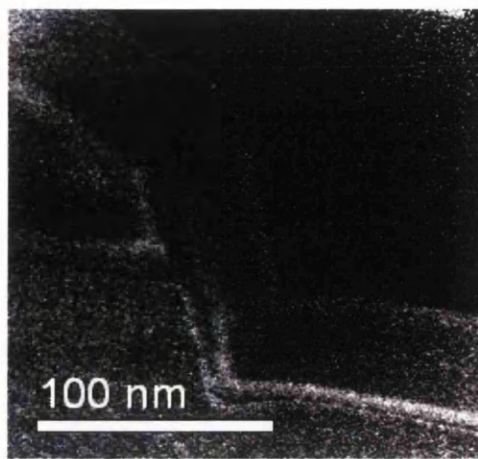


Fig. 5.50 Si L_{2,3}-edges jump ratio image. The experimental conditions used highlight the presence SiO_x

In this case EFTEM has been successful in the qualitative characterization. However, due to the low spatial resolution of this technique, it is hard to understand how the element are distributed across the redeposited layer on the sidewall and the amorphous layer on the GaAs substrate. This is the reason why this sample has been analysed using EELS SI also. As said above, EELS SI gives much more detail than EFTEM but it is more time consuming. Hence it is necessary to choose specific regions to investigate. The experimental conditions used here are the same described in chapter 4 [44].

The regions marked 1, 2, 3 and 4 on Fig. 5.51 correspond to the areas where SI were recorded. Regions 1,2,3 and 4 contain the amorphous layer on the GaAs substrate, the redeposited layer on the sidewall, the unetched GGO layer and the interface between mask and cap layer respectively.

In the analysis below, the spectra in the rows parallel to the interface have been summed.

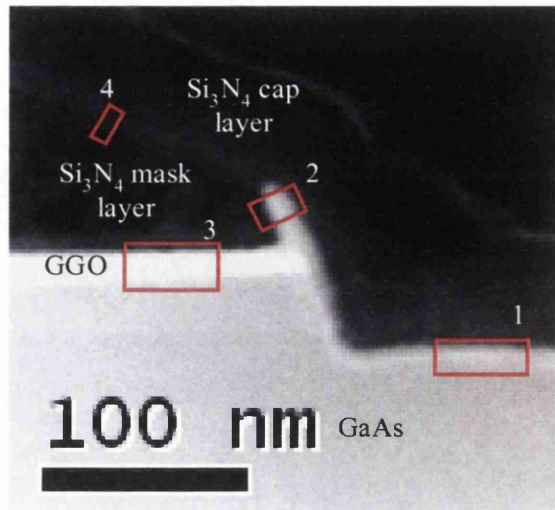


Fig. 5.51 TEM dark field image, the boxes represent the areas where the EELS SI have been acquired.

Fig. 5.52 shows the edge intensities normalised to the same maximum value across region 1 of Fig. 5.52. In this case the EELS SI analysis has been performed in sub-pixel scanning mode using the high-energy setting (480eV-1800eV), a convergence semi-angle of 9mrad, a collection semi-angle of 22mrad, a dispersion of 1eV/channel and a pixel size of 2nm. The concentration has been worked out using Gd₃Ga₅O₁₂ and GaAs standards. This part of the sample has been heavily etched as shown in Fig. 5.53. Therefore, it is expected to be modified.

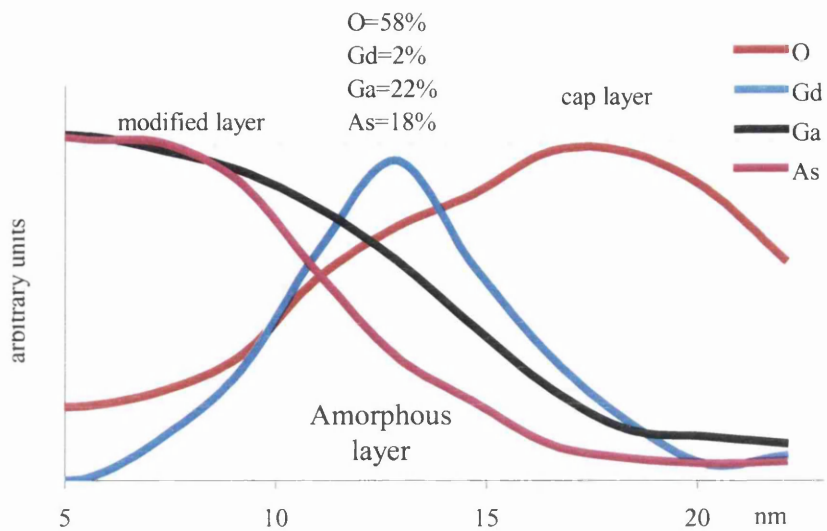


Fig. 5.52 Comparison of the profiles for Gd, O, As and Gd across the region 1 in Fig. 5.51. The atomic percent of all the elements is given for the area richest in Gd.

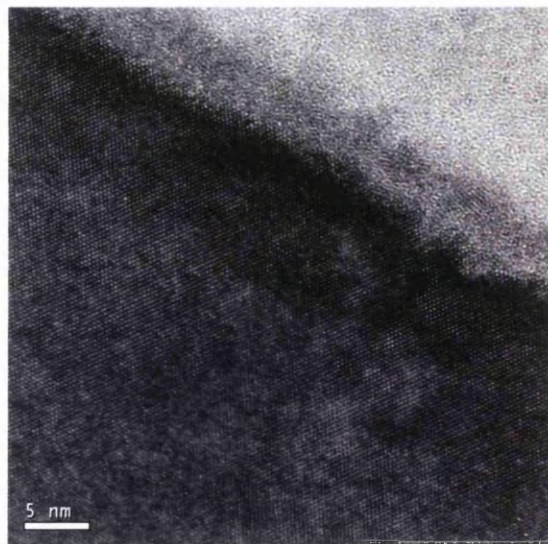


Fig. 5.53. High-resolution TEM bright field image of the amorphous layer on the GaAs substrate on the right hand side in Fig.5.51. It clearly shows the effects of the etching process on the GaAs substrate.

Here there appears to be O in the substrate but it is likely to be oxidation of the surface of the TEM sample. The O concentration rises steeply across the modified layer until it reaches the "SiO_x" at the interface with the SiN. In addition there is a low concentration of residual Gd in the modified layer not seen in the EFTEM map in Fig 5.46.

Fig. 5.54 shows the elemental edge intensities across the redeposited layer in region 2 of Fig. 5.51. The experimental conditions applied for this analysis are the same used in the previous case. They are normalised to their maximum values. The material near the SiN mask is Gd rich and comes the edge where the SiN layer is oxidised. Atomic fractions are given for the points where the Gd and the Ga intensities peak. The O appears uniformly distributed across the layer and its concentration rises towards the mask layer due to the formation of SiO_x. Here As has not been detected.

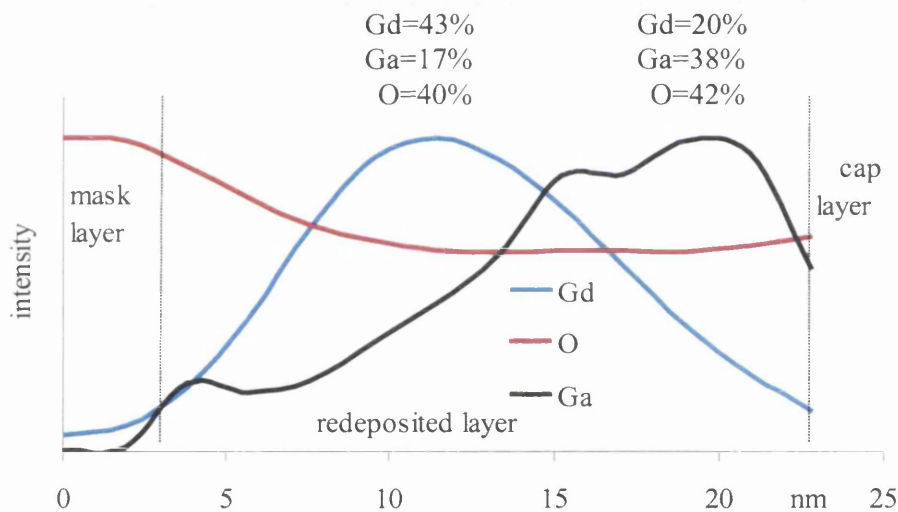


Fig. 5.54 Comparison of the profiles for Gd, O and Gd across the layer in region 2 of Fig. 5.51. This figure shows that the area is mainly composed of Gd, Ga and O. Higher O concentration is on the left side.

The unetched GGO layer in region 3 has been investigated in order to see how the elements are distributed across an unprocessed area. The experimental conditions are slightly different from the previous two investigation cases. The necessity here is to study the interface between the GGO layer and the SiN mask layer. The low-energy setting has been employed in order to

include the Si L_{2,3}-edges and the N K-edge at 99eV and 401 eV respectively. The other Si feature available in the EELS spectrum is the Si K-edge at 1839eV. Using the high-energy setting in the way described above, it is not possible to include the N K-edge and the Si K-edge in the same spectrum. For Fig. 5.55, because the separation of the thresholds is 1440eV which is greater than the maximum range possible in one spectrum i.e. 1340eV set by the minimum dispersion and the number of channels. The data has been acquired using a dispersion of 0.5eV/channel a convergence semi-angle of 9mrad and a collection semi-angle of 13mrad. Fig. 5.55 shows the intensity of Si L_{2,3}-edges, Ga M_{2,3}-edges, O K-edge, N K-edge and Gd N_{4,5}-edges across the unetched GGO layer in region 3 of Fig. 5.51.

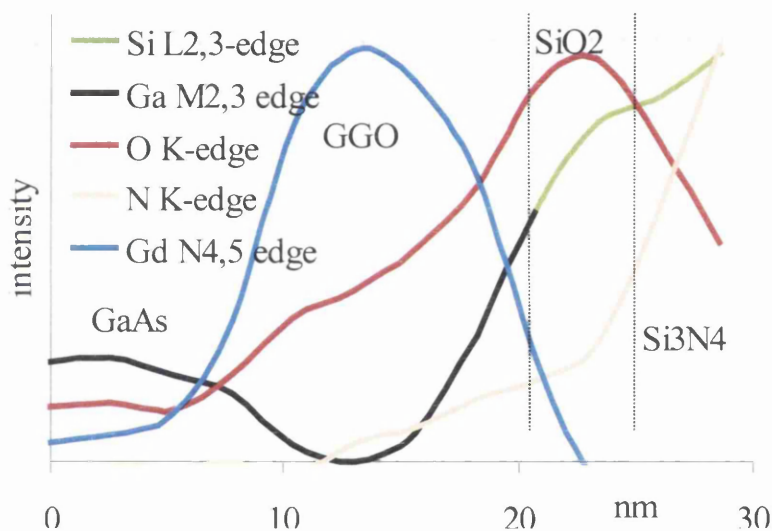


Fig. 5.55 Comparison of the profiles for Si, Gd, O and N normalised to the same maximum. There is a relatively higher concentration of O at the interface with mask layer due to the presence of “SiO_x”.

A few things have to be taken in to account when we look at the results shown in Fig. 5.55. First, the Ga M_{2,3}-edges and Si L_{2,3}-edges signals overlap as they are at 103eV and 99eV respectively. The increase of the intensity profile towards the edge of the GGO layer is due to

the presence of the Si in the mask layer. Because of the overlap, the signal in this interface region is from both Si and Ga. The Gd appears distributed only in the GGO layer as expected. However the signal does not go to 0 in the GaAs as a result of the high background contribution due to the fact that the Gd $N_{4,5}$ -edges at 140eV is used. The Gd $M_{4,5}$ -edges also overlap with the As $M_{2,3}$ -edges. The O concentration rises towards the interface between the GGO and the mask layer. This is due to the presence of the SiO_2 layer at the interface. The SiO_x layer, clearly visible at the interface between the GGO and the SiN mask layer, appears to be 5nm wide. The low loss region of the spectrum is not available and so no correction can be made for the effects of elastic scattering. Hence the O K-edge intensity in the SiO_x appears to be much higher than that in the GGO. As a result, scaling to the maximum signal intensities hides the presence of the Ga_2O_3 template layer, which shows up as the O extending to the left of the Gd, if the O and Gd are normalised to the same height in the GGO layer.

For the investigation of the interface between the mask and cap layer, the fast beam switch system (FBS) was used (section 2.7.8). This allows the acquisition of the low loss and core loss at each pixel using the same experimental conditions. The two spectra can be spliced together and an accurate energy calibration obtained for the Si $L_{2,3}$ -edges. This would allow the threshold of 103.7eV for the edges from the SiN to be distinguished from that of 106.7eV for the edges from the SiO_2 . In this case, the zero loss and the core loss data covered the energy range from -150eV to 520eV and 80eV to 750eV respectively, both with 0.5eV/channel dispersion and were acquired with a convergence semi-angle of 9mrad and collection semi-angle of 13.5mrad.

Fig. 5.56b shows the Si $L_{2,3}$ -edges across the interface between the SiN mask and the SiN cap in region 4 of Fig. 5.51. Both the threshold and shape change because of the " SiO_x " layer at this interface. However the presence of SiO_2 has not been detected as the threshold varies but does not reach the value of 106.7eV. However the peak at the top of the Si $L_{2,3}$ -edges moves systematically on crossing the interface between the mask and the cap layers.

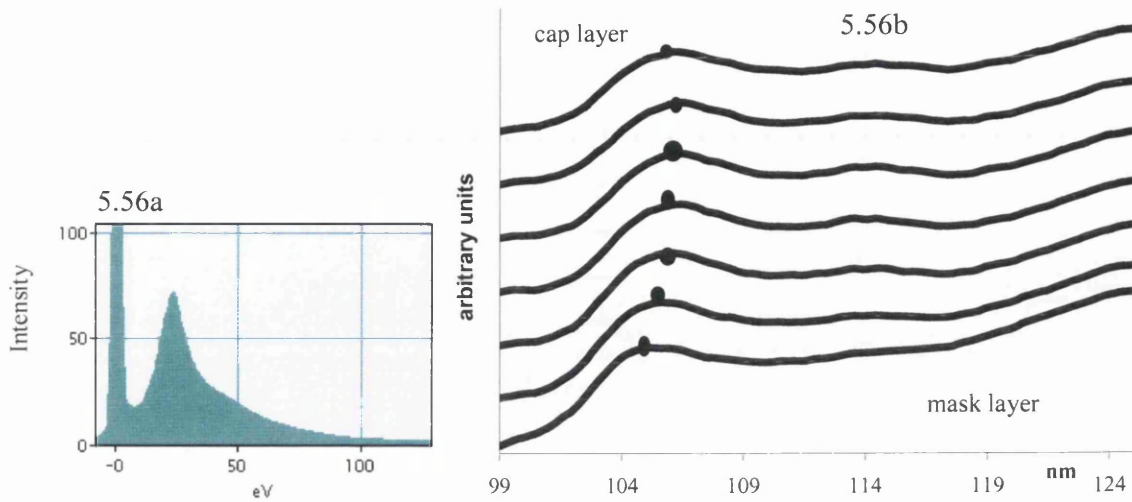


Fig. 5.56b: The $\text{SiL}_{2,3}$ -edge threshold is shifting. In Si_3N_4 it is 103.7eV while in SiO_2 is 106.7eV. The presence of the SiO_x between the mask and the cap layer determines the threshold shifting. All the core loss spectra have been simultaneously acquired with the zero loss in Fig. 5.56a, by using the dual EELS system

By combining EFTEM and EELS SI, it has been possible to characterize in details the effects of the etching process on a GaAs/Ga₂O₃/GGO dielectric gate stack. EELS SI is a powerful technique for the characterization of materials at the nanoscale. It gives both high spatial resolution and sensitivity but it is time consuming. EFTEM provides a rapid indication of the elemental distribution but with lower sensitivity and resolution than EELS SI. The analysis shows that the etching leaves an amorphous layer on the substrate and this contains approximately equal amounts of Ga and As with some residual Gd. There is also an increasing O content towards the surface. Redeposition occurs on the sidewall giving initially Gd and then Ga rich areas as first the GGO and then the substrate is etched. This layer contains oxygen throughout. All the interfaces with the SiN show oxidation to “SiO₂” and all the SiN contains some O.

5.6.5 Conclusions of the analysis of etching processes

The etching process case A has not been successful as only part of the GGO layer has been etched. The etching caused the formation of a thin redeposited layer made of Gd and O, on the sidewall.

The etching process case B seems to be the less unsuccessful among the 3 cases. There is no evidence of the redeposited layer on the sidewall and a modified layer on the GaAs substrate. However the part of the GGO layer next to the sidewall appears damaged as a result of the etching process. There is also evidence of over-etching as the sidewall appears to be much deeper than the other cases. It would be interesting to investigate the effects of this etching process when it is performed at slower rate.

The etching process case C shows the biggest number of effects due to the process. There is the evidence of the formation of a redeposited layer on the sidewall, containing Ga, Gd and O. The surface of the GaAs substrate is modified leading to the formation of an amorphous layer made of Ga, As, O and traces of Gd.

In all the three cases an increase of the O concentration oxidation towards the interface with the SiN has been observed. This is due to the formation of a SiO_x layer.

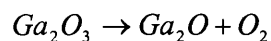
CHAPTER 6: INVESTIGATION OF THE GaAs/Ga₂O₃/GGO INTERFACE REGION

6.1 THE GaAs/Ga₂O₃/GGO INTERFACE

As said in chapter 1, the dielectric oxide layer plays a crucial role for the success of III-V MOSFET's technology. It is well known that the Fermi level of GaAs is pinned at the oxide substrate interface by a very high density of interface states. Until that is overcome, it is not possible to produce a viable III-V MOSFET system. No carrier modulation is obtained when a bias voltage is applied to a gate electrode. To make a GaAs based MOSFET system, it is necessary to fully passivate the GaAs surface obtaining an unpinned interface by eliminating interfacial defects.

The evaporation of O₂ onto a GaAs surface leads to the formation of a pinned Fermi Level at the interface. The O₂ initially displaces surface As atoms and then bonds to the Ga atoms in the second layer. When two O atoms are bonded to a central Ga atom, they withdraw charge from the Ga atom determining the state formation within the gap. The presence of this central atom between two O atoms is the cause of the Fermi level pinning by oxidation.

On the other hand, when Ga₂O is absorbed onto the GaAs surface, it appears to insert into As dimer pairs. Once it has been fully absorbed, a surface reconstruction occurs leaving the surface with (2X2) periodicity. This new surface appears to passivate the surface and change the charge on the initial As surface atoms towards more bulk-like value. The new Ga atoms in the chemisorbed Ga₂O layer as well as the second layer Ga atoms in the substrate have no states in the band gap. Ga₂O molecules are obtained from evaporation of Ga₂O₃ under this reaction:



Hale et al. [8] have revealed that after depositing Ga₂O for a few minutes, some regions of the surface contains a saturated monolayer coverage of Ga₂O. Ga₂O molecules are inserted into As dimers pairs as shown in Fig. 6.1.

With a full monolayer coverage the distance between two As dimers, when the Ga₂O is inserted, is 8Å. If the coverage occurs at a sub-monolayer level, the Ga₂O molecules insert in or between As dimers forming shallow, wide depression. If the surface is not completely saturated with Ga₂O, it is possible to have some disordered regions containing a second amorphous layer of Ga₂O. Although the sticking probability of Ga₂O with respect to the O decreases after the

first monolayer, the high flux of Ga₂O from the effusion cell causes the formation of a random second Ga₂O₃ amorphous layer.

The Ga₂O₃ template layer is composed of a first crystalline monolayer with the Ga₂O molecules inserted into As dimers pairs. Further deposition results in the formation of a stoichiometric amorphous Ga₂O₃ phase.

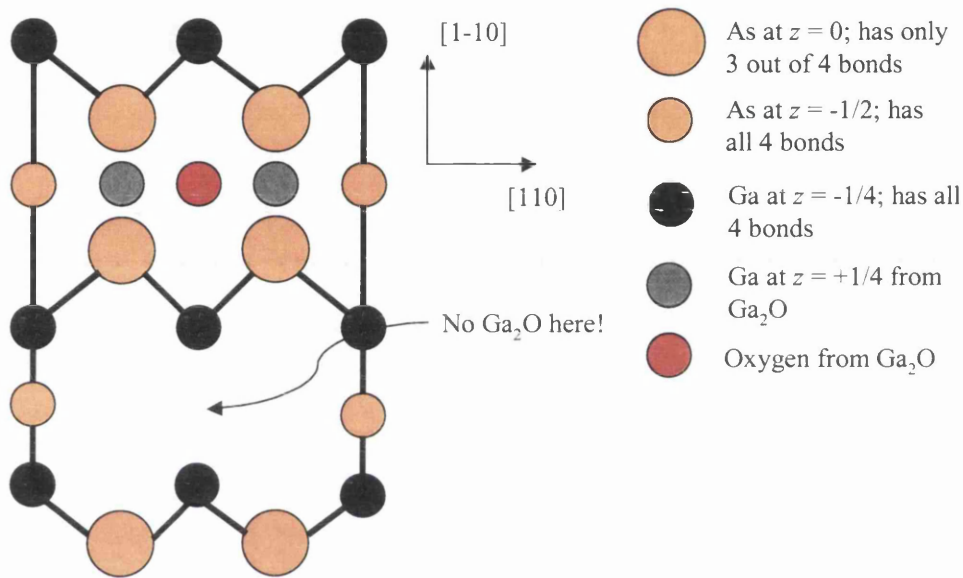


Fig. 6.1 Ball and stick model for an ideal 2x2 surface order of a monolayer coverage of Ga₂O as described by M.J. Hale et al. Journal of Chemical Physics 119, 6719, 2003.

As shown in Fig. 6.1 the interface appears to be different depending on the direction the interface is looked at. In particular, Figs 6.2a and 6.2b show the projection of ball and stick model shown in Fig. 6.1 along the $[110]$ and $[1-10]$ respectively. As shown in Fig. 6.2a $[110]$ projection consists Ga-terminated incomplete dumbbell while $[1-10]$ consists of Ga-terminated, complete dumbbell atoms. The Ga column from Ga₂O however, has only half occupancy and should have lower intensity in HAADF image.

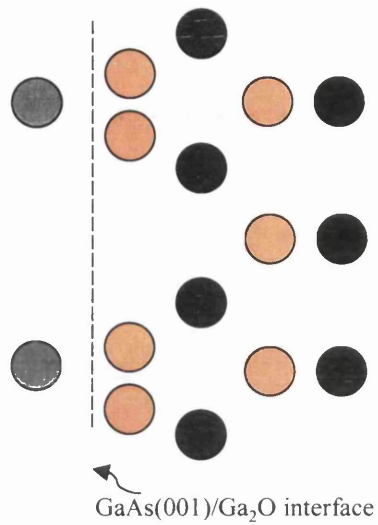


Fig. 6.2a [110] projection of the surface structure shown in Fig 6.1.

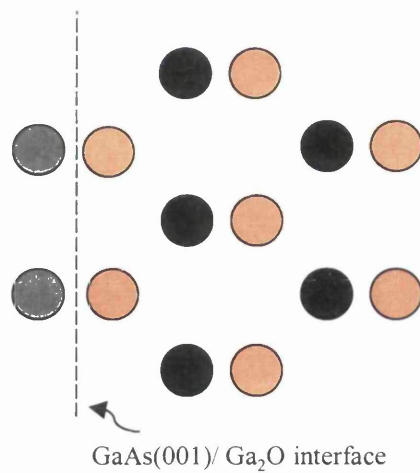


Fig. 6.2b [1-10] projection of the surface structure shown in Fig 6.1.

The aim of this chapter is to investigate the interface GaAs/Ga₂O₃/GGO. The currently accepted description is based on the above model where the monolayer is crystalline and composed of Ga₂O molecules inserted into As dimers pairs. The rest of the template layer is

composed of stoichiometric amorphous Ga_2O_3 . As said above the interface appears to be different under the two different orientations $[110]$ and $[1-10]$. To verify this, ideally the original should be cut off in the two perpendicular directions as shown in Fig. 6.3. The two pieces can be then glued together. In this way it is possible to examine the sample along the two perpendicular directions.

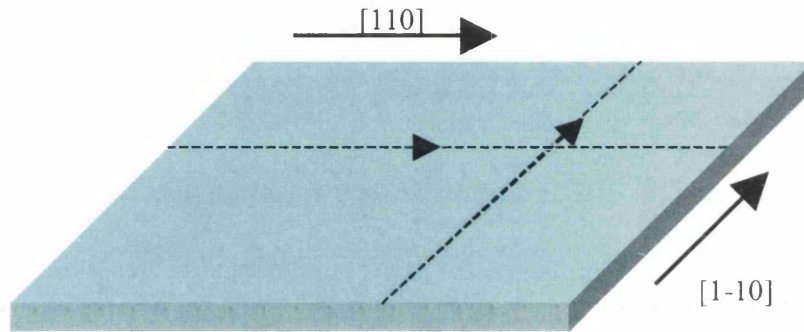


Fig. 6.3 Original wafer cut under the two perpendicular directions. The two arrows indicate the cutting direction.

Here the interface region has been extensively studied using HAADF images in STEM mode. The investigation was carried out in both Tecnai F20 and SuperSTEM1. Some samples have been prepared with the two sides of the cross-sections orientated under the two perpendicular directions. All the images acquired with the SuperSTEM1 were collected along with Dr B. Mendis.

HAADF STEM imaging is a useful tool for characterizing the interfaces between materials with different elemental composition, as the contrast is sensitive to the atomic weight. In particular, technique has been used for studying the interface $\text{GaAs}/\text{Ga}_2\text{O}_3/\text{GGO}$. As said in chapter 3 and 4 the $\text{GaAs}/\text{Ga}_2\text{O}_3/\text{GGO}$ dielectric oxide layer is electron beam sensitive. Hence EELS SI cannot be used for those applications that require longer exposure to the electron beam.

When a HAADF STEM is acquired, the electron dose is spread within the area where the beam is scanned, hence it is less likely to damage the sample.

In this chapter some high-resolution HAADF STEM images are shown. The aim of this type of investigation is to gain a better understanding of the chemistry involved at the interfaces in the channel region and with the dielectric oxide layers.

A good understanding of the chemistry involved at the interfaces in the channel region and between the dielectric oxide layer and the III-V substrate certainly is important for the realisation of high performance MOSFET devices.

A brief description of the HAADF STEM imaging is also given in order to understand better the motivation behind this work and the results presented here in this chapter. All the images presented here were acquired mainly using the Tecnai F20. However some samples have been investigated also with the SuperSTEM1 that is an aberration corrected dedicated STEM. A brief description of main features of the SuperSTEM1 and the method employed to correct the aberration have been given in chapter 2.

6.2 HAADF STEM Imaging

The physical size and the position of the detector in a STEM have a great influence on the acquired image signal and, hence, on the information that can be obtained from a particular specimen. In recent years, high angle annular dark field (HAADF) detectors have become widely used in STEMs. Moreover, most of the results that are presented in this section were obtained from the use of such a detector.

It is known, that the large inner angle of the HAADF detector ($>50\text{mrad}$) excludes most of the coherent elastic diffraction from the specimen [45]. It has also been widely reported that the imaging technique that is associated with the HAADF detector can provide atomic resolution structure images that are, in general, easier to interpret than conventional HR-CTEM images [46]. This is due to the fact that no contrast reversals are observed in HAADF images over a wide range of spatial frequencies. This enables the optimum focus to be established by simply adjusting the focus to obtain the sharpest image possible.

In addition, HAADF images are commonly referred to as atomic number (Z) contrast images since (at high angles) the scattered intensity varies approximately with Z^2 due to Rutherford like scattering. The exact variation with Z depends upon the acceleration voltage, detector angles and the orientation and nature of the atomic columns of the specimen. Furthermore, the

scattered intensity (at high angles) is termed thermal diffuse scattering (TDS) because it is generated by single atoms that are uncorrelated with each other due to the presence of thermal lattice vibrations within the specimen. Hence, the TDS tends to blur out the diffraction pattern at high angles.

As stated above, the HAADF contrast transfer function has no reversal of sign. This is because HAADF imaging is essentially an incoherent imaging technique. There are several reasons for the incoherent nature of this imaging process. First of all, the reciprocity theorem demonstrates that a large STEM detector is equivalent to a large incoherent source in CTEM [13]. Therefore, the large angles of the HAADF detection ensure incoherent imaging. A second reason behind the incoherent nature of HAADF imaging centres on the fact that it is primarily TDS that falls upon the detector. In addition, it has also been shown that for electron probe sizes that are smaller than the distances between the atomic columns in a specimen and for large HAADF detector angles, transverse interference effects between neighbouring columns are minimised [47]. Therefore, as an approximation, the intensity that falls on the HAADF detector ($I(\underline{r}, \underline{r}_p)$) can be described as a convolution of the intensity in the incident probe ($|\psi_p(\underline{r}, \underline{r}_p)|^2$) with the specimen object function ($V(\underline{r}, \underline{r}_p)$) [48]. $V(\underline{r}, \underline{r}_p)$ is, approximately, the probability for scattering out to the large angles of the HAADF detector and is related to the projected atomic specimen potential. Furthermore, the specimen object function is strongly peaked at atom sites and the spatial resolution is limited only by the probe characteristics [49].

The way in which HAADF signals are affected by the nature of atomic columns is still not fully understood. For instance, longitudinal coherence along the vertical direction of atomic columns may exist [47]. However, it is believed that phonons in the specimen are sufficient to destroy any longitudinal coherence effects. Nevertheless, it is evident that the complicated scattering of the electron probe within the specimen has a direct influence on the character of HAADF images. This scattering is (in general) dependent upon the structure, composition and thickness of the material. Furthermore, several studies have also considered the effect of probe channelling down atomic columns [50]. This effect is due to the presence of strong potentials that are generated by the atomic nuclei along the columns. For instance, the strong potentials attract the imaging electrons and force them to propagate close to the columns. However, after a certain depth of crystal, most of the electrons will have been scattered away from a particular column.

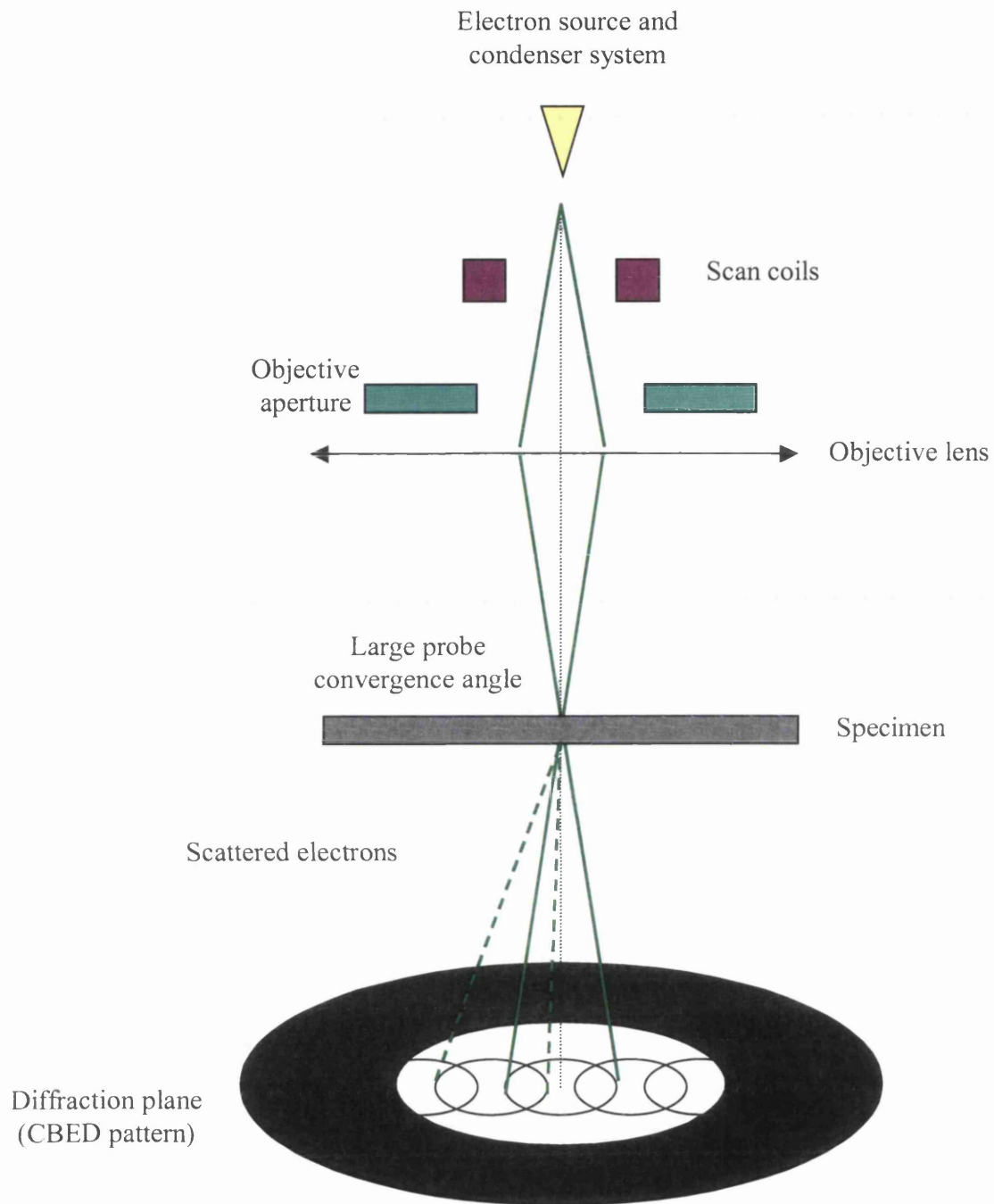


Fig. 6.4 Simple schematic of the imaging process in a scanning transmission electron microscope.

6.2.1 Channelling of the HAADF STEM signal

As said above the channelling effect of the electrons along the column of atoms in a crystal structure is strictly related to the specimen thickness. The specimen thickness is important parameter to take into account when acquiring HAADF STEM images. To understand the effects of the thickness on the HAADF STEM signal intensity, some modelling investigations need to be done. E J Kirkland's computer modelling software was used to carry out the modelling work [65]. This computer program allows the behaviour of an electron microscope to be simulated. A detailed description of E J Kirkland's program is given in Paul Robb's thesis. As far as the work of thesis is concerned, simulations have been carried out for the GaAs using the experimental parameters employed in the F20 and in the SuperSTEM1. In the case of the F20, simulations were carried out by Michael Finnie and in the case of SuperSTEM1 the results were taken from Paul Robb's thesis.

6.2.1.1 SuperSTEM1 case

Fig. 6.5 reveals the value of the intensity that exists on the primary As column and neighbouring Ga column as a function of the specimen thickness. The sum of the six nearest neighbouring dumbbells (6NNs) is also displayed. The value measured at each depth for each column is the sum of the intensity contained within an area 9pixels x 9pixels centred on the respective column position.

As shown in Fig. 6.5, the peak intensity on the primary As column is at a depth of 4nm. The electrons attracted by the strong potential of the As are said to have undergone channelling. Another peak is present at 12nm but it is far less intense than the one at 4nm. The intensity remains very low after a depth of 20nm. After a depth of 20nm basically there is not much intensity left on the As column up to 60nm where it finally drops close to zero. Hence there is channelling up to 20-60nm in the top portion of the crystal. However the strong channelling conditions last up to 20nm after that the background contribution becomes stronger.

The HAADF STEM intensity was also simulated. This type of simulation allows the investigation of the channelling and spreading of the electron intensity effects on the final image from the microscope. Fig. 6.6 shows the simulated HAADF signal for the probe incident on an As column in GaAs crystal structure as function of the specimen thickness. The total HAADF As signal in Fig. 6.6 rises steeply for low crystal depths before increasing linearly for

larger depths. However, in order to measure the actual HAADF signal generated by the As column, the background contribution has to be subtracted. This is shown in Fig. 6.6.

Equivalent behaviour is also observed when the probe is incident on the Ga column. Once again strong channelling condition is observed for the top portion of the crystal structure. However in this case the strong channelling condition persists for a slightly greater depth (24nm). This is due to the fact that Ga is slightly lighter than As, therefore the electrons will be scattered less.

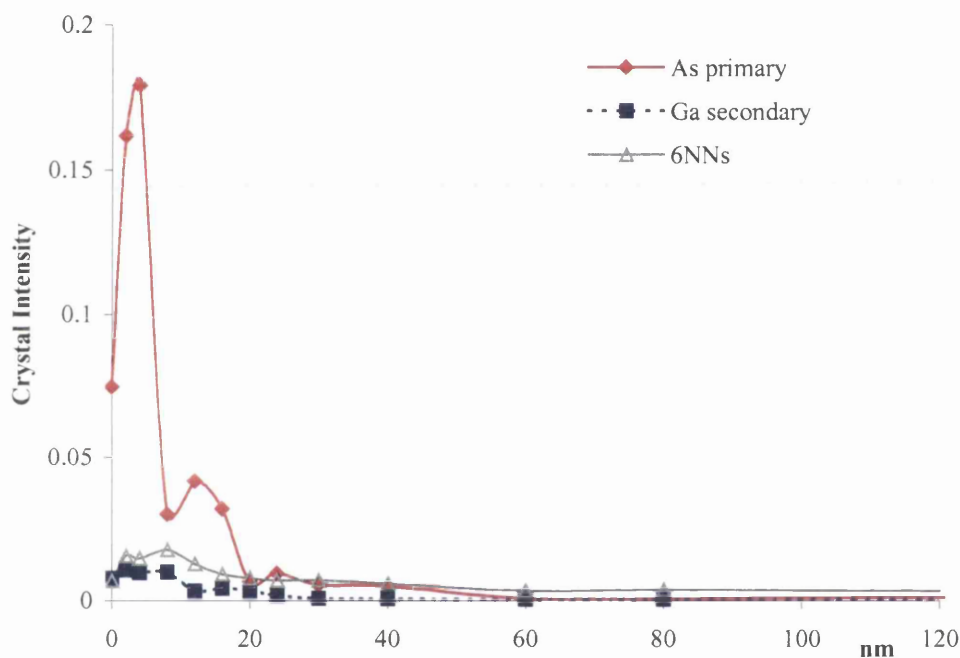


Fig. 6.5 Simulated real space electron intensity along two columns in GaAs [110] as a function of the specimen thickness. The probe is incident on the as column on the top of the surface of the specimen. The intensity of the neighbouring Ga column and the sum of the nearest 6 dumbbells are plotted. The intensity is normalized with respect to the total intensity in the probe. The simulation has been performed using the experimental conditions employed in the SuperSTEM1

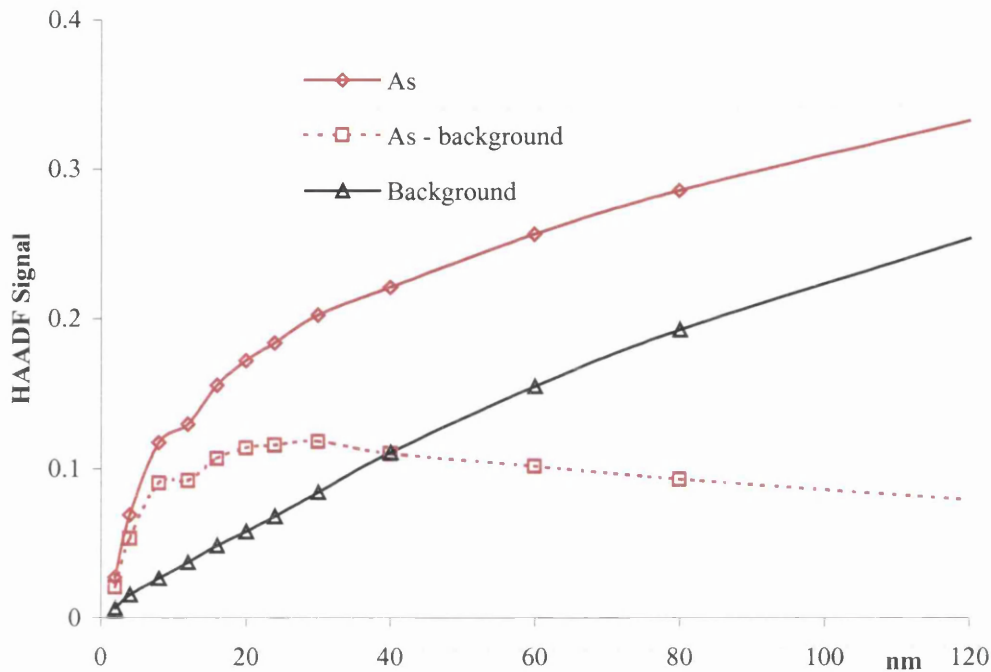


Fig. 6.6 Simulated HAADF STEM intensity for GaAs [110] as a function of the specimen thickness. The probe is incident on the As column. The background signal between the dumbbells is also plotted. The signal is normalised with respect to the intensity that the probe generates in the detector plane in absence of specimen. The simulation has been performed using the experimental conditions employed in the SuperSTEM1.

6.2.1.2 Tecnai F20 case

Few things need to be taken into account before presenting the results obtained using the same experimental parameters employed in the F20. The SuperSTEM1 and the F20 are two different microscopes hence the results might be slightly different. As far as the modelling work is concerned the major differences between the two microscopes are the accelerating voltage which is 200kV and 100kV for the F20 and the SuperSTEM1 respectively, the convergence semi-angle which is larger in the SuperSTEM1 (24mrad) as the spherical aberration coefficient (C_3) is corrected, and the C_3 factor which is different since the SuperSTEM1 is aberration corrected.

Fig. 6.7 shows the value of the intensity that exists on the primary As column and neighbouring Ga column as a function of the specimen thickness in the F20. The sum of the six nearest neighbouring dumbbells (6NNs) is also displayed. As in the previous case the peak intensity on the As column is at a depth of 4nm. However there are two major peaks, one at 20nm and the other one 30nm. After a depth of 40nm, practically no intensity remains on the As column until the intensity finally drops close to zero at a depth of 80nm. However, it is clear that the strong channelling condition only lasts up to 30nm. As a result of the higher accelerating voltage in the F20, the strong channelling condition lasts further than in the SuperSTEM1 (20nm). Fig. 6.8 shows the simulated HAADF signal for the probe incident on an As column in GaAs crystal structure as function of the specimen thickness.

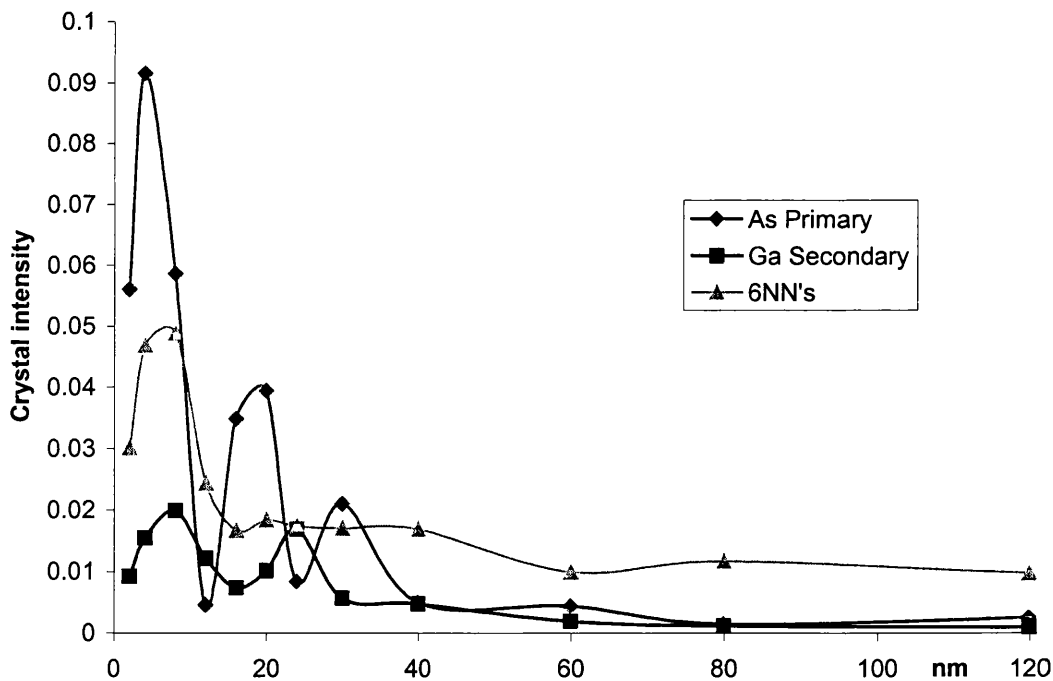


Fig. 6.7. Simulated real space electron intensity along two columns in GaAs [110] as a function of the specimen thickness. The probe is incident on the As column on the top of the surface of the specimen. The intensity of the neighbouring Ga column and the sum of the nearest 6 dumbbells are plotted. The intensity is normalized with respect to the total intensity in the probe. The simulation has been performed using the experimental conditions employed in the F20.

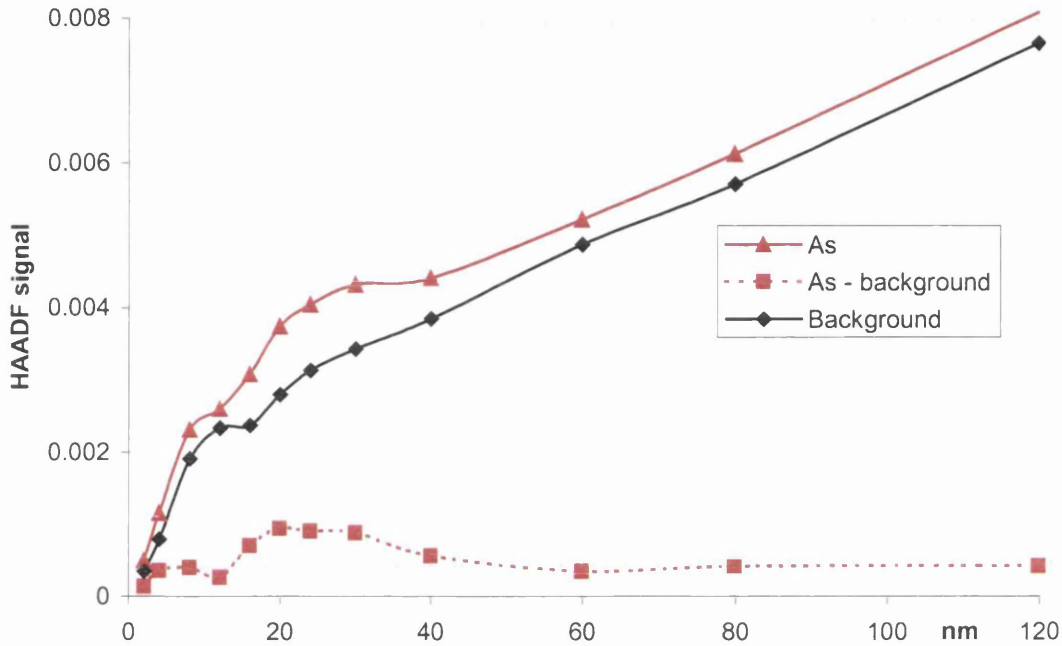


Fig. 6.8 Simulated HAADF STEM intensity for GaAs [110] as a function of the specimen thickness. The probe is incident on the As column. The background signal between the dumbbells is also plotted. The signal is normalised with respect to the intensity that the probe generates in the detector plane in absence of specimen. The simulation has been performed using the experimental conditions employed in the F20.

6.3 EXPERIMENTAL RESULTS OF THE GaAs/Ga₂O₃/ GGO INTERFACE REGION

6.3.1 Investigation of the interface GaAs/Ga₂O₃

In this section some HAADF STEM images of the interface GaAs/Ga₂O₃ are shown. For the purpose of this experiment, a 30nm amorphous Ga₂O₃ has been grown onto the GaAs substrate. The recipe used for the growth of such wide oxide layer is the same employed for the preparation of the thin template layer [9]. The composition of this oxide layer is the same as one of the thin template layer in the standard dielectric gate stack GaAs/Ga₂O₃/GGO.

By comparing the high-resolution STEM images taken from this sample at the interface GaAs/Ga₂O₃ with the ones taken from the same interface but in a full dielectric gate stack with the GGO layer deposited on top of the Ga₂O₃ template, it is possible to obtain a better understanding about the effects of the Gd at the interface GaAs/Ga₂O₃/GGO.

Fig. 6.9a shows a high-resolution HAADF STEM image of the interface GaAs/Ga₂O₃ in a sample where only a wide amorphous Ga₂O₃ layer has been deposited onto the GaAs. This image was acquired using the F20. The interface appears to be quite smooth. The dumbbell rows tend to assume a zig-zag structure with one going deeper than the other one. Taking a profile line across this image, it is possible to measure the intensity of each dumbbell. Looking at Fig. 6.9b, each dumbbell presents the same intensity above the background except for the one closest to the oxide template layer in the red line trace line that appears to be slightly less intense. It also appears to be slightly asymmetric. However, the background level of the intensity tends to decrease as the interface is approached as a result of the variation of thickness. Therefore, the presence of this dumbbell slightly less intense could be due to some thickness or damage effects which can show up at the interface region.

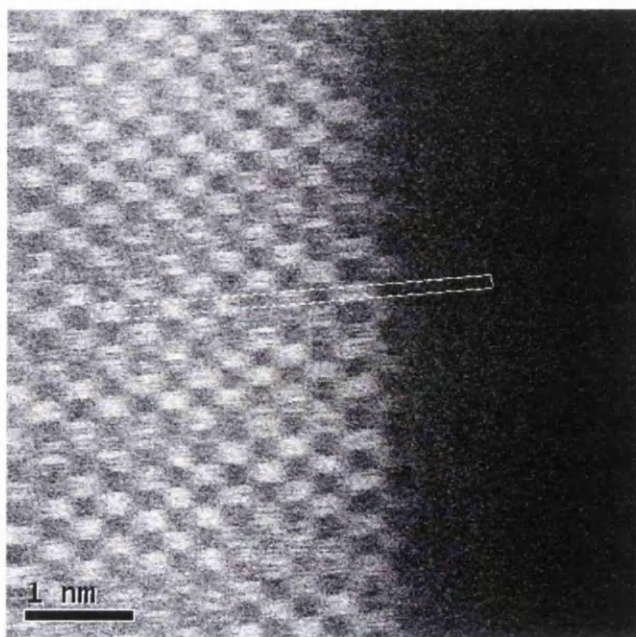


Fig. 6.9a High-resolution HAADF STEM image of the interface GaAs/Ga₂O₃ in a sample where 30nm of Ga₂O₃ have been grown on the GaAs substrate. This image has been acquired in the F20.

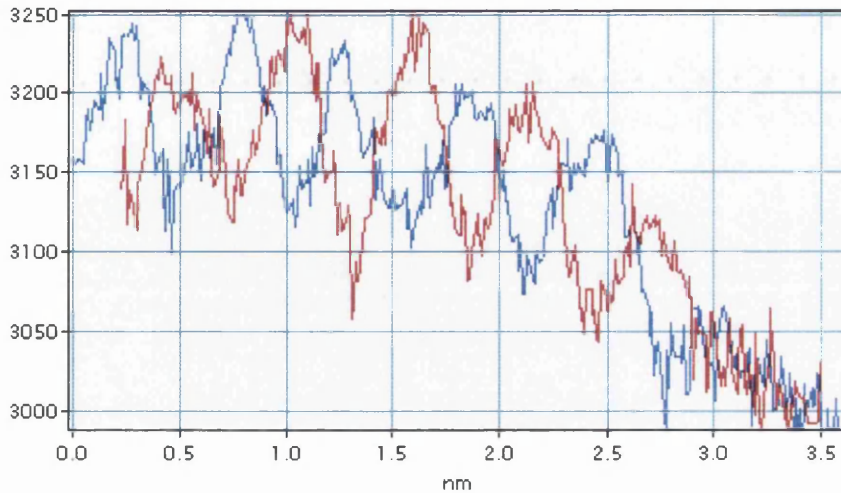


Fig. 6.9b Intensity profile of the region shown in Fig. 6.9b and from the adjacent row of dumbbells.

If the presence of the less-intense dumbbell at the interface is real, this could be due to the presence of the incomplete Ga-terminated dumbbell as shown in Fig. 6.2a when the interface is look at along the [110] direction. However, in this case, the two pieces of the cross-section were cut off along the same direction from the original wafer. Therefore it is not possible to look at this sample along the two perpendicular directions. No information from the other orientation can be extracted. Thus it is not possible to compare these results with ones from the Hale's paper [8].

6.3.2 Investigation of the interface GaAs/Ga₂O₃/GGO

In this section high-resolution HAADF STEM images of the interface region GaAs/Ga₂O₃/GGO are shown respectively from samples A, B and C. The GGO layer presents a Gd concentration of 21%, 25% and 20% in sample A, B and C respectively. Sample C was prepared using a lower substrate temperature during the MBE growth process. This should better preserve the interface region from any damage caused by the growth of the GGO that is likely to affect the quality of the interface region.

6.3.2.1 Sample A

Sample A was investigated only in the F20. Also in this case, the two pieces of the cross-section present the same orientation. Therefore, it is possible to look at the interface along only one direction. Fig. 6.10a shows a HAADF image of the GaAs/Ga₂O₃/GGO interface region. The intensity profiles in Fig. 6.10b show that the dumbbells intensity drops as the Ga₂O₃ layer is approached, indicating some interface roughness. The rise in the signal at the right hand side shows the increasing Gd content. The rate of rise is controlled by both concentration in the film, the TEM specimen thickness and the interface roughness.

Here, the interface region appears relatively rough and presents some irregularities. It looks like the roughness extends for about a monolayer. It is also possible to see some dumbbells extending in the template layer indicating the presence of a sort of ordering at the interface GaAs/Ga₂O₃/GGO. However the interface Ga₂O₃/GGO appears quite rough and irregular.

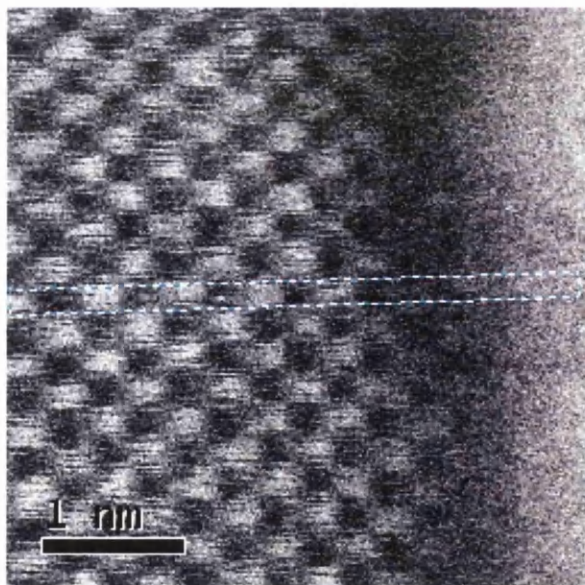


Fig. 6.10a High-resolution HAADF STEM image of the interface region in sample A. The image was acquired with the F20.

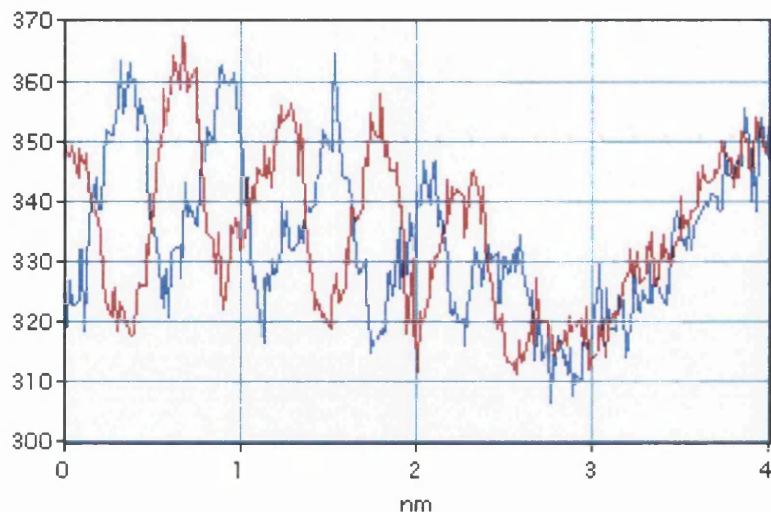


Fig. 6.10b Intensity profile from the selected region in the HAADF image shown in Fig. 7a, and the row down. All dumbbells in the GaAs have the same intensity except for the last one directly on the oxide likely for the presence of the O in the lattice structure in that region.

EELS SI analysis was also performed on this sample to better understand the chemistry at the interface. In this case different experimental conditions were employed. In particular the EELS SI were acquired in the normal mode where the beam sits on the same spot as the size of probe at full half width maximum (FWHM) which is 0.5nm and pixel are similar. Fig. 6.11 shows the O K-edge, Ga L_{2,3}-edges and Gd M_{4,5}-edges extracted from the region across the interface GaAs/Ga₂O₃/GGO. The zero on the x-axis has been set to be the main boundary between the GaAs substrate and the Ga₂O₃ template layer. The extracted edges were processed using the MLLS fitting routine and normalized to the same maximum. The O intensity extends to the left of the Gd intensity at the substrate side of the GGO. This shows the presence of the Ga₂O₃ template layer, which is ~0.7nm wide in this case. Both O and Gd intensities extend to the left towards the GaAs substrate as a result of the roughness of some monolayers along the interface GaAs/Ga₂O₃, the probe size and most importantly the beam spreading. Given a specimen thickness of 25nm, a probe of half angle 9mrad focussed on top of the specimen would have a geometric unit of 0.45nm at the bottom. This gives an idea of how the beam spreads within the specimen without any scattering events.

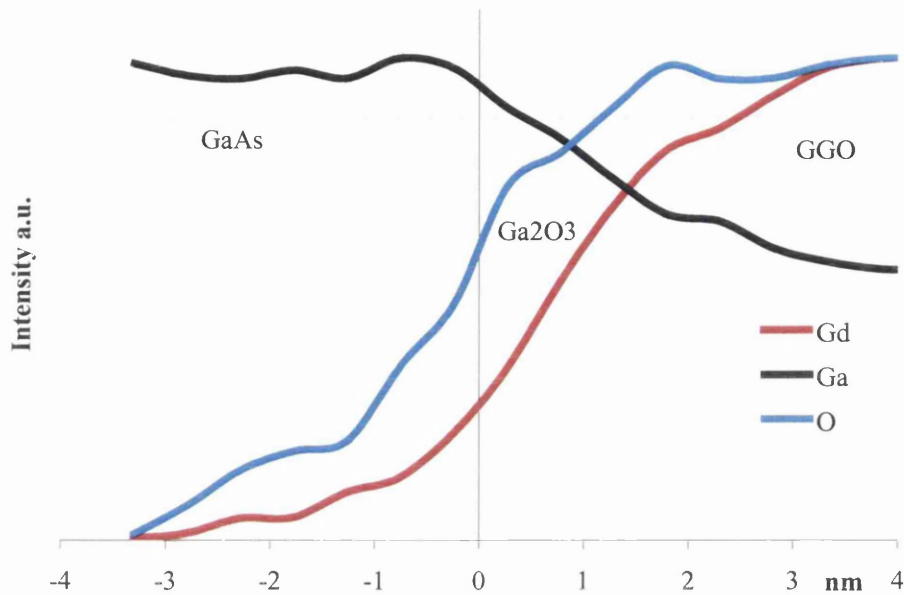


Fig. 6.11 Elemental intensity profiles, normalised to the same maximum intensity, obtained from the SI of the interface region in sample A. Note that O profile extends beyond the Gd at the substrate side because of the Ga₂O₃ template layer.

6.3.2.2 Sample B

Sample B was investigated with both SuperSTEM1 and F20 but only images from the SuperSTEM1 are shown in this thesis as they offer more detail. In the case of this sample, the two pieces of the cross-section were cut off along the two perpendicular orientations as described above. This ensures the possibility to look at the interface along [110] and [1-10] direction. However, it is not possible to classify the two directions as it is unknown how the wafer was cut after the MBE process. Therefore, the two sides of the cross-section orientated under the two perpendicular directions are indicated as side 1 and 2.

Figs. 6.12 and 6.13 show a high-resolution STEM image of the interface region GaAs/Ga₂O₃/GGO in side 1 and 2 of sample B respectively.

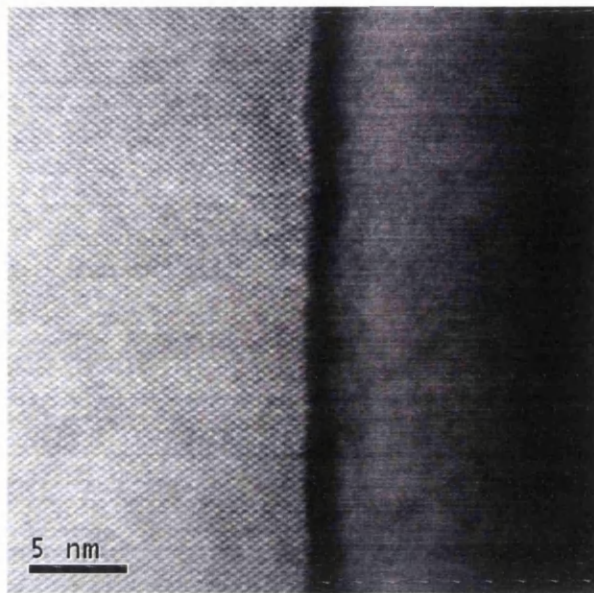


Fig. 6.12 High-resolution image of the interface GaAs/Ga₂O₃/GGO in side 1 of sample B. This image was acquired in SuperSTEM1.

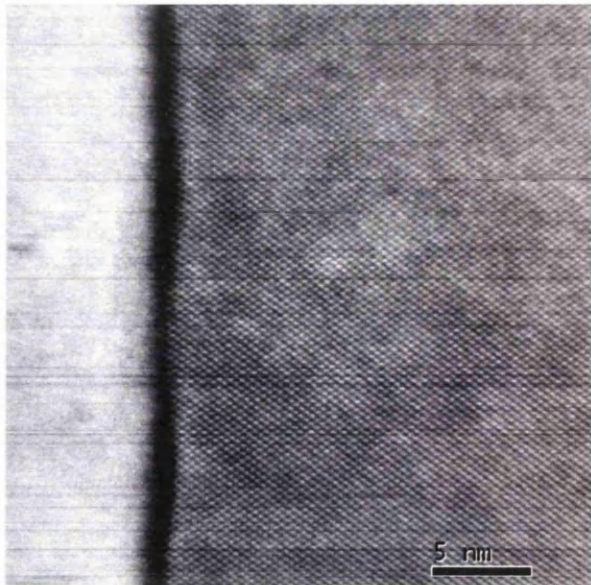


Fig. 6.13 High-resolution image of the interface GaAs/Ga₂O₃/GGO in side 2 of sample B. This image was acquired in SuperSTEM1.

Both sides present some irregularities and appear to be quite rough at the interface level. However the Ga_2O_3 layer in side 2 seems to be thinner than in side 1. Figs 6.14a and 6.15a show a higher-magnification HAADF STEM image of side 1 and 2 respectively. Both images were acquired in the same regions shown in Figs 6.12 and 6.13. Figs 6.14b and 6.15b show the intensity profiles from the selected region in Fig. 6.14a and 6.15a respectively. The interface region shown in Fig. 6.14a appears to be slightly rougher and less sharp. Looking at Fig. 6.14b, each dumbbell presents the same intensity except for the one, closest to the oxide template layer in the red row, which is half as intense. However the FWHM of this dumbbell appears to be the same as one of the nearest dumbbell column. Hence, the lower intensity could be due to some roughness which arises in the region next to the interface. The rise in the signal at the right hand side shows the increasing Gd content. The rate of rise is controlled by both concentration in the film, the TEM specimen thickness and the interface roughness. Looking at the dumbbell intensity profile shown in Fig. 6.15b the last dumbbell column in the blue line is half as intense. However, in this case the FWHM is much smaller than the one of the nearest dumbbell column. According to Hale's paper [8], this side should be projection of the interface along the $[110]$ direction.

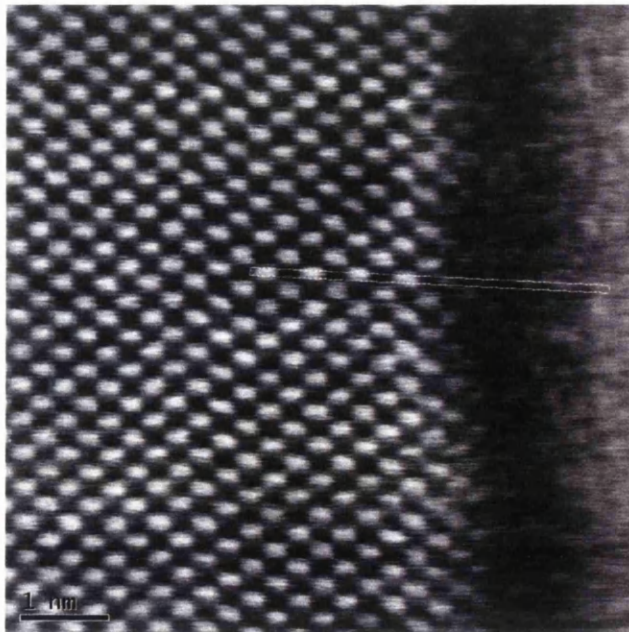


Fig 6.14a Higher-magnification HAADF STEM image of the interface region in side 1 of sample B.

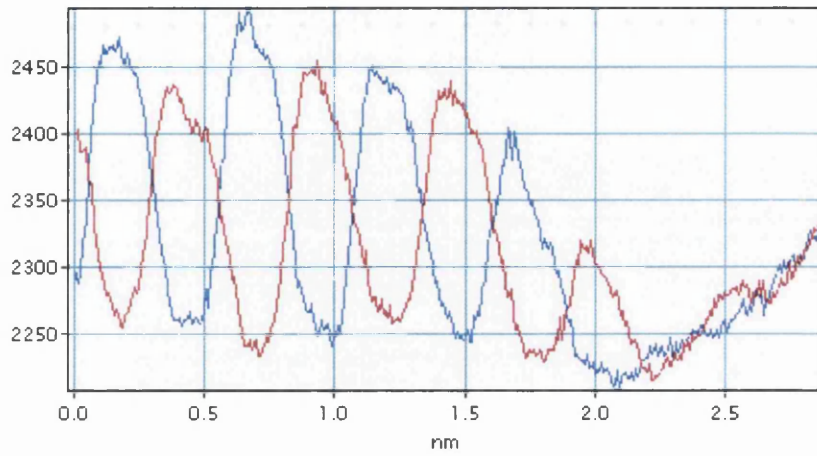


Fig. 6.14b Intensity profile from the selected region in the HAADF image shown in Fig. 6.14a, and the row down.

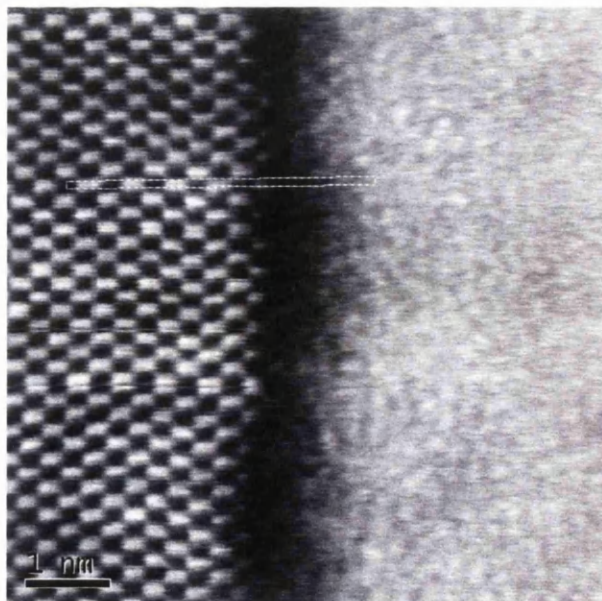


Fig 6.15a Higher-magnification HAADF STEM image of the interface region in side 2 of sample B.

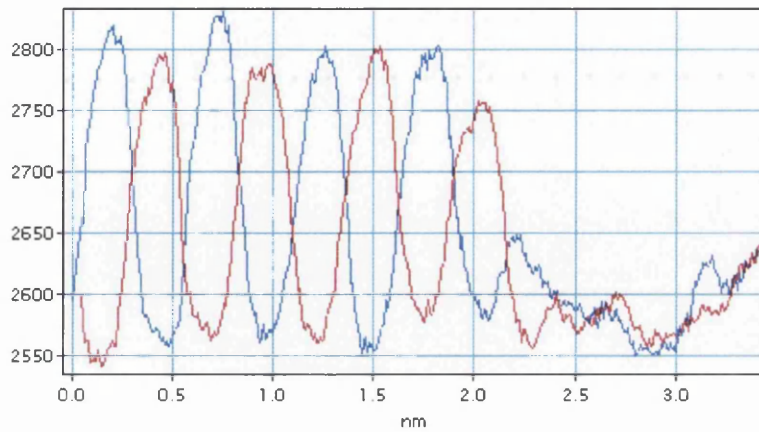


Fig. 6.15b Intensity profile from the selected region in the HAADF image shown in Fig. 6.15a, and the row down.

6.3.2.3 Sample C

Sample C was grown using a lower substrate temperature to ensure a better quality of the interface region. TEM specimen was prepared cutting the wafer off along the two perpendicular directions as shown in Fig. 6.3. Also in this case the two sides in the cross-section are named as side 1 and 2. All the images, shown here, were recorded using the SuperSTEM1. Figs 6.16a and 6.17a show high-resolution HAADF STEM images of side 1 and 2 respectively. In both cases the interface shows a zig-zag structure. The interface in side 2 appears to be smoother and sharper than side 1. This has been observed in sample B as well. However, looking at the dumbbells intensity profile of side 1 shown in Fig. 6.16b, the last two dumbbells in the red row closest to the interface are less intense. In particular the last one is even less intense. Both dumbbells have the same shape with a half of the dumbbell more intense than the other one. Both dumbbells have the same FWHM as all the other dumbbells in the GaAs region of the specimen. The lower intensity is certainly due to the roughness of the interface region which shows up better in one side as seen in sample B.

Looking at Fig. 6.17b, the closest dumbbell to the interface is half intense with the same shape as the last dumbbell shown in Fig. 6.16b. However as shown in sample B, the FWHM of this last dumbbell column is much smaller leading to a potential presence of the half occupied column which shows up when the interface is observed along the [110] direction as shown in Fig. 6.17a.

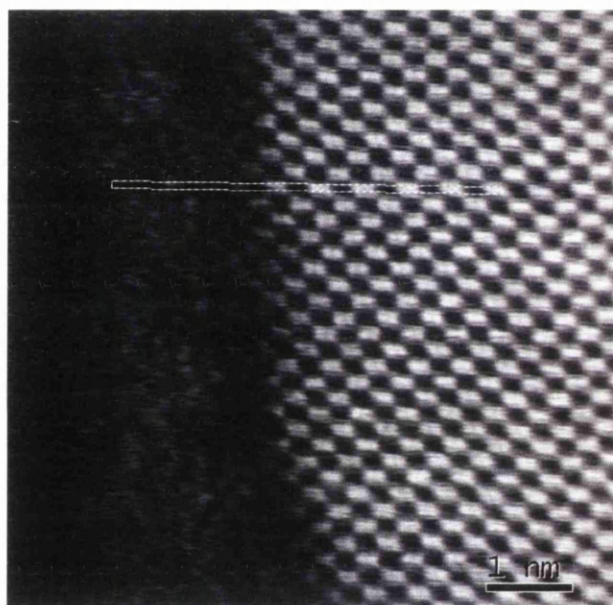


Fig. 6.16a High-resolution HAADF STEM image of the interface region in side 1 of sample C.

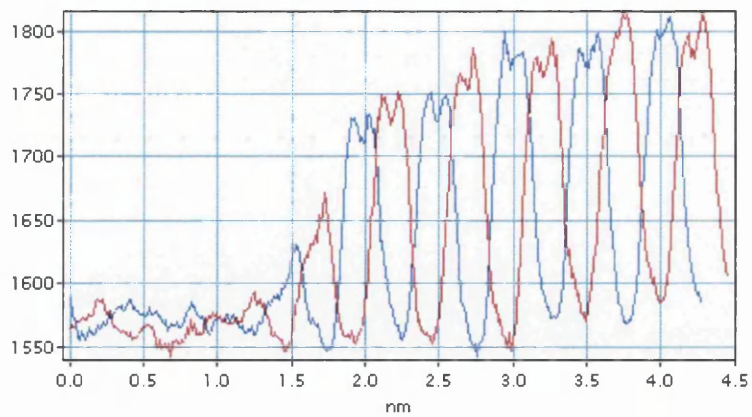


Fig. 6.16b Intensity profile from the selected region in the HAADF image shown in Fig. 13a, and the row down.

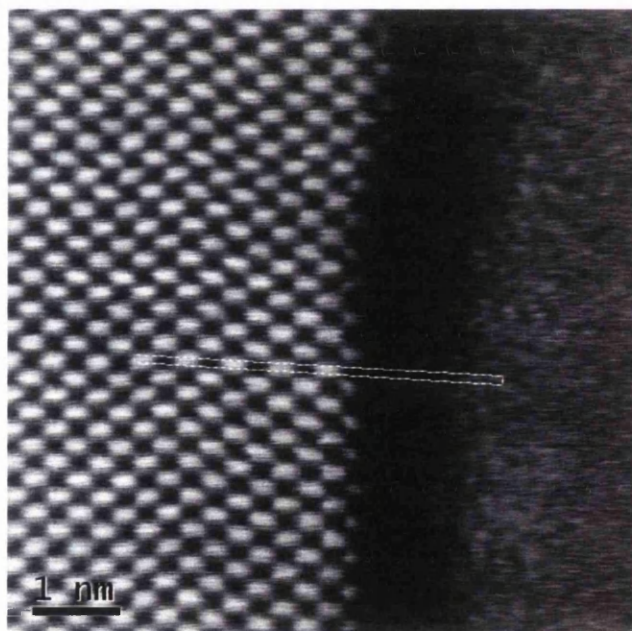


Fig. 6.17a High-resolution HAADF STEM image of the interface region in side 2 of sample C.

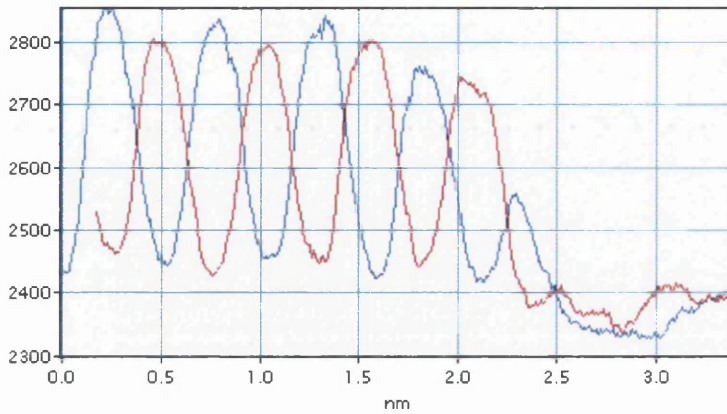


Fig. 6.17b Intensity profile from the selected region in the HAADF image shown in Fig. 6.17a, and the row down.

6.4 CONCLUSIONS

In this chapter a detailed description of the interface region has been given. Three different samples have been investigated. As expected, the lower temperature employed during the MBE growth of sample C, means that it shows the sharpest interface. In the case of sample B and C, images were acquired from the two sides of the TEM cross-section. Both sides were cut under the two perpendicular directions from the original wafer. In both samples, the interface region from one side appears to be sharper than the other one. Apparently, the last dumbbell, in the side showing the sharper interface, from both samples B and C is half as intense. The same thing as been observed in the other side. The only difference is that in the smoother side the FWHM is much smaller while the other one is rougher the same. A possible explanation may be roughness at the interface region which shows up much better when the interface is observed along one particular direction. However at this stage it is important to track the orientation the wafer is cut after the MBE. In this way it will be possible to assign the perpendicular directions [110] and [1-10] to the two sides of the cross section. What described in Hale's paper [8] is

potentially observed in the results shown in this chapter. However further work is necessary in order to understand better how the roughness can interfere on the dumbbell structure.

CHAPTER 7: CONCLUSIONS AND FURTHER WORK

7.1 CONCLUSIONS

In this project, TEM was used to investigate the dielectric oxide layers of several MBE grown GaAs based semiconductor nanostructures as grown and as processed. Up to now, increased MOSFET performance has been obtained essentially by the reduction of all dimensions of the basic MOSFET structure. As a result, the thickness of the gate dielectric is now approaching the point where further reduction will lead to a dramatic increase in the gate leakage current and solutions involving high-k dielectrics on silicon are being considered for the 45nm node [1]. As the 22nm node is approached, further problems are envisaged and GaAs n-type MOSFETs offer a potential way forward as part of a solution in tandem with a p-type MOSFET on a different substrate. GaAs offers a five times advantage of n-type mobility over Si along with the band-gap engineering that is possible in III-V systems. However, pinning of the Fermi level by interface states has prevented successful MOSFET devices being made until recently. Passlack *et al.* [2] have shown that a template layer of Ga₂O₃ grown on an As-terminated GaAs surface by molecular beam epitaxy (MBE) unpins the Fermi level. Using Ga₂O₃ alone leads to a large leakage current. This can be suppressed by incorporating Gd into the dielectric after the first 1.5nm giving gadolinium gallium oxide (GGO). Using this technology, the Glasgow Group has made GaAs MOSFETs with the best reported performance to date [3]. This dielectric stack is usually grown by MBE using 3 different fluxes on the GaAs substrate. Initially the Ga₂O₃ template layer is grown by Ga₂O and oxygen fluxes and after there is an additional flux of Gd in order to create the amorphous GGO. The quality of the resulting gate stack is then evaluated using a variety of methods including photoluminescence, C-V and magneto-transport measurements. The structure and chemistry are investigated by (scanning) transmission electron microscopy ((S)TEM) and electron energy spectroscopy (EELS). EELS is a valuable analytical technique, able to provide detailed information on the chemistry and crystallography within the sample. The presence of characteristic ionisation edges in an EELS spectrum reveals the identity of each element, while careful analysis can provide quantitative information on the overall chemical composition. In this thesis, two approaches to obtain elemental maps have been investigated. The first method is to combine the EELS with scanning transmission electron microscopy (STEM) to give a spectrum image (SI) where an EELS spectrum is collected at each point in the scan. This technique has been widely used and described in chapter 4 for the characterization of several Ga₂O₃/GGO dielectric gate stack layers with different Gd concentration. To convert the intensities to atomic fractions or ratios, either suitable cross-sections or a suitable standard is required. Accurate cross-sections for the Gd M_{4,5}-edges are not available. Thus the first quantitative analysis was performed by calibrating to the composition of one wafer as determined by RBS. As RBS is not particularly sensitive to light elements such as O, the O concentration is assumed to be 60%

throughout the GGO layer in the RBS analysis. However, the use of RBS to provide a calibration standard, based on the assumption of a 60% O concentration, does not allow an independent determination of the O concentration. Thus gadolinium gallium garnet ($\text{Gd}_3\text{Ga}_5\text{O}_{12}$) was investigated as a standard with the GaAs substrate allowing the As to be included where necessary. The comparison between the two datasets obtained using $\text{Gd}_3\text{Ga}_5\text{O}_{12}$ and RBS as standard is reported in chapter 4 for each sample. In most of the cases the agreement is good showing that the GGO is fully oxidised across the layer. However there appear to be systematic changes in the elemental concentration. In some cases they could be due to real variations but in other cases they could just be related to the presence of systematic errors such as surface layers containing O. All the Gd concentrations obtained by EELS were compared with those obtained by RBS for a range of wafers. The agreement is excellent. This further proves the quality of the analysis carried out in this thesis.

The other approach, to get an elemental map of a specific area, employed in this thesis is to use EFTEM as described in chapter 5. It has been shown that EFTEM provides rapid elemental map to identify unknown elements and can give some information on the composition. However it does not have the same sensitivity as EELS SI, therefore it cannot be used to obtain detailed information. In this thesis EFTEM has been widely used to investigate a number of ion etching processes on GaAs/Ga₂O₃/GGO. The aim of this study has been to develop a way to study the effects of etching processes on Ga₂O₃/GGO dielectric gate stacks. This obviously represents a very important issue for fabrication purposes. Electrical properties in MOSFET devices are sensitive to the elemental distribution in the dielectric gate stack, the nature of the interface across the channel and the oxide region and obviously the actual architecture. This is the reason why it is so important to study the effects of etching processes on the dielectric gate stack as they represent the key step in the fabrication process to define the areas where the gate and the ohmic contacts will be placed. One etching process was investigated using EFTEM in combination with EELS SI. Large areas of the sample can be quickly analysed by EFTEM and the regions of interest can be investigated in more details by EELS SI.

Finally in chapter 6, a detailed analysis of the interface GaAs/Ga₂O₃/GGO was carried out using HAADF STEM imaging. High angle annular dark field (HAADF) imaging carried out in the STEM, shown by a lot of other works for different systems, has revealed to be an excellent method for characterizing the interfaces as the contrast is sensitive to the atomic number. Images were acquired using both F20 and SuperSTEM1 electron microscopes. The use of the second one has allowed to get a better insight on the interface as it is fitted with an aberration corrector. Hale's model [8] predicts that the interface appears to be different whether it is observed along the [110] or the [1-10] direction. Thus TEM specimens of two different samples

have been prepared cutting the original wafer off along two perpendicular directions. This ensured the possibility to look at the interface along [110] and [1-10] directions. While some differences are seen, the period doubling predicted by the Hale mode is absent. A more detailed investigation is required.

The work presented in this thesis has helped the overall project to gain a better understanding of the effects of engineering processes on the GaAs/Ga₂O₃/GGO dielectric gate stacks. This has led to the realisation of world performance GaAs based MOSFET devices. In particular, the use of the EELS SI technique has allowed to obtain information on the composition of the GGO layer either in thick and thin GGO layers. MBE growth conditions have been improved relying on the results shown in chapter 4. This has led to the generation of dielectric oxide layers where the composition profile is more controlled. Therefore such oxide layers show less variability on the composition and hence on the electrical characteristics. The results presented in chapter 5

7.2 FURTHER WORK

The work carried out in this thesis has focused on the chemical characterization of the GaAs/Ga₂O₃/GGO dielectric gate stack as grown and as processed. EELS SI has been widely used for the compositional analysis of in thick GGO layer (>30nm). The results for the Gd concentration obtained using EELS SI have been compared with the ones obtained using RBS. The agreement has revealed to be excellent. The compositional analysis has been performed using Gd₃Ga₅O₁₂ and RBS as standards. In the case of the Gd concentration the agreement between the two datasets is good but in the case of the Ga and the O some discrepancies have been encountered. One source of these discrepancies is the presence of a surface layer whose effects show up in the thin regions. Only some results have revealed to be affected by the presence of the surface layer. It is not fully understood how the noise in the extracted Ga L_{2,3}-edges affects the compositional analysis. Another factor to take into account is the shape of the stray emission. It is not clear if it affects the Ga L_{2,3}-edges shape. Hence, further work is necessary in order to improve the signal to noise ratio and to understand the effects of the stray emission on the Ga L_{2,3}-edges.

All the EELS work carried out for this thesis is on the acquisition of the core-loss region of the EELS spectrum. Recently the acquisition of the low-loss region on the GaAs/Ga₂O₃/GGO dielectric gate stack has been carried out. The interpretation of these results is quite

complicated as there are two different interfaces. Therefore, the electron travelling near the interface will be affected by the presence of material on the other side of the interface. It is important to build up a model which ensures to predict the interface region and the effects of the electron delocalisation. However the acquisition of the low-loss region is easier due to the high signal to noise ratio. Some features in the plasmon peak are related to the Gd content in the GGO layer as shown in Figs 7.1 and 7.2 which are the 3-d representation of the extracted plasmon peak from the low-loss EELS SI across the interface region in the dielectric gate stack respectively from a sample where the Gd content is 21% and 25%. The pixel size is 0.5nm. In both cases the GGO region is characterized by the presence of a feature at $\sim 30\text{eV}$ which becomes stronger in the GGO region. However when the Gd concentration is higher, such feature appears to be stronger as shown in Fig.7.2.

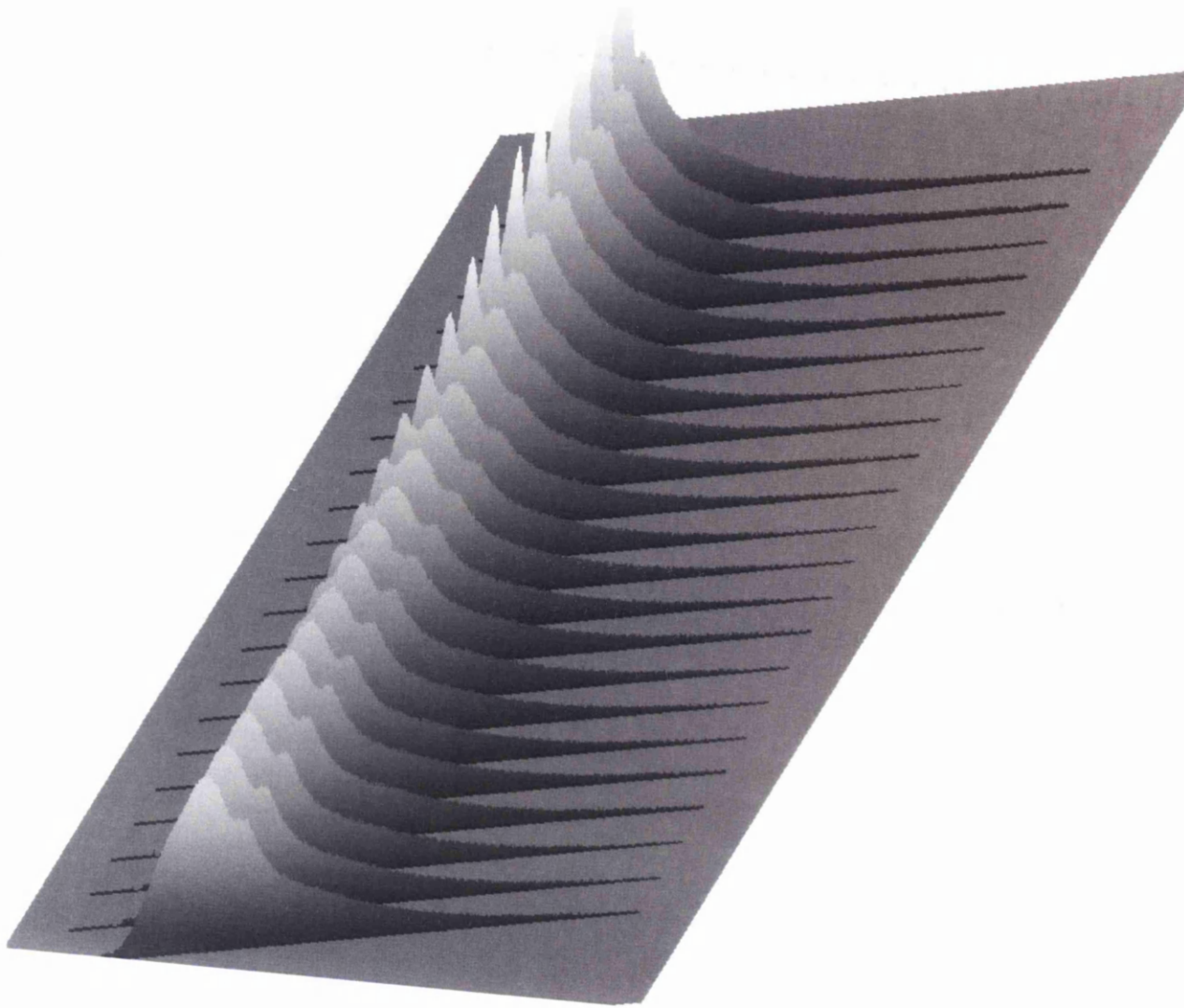


Fig. 7.1 Extracted plasmon peak from low-loss EELS SI of the interface region in sample where the Gd concentration is 21%.

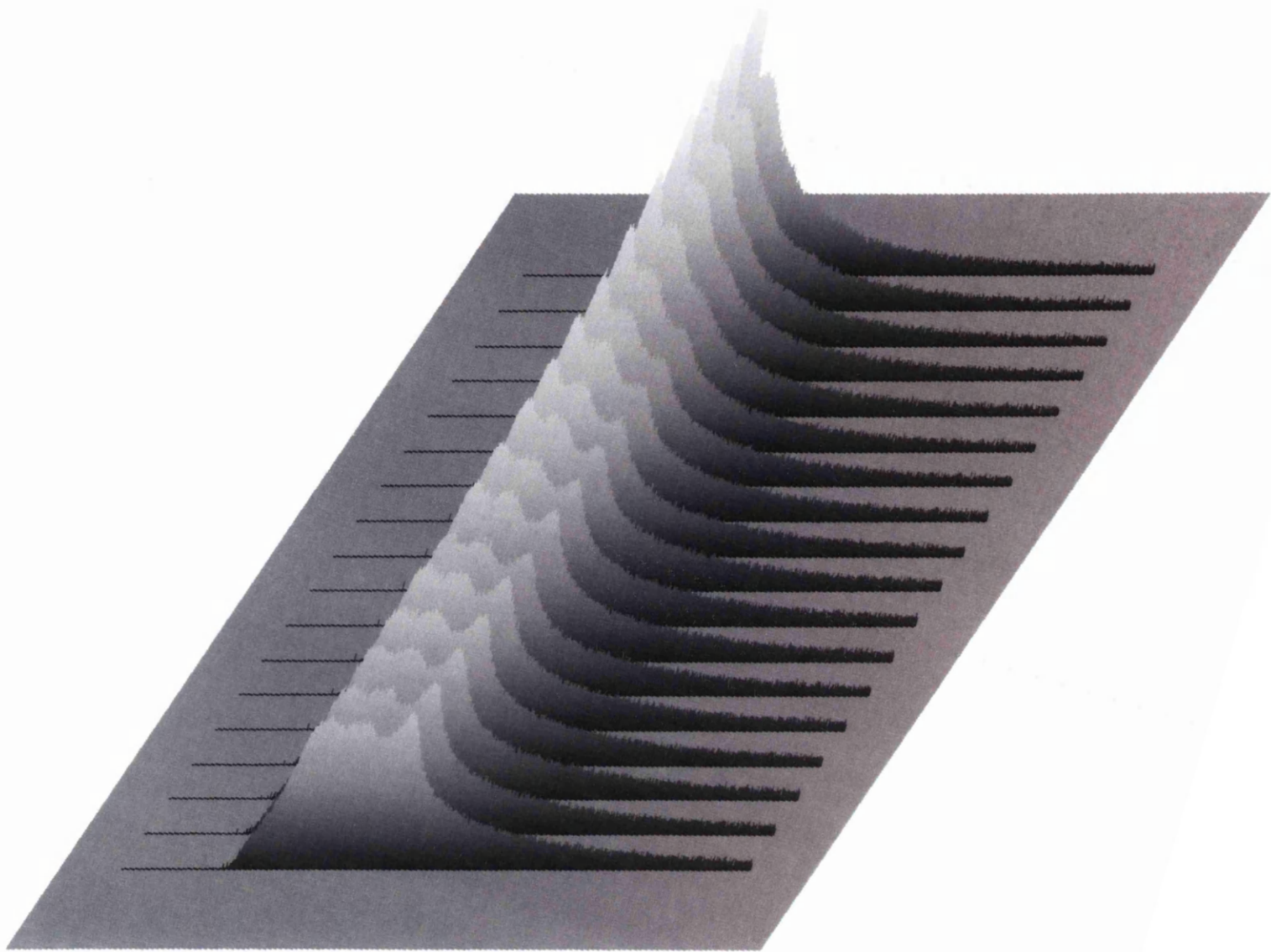


Fig. 7.2 Extracted plasmon peak from low-loss EELS SI of the interface region in sample where the Gd concentration is 25%.

Regarding the high resolution STEM imaging work dealt in chapter 6, there is in interesting information on the surface structure from the preliminary results. Now it is necessary to analyse and attempt a comparison with Hale's model [8] and variations of it. Once the key features required to differentiate between the models are clear, improved images highlighting these features need to be acquired. Further work is also necessary in order to improve our understanding of how the roughness can interfere on the dumbbell structure. Furthermore it is important to track exactly the orientation when the wafer is cut off during the specimen preparation.

REFERENCES

- [1] Y. C. Wang, M. Hong, J. M. Kuo, J. Kwo, J. P. Mannaerts, Y. K. Chen and A. Y. Cho, IEEE ELECTRON DEVICE LETTERS 20, 457, 1999
- [2] M. Passlack, J. K. Abrokwhah, R. Droopad, J. Sexton, A. C. Kummel, C. Overgaard, IEEE 23, 508, 2002
- [3] A. Callegari, P. D. Hoh, D. A. Buchanan, and D. Lacey, Appl. Phys. Lett. 54, 332, 1988
- [4] Passlack M, Medendorp N, Zollner S, Gregory R, and Braddock D, Appl. Phys. Lett. 84, 14, 2521-2523, 2004
- [5] Paterson GW, Wilson JA, Moran DAJ, Hill R, Long AR and Thayne IG, Materials Science Engineering B, 135, 277-281, 2006
- [6] J. Kwo, D. W. Murphy, M. Hong, J. P. Mannaerts, R. L. Opila and A. M. Sergent, J. Vac. Technol. B 17, 1294, 1999
- [7] M. Passlack, N. Menendorp, R. Gregory and D. Braddock, Appl. Phys. Lett. 83, 5262, 2003
- [8] Hale MJ, Yi SI, Sexton JZ, Kummel AC and Passlack M, Journal of Chemical Physics 119, 6719, 2003
- [9] Holland M, Stanley CR, Reid W, Patterson GW, Long AR, Longo P, Scott J, Craven AJ and Thayne IG, J. Vacuum Science B, 25, 1024-1028, 2007
- [10] Droopad R, Abrokwhah J, Rajagopalan K, Adams L, England N, Uebelhoer D, and Passlack M, J. of Crystal Growth, 301-302, 139-144, 2007
- [11] Egerton RF, Electron Energy Loss Spectroscopy in the Electron Microscope, Plenum Press, NY, 1996
- [12] McComb DW, Brydson R, Hansen PL, Payne RS, J. Phys. Cond. Mat., 4, 8363, 1992
- [13] D. B. Williams and C. B. Carter, Transmission electron microscopy, Plenum Press, 1996
- [14] Robert D, Heidenreich, Fundamentals of transmission electron microscopy Volume XIII, Interscience monographs and texts in physics and astronomy, John Wiley & Sons, Inc., 1964
- [15] J.A. Belk, Electron microscopy and microanalysis of crystalline materials, Applied Science Publishers LTD, 1978
- [16] Rodenburg JM, Macak EB, Microscopy and Analysis (UK), 90, 5-7, 2002
- [17] Egerton RF, Cheng SC, Ultramicroscopy, 21, 231, 1987
- [18] Craven AJ, Garvie LAJ, Brydson R, Amer. Mineral., 79, 411, 1994
- [19] Scott AJ, Brydson R, MacKenzie M, Craven AJ, Phys. Rev. B, 63, 245105, 2001
- [20] Tossel JA, J. Phys. Chem. Solids, 34, 307, 1973

- [21] Paxton AT, Craven AJ, Gregg JM, McComb DW, *J. Microsc.*, 210, 35, 2003
- [22] Rehr JJ, Albers RC, *Rev. Mod. Phys.*, 72, 621, 2000
- [23] Rehr JJ, *J. Phys. Cond. Matter*, 15, 647, 2003
- [24] Lee PA, Pendry JB, *Phys. Rev. B*, 11(8), 2795, 1975
- [25] Ankudinov AL, Ravel B, Rehr JJ, Sims J, Hung H, *Phys. Rev. B*, 58(12), 7565, 1998
- [26] De Groot FMF, *J. Elect. Spectros. Rel. Phenom.*, 67, 529, 1994
- [27] Zabinsky, SI, Rehr JJ, Ankudinov AL, Albers RC, Eller MJ, *Phys. Rev. B*, 52(4), 2995, 1995
- [28] Crozier PA, *Phil. Mag. B* 61, 311, 1990
- [29] Longo P, Craven AJ, Holland M, Moran DAJ and Thayne IG, submitted to *Microelectronic Engineering*
- [30] Shuman H, Somlyo AV, Safer D, Frey T, Somlyo AP, *Scan. Elec. Microsc.*, 737, 1985
- [31] Krivanek OL, Gubbens AL, Delby N, *Microsc. Microanal. Microst.*, 2, 315, 1991
- [32] Krivanek OL, Gubbens Al, Kundmann MK, Carpenter GC, *Proceedings of 51th EMSA Meeting*, San Francisco Press, 586, 1993
- [33] Crozier PA, *Ultramicroscopy*, 58, 157, 1995
- [34] Hofer F, Warbincler P, Grogger W, *Ultramicroscopy*, 59, 15, 1995
- [35] Shuman H, Chang CF, Somlyo AP, *Ultramicroscopy*, 19, 121, 1986
- [36] Hoffer F, Grogger W, Kothleitner G, Warbincler P, *Ultramicroscopy*, 67, 83, 1997
- [37] Hofer F, *Ultramicroscopy*, 21, 63, 1987
- [38] Colliex C, *Ann. New York Acad. Sci.*, 483, 311, 1986
- [39] Navidi-Kamai T, Kohl H, *Ultramicroscopy*, 81, 223, 2000
- [40] Crozier PA, Chapman JN, Craven AJ and Titchmarsh, *J. Microsc.* 146, 1, 1987
- [41] Egerton RF, *Ultramicroscopy*, 9, 387, 1982
- [42] Egerton RF, *Scanning Electr. Microsc.*, 2, 505, 1984
- [43] Reimer L, *Adv. Electron. Electron Phys.*, 81, 43, 1991
- [44] Longo P, Scott J, Craven AJ, Hill RWJ and Thayne IG, accepted for publication in the proceedings of EMAG 2007.
- [45] Pennycook SJ and Jesson DE, *Physical Review Letters*, 64, 1990
- [46] Pennycook SJ and Nellist PD, *Scanning Microscopy*, 11, 81, 1197
- [13] Williams and Carter, *Transmission electron Microscopy*, Plenum Press, 1996
- [47] Pennycook SJ et al., *Ultramicroscopy* 37, 14, 1999
- [48] Kirkland EJ, Plenum Press, New York, 1998

- [49] Browning ND et al., EELS in the STEM, *Micron*, 28, 313, 1997
- [50] Dwyer C and Etheridge J, *Ultramicroscopy*, 96, 343, 2003
- [51] Rodenburg JM and Lupini AR, Institute of Physics Conference Series N. 161 (EMAG 1999), 339
- [52] Krivanek OL et al., *Ultramicroscopy* 78, 1, 1999
- [53] Knoll M and Ruska E, *Physik Z*, 78, 318, 1932
- [54] Tecnai on line help manual
- [55] Cowley JM, *Ultramicroscopy*, 4, 413, 1979
- [56] Cowley JM, *Ultramicroscopy*, 7, 19, 1981
- [57] Scherzer O., *Z Physik*, 101, 593, 1937
- [58] Valera M et al., *Annual Review of Material Research*, 35, 359, 2005
- [59] Krivanek OL et al., *Ultramicroscopy*, 78, 1, 1999
- [60] Nellist PD et al., *Science*, 305, 2004
- [61] Krivanek OL, Delby N and Lupini AR, *Ultramicroscopy*, 78, 1, 1999
- [62] Delby et al., *Journal of Electron Microscopy*, 50, 177, 2001
- [63] Craven AJ, Wilson AJ and Nicholson WAP, *Ultramicroscopy*, 92, 165, 2002
- [64] Gatan Digital Micrograph Software version 3.4
- [65] Kirkland EJ, Plenum Press, New York, 1998